Q-SWITCHING AND MODE-LOCKING PULSE GENERATION IN YTTERBIUM-DOPED FIBER LASERS USING NANOMATERIAL SATURABLE ABSORBERS

AHMED HASAN HAMOOD AL-MASOODI

FACULTY OF ENGINEERING
UNIVERSITY OF MALAYA
KUALA LUMPUR

2017

Q-SWITCHING AND MODE-LOCKING PULSE GENERATION IN YTTERBIUM-DOPED FIBER LASERS USING NANOMATERIAL SATURABLE ABSORBERS

AHMED HASAN HAMOOD AL-MASOODI

THESIS SUBMITTED IN FULFILMENT OF THE REQUIREMENTS FOR THE DEGREE OF DOCTOR OF PHILOSOPHY

FACULTY OF ENGINEERING
UNIVERSITY OF MALAYA
KUALA LUMPUR

2017

UNIVERSITY OF MALAYA

ORIGINAL LITERARY WORK DECLARATION

Name of Candidate: AHMED HASAN HAMOOD AL-MASOODI

Matric No: KHA140061

Name of Degree: Doctor of Philosophy

Title of Project Paper/Research Report/Dissertation/Thesis ("this Work"):

Q-SWITCHING AND MODE-LOCKING PULSE GENERATION IN YTTERBIUM-DOPED FIBER LASERS USING NANOMATERIAL SATURABLE ABSORBERS Field of Study: PHOTONICS

I do solemnly and sincerely declare that:

(1) I am the sole author/writer of this Work;
(2) This Work is original;
(3) Any use of any work in which copyright exists was done by way of fair dealing and for permitted purposes and any excerpt or extract from, or reference to or reproduction of any copyright work has been disclosed expressly and sufficiently and the title of the Work and its authorship have been acknowledged in this Work;
(4) I do not have any actual knowledge nor do I ought reasonably to know that the making of this work constitutes an infringement of any copyright work;
(5) I hereby assign all and every rights in the copyright to this Work to the University of Malaya ("UM"), who henceforth shall be owner of the copyright in this Work and that any reproduction or use in any form or by any means whatsoever is prohibited without the written consent of UM having been first had and obtained;
(6) I am fully aware that if in the course of making this Work I have infringed any copyright whether intentionally or otherwise, I may be subject to legal action or any other action as may be determined by UM.

Candidate's Signature Date:

Subscribed and solemnly declared before,

Witness's Signature Date:

Name:

Designation:

Q-SWITCHING AND MODE-LOCKING PULSE GENERATION IN YTTERBIUM-DOPED FIBER LASERS USING NANOMATERIAL SATURABLE ABSORBERS

ABSTRACT

This research work focuses on exploring various new nanomaterials for saturable absorber (SA) application in generating Q-switched and Mode-locked pulses operating at 1 μm region. These nanomaterials are Molybdenum disulfide (MoS_2), Black Phosphorus (BP), Topological Insulator (TI): Bismuth (III) Selenide (Bi_2Se_3), Bismuth (III) Telluride (Bi_2Te_3), and antimony telluride (Sb_2Te_3), and metal oxide: Nickle Oxide (NiO) nanoparticles and cobalt oxide (Co_3O_4) nanocubes. The fiber laser employs Ytterbium-doped fiber (YDF) as a gain medium. Firstly, molybdenum disulfide (MoS_2) was proposed. The Q-switched laser was obtained by using few layers MoS_2, which was mechanically exfoliated by using a scotch tape. The SA was sandwiched between two fiber ferrules to form a fiber compatible Q-switcher. By incorporating the SA inside the YDFL cavity, a stable pulse laser operating at 1070.2 nm wavelength was generated with the repetition rate was tunable from 3.817 to 25.25 kHz. A passively mode-locked YDFL was demonstrated using a few layered MoS_2 film which was obtained by a liquid phase exfoliation technique. The mode-locking pulses have a repetition rate of 18.8 MHz and pulse energy of 0.1 nJ. Secondly, mechanically exfoliated Black phosphorus (BP) was proposed for both Q-switching and mode-locking pulses generation. The Q-switched laser has a pump threshold of 55.1 mW, a pulse repetition rate that is tunable from 8.2 to 32.9 kHz, the narrowest pulse width of 10.8 μs and the highest pulse energy of 328 nJ. BP based mode-locked YDFL was obtained by improving the SA preparation. The laser operated at 1033.76 nm with a fixed repetition rate of 10 MHz. Passively Q-switched YDFLs was also successfully demonstrated using a few-layers Bi_2Se_3, Bi_2Te_3 and

antimony telluride (Sb_2Te_3) based SAs. For instance, a Sb_2Te_3 film based Q-switched YDFL produced pulse repetition rate, which was tunable from 24.4 to 55 kHz with the maximum pulse energy of 252.6 nJ at 82.3 mW pump power. The mode-locked YDFL operating at 24.2 MHz repetition and 18.8 ps pulse width were also realized with Sb_2Te_3 based SA. Finally, two transition metal oxide nanomaterials: Nickel Oxide (NiO) and cobalt oxide (Co_3O_4) were embedded into a polymer film, making it an SA device for both Q-switched and mode-locked YDFLs. Stable Q-switched and mode-locked YDFLs were realized with both materials. For instance, the mode-locked Co_3O_4 based YDFL was operated at 1035.8 nm wavelength with a fixed repetition rate of 20 MHz and picoseconds pulse width. In short, an efficient and low-cost Q-switched and mode-locked YDFLs operating in 1 μm region have been successfully achieved by utilizing various new nanomaterials as SA.

Keywords: Q-switching, Mode-locking, Ytterbium-doped fiber (YDF), Saturable Absorber (SA).

PENJANAAN DENYUTAN Q-SUIS DAN MOD-KUNCI DALAM LASER GENTIAN BERDOP YTTERBIUM DENGAN MENGGUNAKAN BAHAN PENYERAP TEPU NANO

ABSTRAK

Penyelidikan ini tertumpu kepada kerja-kerja penerokaan bahan-nano baharu sebagai penyerap tepu (SA) bagi penghasilan denyut suis-Q dan mod-kunci yang beroperasi pada kawasan 1 μm. Bahan-nano ini adalah molibdenum disulfida (MoS_2), fosforus hitam (BP), topologi penebat (TI): Bismut (III) selenida (Bi_2Se_3), Bismut (III) Telluride (Bi_2Te_3), dan telluride antimoni (Sb_2Te_3), dan logam oksida: Nikel oksida (NiO) zarah-nano dan kobalt oksida (Co_3O_4) kiub-nano. Laser gentian menggunakan gentian terdop-Ytterbium (YDF) sebagai medium gandaan. Pada awalnya, molibdenum disulfida (MoS_2) telah dicadangkan. Laser suis-Q diperolehi dengan menggunakan beberapa lapisan MoS_2 yang telah dikelupas secara mekanikal dengan menggunakan pita lekat. SA telah diapit di antara dua *ferrules* gentian untuk membentuk gentian Q-pengsuisan. Dengan menggabungkan SA kedalam rongga YDFL, operasi denyut laser yang stabil telah dihasilkan pada panjang gelombang 1070.2 nm dengan kadar ulangan boleh laras dari 3.817 sehingga 25.25 kHz. YDFL mod-kunci pasif telah didemostrasikan dengan mengguna filem berlapis MoS_2 yang diperolehi dengan menggunakan teknik pengelupasan fasa cecair. Denyut mod-kunci mempunyai kadar pengulangan 18.8 MHz dan tenaga denyut sebanyak 0.1 nJ. Pada bahagian kedua, BP yang dikelupas secara mekanikal telah dicadangkan untuk penjanaan denyut Q-suis dan mod-kunci. Laser Q-suis mempunyai ambang pam 55.1 mW, kadar ulangan denyut boleh laras dari 8.2 sehingga 32.9 kHz, lebar denyut yang paling sempit 10.8 μs dan tenaga denyut tertinggi 328 nJ. YDFL mod-kunci berasaskan BP diperolehi dengan meningkatkan mutu penyediaan SA. Laser beroperasi pada 1033.76 nm dengan kadar ulangan tetap pada 10 MHz. Pasif YDFL Q-suis juga berjaya dihasilkan menggunakan beberapa lapisan Bi_2Se_3,

Bi_2Te_3 dan telluride antimoni (Sb_2Te_3) berasaskan SA. Sebagai contoh, filem Sb_2Te_3 berasaskan YDFL Q-suis menghasilkan kadar pengulangan denyut boleh laras dari 24.4 sehingga 55 kHz dengan tenaga denyut maksimum 252.6 nJ pada kuasa pam 82.3 mW. Operasi YDFL mod-kunci pada kadar ulang 24.2 MHz dan 18.8 ps lebar denyut juga direalisasikan dengan SA berasaskan Sb_2Te_3. Akhir sekali, dua peralihan logam oksida bahan-nano: Nikel Oksida (NIO) dan kobalt oksida (Co_3O_4) telah terbenam ke dalam filem polimer, menjadikannya peranti SA untuk kedua-dua YDFL Q-suis dan mod-kunci. YDFL Q-suis dan mod-kunci yang stabil dapat dicapai dengan kedua-dua bahan tersebut. Sebagai contoh, YDFL mod-kunci berasaskan Co_3O_4 telah beroperasi pada panjang gelombang 1035.8 nm dengan kadar ulangan tetap 20 MHz dan lebar denyut pikosaat. Secara ringkasnya, YDFL Q-suis dan mod-kunci beroperasi di kawasan 1 μm yang cekap dan murah telah berjaya dicapai dengan menggunakan bahan-nano baharu sebagai SA.

Kata kunci: Q-suis, Mod-kunci, Gentian Terdop-Ytterbium (YDF), Penyerap Tepu (SA).

ACKNOWLEDGEMENTS

I would like to express my greatest gratitude to my supervisors Prof. Ir. Dr. Sulaiman Wadi Harun and Prof. Dr. Hamzah Bin Arof for their continuous guidance and patience towards my research development process. They have guided me strictly to make sure that I could produce my best effort. They have spent their valuable time to discuss all problems and issues I had faced.

In addition, I would like to greatly thank my family for their continuous support and help, especially my parents who always care for my study and try to be patient for my absence, thanks to them for understanding and giving me this chance to complete my PhD research.

Last but not least, I want to take this opportunity and thank all my friends who gave me their words of encouragement and motivated me to finish my PhD research.

Thank you

TABLE OF CONTENTS

LIST OF FIGURES

LIST OF TABLES

LIST OF SYMBOLS AND ABBREVIATIONS

For examples:

LD	:	Laser Diode
UV	:	Ultra-voilet
Yb	:	Ytterbium
Yb^{3+}	:	Ytterbium ion
YDF	:	Ytterbium-doped fibe laser
YDFL	:	Ytterbium-Doped Fiber Laser
EDFL	:	Erbium-Doped Fiber Laser
SA	:	Saturable Absorber
CVD	:	Chemical Vapour Deposition
LPE	:	Liquid phase exfoliation
CW	:	Continuous Wave
DMF	:	*N*-dimethylformamide
DI	:	Deionized
YDF	:	Ytterbium-Doped Fiber
WDM	:	Wavelength division multiplexer
FWHM	:	Full-Width at Half Maximum
FWM	:	Four-wave mixing
OSA	:	Optical Spectrum Analyzer
OSC	:	Oscilloscope
OPM	:	Optical power meter
SNR	:	signal-to-noise ratio
PC	:	Polarization Controller
PVA	:	Polyvinyl Alcohol

PEO	:	Polyethylene Oxide
RE	:	Rare-Earth
SDS	:	Solium Dedecyl Sulfate
SMF	:	Single Mode Fiber
SRS	:	Stimulated Raman Scattering
NPR	:	Nonlinear Polarization Rotation
NA	:	Numerical aperture
GVD	:	Group Velocity Dispersion
MOCVD	:	Metal-organic chemical vapor deposition
RF	:	Radio Frequency
TBP	:	Time-Bandwidth Product
1D	:	One-Dimensional
2D	:	Two-Dimensional
SESAMs	:	Semiconductor Saturable Absorber Mirrors
CNTs	:	Carbon Nanotubes
TMDs	:	Transition Metal Dichalcogenides
MoS_2	:	Molybdenum disulfide
PB	:	Black Phosphorus
TIs	:	Topological Insulators
Bi_2Se_3	:	Bismuth (III) Selenide
Bi_2Te_3	:	Bismuth (III) Telluride
Sb_2Te_3	:	Antimony Telluride
Te	:	Tellurium
NiO	:	Nickle Oxide
Co_3O_4	:	Cobalt (II, III) oxide
TiO_2	:	Titanium dioxide

E_v	:	Energy level of valance band
E_c	:	Energy level of conduction band
T_{BL}	:	Time Bandwidth Product
$Sech^2$	:	Hyperbolic-secant-squared
XRD	:	X-ray Powder Diffraction
TEM	:	Transmission electron microscopy
FESEM	:	Field Emission Scanning Electron Microscopy
GNS	:	Graphene nanosheets
SML	:	Self-mode locking
TDFL	:	Thulium doped fiber laser

CHAPTER 1: INTRODUCTION

1.1 Overview of Laser and Pulse Fiber Laser

Lasers have many applications in our daily life, such as being used in households' appliances, hospitals' tools and communication means. Fiber lasers are one type of lasers that have undergone a lot of development efforts in the last two decades. They have become the main focus of interest to many researches, due to their high reliability, improved beam quality, lower noise floor and higher power application; as compared to the solid state and semiconductor lasers. Laser is found in various industrial applications such as material processing, optical communications, spectroscopy and imaging (Siegman, 1986; H. Zhang et al., 2009). The laser operating regimes can be classified on the basis of temporal characteristic of optical output power. Concentrating the available energy in a single, short optical pulse, or in a periodic sequence of optical pulses; transient laser behavior can generate higher peak power than the one shown by the continuous wave (CW) laser. The most important regimes are continuous wave (CW), Q-switching, mode-locking, and Q-switched mode-locking.

Fiber lasers have a broad range of applications ranging from industry to optical communication. Various laser setup generates pulse with different and distinctive pulse characteristics. Subsequently, each laser setup can be tailored to accommodate for one or some other applications. For an instance, Q-switched laser with high peak intensity and high pulse energy is suitable for micromachining and drilling which benefits the medical, electronic and automotive industry (Nikumb et al., 2005). Q-switched lasers are also used in the medical fields especially in eye and dental surgery (Plamann et al., 2010; Serbin et al., 2002). Eye surgery is one of the applications of pulsed laser by which the system is known as the laser-assisted in situ keratomileusis (LASIK) (Kezirian et al., 2004). In LASIK, ultra-voilet (UV) laser is also used to photo-ablate the corneal tissue rather than mechanical cutting since the later will somehow damage the surface layer or cornea and

the surrounding cells. Moreover, Q-switched laser is invested heavily to mark information such as batch number, manufactured date and logo in the electronic semiconductor manufacturing industry (Noor et al., 1994). On the other hand, mode-locked lasers can be used to generate ultra-short pulses train. Ultra-short pulsed fiber lasers have attracted widespread interests because of their useful applications in many areas such as micromachining, communication, and optical systems (Bao et al., 2009; Norihiko Nishizawa, 2014).

Both Q-switched or mode-locked fiber lasers can be generated by either active or passive techniques. The active technique was usually realized by integrating an external controller device such as acoustic-optic modulator to actively modulate the light of the intracavity (Bello-Jiménez et al., 2010). On the opposite side, the passive technique utilizes saturable absorption of optical material to change the intra-cavity light and generates pulsed laser in the cavity (De Tan et al., 2010). Passive Q-switching laser operation depends on the gain medium as well as the saturable absorber (SA) which acts as a Q-switcher and it occurs when the photon flux starts to show a gain, fixed loss and saturable loss in the SA after many round-trips. The first SA was demonstrated in 1966 to generate pulses in Nd: glass laser (Stetser et al., 1966).

Passive mode-locking uses SA in a laser cavity to produce pulses of light of extremely short duration, on the order of nanoseconds to picoseconds. The basis of the technique is to induce a fixed-phase relationship between the longitudinal modes of the laser's resonant cavity. The repetition rate is defined as a free spectral range of cavity in MHz for few meter fiber laser cavity (H. Zhang et al., 2010). The main point for generation mode-locking fiber laser is to get higher repetition rate. The passive Q-switched and mode-locking method has become a commonly explored in recent years because of its simplicity as opposed to the active method (Grelu et al., 2012; A. P. Luo et al., 2011; H. Zhang et

al., 2010). To date, many passive techniques are proposed and demonstrated to generate Q-switched and mode-locked fiber lasers. Therefore, this study aimed to demonstrate Q-switched and mode-locked fiber lasers operating at 1 micron region using new types of SAs.

1.2 Recent Progress in Saturable Absorber Technology

Saturable absorption is a property of materials where the absorption of light decreases with increasing light intensity. Most materials show some saturable absorption, but often only at very high optical intensities (close to the optical damage). At sufficiently high incident light intensity, atoms in the ground state of a saturable absorber (SA) material become excited into an upper energy state at such a rate that there is insufficient time for them to decay back to the ground state before the ground state becomes depleted, and the absorption subsequently saturates. Figure 1.1 shows a simple description of the basic principle of the SA that is based on energy levels of the SA material for the valence band (E_v) and conduction band (E_c). Electrons in the valence band are excited up to the conduction band by the incident light. Most of photons are absorbed for low intensity and negligible number for high intensity due to the occupation of electronic density of states in the conduction bands. Thus, the saturable absorption appears depending on the transparency of the optical intensity.

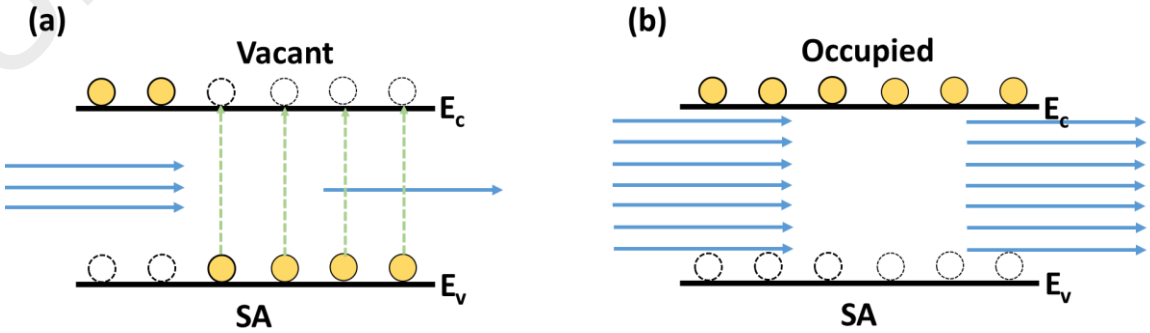

Figure 1.1: Schematic diagram of the saturable absorber's principle for (a) low incident light intensity (b) high incident light intensity

For an optical fiber system, the SA is inserted into the laser cavity. The light is passed through the SA in both high and low intensities. A high proportion of constituent photons in low-intensity light will be absorbed by the electrons at the valance band then excite of these electrons to the conduction band of the SA. In the other hand, the absorbance of the photons will decrease at high intensity. During each round trip, an intensity-dependent attenuation is created and appears in the low loss for high intensity and high loss for low intensity leading to not passing of an optical pulse through the SA (Kashiwagi et al., 2010). Therefore, the passed light through the saturable absorber leads to high-intensity contrast and starts to oscillate in the pulsed state. The key parameters for a saturable absorber are its wavelength range (where it absorbs), its dynamic response (how fast it recovers), and its saturation intensity and fluence (at what intensity or pulse energy it saturates). They are commonly used for passive Q-switching and mode-locking.

Up to date, there are various kind of SAs have been proposed such as semiconductor saturable absorber mirror (SESAM) (M. Zhang et al., 2009), graphene (Z. Sun et al., 2010), and carbon nanotube (CNT) (Della Valle et al., 2006). SESAMs were widely used since they have excessive flexibility, stability, and fast amplitude modulation. However, they have many drawbacks such as greater pricey, tough fabrication strategies, narrower wavelength operation range and contain a limited bandwidth of optical response (Ursula Keller et al., 1996). Thus, other SA materials have gained the attention of researchers due to their high overall performance, cheaper and broadband operation in the optical laser. In more recent years, CNTs and graphene had been commonly investigated in understanding all pulse fiber lasers due to their extensive absorption range and proper compatibility with optical fibers. However, CNTs and graphene have comparatively low modulation depth, which restricted their application for high power pulsed fiber lasers (Ahmed et al., 2014; Tolstik et al., 2014).

A new family of 2D nanomaterial; such as Black Phosphorus (BP) and molybdenum disulfide (MoS_2), is also drawing more interest for both Q-switching and mode-locking fiber laser applications. Topological insulators (TIs) have been shown to be capable of generating Q-switched and mode-locked lasers (Y. Chen et al., 2014; H. Liu, X.-W. Zheng, et al., 2014). Since TIs have a large modulation depth with an efficient saturable absorption property, they are suitable for making SAs. Very recently, a new kind of metal nanoparticles material such as gold, silver nanoparticles and titanium dioxide (TiO_2) were also investigated and demonstrated as a SA for Q-switched and mode-locked fiber laser (H Ahmad, Siti Aisyah Reduan, et al., 2016; Glubokov et al., 2014; T. Jiang et al., 2013). In this thesis, four types of passive SAs; Black phosphorus, MoS_2, TIs and transition metal oxide are explored for generating Q-switching and mode-locking pulses in Ytterbium-doped fiber laser (YDFL) cavity.

1.3 Research Objectives

The aim of this work to fabricate and demonstrate an efficient and low-cost Q-switched and mode-locked YDFLs operating in 1 μm region by utilizing new nanomaterials as SA. The following objectives have been outlined to achieve the aim;

1. To fabricate and characterize several types of nanomaterials based SAs, Molybdenum disulfide (MoS_2), Black Phosphorus (BP), Topological Insulators (TIs), Nickle Oxide (NiO) nanoparticles, and Cobalt oxide (Co_3O_4) nanocubes.
2. To demonstrate the capability of the fabricated materials saturable absorber (SA) to generate high pulse energy of Q-switched Ytterbium-Doped Fiber Laser.
3. To investigate and demonstrate the generation of the mode-locking pulses in YDFL cavity using the fabricated nanomaterials as SA.

1.4 Overview of the Thesis

This thesis is organized into seven main chapters, which report the comprehensive study of Q-switched and mode-locked pulse laser generations using several types' nanomaterial as SAs. The current Chapter gives a brief introduction on the recent development of pulsed fiber lasers and SAs as well as highlighting the motivation of this work. Besides, the objectives of this study are also described. Chapter 2 briefly describes the overview of fiber laser technologies especially for operation at 1 μm region and provides a detailed of several new materials used to generate pulses fiber lasers. The description on Q-switched and mode-locked methods using several types of nanomaterial as passive SAs are also discussed in this chapter.

Chapter 3 demonstrates both Q-switched and mode-locked fiber lasers using ytterbium-doped fiber (YDF) as a gain medium and MoS_2 as SA. Firstly, a Q-switched YDFL is demonstrated using a few layers of MoS_2, which are mechanically exfoliated from a natural MoS_2 crystal using a scotch tape. The SA is sandwiched between two fiber ferrules to form a fiber compatible Q-switcher. Secondly, a mode-locked YDFL is also realized using another MoS_2 based SA, which was realized by embedding the MoS_2 into a polymer film.

In Chapter 4, both Q-switching and mode-locking operations in 1 μm region are demonstrated using Black Phosphorus (BP) as SA. The first sub-chapter describes a Q-switched YDFL using a newly developed multi-layer BP SA. The second sub-chapter describes the performance of mode-locking by incorporating the BP SA into the YDFL cavity as SA. Chapter 5 is divided into two main sub-chapters. In the first sub-chapter, the comparison of Q-switching performance in YDFL cavity by using two types of topological insulator TI: Bismuth (III) Selenide (Bi_2Se_3) and Bismuth (III) Telluride

(Bi_2Te_3) as SA, is described. In the second sub-chapter, Antimony telluride (Sb_2Te_3) SA was used for generating Q-switching and mode-locking pulses train in YDFL cavity.

Two new types of transition metal oxide nanomaterials; laser; Nickel Oxide (NiO) and cobalt oxide (Co_3O_4) are explored as SA for Q-switching and mode-locking operations in 1 μm region. These materials are embedded into a polymer film and sandwiched between two fiber ferrules, making it an SA device. Chapter 7 provides the summary, analysis and review of all the results achieved in this study.

CHAPTER 2: LITERATUER REVIEW

2.1 Introduction

This chapter begins with a brief overview of the fiber laser technology for 1-micron region, which describes the ytterbium doped fiber (YDF) as the gain medium. Passive laser pulse formation is also presented in this chapter, which divided into two techniques (Q-switching and mode-locking). Nonlinear effects in optical fiber and saturable absorption are also described in this chapter. The enhanced focus is given to saturable absorber (SA) devices, where a few new materials such as the transition metal dichalcogenides (TMDs), Black phosphorous (BP), Topological insulator (TIs) and transition metal oxide are briefly described. The fabrication techniques of these SA materials are also covered in this chapter.

2.2 Fiber Laser Technology for 1-micron Region

Fiber lasers have gained more attention by many researchers as a promising laser configuration after it was firstly discovered in 1961 (Koester et al., 1964; Snitzer, 1961). Lasers were played an attractive role in the development of photonic technologies since the first laser demonstration by Maiman (Maiman, 1960). Lasers use the quantum impact of excited emission to produce light and they are constructed based on the following elements; an active medium as a gain provider, a pumping source to produce the energy and an optical cavity to reinforce and control the optical field (Agrawal et al., 1986). Ytterbium-doped fiber laser (YDFL) is the most efficient fiber lasers, which has many applications in various areas.

Ytterbium (Yb) is a chemical element that belongs to the group of rare earth metals. It is used as a laser active dopant in the form of the trivalent ion Yb^{3+} to generate laser in 1 micron region. Figure 2.1 shows a sub-level Strark splitting in energy diagram of Yb^{3+} ions and the sub-level splitting is depended on the position and concentration of Yb^{3+}

glass (Barua et al., 2008; Y. Qiao et al., 2008). In other words, Yb^{3+} has a very simple electronic level structure, with only one excited state manifold ($^2F_{5/2}$) within the reach from the ground-state manifold ($^2F_{7/2}$) as seen in the same figure.

Figure 2.2 shows the ytterbium-doped fiber (YDF) cross-section of emission and absorption (Y. Qiao et al., 2008). Ytterbium displays a broadband absorption spectrum becoming multi-wavelength pumping and then turning into a high power operation. This wide absorption spectrum additionally permits the utilization of unstabilized and low-cost pumps, providing the design and lower cost in overall as well as a stable high power fiber lasers in long-term. The simple electronic structure excludes excited-state absorption and also a variety of detrimental quenching processes. The upper state lifetimes are typically in the order of 10 to fs, which is beneficial for Q-switching and mode-locking pulses. The Yb^{3+} ion possesses a number of emission transitions within the 950 – 1100 nm wavelength range. Furthermore, the homogeneous and inhomogeneous broadening of these transitions within a glass host, leads to a wide and continuous emission spectrum in the 1 micron band, as shown in Figure 2.2. The lifetimes of emission and absorption spectrum depend on the host materials (Weber et al., 1983).

The broadened absorption and emission transitions that make up the above spectrum occur between sublevels of the ground and the first excited states of Yb. Note that Yb degeneracy was lifted due to the Stark effect. The electronic configuration of Yb^{3+} is [Xe] $4f^{13}$, which results in the following values for the orbital, spin and total angular momentum quantum numbers: $L = 3$, $S = \frac{1}{2}$ and $J = \frac{5}{2}, \frac{7}{2}$.

Applying Hund's rules produces the term symbols $^2F_{7/2}$ for the ground state as well as for the excited state (Griffiths, 2016). In the absence of an external perturbation, each of these states further consists of *2J+1* degenerate (equal energy) angular momentum states, corresponding to the allowed values of m^j.

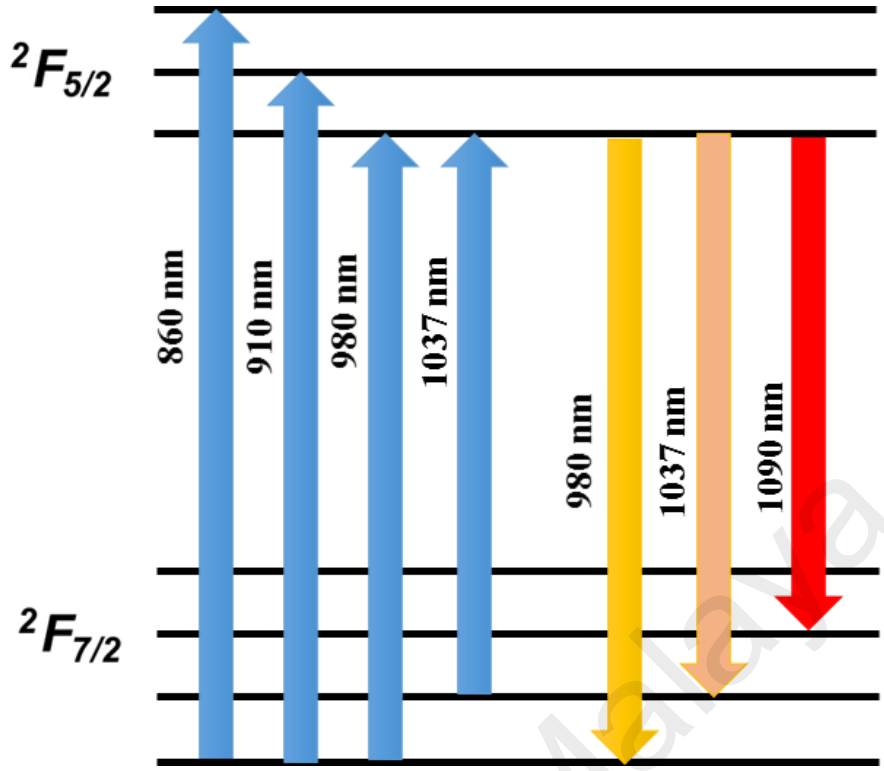

Figure 2.1: Sub-level Strark splitting in energy diagram of Yb^{3+} ions

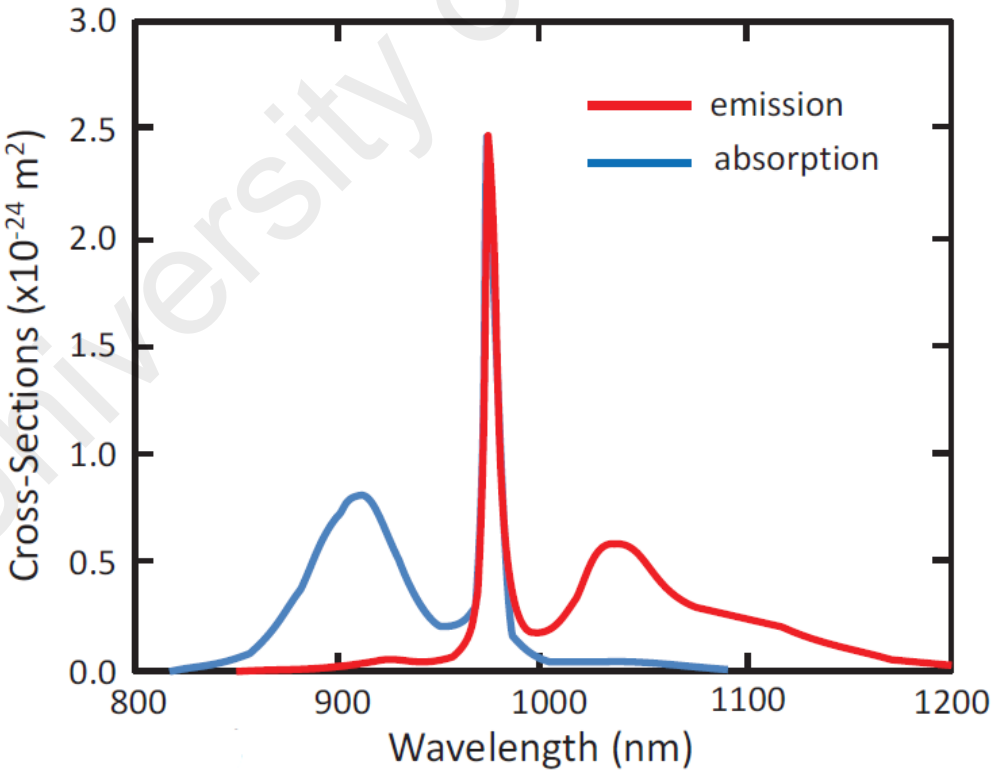

Figure 2.2: Typical emission and absrption spectra of Ytterbium doped fiber (YDF)

Applying Hund's rules produces the term symbols $^2F_{7/2}$ for the ground state as well as for the excited state (Griffiths, 2016). In the absence of an external perturbation, each of these states further consists of *2J+1* degenerate (equal energy) angular momentum states, corresponding to the allowed values of m^j. The degeneracy of these states may be lifted through the application of an external electric field, which turns each set of the degenerate states into a manifold of Stark levels. The external field polarizes the atom and thereafter interacts with the resulting dipole moment as per to the interaction potential (*EV).* Since the interaction is dependent on only the magnitude of *m,* it consists of *J+½* Stark levels. As for the case of Yb^{3+}, this implies that the $^2F_{7/2}$ ground state manifold is split into four Stark levels and the $^2F_{5/2}$ excited state is split into three Stark levels. It was shown that the absorption transitions between each of these manifolds occur from the lowest energy ground state Stark level, terminating each of the three excited state Stark levels (See Figure 2.3) (S. Dai et al., 2002; C. Jiang et al., 2000). The fluorescence transitions begin at the lowest energy $^2F_{5/2}$ Stark level and terminate on each of the $^2F_{7/2}$ Stark levels. These three absorption lines and four emission lines are then homogeneously and inhomogenously broadened due to their presence in an amorphous glass host, which forms continuous absorption and emission spectra, as shown in Figure 2.2.

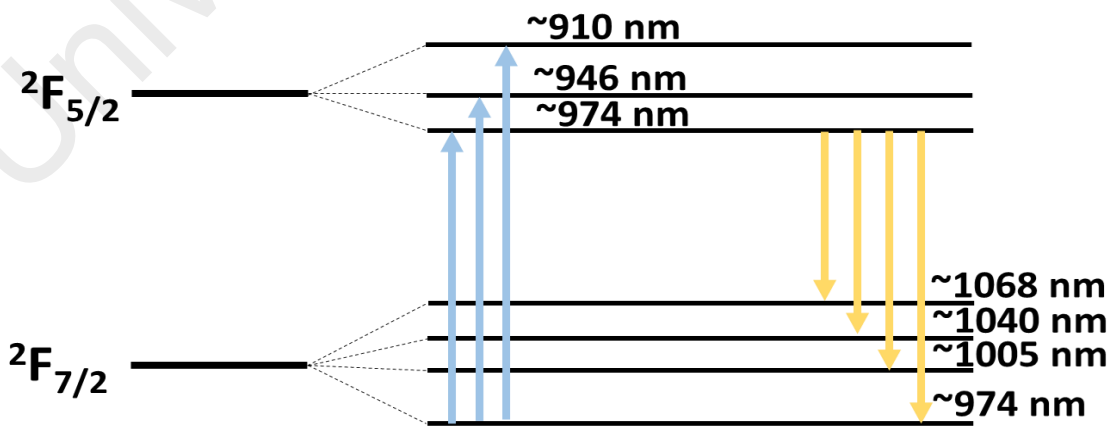

Figure 2.3: Stark levels and absorption and fluorescence transitions for Yb^{3+}. The transitions are labeled on the terminating energy level with the absorbed or emitted photon wavelength. Values for the absorbed or emitted wavelengths obtained from (S. Dai et al., 2002)

The cross-sections of the emission and absorption are also known as the range of efficiency in fiber laser system. At the side of the fiber parameters, the emission and absorption focus on the power extraction efficiency and signal saturation energy. The chosen pump wavelength depends on the heat dissipation during the quantum defect, absorption and total fiber length. Figure 2.4 shows the schematic efficiency of YDFLs. Besides the quantum defect, there are impossible to avoid the loss contribution from excess pump, signal losses, and non-optimized cavity. By selecting convenient core and cladding materials and a suitable design, these losses can be minimized (Zervas, 2014).

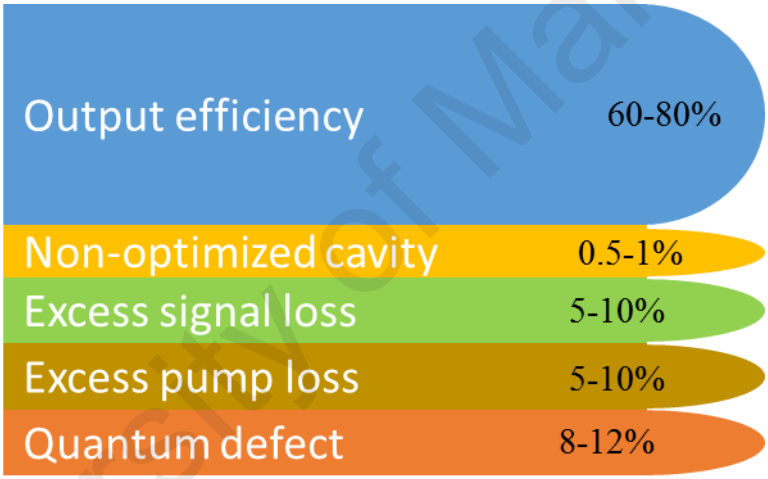

Figure 2.4: The schematic efficiency of YDFLs (Zervas, 2014)

The field applied to the Yb^{3+} ions is highly dependent on the glass host composition as well as any co-dopants and their concentrations. As a result, it is possible to control both, the transition wavelengths as well as the transition strengths, to a large degree by altering these properties (Barua et al., 2008). A large number of ytterbium-doped glasses are now available commercially in both bulk and fiber form. In this thesis, a commercial YDF, which was drawn from ytterbium-doped phosphosilicate glass, is used as a gain fiber. The operating regimes of the laser can be classified on the basis of temporal characteristics of output emission.

2.3 Pulse Formation in Fiber Laser Cavity

Short and ultrafast pulsed fiber lasers have broadly drawn in enthusiasm in recent years because of their application advantages, for example, in areas of communication, medicine and micromachining and additionally inclination being compact, simple to setup and cost-effective (Grelu et al., 2012; Sotor, Sobon, Macherzynski, et al., 2014). These lasers could be Q-switched or mode-locked fiber lasers, which can be generated by either active or passive techniques. The active technique was usually realized by integrating an external controller device such as acoustic-optic modulator to actively modulate the light of the intracavity (Bello-Jiménez et al., 2010). On the opposite side, the passive technique utilizes saturable absorption of optical material to change the intra-cavity light and generates pulsed laser in the cavity (De Tan et al., 2010). This section explains about the working principles of Q-switching and mode-locking operation and reviews about the previous works on both lasers.

2.3.1 Q-Switching Technique

Q-switching is a technique to achieve high energy laser pulses by inserting an intra-activity loss to modify the quality factor Q of the resonator. The Q-factor expression equation is shown as follows; (Svelto et al., 1998)

$$Q = \frac{2\pi E_s}{E_l} \qquad (2..1)$$

where 2π as a product, E_s is the ratio of stored energy in the resonator, and E_l is the loss energy per resonator cycle. Passive Q-switching laser operation depends on the gain medium as well as the saturable absorber (SA) which acts as a Q-switcher and it occurs when the photon fluxes start to show gain, fixed loss and saturable loss in the SA after many round-trips.

The Q-switching pulse output performances are analyzed by parameters, such as pulse width, repetition rate, peak power, and pulse energy. The range of pulse repetition rate is commonly in kHz and pulse width in µs. Comparison to mode-locking technique, Q-switching has comparatively for much longer pulse width, far lower in repetition rate that matching to the time among two sequential pulses for restoring the emitting energy and depend on the electron's lifetime in the excitation state inside the gain medium. The advantages of Q-switching technique is easier to achieve the pulses with no reaching the equilibrium between nonlinearity and dispersion of the medium, which is necessary for mode-locking technique (Popa et al., 2011).

A passively Q-switched laser includes a SA into the cavity and thus no external modulator is needed and the cavity loss is modulated by the SA to obtain a Q-switching pulses train. The inclusion of SA modulates the Q factor to periodically emit light as a pulse train with a kHz repetition rate range and pulse width ranging from ns to µs. SA can also be exhibited artificially by polarization effect, such as nonlinear polarization rotation (NPR) (Z.-C. Luo et al., 2012). So far, many passive SAs are also reported for Q-switching such as single and multiple walled carbon nanotubes (Ahmed et al., 2015), graphene (Z. Luo et al., 2010), topological insulator (Z. Yu et al., 2014) and Molybdenum Disulfide (MoS_2) (Z. Luo et al., 2014).

The SA transmission or reflection depends on the light intensity, where low light intensity will be absorbed by the material and high light intensity will be released depending on the material recovery time. For instance, Q-switched YDFL was reported using topological insulator Bi_2Se_3 SA to generate pulses with a repetition rate ranging from 8.3 to 29.1 kHz (Z. Luo et al., 2013). A few-layer molybdenum di-selenide ($MoSe_2$) SA was also used for Q-switching generation in 1 µm region (Z. Luo et al., 2013; Woodward et al., 2015). More recently, black phosphorus (BP) based SA was also used

to realize a tunable Q-switched YDFL with a pulse energy of 7.1 nJ (Harith Ahmad et al., 2016).

Table 2.1: Several Q-switched Fiber Lasers using nanomaterials based on SAs

Pulse laser	**Materials**	**Max pulse energy (nJ)**	**Min pulse duration (µs)**	**Repetition rate (kHz)**	**λ (nm)**	**ΔT (%)**	**Ref.**
YDF	CNTs	143.5	12.18	7.9–24.27	1060.2	-	(Kasim et al., 2014)
YDF	CNTs	18.4	1	30-50	1061	-	(Li et al., 2013)
YDF	Graphene	46	~70 ns	140–257	1064.2	20	(J. Liu et al., 2011)
YDF	Graphene	141.8	1.3	28.9-110	1027	8	(L Zhang et al., 2012)
YDF	MoS_2	6.9	2.2	58-105	1068.2	-	(R. I. Woodward et al., 2014)
YDF	MoS_2	32.6	5.8	6.4-28.9	1066.5	1.6	(Z. Luo et al., 2014)
YDF	$MoSe_2$	116	2.85	60- 74.9	1060	4.7	(Woodward et al., 2015)
YDF	BP	2.09	1.16	52.52-58.73	1038.68 & 1042.05	73	(Rashid et al., 2016)
YDF	BP	7.1	4	6.0–44.8	1056.6-1083.3	73	(Harith Ahmad et al., 2016)
YDF	Bi_2Se_3	17.9	1.95	8.3–29.1	1067	3.8	(Z. Luo et al., 2013)
YDF	Bi_2Se_3	6.2	2.1	14.9–62.5	1050.4	39.8	(Haris et al., 2017)
YDF	Bi_2Te_3	38.3	1	35-77	1056	2.5	(Junsu Lee, Koo, Chi, et al., 2014)

Table 2.1 compares several Q-switched YDFLs, which were obtained using 2D nanomaterials and other common materials. The maximum pulse energy of 141.8 nJ was successfully achieved using graphene based SA (L Zhang et al., 2012). This high energy pulse laser is suitable for applications in sensing, communication, and material processing. The wavelength of operation for the Q-switched YDFLs is 1027 nm (L Zhang et al., 2012) and 1083.3 nm (Harith Ahmad et al., 2016). The maximum repetition rate and pulse duration were 257 kHz (J. Liu et al., 2011) and 1 µs (Junsu Lee, Koo, Chi, et al., 2014; Li et al., 2013) respectively. Among those materials, the maximum modulation depth of 73% was obtained with the BP SA (Harith Ahmad et al., 2016; Rashid et al., 2016). The high modulation depth is advantageous to suppress the wave-breaking and produces high pulse energy.

2.3.2 Mode-locking Technique

Mode-locking is a technique to generate an ultrashort pulse laser. It can be realized using a passive technique based on SA. An ultrashort pulse can emerge when a SA modulates the loss once per cavity round-trip and all longitudinal modes have a fixed phase relationship. Thus, the mode-locking of the oscillating laser produces an ultrashort pulses train (ranging from ns to fs duration) at a defined repetition rate in MHz corresponding to the free spectra range of laser cavity or the number of obtained pulses per second (H. Zhang et al., 2010). The estimation of pulse repetition rate, f in passive mode-locking technique is given by:

$$Repetition\ rate, f\ (ring\ cavity) = \frac{c}{nL} \tag{2.2}$$

where c, n, and L denote the speed of light ($3 \times 10^8 ms^{-1}$), refractive index of the medium (1.46 for silica fiber), and total cavity length, respectively. It is shown from the equation that the repetition rate is determined by the total cavity length for a passive

mode-locking, and therefore, the higher pulse repetition rate is obtained for a shorter cavity length.

The pulse width of the laser indicates the full width at half maximum (FWHM) of the power versus time and a very short pulse width can be realized by a mode-locked laser. The higher numbers of longitudinal modes that have a fixed phase relationship can translate to a shorter pulse width. The short pulse duration of the mode-locking mode is useful for many applications including fast optical data transmission, and time-resolving process. The relationship between pulse width and bandwidth of the optical fiber pulses is referred to a time-bandwidth product (TBP). As described by the principle of Heisenberg, the TBP of the pulse is impossible to drop below a limit of T_{BL},

$$T_{BL} \leq \Delta t \times \Delta v \tag{2.3}$$

where Δt and Δv denote the temporal width (in seconds) and the spectral width (in hertz) of the pulse, which measured at FWHM. The limit of TBP or T_{BL} is depended on the pulse shape as described in Table 2.2. The bandwidth of the pulse is depended on the spectral bandwidth and operating wavelength of the output spectrum of the laser. It is given as;

$$The\ bandwdith\ (BW)\ = \Delta\lambda \times \frac{c}{\lambda^2} \tag{2.4}$$

where $\Delta\lambda$ is th spectral bandwidth at FWHM, and λ is the center of the wavelength of output spectrum. The pulse width is given as;

$$Pulse\ width\ (PW) = \frac{T_{BL}}{BW} \tag{2.5}$$

From both equations 2.4 and 2.5, it is obtained that the pulse width can also be estimated from a given optical bandwidth. Generally, the pulse width of mode-locking pulses is usually measured by using an auto-correlator, which its function according to

the estimated pulse shape. The pulse shape consists of Gaussian, and Secant hyperbolic, depending on the output spectrum, characteristic of the mode-locking operation, and total cavity dispersion. The Gaussian pulse shape is obtained when the cavity dispersion is closed to zero or equal to zero as in a stretched pulse laser. Table 2.2 compares the output pulse train and an ideal TBP for two types of pulse shapes.

Table 2.2: Comparison of two types of pulse shapes

Pulse shape	$\boldsymbol{I(t)}$	$\boldsymbol{T_{BL}}$**, Time bandwidth product**
Gaussian	$\exp(-\frac{6lnt^2}{\Delta t^2})$	0.441
Secant hyperbolic	$\mathrm{sech}^2(\frac{1.76t}{\Delta t})$	0.315

Passively mode-locked fiber lasers are widely explored in recent years by utilizing saturable absorption of optical materials. Various SAs have been demonstrated so far such as semiconductor saturable absorption mirror (SESAMs) (L. Sun et al., 2010), carbon nanotubes (CNTs) (Solodyankin et al., 2008), and graphene (Z. Sun et al., 2010). Mode-locking pulses have also been demonstrated in the various fiber laser cavities (Solodyankin et al., 2008; Z. Sun et al., 2010). Other nanomaterials such as MoS_2 and BP were also used for mode-locking pulses generation. For instance, Wang et al. demonstrated tunable mode-locked fiber laser that operates at 1.5 μm using MoS_2, which was obtained through liquid phase exfoliation (K. Wang et al., 2013). By using a double clad fiber, MoS_2 based (Rusdi et al., 2016) and BP based (Hisyam et al., 2017) were also demonstrated. Table 2.3 summarizes the performance of YDFL, which was demonstrated using various active fibers and nanomaterials SA as a mode-locker. The maximum pulse energy of the mode-locked lasers was about 32 nJ, which was obtained by using Sb_2Te_3 topological insulator materials as SA (Kowalczyk, Boguslawski, et al., 2016). The highest

repetition rate and shortest pulse duration were 21.5 MHz (Li et al., 2013) and 0.272 ps (Su et al., 2016) respectively.

Table 2.3: Mode-locked Fiber Lasers by nanomaterials based SAs

Gain fiber	Materials	Pulse energy (nJ)	Pulse duration (ps)	Repetition rate (MHz)	λ (nm)	ΔT (%)	Ref.
YDF	CNTs	-	310 ps	21.5	1060	-	(Li et al., 2013)
YDF	Graphene	0:41	580ps	0.9	1069.8	8	(L. Zhao et al., 2010)
YDF	MoS_2	3.1	656 ps	6.74	1042.6	10.47	(Du et al., 2014)
YDF	MoS_2	-	800ps	6.566	1054.3	9.3	(H. Zhang et al., 2014)
Yb, Lu: CALGO	BP	6.48	0.272ps	63.3	1053.4	10.95	(Su et al., 2016)
YDF (Double-clad)	BP	5.93	7.54 ps	13.5	1085.58	8	(Hisyam et al., 2017)
YDF	Bi_2Te_3	-	960ps	1.11	1064.47	19.1	(Yan et al., 2015)
YDF	Bi_2Te_3	0.599	230 ps	1.44	1057.82	1.8	(Junsu Lee et al., 2015)
YDF	Sb_2Te_3	32	0.38 ps	17.07	1039.4	-	(Kowalczyk, Bogusla wski, et al., 2016)

2.4 Optical Fiber Nonlinearity

The function of optical nonlinearity uses in many photonics applications. The materials have a linear reaction when the light intensity is low, which the light properties of

amplitude, polarization and phase may be modified, however no generation of new frequency component. Comparing with linear, the nonlinear response of materials obtains when the intensity of incident light is high, and that have numerous origins of nonlinear optics. There are two famous affection of nonlinearity in the materials, which are, Kerr effect and saturable absorption. Kerr effect has no energy changing between the materials and light, which is an effective model of elastic nonlinearity, associated to a harmonic motion of electrons and mostly under a light of intensive electromagnetic field. On the other hand, the linear and nonlinear reactions under electrical field (E) can be used to describe the overall polarization (P) as follows (Boyd, 2003);

$$P = \varepsilon_0(X^{(1)} \cdot E + X^{(2)} : E + X^{(3)} + \cdots) \tag{2.6}$$

where ε_0, $X^{(1)}$, $X^{(2)}$, $X^{(3)}$ represents the vacuum permittivity, linear response of material (first order), two frequency effects (second harmonic generation), and three frequency effects (four-wave mixing), respectively.

The refractive index, n under highly intensity I in optical fiber is given by;

$$n = n_2 I + n_0 \tag{2.7}$$

where, n_2 is the parameter of nonlinearity that mainly used to depict Kerr effect, and n_0 is the linear refractive index. Saturable absorption involves an energy exchange in between light and materials and it is considered as an inelastic nonlinear effect. The nonlinear absorption of the materials under the field of light is normally related to the imaginary part of $X^{(3)}$.

When a light beam shines on a nanomaterial, electrons in the valence band are excited to the conduction band. Then these electrons gradually lose their energy due to various scattering effects and fall down to a lower position in the conduction band. When there

are many electrons excited at the same time by a highly intense light beam, the conduction band will be completely filled with electrons and no more photons will be absorbed. In this case, the absorption of the material is reduced and the material is known as "saturated" or bleached". Such a material is called a saturable absorber (SA). The word "bleached" is used because early saturable absorbers are mostly dyes.

The nonlinear absorption, $a(I)$ according to a sample two- level SA equation is given by (Garmire, 2000);

$$a = \frac{a_s}{1 + {}^{I}/_{I_{sat}}} + a_{ns} \tag{2.8}$$

where a_s is the modulation depth, I is the input intensity, I_{sat} is the saturation intensity, and a_{ns} is the non-saturable absorption. When the light intensity is low, the absorption is equal to $a_s + a_{ns}$ and when the intensity is high, the absorption is equal to a_{ns}. Two photon absorption (TPA) is also a nonlinear absorption effect in the materials which means the electrons absorb two photons simultaneously to be excited to the conduction band. When the light intensity is very high, TPA becomes significant enough and should be taken into consideration. The saturable model of TPA effect (J. Wang et al., 2010);

$$a = \frac{a_s}{1+{}^{I}/_{I_{sat}}} + a_{ns} + \beta I \, , \tag{2.9}$$

where β is the TPA coefficient. The transmission T is also given by:

$$T = \exp(-a) = \exp\left(-\frac{a_s}{1+{}^{I}/_{I_{sat}}} - a_{ns} - \beta I\right)$$

$$\approx \left(1 - \beta I - \frac{a_s}{1 + {}^{I}/_{I_{sat}}}\right)\exp(-a_{ns}) \tag{2.10}$$

Sometimes Equations (2.8) – (2.10) do not function admirably with the measuring data due to the requirement term ($\frac{1}{1+{}^{I}/_{I_{sat}}}$) that needs a wide transition region in order to change the state from unsaturated to saturated state.

Several researchers reported about the nonlinear measurement of saturable absorption that the transition region is narrower than the model. Therefore, the following modified model is widely used (Z. Tian et al., 2015);

$$T = 1 - a_s \exp(-\frac{I}{I_{sat}}) - a_{ns} \tag{2.11}$$

In general, the two measurement methods (Z-scan and two arm measurement) are normally used to characterize the Kerr effect and saturable absorption of nanomaterials. There are two measurement techniques to characterize the Kerr effect and saturable absorption of nanomaterial. The Z-scan technique is used to measure the nonlinear absorption and nonlinear refractive index. In the Z-scan technique, the material is converted along the Z direction through the beam waist of a focused Gaussian laser beam in a narrow focusing configuration. Thus, when the material passes through the focus, the irradiance drops along with the nonlinear effects (Sheik-Bahae et al., 1990). The two-arm measurement setup of nonlinear absorption is also reported to get the modulation depth of the material (Z. Tian et al., 2015). It has a simple configuration and easier to determine the absorption of the material. The two-arm measurement setup of nonlinear absorption is shown in Figure 2.5. The mode-locked pulse from laser system is amplified using an optical amplifier to obtain a high gain peak power output to efficiently saturate the SA sample. The amplified output is connected to a variable optical attenuator before it is divided into two by a 50:50 optical coupler. The first optical power meter is linked to one port of coupler and the second port of coupler is linked to the SA sample and then the second optical power meter. The power dependent absorption measurement of the sample

can be obtained by changing the input laser source. The absorption curve can be fitted with Equation (2.11) to estimate the modulation depth and other nonlinear parameters of the SA sample.

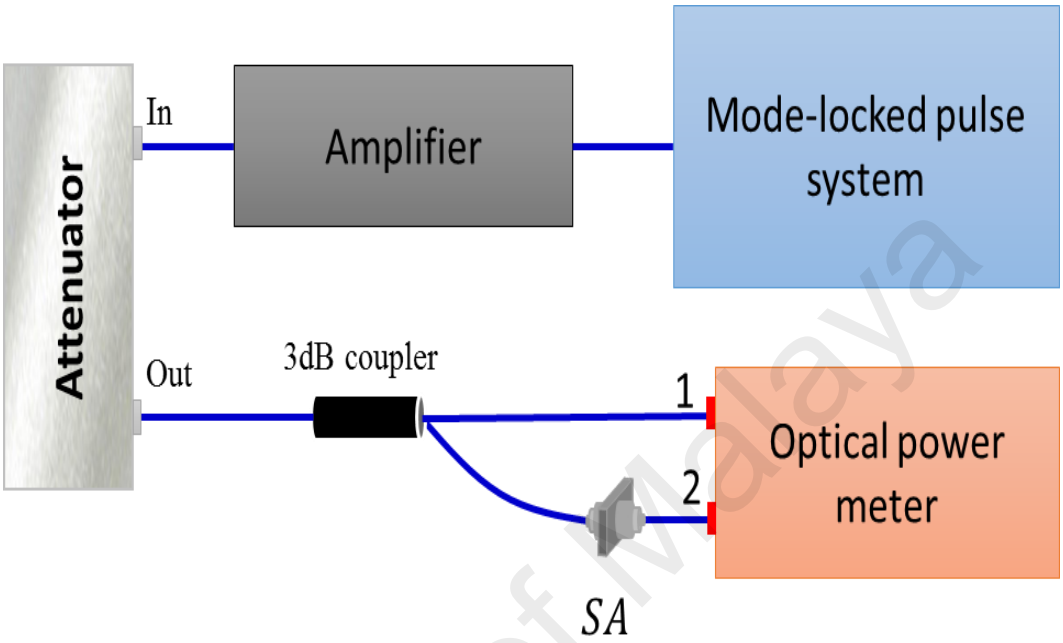

Figure 2.5: Two-arm measurement setup of nonlinear absorption

2.5 Saturable Absorber Device

A saturable absorber (SA) is a device to modulate an optical loss inside the cavity so that it can function as a Q-switcher or mode-locker. Generally, SA effect can be realized by two approaches. The first technique uses real SAs (materials) that make the nonlinear effects reduce in absorption level and increase the light intensity. The second technique uses artificial SAs (devices), and that produce nonlinear effects into mimic the action of a real saturable absorber by inducing an intensity-dependent transmission.

The comprising of SA into the fiber laser cavity can generate pulsation either Q-switching or mode-locked, while the output properties depend on the laser cavity design and SA properties. Figure 2.6 shows the development historical of SA technologies. The first SA was a dye (Ippen et al., 1972) and the development of SA technology was slowly

evolved. A stable mode-locked pulses train was realized by using semiconductor saturable absorber mirror (SESAM) in the early 1990s (Keller et al., 1992; Zirngibl et al., 1991). Consequently, SESAM has become a successful method as SA for generation Q-switched and ultrafast mode-locked pulses from fiber lasers (L. Zhang et al., 2010). Nevertheless, its application is still limited due to their difficult fabrication methods, complex design, expensive cost and narrower wavelength operation range. These limitations are leading studies into new materials such as nanomaterials where their size that decreased dimensionally results in sturdy quantum confinement and extraordinary optoelectronic properties (Eda et al., 2013; Novoselov et al., 2005).

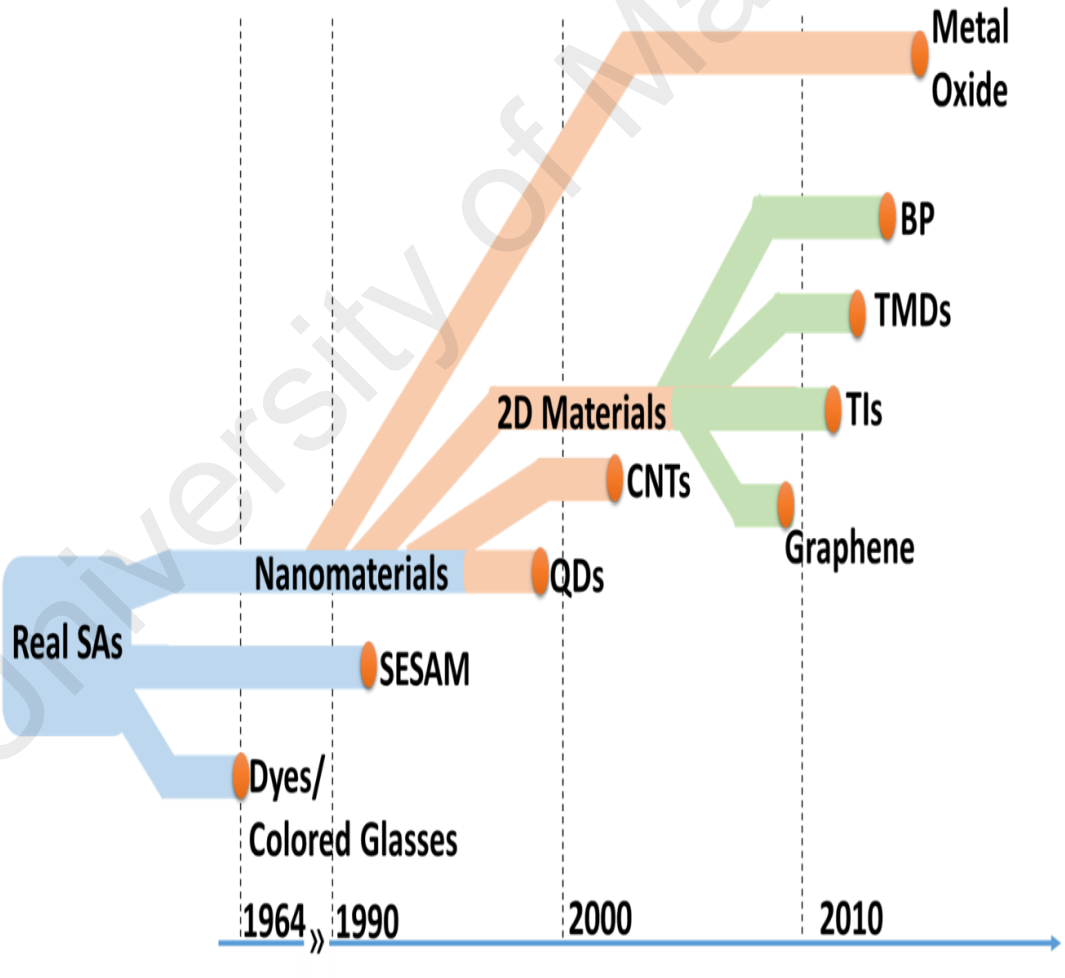

Figure 2.6: The evolution of SA technologies

In 1997, the first pulse generation using quantum-dot doped glasses (QD) as saturable absorbers was demonstrated (Guerreiro et al., 1997). After few years, new nanomaterials such as 1D carbon nanotubes (CNTs) and 2D graphene had drawn the great attention for pulses generation in various fiber laser setups (Bao et al., 2009; Set et al., 2004). Besides graphene, other 2D family materials that can be extracted as monolayer and few-layer crystals from a variety of bulk materials, such as topological insulators (TIs), transition metal dichalcogenides (TMDs) and black phosphorous (BP) are also gained interests (Eda et al., 2013; Kambe et al., 2014; Novoselov et al., 2005; Xia et al., 2014).

More recently, transition metal oxide material was also explored as a SA for generation Q-switching and mode-locking pulses in fiber laser (H Ahmad, Siti Aisyah Reduan, et al., 2016; Mao et al., 2017; Nady, Ahmed, Latiff, Ooi, et al., 2017). In this section, a number of new nanomaterials are introduced. These materials will be explored and used in this work for Q-switcher and mode-locker in YDFL cavity.

2.5.1 Transition Metal Dichalcogenides (TMDs)

Recently, 2D materials in layers form are building blocks for the next generation photonics technology, due to their planar quantum confinement and absence of inter-layer interactions leading to make more functional and flexible photonic devices such as graphene and transition metal dichalcogenides (TMDs). TMDs made of sandwiched metal atoms between two layers of chalcogen atoms, are the most used in electronic and optics devices owing to their direct band gap (Conley et al., 2013). Molybdenum disulfide (MoS_2) is one of the TMDs and its crystal structure is shown in Figure 2.7. It has 1.29 eV of band gap and good absorption coefficient of the light compared with graphene which has zero band gap. Due to this property, it is widely utilized in microelectronics devices (Wen et al., 2017) and as a catalyst (Voiry et al., 2013).

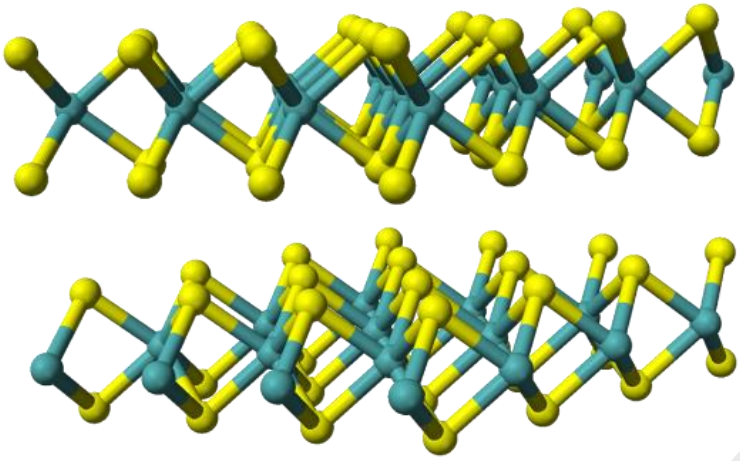

Figure 2.7: Crystal structure of MoS_2.

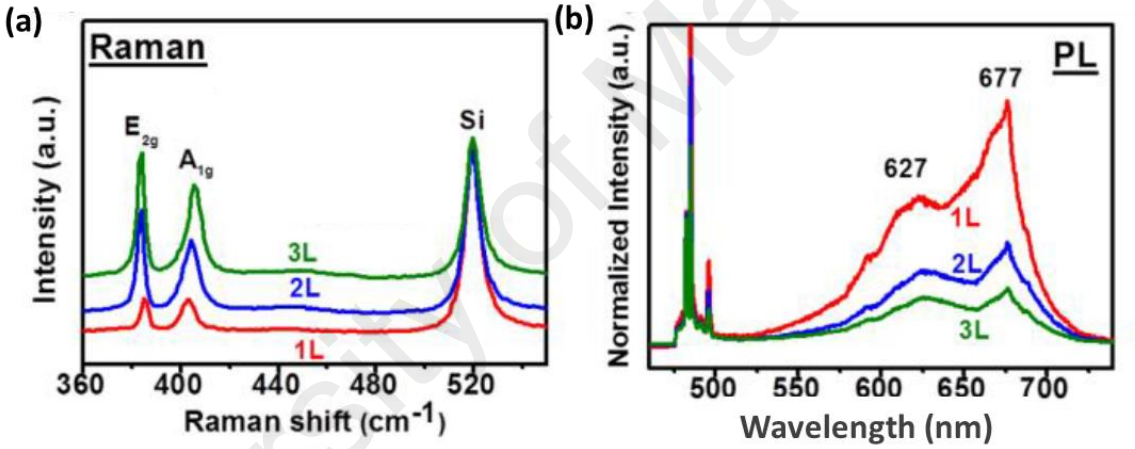

Figure 2.8: (a) Raman spectra (b) PL spectra of monolayer (1L), bilayer (2L) and trilayer (3L) MoS_2 sheets (Y. H. Lee et al., 2012)

Exfoliation of MoS_2 layers can be achieved mechanically to produce high quality nanosheets (H. Li et al., 2014) and ultrasonically in liquid phase (Jawaid et al., 2015). The liquid phase exfoliation is the most promising method to produce of 2D materials in large scale. Figure 2.8 shows the Raman spectra and photo-luminescent emissions for a high quality of MoS_2 which were prepared using chemical vapor deposition. Raman characteristic bands around 403.8 and 385.8 cm^{-1} that increase with increasing of the layers of MoS_2 exfoliation while PL spectra decrease with increasing in the layers of

MoS_2 exfoliation which shows two peaks in a visible range around 627 and 677 nm (Y. H. Lee et al., 2012).

2.5.2 Black Phosphorous

Another interesting 2D nanomaterial is black phosphorus (BP). It has thin atomic layers of phosphorene sheets, as shown in Figure 2.9 to produce an excellent optical and electrical properties. The band gap of a monolayer of BP is 1.88 eV and it is widely used in electronic and optoelectronic devices due to its direct band gap and excellent conductivity properties (Han Liu, Yuchen Du, Yexin Deng, & D Ye Peide, 2015). BP exfoliated layers can be produced by mechanical exfoliation using scotch-tape-based micro-cleavage and by liquid exfoliation. Scotch-tape-based micro-cleavage exfoliates mechanically the black phosphorus layers on scotch-tape and then it is transferred on substrate finally cleaned and heated to 180^{o}C to remove the rest solvent, while liquid exfoliation is used to exfoliate the black phosphorus layer by sonicating the bulk black phosphorus powder in organic liquid. High mobility and stability of BP is normally achieved using scotch-tape-based micro-cleavage method (X. Chen et al., 2015).

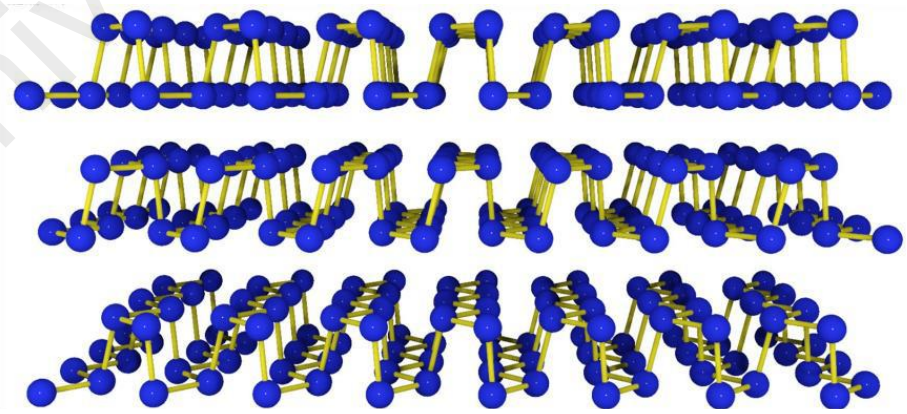

Figure 2.9: Crystal structure of few-layer black phosphorus

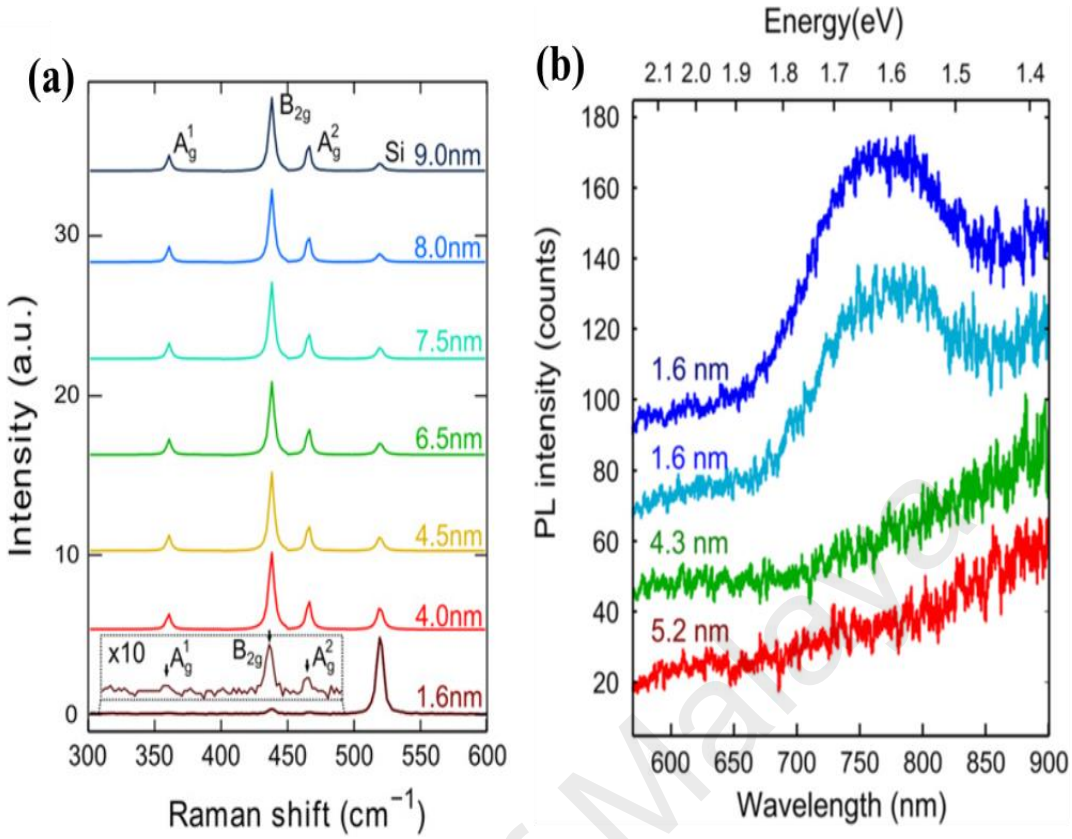

Figure 2.10: (a) Raman spectra (b) PL spectra of black phosphorus at different thicknesses (Castellanos-Gomez et al., 2014)

Black phosphorus has three peaks for Raman spectra around 362.1, 439.5 and 467.7 cm^{-1} and this peaks remain at the same crystalline of this material with increasing in the material layers while appears one peak for photo-luminescence (PL) spectra for few layers at around 1.6 eV of photon energy, as shown in Figure 2.10 (Castellanos-Gomez et al., 2014).

2.5.3 Topological Insulator

Topological insulator (TI) materials are new kind of electronic state of matter, which have to conduct states on the surface so the electrons can only move along the surface of the materials, and are an insulator in its interior that can support the conductive surface states. Three main compounds of TI materials are Bismuth (III) Selenide (Bi_2Se_3), Bismuth (III) Telluride (Bi_2Te_3), and Antimony telluride (Sb_2Te_3).

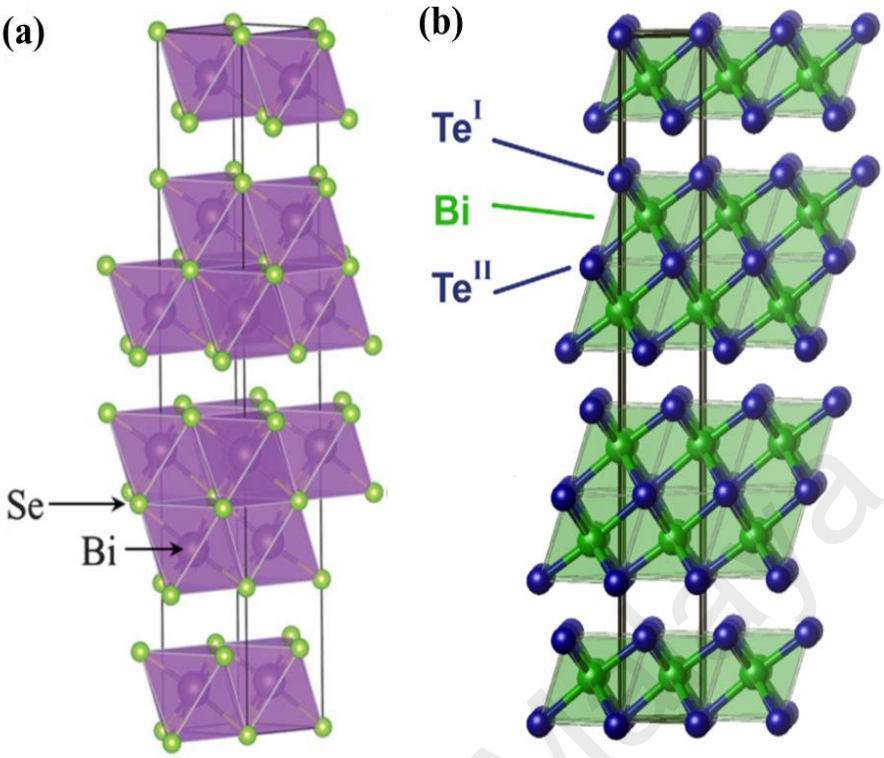

Figure 2.11: The crystal structure of (a) Bi_2Se_3, and (b) Bi_2Te_3 (Cava et al., 2013; Zurhelle et al., 2016)

The Bi_2Se_3 and Bi_2Te_3 are binary chalcogenides of bismuth Bi_2X_3 with complex layer structures, as shown in Figure 2.11, the crystal structure of Bi_2Se_3 and Bi_2Te_3, and directly react with the elements at 500-900^oC. Bi_2Se_3 and Bi_2Te_3 have small band gaps about 1.35 and 1.21 eV, respectively, so they exhibit semiconductor properties. They can be used in television cameras, optoelectronic and switching devices, and thermoelectric refrigerator due to their properties as thermoelectric and semiconducting materials. These materials can be synthesized by physical or chemical methods (Kong et al., 2010). Chemical methods are widely used to prepare thin film of TI materials due to easy fabrication and large surface deposition (Anwar et al., 2014).

For structure mode of TI materials, the vibration modes were detected in Raman spectra as reported by Liu et al. (X. Liu et al., 2011), which are three peaks for Bi_2Se_3 and two peaks for Bi_2Te_3 at small range from 50- 200 cm^{-1}, as shown in Figures 2.12.

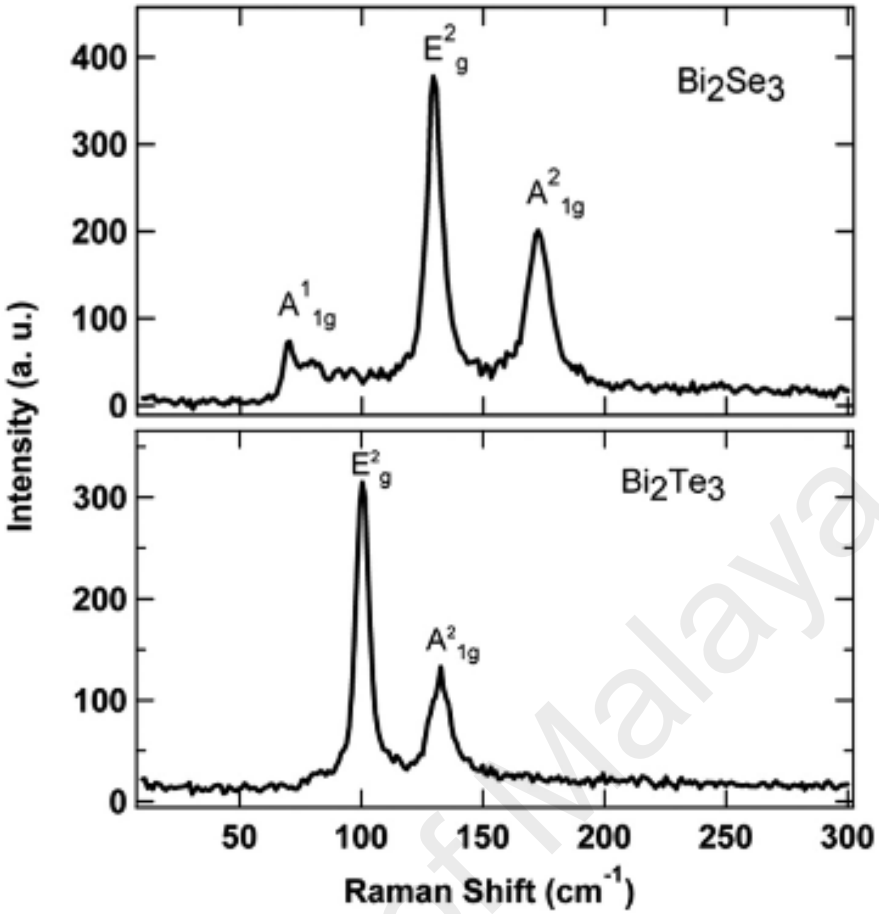

Figure 2.12: Raman spectra of Bi_2Se_3 and Bi_2Te_3 (X. Liu et al., 2011)

2.5.4 Transition Metal Oxide

Metal oxide nanoparticles are particles contained oxygen and metal in 1 to 100 nm in size so have a high surfacing to volume ratio. They can be used to optimize light absorption and to enhance the stiffness, toughness, and probably the service life of polymeric materials. Among of these nanoparticles, nickel oxide (NiO) nanoparticles, which the crystal structure of cubic NiO is shown in Figure 2.13, is high capacitance, low cost, high chemical/ thermal stability and environmental friendly. NiO nanoparticles are used as electrode material in supercapacitor, fuel cells, batteries, electrochromic films, dye-sensitized photocathodes and organic solar cells due to their catalytic, magnetic, and conductivity properties (J. Cheng et al., 2015; Kwon et al., 2016; Rai et al., 2013).

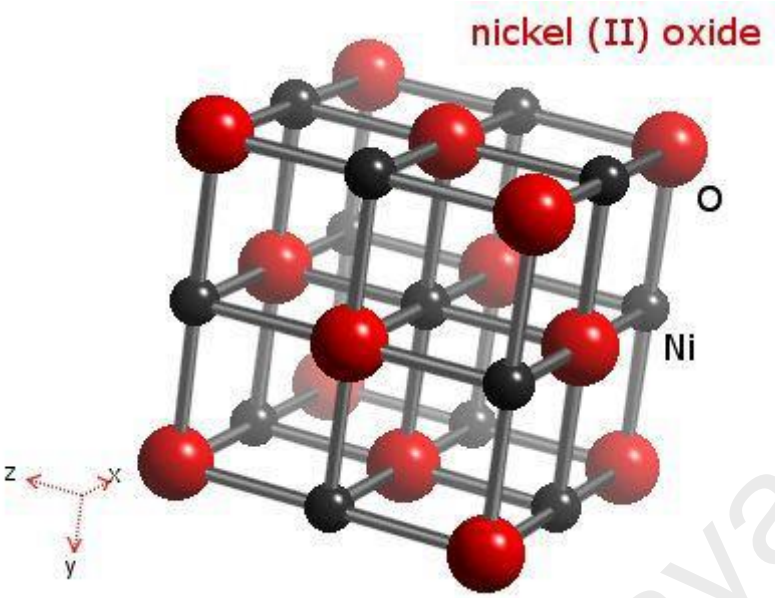

Figure 2.13: Crystal structure of cubic NiO

There are several methods to synthesize NiO nanoparticles such as hydrothermal, sonochemical, solvothermal, sol–gel, pulsed laser deposition, thermal decomposition and anodic plasma (Fasaki et al., 2012; Santhoshkumar et al., 2016; Zorkipli et al., 2016). To produce a thin film without using any surfactants and complex process, sonochemical method is used to synthesize nanostructure depending on the nucleation, growth and tiny bubbles collapse violently in a liquid medium. Thermal treatment is done to calcine the nanostructures into solid state which appear in different sizes with different calcination temperatures.

Cobalt (II, III) oxide (Co_3O_4) is also a transition metal oxide and a p-type semiconductor. It is a black antiferromagnetic solid and has two valence Co ions, as a mixed valance compound, Co^{II} and Co^{III}. The Co^{II} is a magnetic and occupies 1/8 of the tetrahedral sites while Co^{III} is a diamagnetic and occupies ½ of the octahedral sites of the cubic close-packed lattice of the oxide anions and its formula is sometimes written as $Co^{II}Co^{III}_2O_4$, as shown the crystal structure of Co_3O_4 in Figure 2.14 (Heinz et al., 2013; Singh et al., 2016). Due to the owning the nanostructures unique electrical, optical,

magnetic and catalytic properties as compared to the bulk structure, Co_3O_4 nanocubes are recently a promising candidate for the application in a sensor, electrochemical devices, Li-ion batteries and photocatalysis.

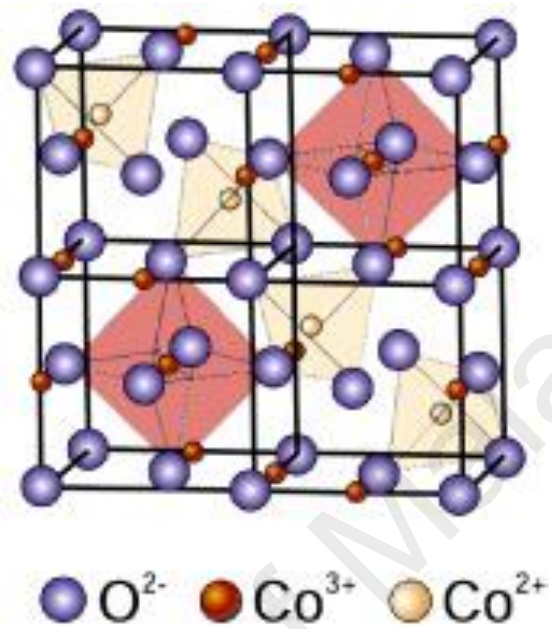

Figure 2.14: Crystal structure of Co_3O_4

There are various techniques to synthesis cobalt oxide nanostructures, such as microwave assisted solvothermal, thermal decomposition and hydrothermal techniques (He et al., 2004; Numan et al., 2016; C. Sun et al., 2011). Hydrothermal method is widely used for the synthesis of Co_3O_4 nanocubes which is generally based on wet chemical route and defined as a crystal growth under various synthesis parameters such as temperature, time, pressure and concentration of precursors (Rahman et al., 2009). The structure property of the Co_3O_4 nanocubes is obtained by TEM image and XRD spectra. Feng has reported the synthesis of the Co_3O_4 nanocubes via hydrothermal process at low temperature around 160°C that is presented in TEM images in Figure 2.15 (Feng et al., 2014). Kang and Zhou has characterized a high crystallization in the cubic crystal system of the Co_3O_4 nanocubes that appeared in the XRD spectra without any noticeable

impurities, as shown in Figure 2.16 with JCPDS 42-1467 patterns, via using hydrothermal process (Kang et al., 2015).

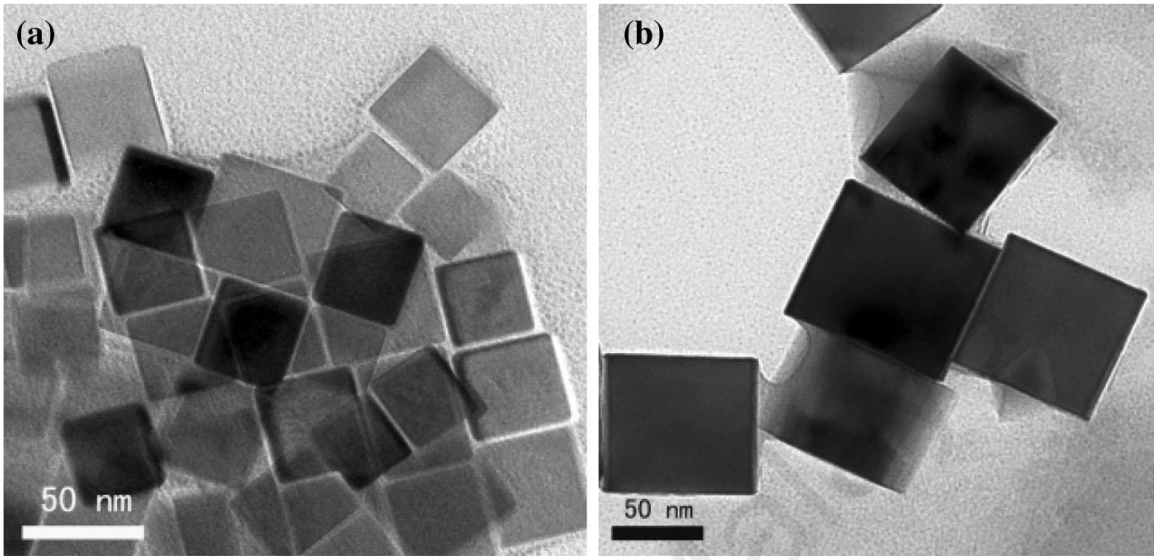

Figure 2.15: TEM images of Co_3O_4 nanocubes synthesized via hydrothermal process at (a) 150°C (b) 160°C (Feng et al., 2014)

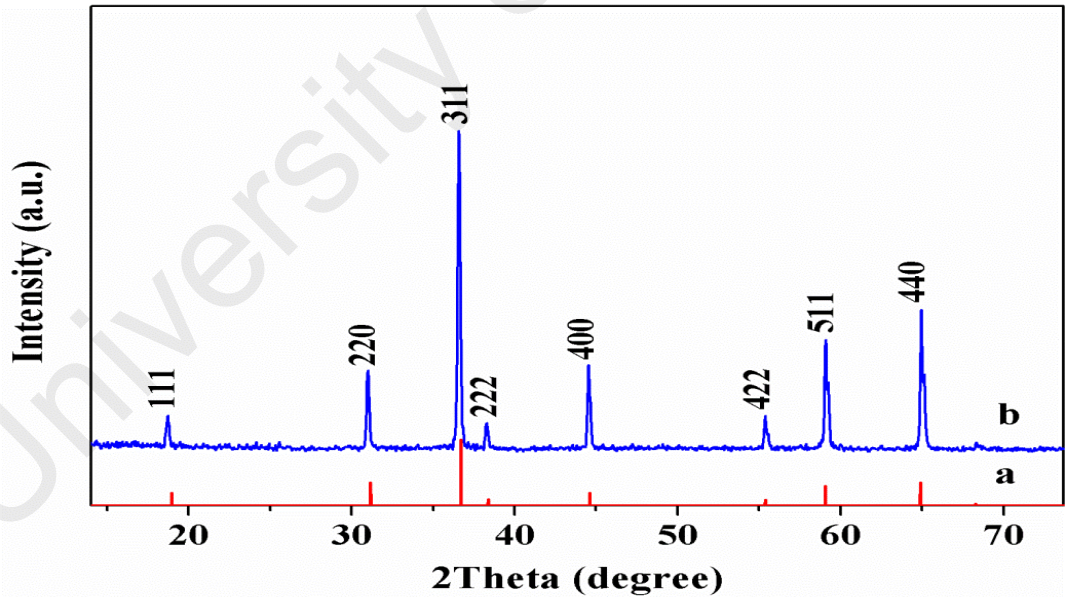

Figure 2.16: XRD patterns of (a) JCPDS 42-1467 and (b) Co_3O_4 nanocubes (Kang et al., 2015)

The structure property of the Co_3O_4 nanocubes is characterized via Raman spectroscopy. Five peaks were observed in the Raman spectrum which is corresponded

to three F_{2g}, one E_g and one A_{1g} of the Raman active modes for the Co_3O_4 nanocrystal as marked in Figure 2.17 (Feng et al., 2014).

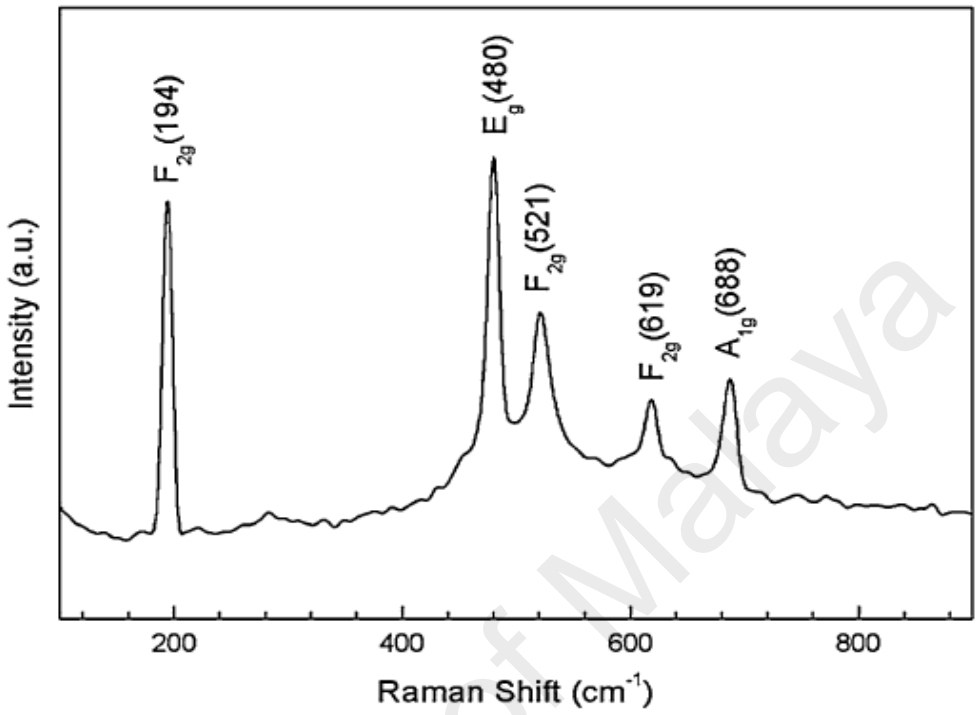

Figure 2.17: Raman spectrum of Co_3O_4 nanocubes (Feng et al., 2014).

2.6 Fabrication of SA

Major efforts have been considered to synthesis of controllable, uniformity and large scale of nanomaterials layer using different top-down and bottom-up fabrication approaches, including mechanical exfoliation, chemical exfoliation and chemical vapor deposition (CVD) (Johal, 2013; HF Liu et al., 2015; Yuan et al., 2016). Prior the preparation of the nanomaterials layer, there are different methods that can prepare the nanomaterials in the nanoscale from the bulk materials mainly using physical and chemical methods such as hydrothermal, sonochemical, solvothermal, sol–gel, pulsed laser deposition and thermal decomposition (Alagiri et al., 2012; Aslani et al., 2011; Fasaki et al., 2012; X. Liu et al., 2005; Sietsma et al., 2007). Here, the fabrication methods are briefly described.

2.6.1 Mechanical Exfoliation Techniques

Nanomaterials can be prepared by using an exfoliation of the bulk materials which can be peeled into a layer by layer. That is due to the weak bonding between atoms mainly van der Waals bond which the intermolecular force is weak. Therefore, the material crystal is easy to dissociate between layers under the external force. This method is preferred for 2D nanomaterials fabrication due to low cost, easy and less time fabrication and produces high quality and a large area of the 2D nanomaterials. The graphene and TI layers can be prepared by stripping the graphite and TI bulk materials. Hong et al. reported the preparation of Bi_2Se_3 nanoribbons by exfoliation down of the bulk material to a few quintuple layers (Hong et al., 2010). Graphene was prepared by mechanical exfoliation using scotch-tape–based micromechanical cleavage(Yi et al., 2015). The process of this method is shown in Figure 2.18.

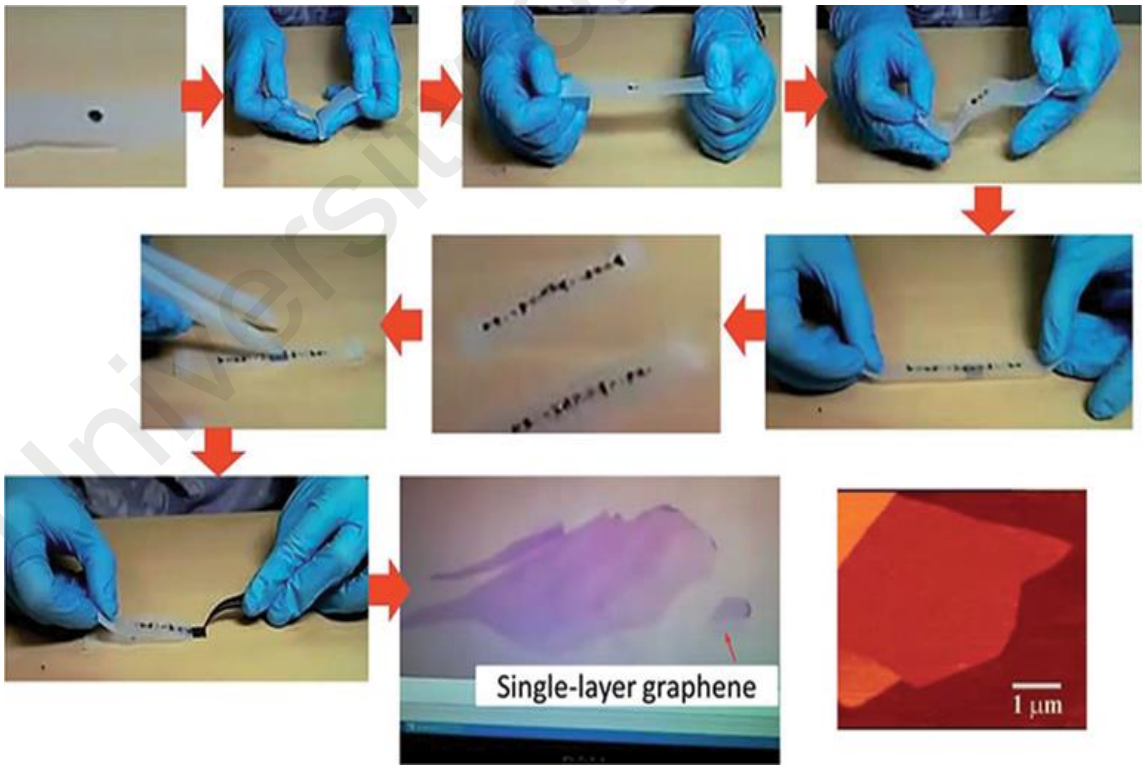

Figure 2.18: An illustrative procedure of the Scotch-tape–based micromechanical cleavage for graphene (Yi et al., 2015)

2.6.2 Liquid Phase Exfoliation Technique

2D nanomaterials can also be prepared using liquid phase exfoliation (LPE) approach, which is based on breaking layered materials into 2D nanomaterials. A chosen solvent is added to the layered materials that are easy to suspend and break the material crystal in the solvent. The LPE process depends on three general steps, dispersion the bulk material into the chosen solvent, sonication then centrifugation. The propagation of high amplitude sonication waves in the sonication process induces the shear forces and cavitation in the solution leading to shearing the crystal. Recently, this method is widely used for exfoliation layered materials such as black phosphorous and transition metal dichalcogenides (Gupta et al., 2016; S. Lin et al., 2017). Cui et al. has successfully fabricated the graphene using solvothermal-assisted exfoliation process in acetonitrile (ACN) solvent, with the production of the graphene nanosheets (GNS) (Cui et al., 2011). The detailed mechanism of the solvothermal exfoliation processes of graphene is schematically illustrated in Figure 2.19.

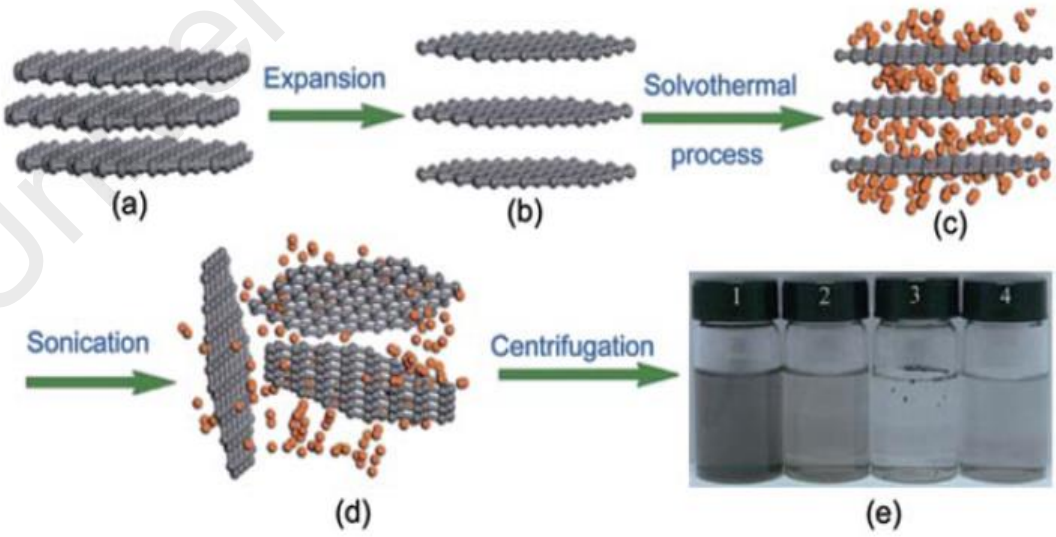

Figure 2.19: Solvothermal exfoliation processes of graphene (Cui et al., 2011)

2.6.3 Sonochemical Technique

Sonochemical technique is one of the promising method to synthesis nanomaterials especially transition metal oxide nanoparticles due to not using any surfactant and complex process (Kis-Csitári et al., 2008; Kumar et al., 2000). The sonochemical is considered the effect of ultrasound in forming acoustic cavitation in liquids that results in the enhancement of the chemical reaction in the solution mainly the nucleation, growth and tiny bubbles. Mousavi et al reported about the synthesis of Tellurium (Te) nanoparticles via ultrasonics sonochemical method while Te nanorods were produced in the absence of ultrasonic waves that is illustrated in Figure 2.20 (Mousavi-Kamazani et al., 2017). In addition, NiO nanostructure was successfully synthesized using facile sonochemical method following by calcination process. The NiO nanoclusters were formed at 250 °C of calcination temperature (Duraisamy et al., 2016).

Figure 2.20: Schematic diagram of the formation of Te nanoparticles and effect of ultrasonic irradiation on the particle size and morphology (Mousavi-Kamazani et al., 2017)

2.6.4 Other Techniques

In addition to the above techniques, there are other fabrication techniques. In 2014, Liu et al had synthesized a high quality of Bi_2Se_3 layers using chemical vapor deposition (CVD) system using high purity Se and Bi_2Se_3 powder as source materials (M. Liu et al.,

2014). Bi_2Te_3 thin film on GaAs substrate was fabricated using a new technology called Metal-organic chemical vapor deposition (MOCVD). Moreover, the pressure and temperature are important in the MOCVD technique that leads to increase in the mobility of Bi_2Te_3 at 7400 $cm^2/V.s$ at 15 K from the bulk carrier mobility (350 $cm^2/V.s$) at 30 K (Cao et al., 2012).

CHAPTER 3: MOLYBDENUM DISULFIDE AS SATURABLE ABSORBER

3.1 Introduction

Fiber lasers use trivalent rare-earth ions such as ytterbium, erbium, and thulium, which was doped into glass hosts as a gain medium. At 1962, the first laser performance based on ytterbium-doped silicate fiber was investigated. Then, the Yb^{3+} has gained a widespread interest as a gain medium to replace the conventional inefficient Nd^{3+}. This is attributed to the Nd^{3+} which operates based on four level transition, while Yb^{3+} has only three level and quasi-three level transitions. The ytterbium-doped fiber (YDF) is attractive as a gain medium because it has a simple energy level structure, high reliability, compact and the lasing wavelength at 1 μm, within the low-loss of optical laser as well as it is capable for producing high output power.

Q-switched and mode-locked lasers with the advantages of compactness and flexibility, have attracted much attention in recent years due to their potential applications in laser material processing, remote sensing, telecommunication and medicine (Bao et al., 2011; S. Harun et al., 2012; Ursula Keller et al., 1996). Pulsed YDF lasers (YDFLs) operating in 1 micron region have been widely investigated due to their excellent efficiency (Harith Ahmad et al., 2016; Akulov et al., 2007; Al-Masoodi et al., 2014) . They are normally obtained using active approaches by inserting an acoustic-optic or an electron-optic modulator into the laser cavity. Recently, passive methods are also widely explored for both Q-switching and mode-locking in fiber lasers by utilizing the saturable absorption of optical materials (i.e. saturable absorbers, SAs). In the past, several kinds of SAs such as semiconductor saturable absorber mirrors (SESAMs) (Ge et al., 2009; X. Wang et al., 2010), carbon nanoutbes (CNTs) (Garnov et al., 2007; Zhou et al., 2010), graphene (J Lee et al., 2013) have been successfully used to passively generate both Q-switched and mode-locked fiber lasers. Although SESAMs have been well developed and commercially available for the past two decades, they exhibit obvious disadvantages such

as complex fabrication, expensive packaging and low damage threshold. Graphene and carbon materials have the advantages of low cost, easy fabrication and operable in a wide wavelength range. Mode-locking pulses have been demonstrated using graphene and carbon nanotubes (CNTs) as SA in the various fiber laser cavities based on erbium- (Mou et al., 2012; Z. Sun et al., 2012; Xu et al., 2012), ytterbium- (H.-R. Chen et al., 2014; X.-H. Li et al., 2012; L. Zhao et al., 2010) and thulium- (Cho et al., 2009; H. Zhang et al., 2009) doped fiber gain medium. The operation wavelength of CNT is related with diameter of the nanotubes. Graphene has a 2D zero-bandgap semiconductor material and low absorption co-efficiency, which gives it the advantages of wideband saturable absorption as well as ultra-fast recovery time. These advantages lead researchers to 2D materials.

In this chapter, molybdenum disulfide (MoS_2) is proposed as SA for generating Q-switched and mode-locked pulses train in YDFL cavity. A passively Q-switched YDFL is demonstrated using a mechanically exfoliated from a natural MoS_2 crystal. The few layer MoS_2 is obtained by using a scotch tape, which is then sandwiched between two fiber ferrules to form a fiber compatible Q-switcher. By introducing the MoS_2 SA into the YDFL cavity, a stable pulse laser is generated at 1070.2 nm wavelength with repetition rate is tunable from 3.817 to 25.25 kHz. A mode-locked YDFL is also realized using another MoS_2 based SA, which was realized by embedding the MoS_2 into a polymer film. The mode-locked laser cavity is constructed based on a 10.6 m long cavity with normal dispersion of 0.242 ps^2/km.nm at 1030 nm.

3.2 Passively Q-switched Ytterbium Doped Fiber Laser with Mechanically Exfoliated MoS_2 Saturable Absorber

Compact and flexible passively Q-switched fiber lasers have opened up new applications in laser material processing, remote sensing, telecommunications and

medicine (Laroche et al., 2002; Leigh et al., 2007; Z. Luo et al., 2013). One of the most effective methods for realizing a Q-switching pulse train in fiber laser cavity is through the use of a SA device as a Q-switcher. In the past, various SAs namely semiconductor saturable absorber mirror SESAM (Hakulinen et al., 2007), carbon nanotubes CNTs (S. Harun et al., 2012; Li et al., 2016) and graphene (Al-Masoodi et al., 2015; Ismail et al., 2013), have been successfully used to passively generate Q-switched fiber lasers. Even today, researchers are still searching for new SAs which possess desirable characteristics such as wavelength-independent saturable absorption, low saturable optical intensity, high damage threshold, and excellent fiber compatibility.

More recently, Molybdenum Disulfide (MoS_2) has also been tested as an SA for mode-locking and Q-switching (Dong et al., 2015; Z. Lin et al., 2016; H. Liu, A.-P. Luo, et al., 2014; Z. Luo et al., 2014; K. Wang et al., 2013; R. Woodward et al., 2014; Zhan et al., 2015; H. Zhang et al., 2014). For instance, Wang et al. investigated the saturable absorption property of two-dimensional (2D) MoS_2 nanosheets for ultrafast laser applications (K. Wang et al., 2013). Other reported works indicate that MoS_2 has a higher modulation depth than that of graphene (~2.3% per layer) (H. Cheng et al., 2016; Tang et al., 2013; K. Wang et al., 2014; S. Zhang et al., 2015). In this section, a new passively Q-switched YDFL is demonstrated using a newly developed MoS_2 based SA as a SA. The MoS_2 SA was prepared by mechanically exfoliating the crystal using a scotch tape and sandwiching the tape with acquired flakes between two fiber ferrules using a fiber connector. The laser operates at 1070.2 nm with a high pulse energy of 295.45 nJ. The proposed laser produces a higher pulse energy compared to the previous works on MoS_2 based Q-switched fiber lasers, which so far only reported the maximum pulse energy of 126 nJ (Z. Luo et al., 2014; R. Woodward et al., 2014). The laser also performs competitively compared to similar lasers in 1 μm region that use other 2D materials as SAs (X. Li et al., 2014; Tang et al., 2013).

3.2.1 Fabrication and Characterization of Mechanically Exfoliated MoS_2 based SA

MoS_2 is a nanomaterial which has extraordinary electronic and optical properties (Mak et al., 2010). The MoS_2 layers used in the construction of the SA were obtained by mechanical exfoliation method, which was performed without using any chemical substance and costly instrument. The fabrication process is summarized in Figure 3.1. Figure 3.1 (a) shows the relatively thin flakes that was evenly peeled off a natural MoS_2 crystal by scotch tape. The flakes attached to the scotch tape was repeatedly pressed to make it thin enough to transmit light with a high efficiency. Then a tiny piece of the MoS_2 tape was cut and placed onto the end face of a FC/PC fiber connector ferrule after applying index matching gel as shown in Figure 3.1 (b). After connecting it with another FC/PC ferrule with a standard flange adapter, the all-fiber MoS_2 SA was finally completed and ready to be used. It was learned that if a clean scotch tape is placed onto the end face of fiber connector, the cavity will fail to generate Q-switching regime.

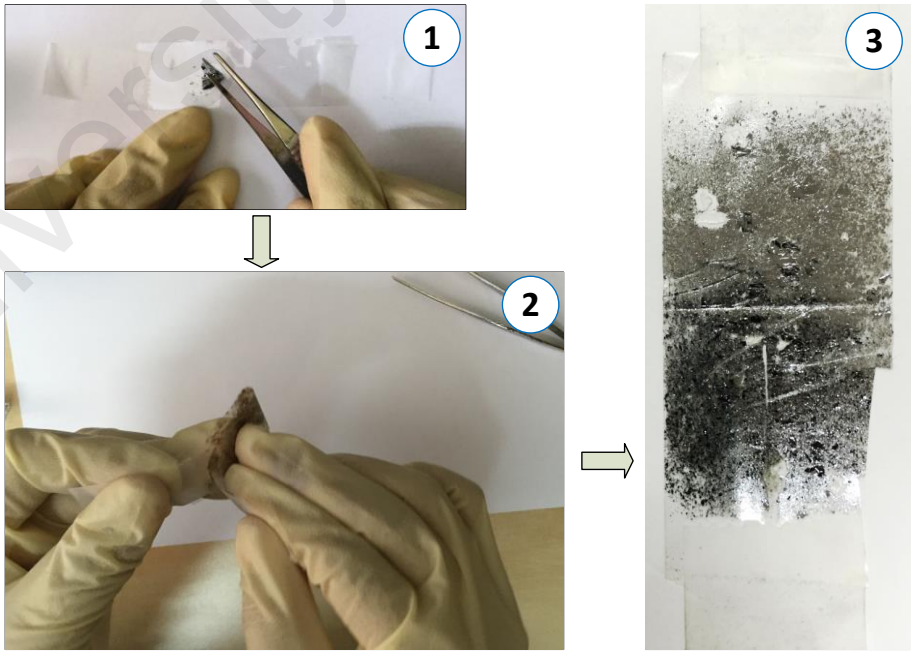

(a)

Figure 3.1: Mechanical exfoliation method; (a) Simple peeling process, and (b) MoS_2 tape at standard FC/PC connector ferrule end surface

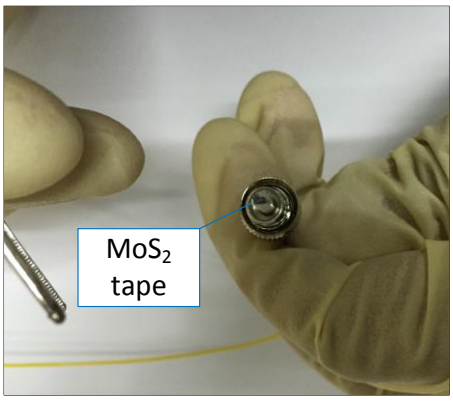

(b)

Figure 3.1, continued

Raman spectroscopy was then performed on the fabricated MoS_2 SA. Figure 3.2 (a) shows the Raman spectrum recorded by a spectrometer when a 514 nm beam of an Argon laser was radiated on the MoS_2 tape for 10 seconds with an exposure power of 10 mW. As shown in the figure, the sample exhibits two characteristic peaks in parallel with two phonon modes; out of plane vibration of Sulfide atoms at 408 cm^{-1}, and in plane vibration of Molybdenum and Sulfide atoms at 383 cm^{-1} with a frequency difference of 25 cm^{-1}. This frequency difference indicates that the prepared tape contains the layers of MoS_2 (H. Li et al., 2012). Following other reported results (Wu et al., 2015), the full-width-half-maximum (FWHM) of E_{2g}^1 and A_{1g} bands were calculated to be 5.0 and 5.5 cm^{-1}, respectively. Figure 3.2 (b) shows the linear absorption of the SA within a wavelength range from 1520 to 1600 nm. It was obtained by transmitting a broadband light source through the MoS_2 tape. As shown in the figure, the absorption follows a flat profile across the wavelength region. The inset of Figure 3.2 (b) shows the absorption spectra within UV-Vis region. From the figure, two exciton peaks of MoS_2 are noticeable at 612 nm and 670 nm. These peaks correspond to the interband excitonics transition at 2.03 eV and 1.85 eV, respectively. The absorption spectra obtained are comparable to those found in the previous studies (M. H. M. Ahmed et al., 2016).

The nonlinear optical response property of the MoS_2-SA tape was further investigated to confirm its saturable absorption. This was done by applying a balanced twin-detector measurement technique. A self-constructed mode-locked fiber laser (1557 nm wavelength, 1.5 ps pulse width, 17.4 MHz repetition rate) was used as the input pulse source. As in the work of Fu et al., a mode-locked laser source was launched to generate lasers at 1, 1.5 and 2 µm (Fu et al., 2014). In this work, the transmitted power was recorded as a function of incident intensity on the device by varying the input laser power. The experimental data for transmission were fitted to a simple two-level SA model;

$$T(I) = 1 - \alpha_s * exp\,(-I/I_{sat}) - \alpha_{ns}) \tag{3.1}$$

where $T(I)$ is the transmission, α_s is the modulation depth, I is the input intensity, I_{sat} is the saturation intensity, and α_{ns} is the non-saturable absorption. The nonlinear transmission of the MoS_2 on the scotch tape is shown in Figure 3.2 (c). As seen, the modulation depth, non-saturable intensity, and saturation intensity are 11.3 %, 23.0 %, and 23.5 MW/cm^2, respectively.

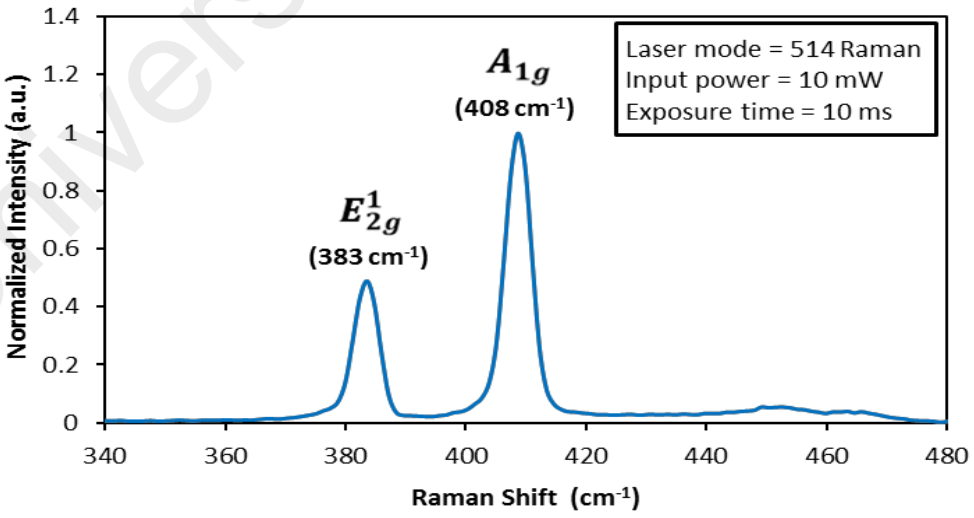

(a)

Figure 3.2: Optical characteristic of the MoS_2 tape. (a) Raman spectrum. (b) Linear absorption. Inset image is absorption at UV-Vis region. (c) Nonlinear transmission

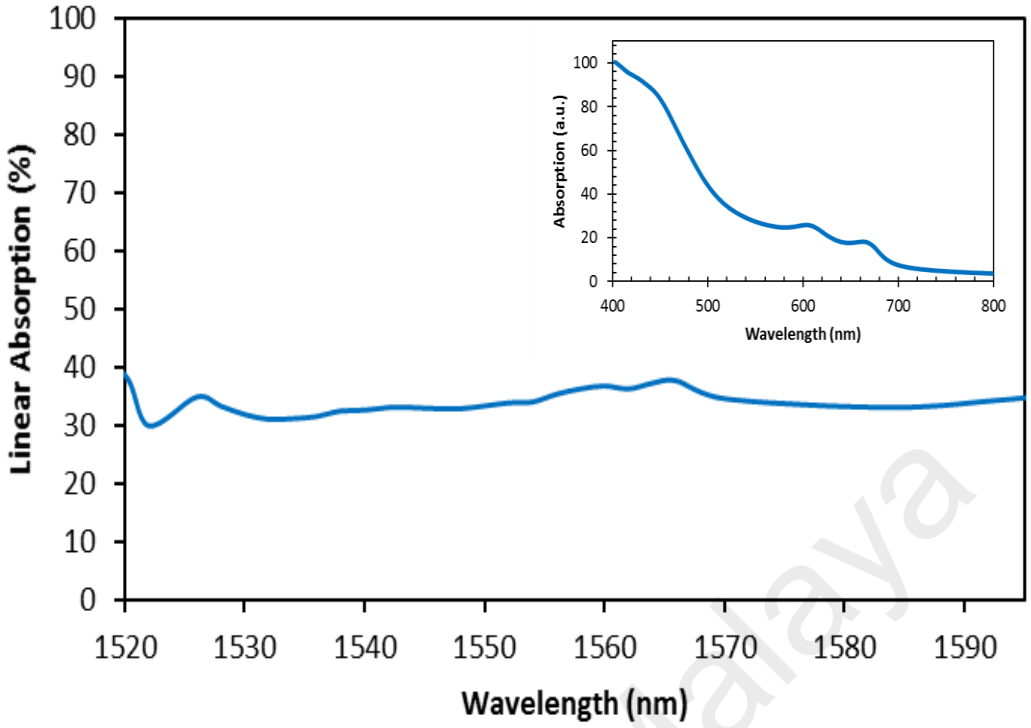

(b)

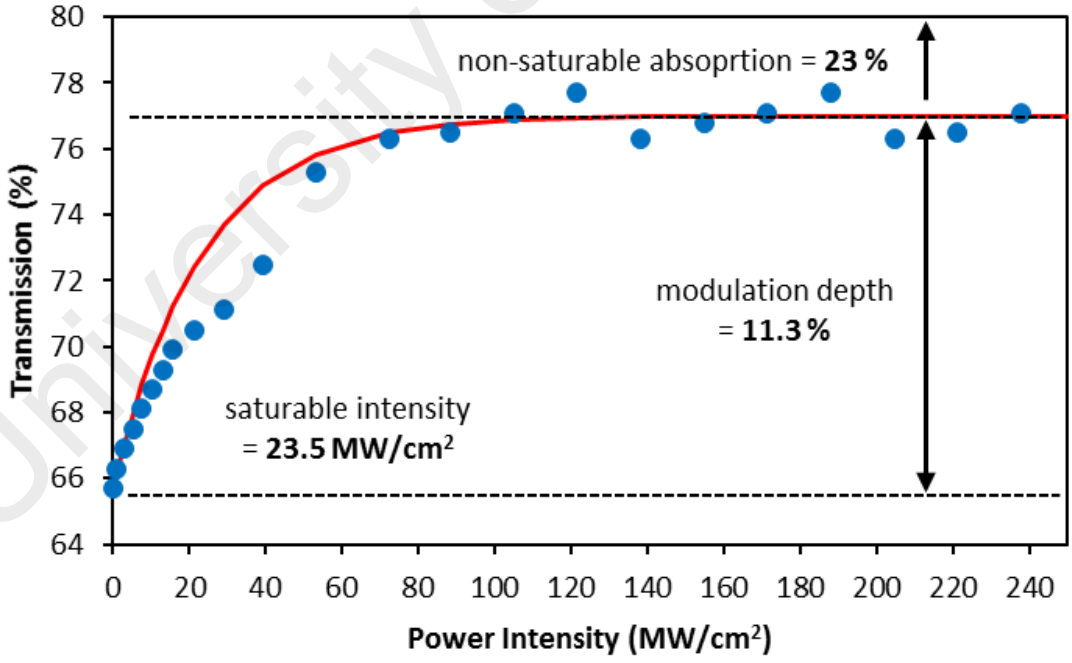

(c)

Figure 3.2, continued

3.2.2 Experimental Setup

The experimental setup of the proposed MoS_2 based Q-switched YDFL is schematically shown in Figure 3.3. The laser cavity consists of a 980/1030 nm wavelength division multiplexer (WDM), 1.5-m long of Ytterbium-doped fiber (YDF), MoS_2 SA, an isolator and a 3 dB output coupler in a ring configuration. The YDF used as a gain medium, has a numerical aperture of 0.20, a core and cladding diameters of 4 and 125 µm, respectively, as well as ion absorption of 280 dB/m at 920 nm. A unidirectional operation of the laser cavity is obtained by using an isolator. The output of the YDFL is collected from the cavity via a 50:50 coupler, which retains 50% of the light in the laser ring cavity for oscillation. The 3dB coupler was used to increase the cavity loss to avoid mode-locking instability and achieve a stable Q-switching operation. The optical spectrum analyser (OSA) used for analyzing the Q-switching has a spectral resolution of 0.02 nm. The oscilloscope is used to observe the output pulse train of the Q-switched laser.

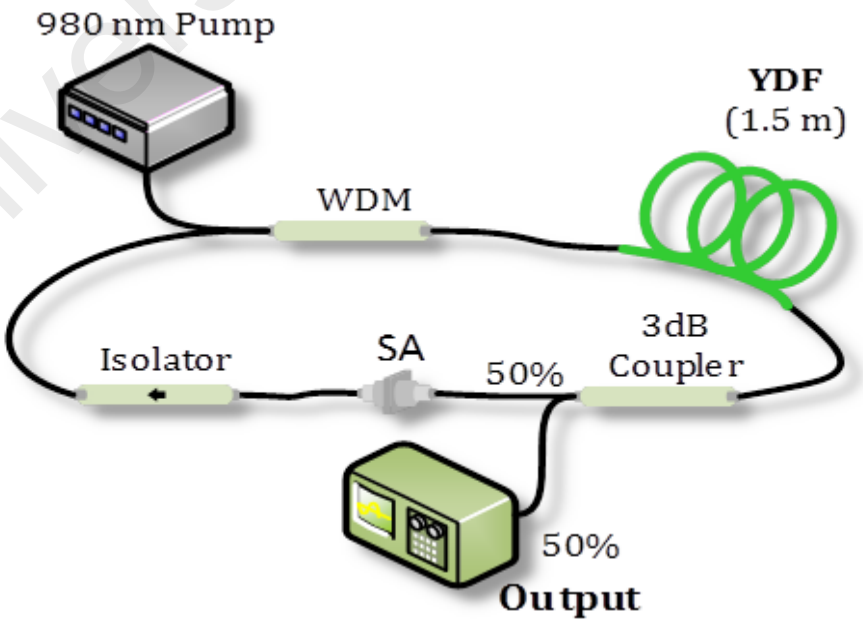

Figure 3.3: Experimental setup for Q-switched YDF fiber ring laser using SA

3.2.3 Q-switching Performance

The YDFL started lasing in Q-switched mode at a pump power of 49.57 mW. When the pump power was gradually increased from 49.57 mW to 87.2 mW, the repetition rate of the pulse increased in response. This is a typical feature of passive Q-switching. Figure 3.4 shows the optical spectra of the Q-switched YDFL at three different pump powers of 49.57 mW, 71.3 mW, and 87.2 mW. While the peak of the YDFL stays fixed at 1070.2 nm, its 3 dB spectral bandwidth widens with the increase in pump power. The bandwidth are 0.2 nm, 0.4 nm and 0.5 nm at the three pump powers respectively. To verify that the passive Q-switching was attributed to the MoS_2 SA, the MoS_2 tape was removed from the ring cavity. In this case, no Q-switched pulses were observed on the oscilloscope, even when the pump power was adjusted to a wide range. This finding confirms that the MoS_2 SA was responsible for the passively Q-switched operation of the laser.

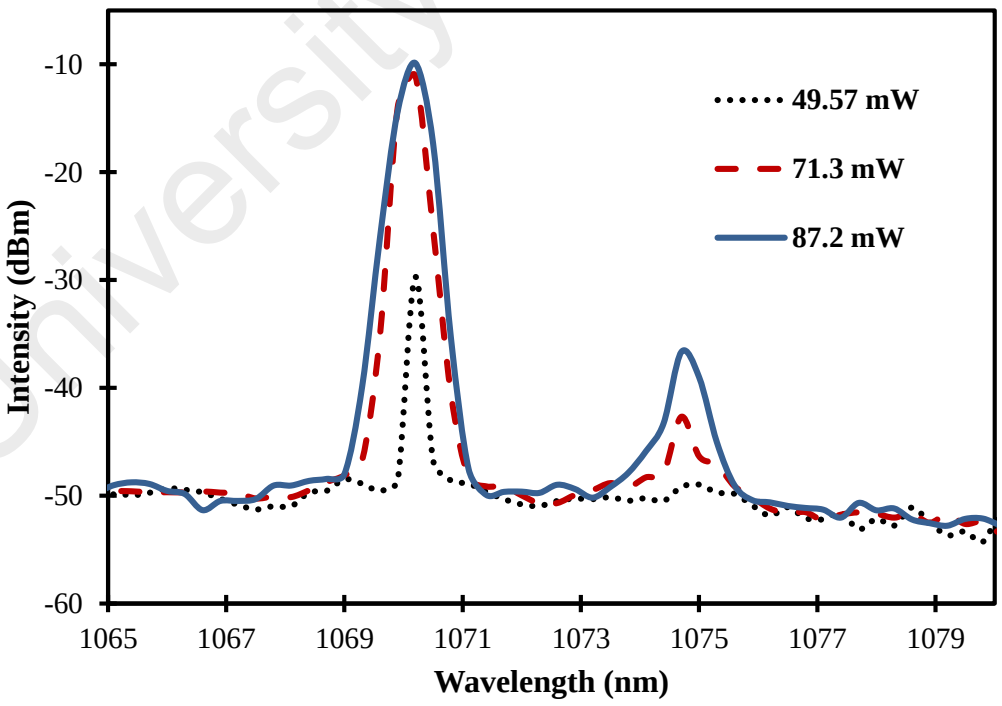

Figure 3.4: Optical spectra of the Q-switched YDFL configured with the MoS_2 SA at different pump power of 49.57 mW, 71.3 mW, and 87.2 mW

Figure 3.5 (a), (b) and (c) show the pulse trains and single-pulse envelops of the Q-switched YDFL at pump powers of 49.57, 71.3, and 87.2 mW, respectively. As the pump power increases, more energy can be stored in the laser cavity and this contributes to the rise in the repetition rate accompanied by the reduction in pulse width (Y. Chen et al., 2014). For pump powers of 49.57, 71.3, and 87.2 mW, the attained repetition rates are 3.817 to 17.54 and 25.25 kHz while the corresponding pulse widths are 26.09, 11.27 and 11.33 µs, respectively. The attributes of the pulse a Q-switched laser mainly depend on the gain medium, SA and pump power.

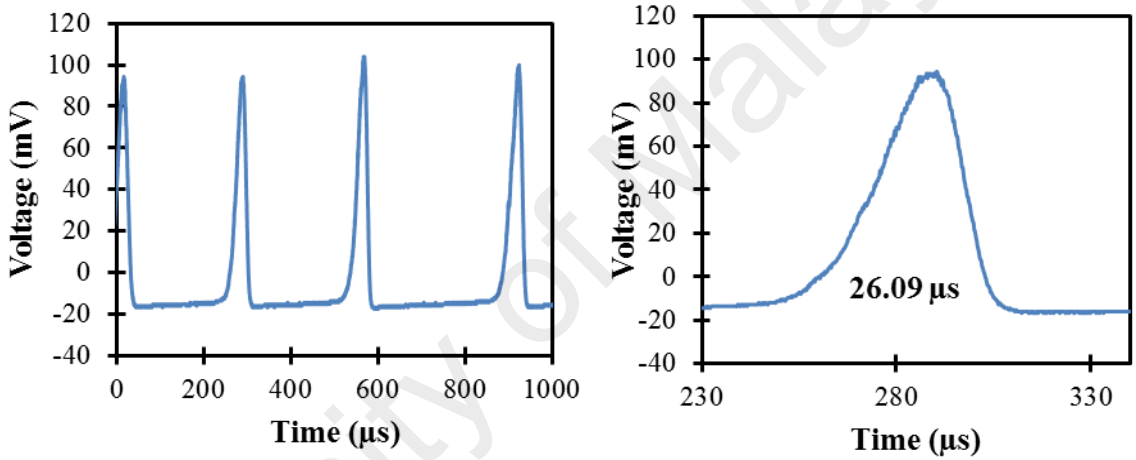

(a) 49.57 mW (Repetition rate of 3.817 kHz)

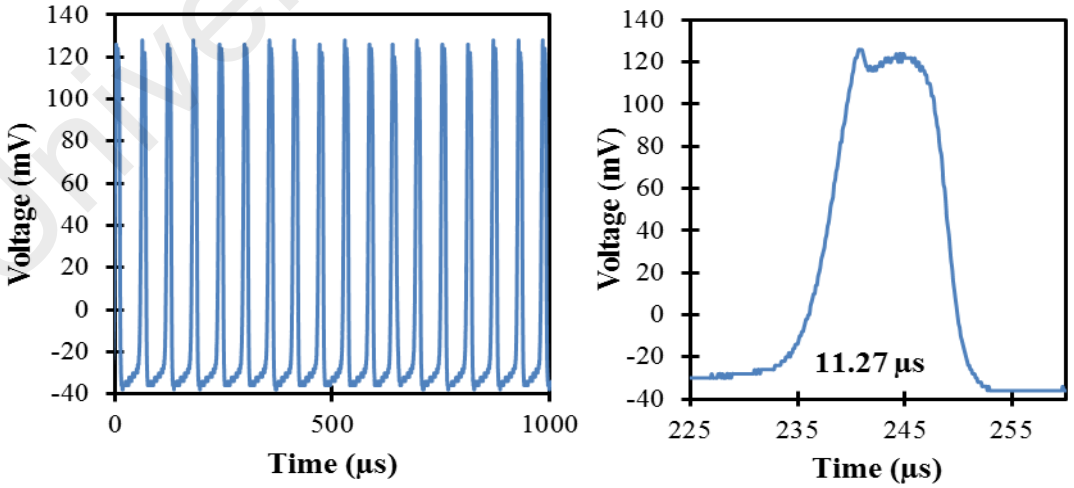

(b) 71.3 mW (Repetition rate of 17.54 kHz)

Figure 3.5: Pulse trains and single-pulse envelop of the Q-switched YDF using MoS_2 with different pump powers of (a) 49.59 mW, (b) 71.3 mW, and (c) 87.2 mW

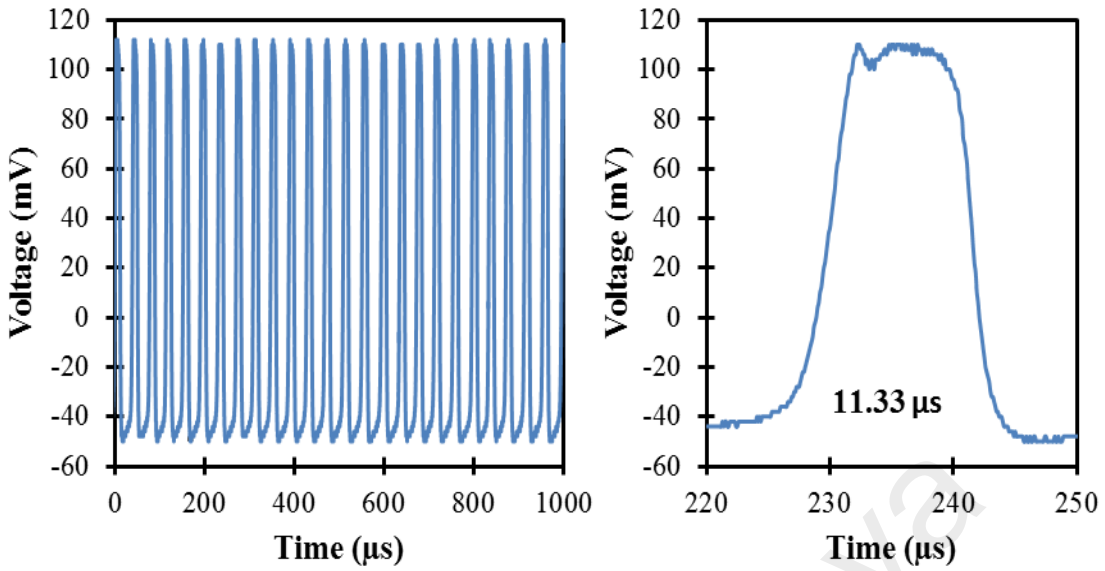

(c) 87.2 mW (Repetition rate of 25.25 kHz)

Figure 3.5, continued

Figure 3.6 shows the repetition rate and pulse width of the Q-switched YDFL as a function of the pump power. As the pump power increases from 49.57 to 87.2 mW, the repetition rate grows from 3.817 to 25.25 kHz. Throughout the experiment, the output was stable and no amplitude modulations were observed. This indicates that there was no self-mode locking (SML) effect during the Q-switching operation. On the other hand, the pulse width decreases from 26.09 µs to 11.33 µs. As the pump power exceeds 71.3 mW, the pulse width stays nearly unchanged, which clearly indicated that the SA was saturated. It was reported that the pulse width of a passively Q-switched laser depends on the cavity round-trip time and the modulation depth of the SA (Zayhowski et al., 1991). Therefore, the minimum pulse duration obtained in our experiment can surely be narrowed by shortening the cavity length and improving the modulation depth of the MoS_2 layer.

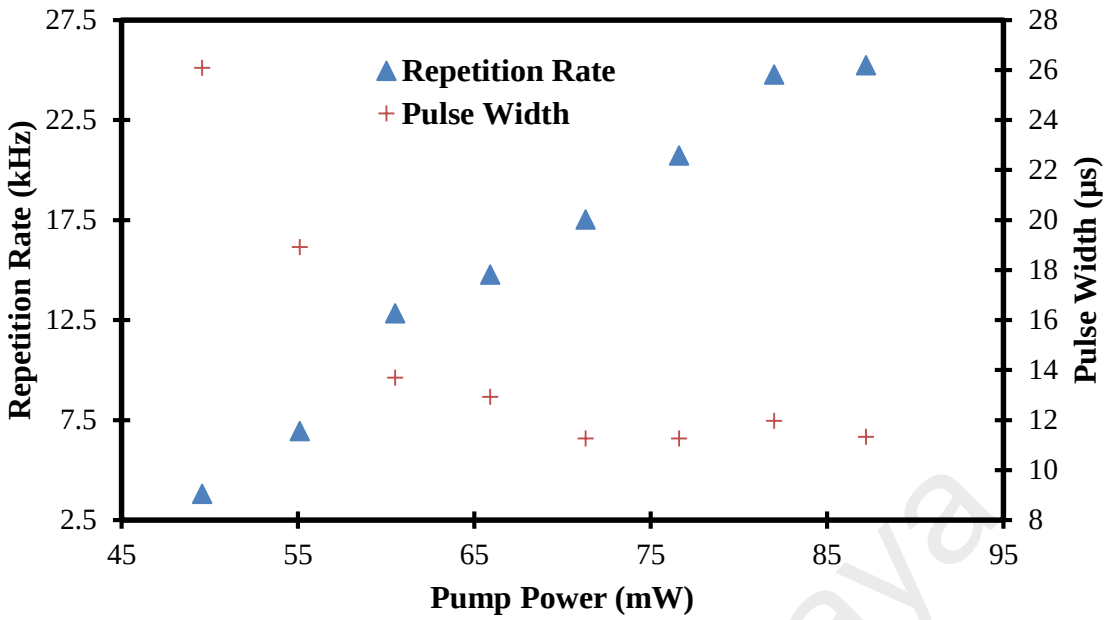

Figure 3.6: Pulse repetition rate and pulse width of the proposed Q-switched YDFL versus incident pump power

Figure 3.7 shows the dependency between average output power and single pulse energy of the proposed Q-switched YDFL against the pump power. As shown, the average output power increases linearly from 0.542 to 7.46 mW while the pulse energy also increases from 142 to 295.45 nJ as the pump power rises from 49.57 to 87.2 mW. The pulse energy is calculated based on the measured average output power and the repetition rate. When the pump power goes past 87.2 mW, the Q-switched pulse train becomes unstable or disappears, as typically observed in certain passively Q-switched fiber lasers (Z. Luo et al., 2013). Subsequently, when the pump power is reduced to a level below 87.2 mW, the stable Q-switched pulse train reappear. Hence, the unstable Q-switched operation at high pump power may be attributed to over-saturation of the MoS_2 SA rather than to thermal damage (Z. Luo et al., 2013). Figure 3.8 shows the RF spectrum of the Q-switched YDFL at the pump power of 87.2 mW, for which the pulse repetition rate is 25.25 kHz, matching the oscilloscope data of Figure 3.5 (c). The RF signal-to-noise ratio (SNR) is about 30 dB with no spectral modulation, indicating that the passively Q-switching operation is stable.

It is worthy to note that the mode-locking pulses train was failed to be obtained with the current SA. This is most probably due to the large number of MoS_2 layers in the SA as well as the high loss at the scotch tape. Therefore, a new SA was developed in the next section using a liquid phase exfoliation method.

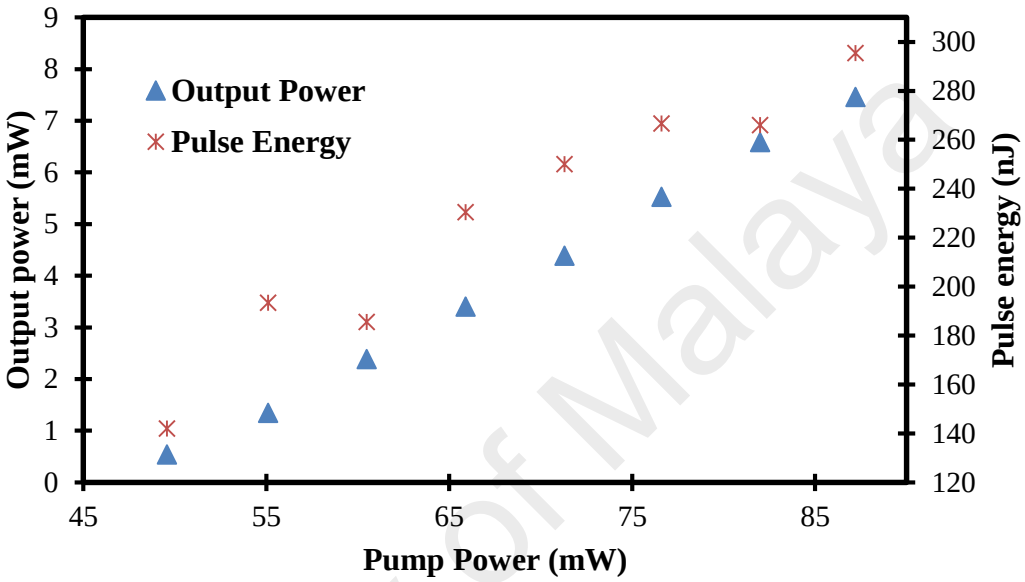

Figure 3.7: Average output power and pulse energy of the proposed Q-switched YDFL versus incident pump power

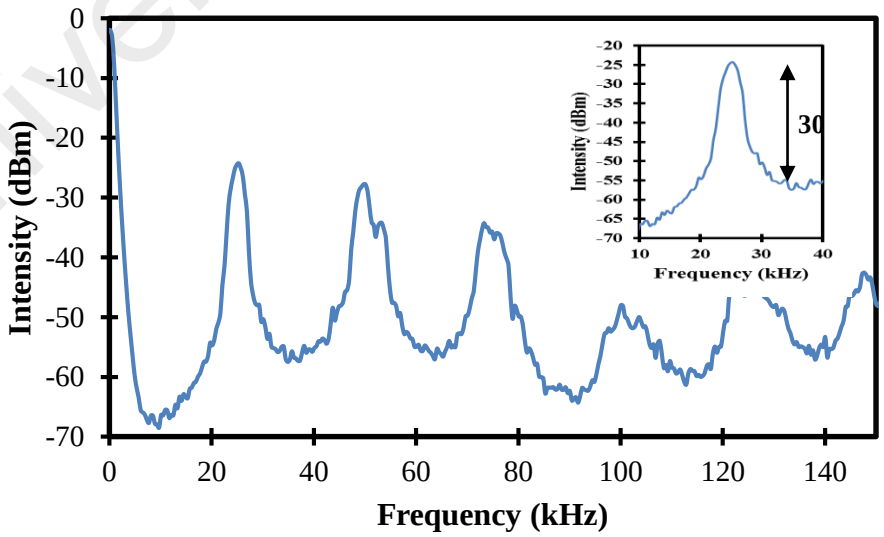

Figure 3.8: RF spectra of the Q-switched YDFL at the pump power of 87.2 mW with 150 kHz span. Inset is an enlarge image of 25.25 kHz repetition rate

3.3 Passively Mode-locked YDFL Operation with Few Layer MoS_2 Embedded into Polyvinyl Alcohol Composite Polymer as a SA

In the recent years, mode-locked fiber lasers have extensively engaged interest due to their application benefits, such as micromachining, communication, and optical systems; as well as their nature being compact, cost-effective and easy to setup (Grelu et al., 2012; Lecaplain et al., 2012). Active mode-locking pulse train can be achieved by inserting electronic switching such as acousto-optic modulator (Ryu et al., 2007). Passively mode-locked fiber lasers are also widely explored in recent years by utilizing saturable absorption of optical materials. Various SAs have been demonstrated so far such as SESAMs (L. Sun et al., 2010; M. Zhang et al., 2009), carbon nanotubes (CNTs) (Mou et al., 2012; L Zhang et al., 2011), and graphene (Z. Sun et al., 2012; Z. Sun et al., 2010). SESAMs are good SA device which can be used to generate a mode-locked fiber laser in both 1 μm and 1.5 μm regions (L. Chen et al., 2009; M. Zhang et al., 2009). However, its application is still limited due to their difficult fabrication methods, complex design, expensive cost and narrower wavelength operation range.

To date, another 2D nanomaterial, MoS_2 is also drawing more interest especially for mode-locked fiber laser applications. The reason for this growing interest is due to its material's thickness, which gives an excellent optical laser properties as well as the band-gap (M. Ahmed, A. Latiff, H. Arof, H. Ahmad, et al., 2016; H. Liu, A.-P. Luo, et al., 2014). Until today, only a few works have been reported on MoS_2 based SA (M. Ahmed, A. Latiff, H. Arof, H. Ahmad, et al., 2016; Du et al., 2014; H. Liu, A.-P. Luo, et al., 2014; Sathiyan et al., 2016; M. Zhang et al., 2015). In the previous section, a Q-switched EDFL was demonstrated using a mechanically exfoliated MoS_2 as a Q-switcher. In this section, a passively mode-locked YDFL is demonstrated using a few layered MoS_2 as a SA. The few layer of MoS_2 polymer is a composite of liquid phase exfoliation (LPE) of chemically pristine crystal. A small piece of MoS_2 polymer film was inserted in the YDFL cavity,

sandwiching it in between two fiber optical ferrules with a connector to obtain mode-locking pulses with repetition rate of 18.8 MHz and pulse energy of 0.1 nJ. The LPE method is simple, cheap and does not require any complicated procedures.

3.3.1 Fabrication and Characterization of the MoS_2 Film as SA

The liquid phase exfoliation (LPE) process for MoS_2 exfoliation was carried out in two steps as shown in Figure 3.9. The bulk MoS_2 crystals were first mixed together with a solvent that gets a comparable surface energy with MoS_2 (~75 $mJ \cdot m^{-2}$) (Cunningham et al., 2012). Likewise, Dimethylformamide (DMF) solvent was chosen with a concentration of 5 mg/ml for this work. Following, the second step was to exfoliate the material through a sonication process. In this process, local pressure variations were generated to sufficiently separate the atomic layers of the bulk crystal (Coleman et al., 2011; Hasan et al., 2010) in the solvent to produce a dispersion, which was rich in few-layer flakes (Coleman et al., 2011). Then, the MoS_2 dispersion was kept to be ultra-sonicated for 24 hours before it was centrifuged for 1 hour at ~3000 rpm. This allowed the un-exfoliated sediment to settle at the bottom since the larger flakes descended more rapidly than the exfoliated few-layer flakes in the centrifuge cell (Bonaccorso et al., 2013). The top portion of the dispersion containing few-layer flakes was taken out for further composition fabrication process.

A few procedures were followed in the second step to produce MoS_2 polymer film for this experiment. Firstly, ~10 ml of decanted MoS_2 dispersion was put together with a 10 mg/ml concentrated ~20 ml of polyvinyl alcohol (PVA) solution. This solution was a result of ~200 mg of PVA being dissolved in 20 ml of deionized water. By this, 30 ml of MoS_2-PVA was prepared, which was then heated at a temperature of ~80 °C and stirred with a magnetic object until the solution was brought down to an approximate volume of ~10 ml. These series of actions took around 7 hours to be done, following which the

resulting MoS_2-PVA solution was placed in a glass substrate and put in an oven for 4 hours at a temperature of ~80 °C in order to dry and obtain a composite film with a thickness of ~40 µm.

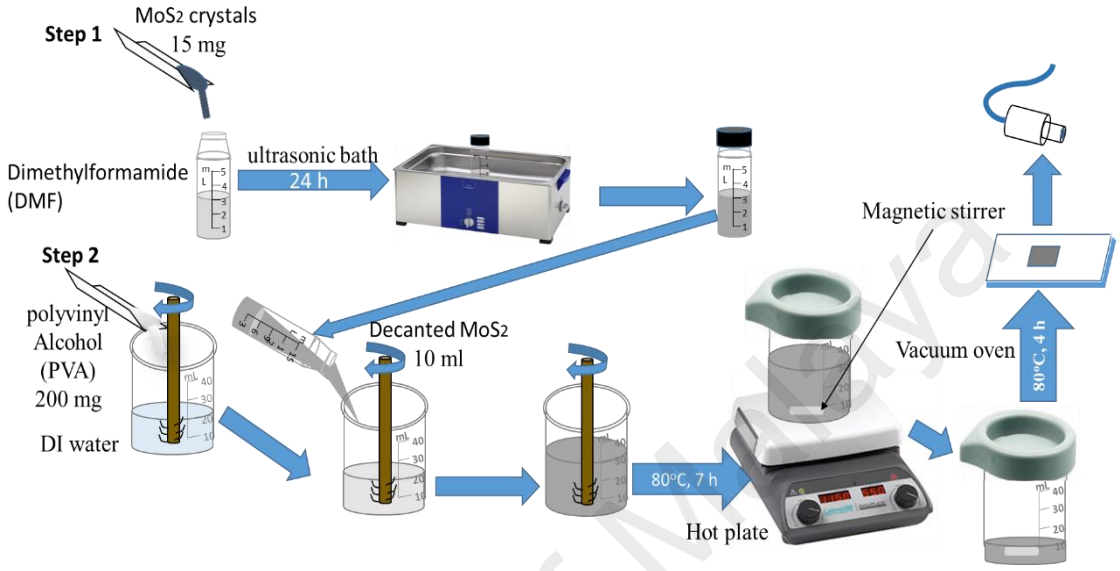

Figure 3.9: The fabrication process of MoS_2 PVA film

Field emission scanning electron microscopy (FESEM) and Raman spectroscopy were performed on the fabricated MoS_2–PVA film sample. Figure 3.10 (a) shows the FESEM image that illustrates a MoS_2 nanoplatelets embedded with small particles in average sizes from 3-10 µm with slight bends. Figure 3.10 (b) presents the Raman spectrum recorded using a spectrometer at a 514 nm beam of an Argon-ion laser that was radiated on the film for 10 seconds with an exposure power of 10 mW. As shown in the figure, the sample displays two signature peaks at 383 cm^{-1} and 407 cm^{-1} which are related to in-plane vibration of Molybdenum and Sulfide atoms and out of plane vibration of Sulfide atoms respectively. The frequency difference was recorded to be 24 cm^{-1}. It was observed that the E_{2g}^1 mode according to the in-plane motion shifted to a shorter wavelength after complete exfoliation. This indicated that the number of layers of MoS_2 were in the range of 2-5 layers (H. Li et al., 2012).

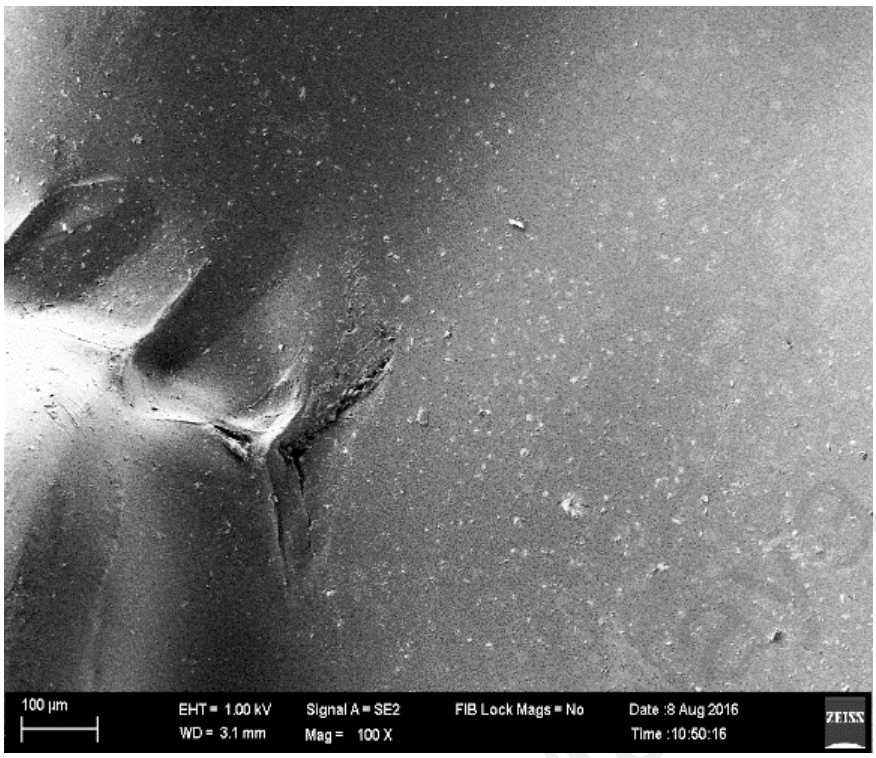

(a)

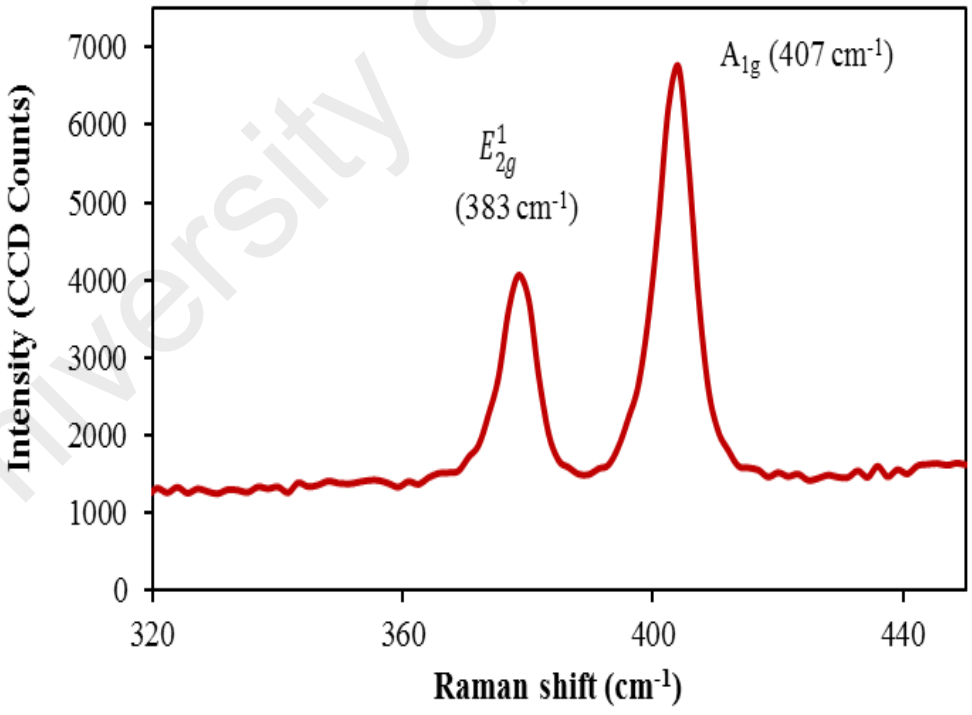

(b)

Figure 3.10: (a) FESEM image and (b) Raman spectrum of the MoS_2-polymer composite film

A nonlinear absorption measurement was also performed on the fabricated MoS_2-PVA film to confirm its saturable absorption as shown in Figure 3.11 (a). In the experiment, a stable mode-locked fiber laser operating at 1565 nm wavelength with repetition rate of 15 MHz and pulse width of 0.9 ps, was employed as the input pulse source. The mode locking signal results were then amplified using an erbium-doped fiber amplifier (EDFA) in order to obtain a high peak power output to efficiently saturate the MoS_2 sample. The output port of the amplifier was connected with a variable optical attenuator to control the launching output power to the system before it is launched into a 3dB optical coupler and two optical power meters. The first optical power meter was linked to one port of coupler and the second port of coupler was linked to the MoS_2 film sample then connected into the second optical power meter. The resultant characteristic of MoS_2 film as SA is shown in Figure 3.11 (b).

The absorption power was recorded as a function of incident intensity on the device by modifying the input optical laser power. The experimental data for absorption were prepared depending on the two-levels of SA model (Garmire, 2000).

$$a(I) = \frac{\alpha_s}{1 + I/I_{sat}} + \alpha_{ns} \tag{3.2}$$

where $a(I)$, α_s, I, I_{sat} and α_{ns} are stand for absorption, modulation depth, input intensity, saturation intensity, and non-saturation loss respectively. For the MoS_2 sample that was used in this work, the modulation depth, non-saturable intensity, and saturation intensity were measured to be approximately 9.7 %, 10.9 %, and 40 MW/cm^2, respectively.

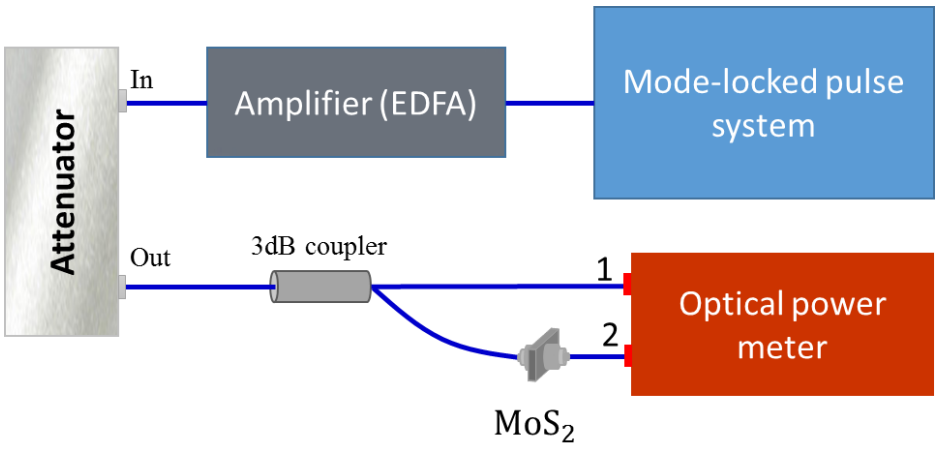

(a)

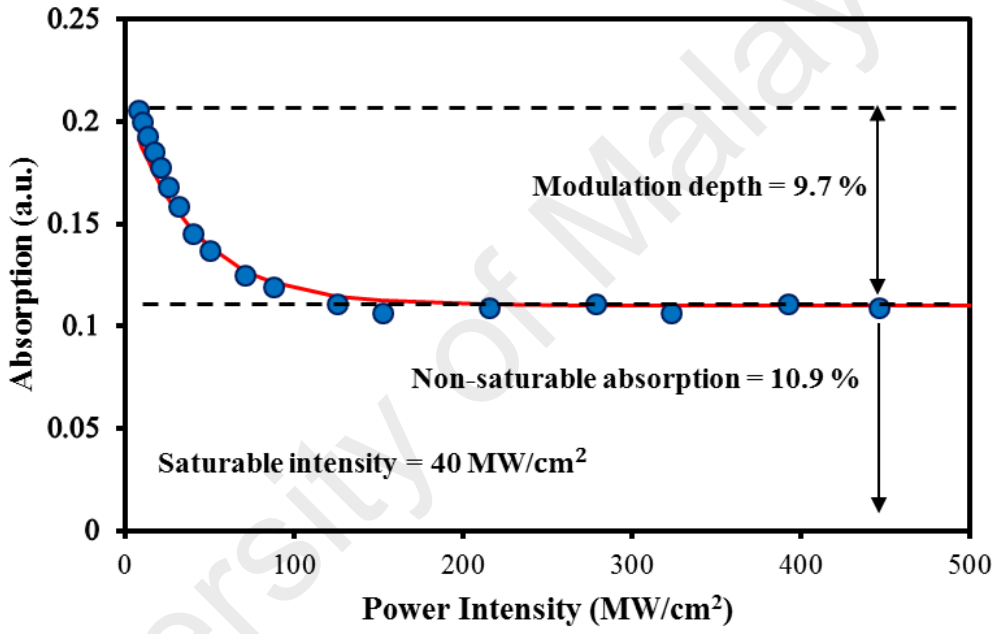

(b)

Figure 3.11: The nonlinear absorption measurement of MoS_2-SA. (a) Experimental setup for nonlinear measurement. (b) Nonlinear absorption curve

3.3.2 Configuration of the Mode-Locked Laser

The proposed configuration of mode-locked YDFL with MoS_2 SA is shown in Figure 3.12. It uses a 0.7 m long of Ytterbium-doped fiber (YDF) with 1300 dB/m peak absorption at 977 nm as a gain medium. The YDF was pumped by a 974 nm laser diode through a 980/1060 nm wavelength division multiplexer (WDM). An isolator is used in the ring cavity to avoid backward reflection as well as ensure unidirectional operation.

The MoS_2 SA device was composed by sandwiching the fabricated MoS_2 PVA film in between two fiber ferrules via an adapter as shown in the inset of Figure 3.12. It is incorporated into the laser cavity to act as a mode-locker for generating ultrashort pulses train. A 10 dB coupler is used to tap out the output laser while allowing 90% of the photons to oscillate inside the cavity. The cavity length is measured to be about 10.6 m with normal dispersion of 0.242 ps^2/km.nm at 1030 nm. The output spectrum of the laser is measured by an OSA with a 0.02 nm spectral resolution while the temporal characteristic of the laser is investigated using an oscilloscope coupled with a 2-GHz photodetector. The RF spectrum is measured by an RF spectrum analyzer with a range operation from 9.0 kHz to 7.8 GHz.

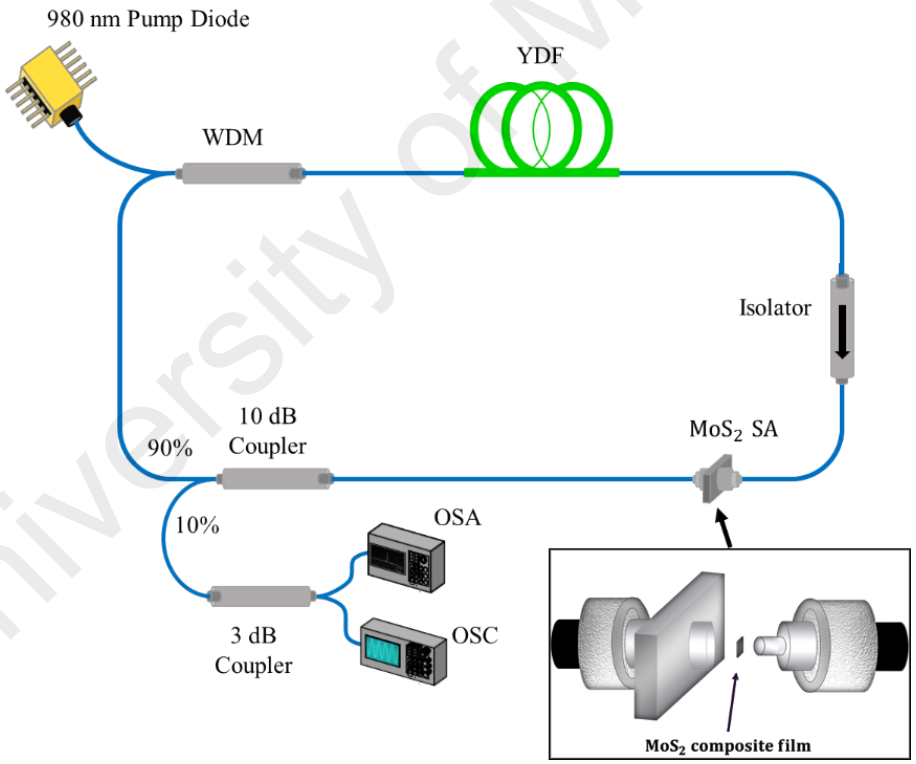

Figure 3.12: Experimental setup for mode-locked YDFL with MoS_2 based SA. Inset shows how the MoS_2 PVA film is incorporated in the laser cavity

3.3.3 Mode-locking Performance

At first, we observed a continuous wave (CW) laser operation when the pump power reached to 58.0 mW. As the pump power was further increased to 78.7 mW, the self-

started and stable mode-locked pulse train was generated. The mode-locked pulse train was maintained with further increase in pump power up to the maximum pump power of 202.9 mW. Figure 3.13 (a) shows the output spectrum of the mode-locked laser at pump power of 202.9 mW. The peak wavelength was centered at 1073.86 mW with 3dB bandwidth of 0.06 nm without Kelly sideband, which indicates that the pulses operate in normal dispersion.

The typical mode-locking pulse train at pump power of 202.9 mW is shown in Figure 3.13 (b). It is observed that the peak to peak spacing of the pulse train was about 53 ns, which equals to the repetition rate of 18.8 MHz. The repetition rate obtained is corresponded with the fundamental frequency for cavity length of 10.6 m. As shown in the figure, the pulse width is measured to be 3.12 ns, which is a lot broader than the actual pulse width. This is attributed to the oscilloscope resolution limitation. To estimate the actual pulse width, we used mathematical calculation based on time bandwidth product (TBP). Assuming that the TBP is 0.441 for Gaussian pulse profile (Hisyam et al., 2017) minimum possible pulse width is calculated to be approximately 28.3 ps.

Figure 3.13 (c) shows the output power and pulse energy of the mode-locked laser at various pump powers. As seen in the figure, both output power and pulse energy linearly increased with the pump power. At the maximum pump power of 202.9 mW, the maximum output power and pulse energy are obtained at 1.84 mW and 0.1 nJ, respectively. Figure 3.13 (d) shows the RF spectrum for YDFL laser. The fundamental frequency of the laser is obtained at 18.8 MHz with a SNR of more than 30 dB, which indicates the stability of the mode-locking operation. It is worthy to note that there is no appearance of fundamental frequency noticed as the MoS_2 is taken off at all level of pump power.

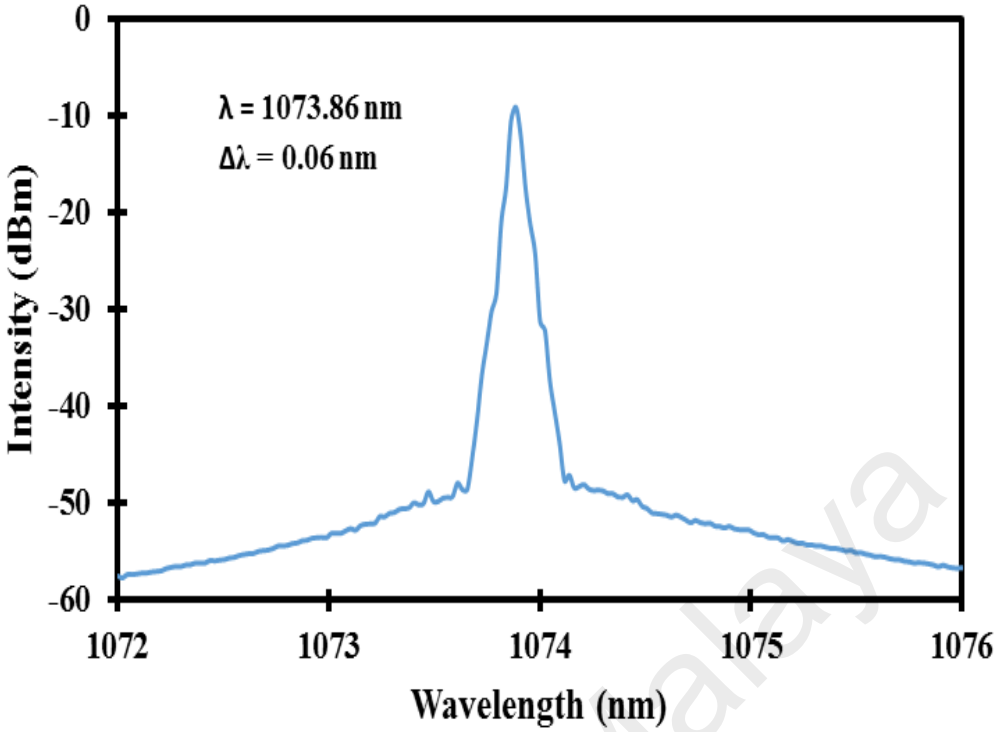

(a)

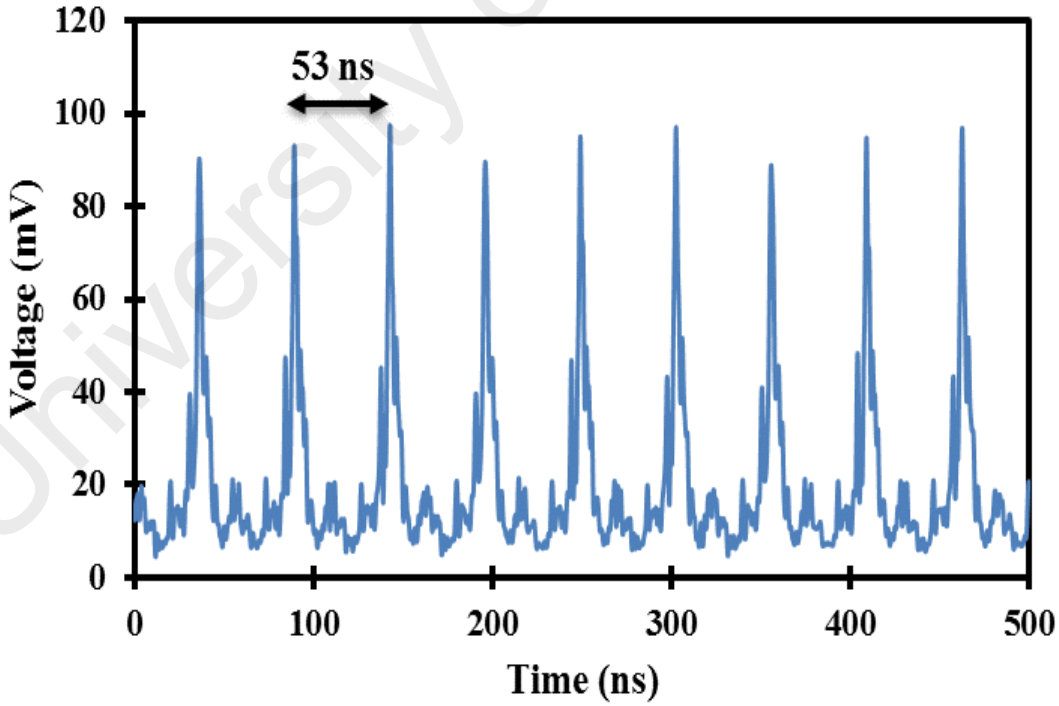

(b)

Figure 3.13: Mode-locked YDFL performances. (a) Output spectrum and (b) Oscilloscope train at maximum pump power. (c) Output power and pulse energy. (d) RF spectrum

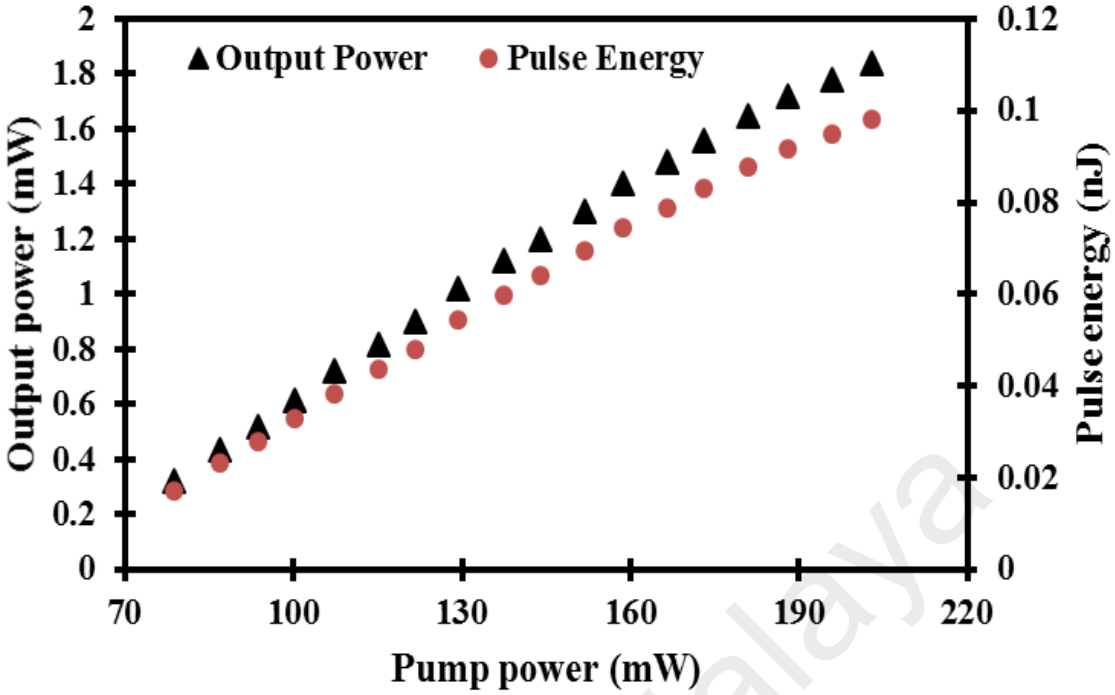

(c)

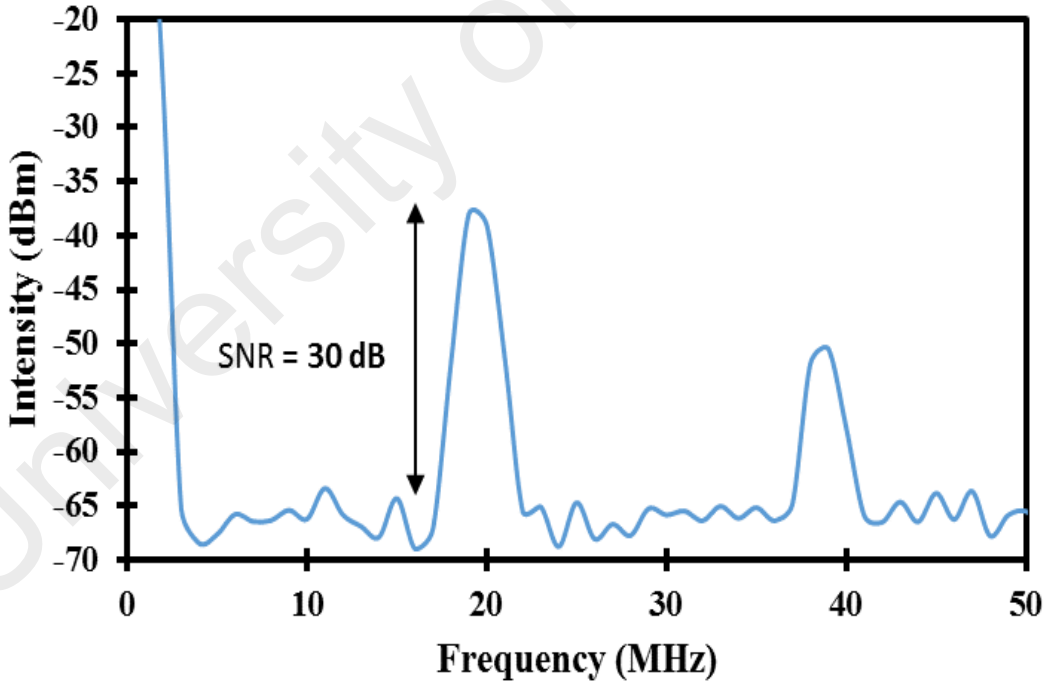

(d)

Figure 3.13, continued

3.4 Summary

In this chapter, a simple and compact passive Q-switched and mode-locked YDFL was successfully demonstrated using MoS_2 based SA. It was found that a Q-switching operation at 1μm region can be realized by using a bulk layer of MoS_2 tape, which was obtained by a mechanical exfoliation technique. The tape was sandwiched between two fiber ferrules to form the fiber compatible MoS_2 based Q-switcher. A Q-switched pulse train operating at 1070.2 nm was obtained as the 980 nm pump power reached the threshold value of 49.57mW and it continued to operate stably until 87.2 mW. The corresponding pulse repetition rate was tunable from 3.817 to 25.25 kHz. The lowest pulse width was 11.33 μs and the maximum pulse energy was 295.45 nJ.

In the other hand, a passive mode-locked with 0.7 m long of YDF as a gain medium was successfully reported using a few layered MoS_2 PVA film as a mode-locker. The MoS_2 film was obtained based on a LPE of MoS_2 crystal. Stable and self-starting passive mode-locking pulses were achieved within the pump power of 78.7 mW to 202.9 mW. It operates at 1073.86 nm with a fixed repetition rate of 18.8 MHz with picoseconds pulse width. The maximum pulse energy was calculated to be approximately 0.1 nJ at pump power of 202.9 mW. This piece of work tackled an important aspect that contributes to study nonlinear optical properties of MoS_2, which may in turn guide to future paths for ultrafast photonics applications. These experimental results suggest that MoS_2 is a promising material for pulsed laser applications.

CHAPTER 4: BLACK PHOSPHORUS AS SATURABLE ABSORBER

4.1 Introduction

As discussed in the previous chapters, passively Q-switched and mode-locked fiber lasers have gained widespread attention due to their advantages in compactness and flexibility, and potential applications in medicine, telecommunications, remote sensing and laser material processing. To date, many forms of saturable absorber (SA) have been used in generating these lasers including semiconductor saturable absorber mirror (SESAM) (U. Keller et al., 1996), single-walled carbon nanotubes (SWCNTs) (S. W. Harun et al., 2012) and graphene (H.-P. Li et al., 2014; J. Zhao et al., 2014). Despite the successful implementation of these SAs, researchers are still looking for new SAs with better characteristics in terms of wavelength-independent saturable absorption, low saturable optical intensity, fiber compatibility and high damage threshold. Recently, topological insulators (TIs) and Molybdenum disulfide (MoS_2) have also been identified as potential SAs for mode-locking and Q-switching (Y. Chen et al., 2013; Z. Luo et al., 2013; Ren et al., 2015).

In the previous chapter, MoS_2 as SA was proposed and reported for generating both Q-switching and mode-locking in Ytterbium-doped fiber laser (YDFL) cavity. Another 2D material: a black Phosphorus (BP) dubbed as the newly emerging allotrope, has gained much attention for potential applications in the next-generation optoelectronics devices such as sensor, field-effect transistors and solar cells (Abbas et al., 2015; J. Dai et al., 2014; L. Li et al., 2014). Multi-layer BP has a similar structure as bulk graphite. In a single layer, each phosphorus atom is covalently bonded with three adjacent phosphorus atoms to form a stable honeycomb structure, and different layers are stacked together by van der Waals interaction (Han Liu, Yuchen Du, Yexin Deng, & Peide D. Ye, 2015). It has the common properties of 2D materials such as wideband absorption, ultrafast carrier dynamics and planar characteristic (J. Qiao et al., 2014). The BP comprises only the

elemental “phosphorus” and thus it could be easily peeled off by mechanical exfoliation. Tunable Q-switched fiber laser was demonstrated based YDFL using Black Phosphorus (BP) as SA with maximum pulse energy of 7.1 nJ (Harith Ahmad et al., 2016). In another work, dual wavelength Q-switched YDFL with maximum pulse energy of 2.09 nJ. Mode-locking pulse was also generated in double cladding YDF laser using BP as SA with repetion rate of 13.5 MHz and pulse duration of 7.54 ps (Hisyam et al., 2017).

In this chapter, Black phosphorus (BP) is proposed as new SA for operation at 1 micron region. Both Q-switching and mode-locking operations are demonstrated using a ytterbium doped fiber (YDF) as a gain medium. At first, a Q-switched YDFL is demonstrated using a newly developed multi-layer BP SA. The SA is prepared by fixing the BP material onto a sticky tape using a mechanical exfoliation technique as described in the previous chapter. The BP tape is placed between two ferrules and incorporated in YDFL cavity to achieve a stable Q-switching pulse operating at 1.0 μm region. The laser has a pump threshold of 55.1 mW, a pulse repetition rate that is tunable from 8.2 to 32.9 kHz, and the narrowest pulse width of 10.8 μs. The highest pulse energy of 328 nJ is achieved at the pump power of 97.6 mW.

In mode-locking experiment, the BP SA is prepared using a slightly different method to reduce the device loss and thus enable the mode-locking operation. The SA is prepared by mechanically exfoliation of the BP crystal and fixed the acquired flakes onto the end surface of a standard FC/PC fiber connector. By incorporating the BP SA into the YDF laser cavity, a stable mode-locked operation is obtained at 1033.76 nm wavelength and the repetition rate of 10 MHz. The maximum pulse energy and peak power are almost 2.7 nJ and 0.83 kW respectively at the maximum pump power of 200 mW. These experimental results indicate that the BP SA can be used successfully to generate stable Q-switching and mode-locking pulses train at 1 μm region.

4.2 BP SA for Q-switching

In this section, a passively Q-switched YDFL is demonstrated using multi-layer BP based SA, which was obtained by mechanical exfoliation method. Mechanical exfoliation is advantageous mainly because of its simplicity and reliability, where the entire fabrication process is free from complicated chemical procedures and costly instruments.

4.2.1 Fabrication and Standard Characterization of the BP based SA

The multi-layer BP used in our experiment was prepared by peeling bulk-structured BP 2D thin layers using a scotch tape. Here, a large block of commercially available BP crystal (with purity of 99.995 %) was used as a raw material. Then, the flakes on the scotch tape was repeatedly pressed to form a thin layer of BP, thin enough to transmit light with a high efficiency. Afterward, a small piece of the BP tape was cut out and attached onto a standard FC/PC fiber ferrule end surface with the aid of index matching gel. After connecting it with another FC/PC fiber ferrule with a standard flange adapter, the all-fiber BP based SA was finally ready. The entire preparation process is illustrated in Figure 4.1.

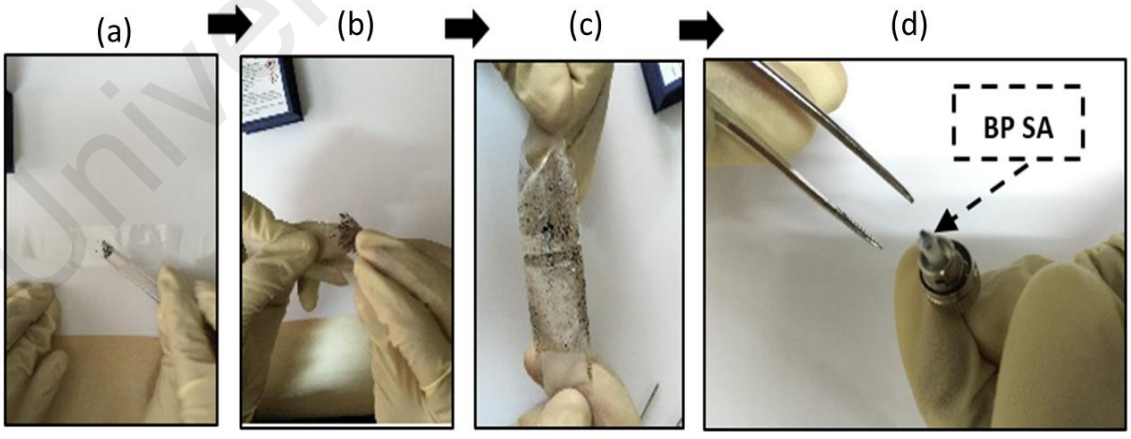

Figure 4.1: The preparation flow of BP-SA by using the mechanical exfoliation method. (a) The peeling BP crystal is place onto a sticky tape. (b) The crystal is thinned to the small flakes by repeatedly pressing the flakes onto a sticky tape. (c) The image of the BP tape after the thinning process. (d) Attaching the BP tape onto the ferrule

The bandgap of a single layer of BP is relatively higher compared to the multi-layer. This leads to the use of a higher photon energy to excite the electron into the conduction band. The single layer needs a high energy for electron excitation due to the increase in its bandgap and has only 2.8% absorption of a single layer. However, multi-layer BP has a relatively narrow direct bandgap and that was considered a promising saturable absorber for the long wavelength range and has a higher modulation depth (F. Wang, 2017).

The composition of the multi-layer BP tape is examined by the energy dispersive spectroscopy (EDS) on the Field Emission Scanning Electron Microscopy **(**FESEM). Presence of the BP material on the scotch tape adhesive surface was confirmed by the presence of the high peak of phosphorus in the spectroscopy as shown in Figure 4.2. The inset in Figure 4.2 shows the FESEM image, which confirms the existence of uniform multi-layer phosphorus and the absence of > 1 μm aggregates or voids in the tape, which otherwise result in non-saturable scattering losses.

Raman spectroscopy was also performed on the prepared BP tape sample. Figure 4.3 shows the Raman spectrum, which is recorded by a spectrometer when a 514 nm beam of a Argon ion laser is radiated on the tape for 10 ms with an exposure power of 10 mW. As shown in the figure, the sample exhibits three distinct Raman peaks at 359 cm^{-1}, 434 cm^{-1} and 460 cm^{-1} (Sugai et al., 1985), corresponding to B_{2g} and vibration modes of a layered BP. While B_{2g} and modes correspond to the in-plane oscillation of phosphorus atoms in the BP layer, the mode corresponds to the out-of-plane vibration. The thickness for single-layer BP is about 0.8 nm (Andres et al., 2014), thus the prepared BP based SA is expected to consist of 250 layers.

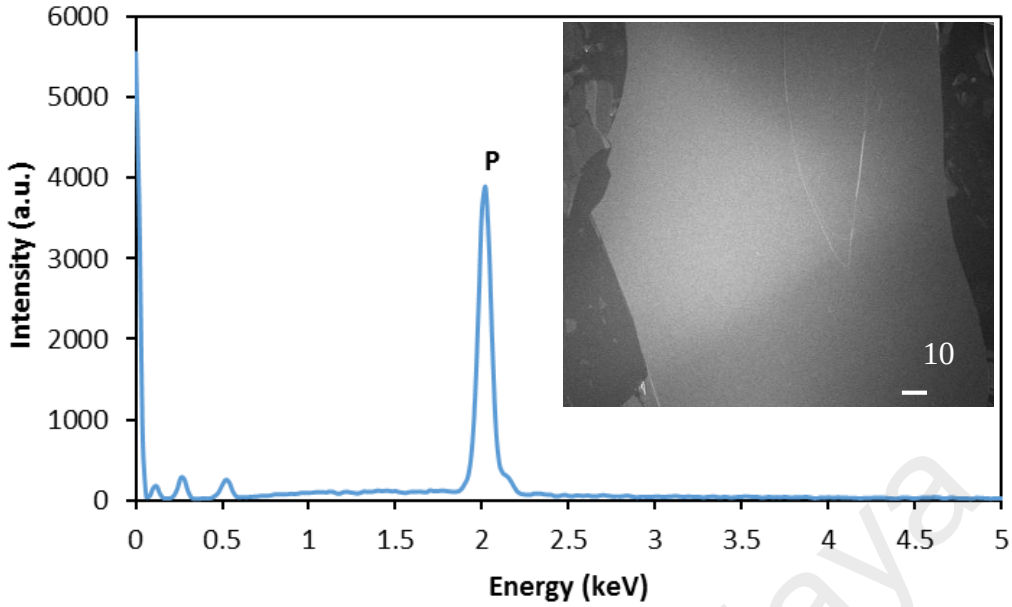

Figure 4.2: EDF data from the FESEM image of the prepared BP tape, which confirms the presence of phosphorus. Inset: the FESEM image

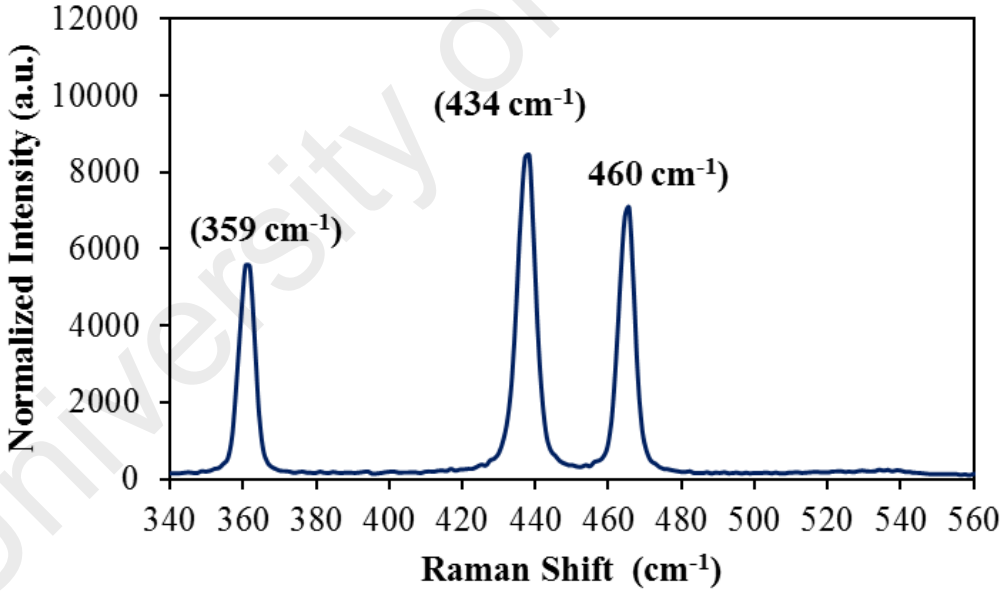

Figure 4.3: Raman spectrum of the multi-layered BP tape

4.2.2 Nonlinear Saturable Absorption of BP-SA

The nonlinear optical response property for the multilayer BP on the scotch tape was also investigated to confirm its saturable absorption by applying an absorption technique. A self-constructed mode-locked fiber laser (1557 nm wavelength, 1.5 ps pulse width, 17.4

MHz repetition rate) was used as the input pulse source. The transmitted power and a reference power for normalization are recorded as a function of incident intensity on the tape by varying the input laser power. With increasing peak intensity, the material absorption decreases as shown in Figure 4.4, confirming the saturable absorption characteristic of the multi-layer BP. The experimental data for absorption are fitted according to a simple two-level SA model (Mu et al., 2015),

$$\alpha(I) = \frac{\alpha_s}{1 + I/I_{sat}} + \alpha_{ns} \qquad (4.1)$$

where $\alpha(I)$ is the absorption, α_s is the modulation depth, I is the input intensity, I_{sat} is the saturation intensity, and α_{ns} is the non-saturable absorption. As shown in Figure 4.4, the modulation depth, non-saturable intensity, and saturation intensity are 7 %, 58 % and 0.0025 MW/cm^2, respectively. Taking into account its nonlinear optical response leading to absorption saturation at relatively low fluence, the mechanically exfoliated BP meets basic criteria of a passive SA for fiber lasers.

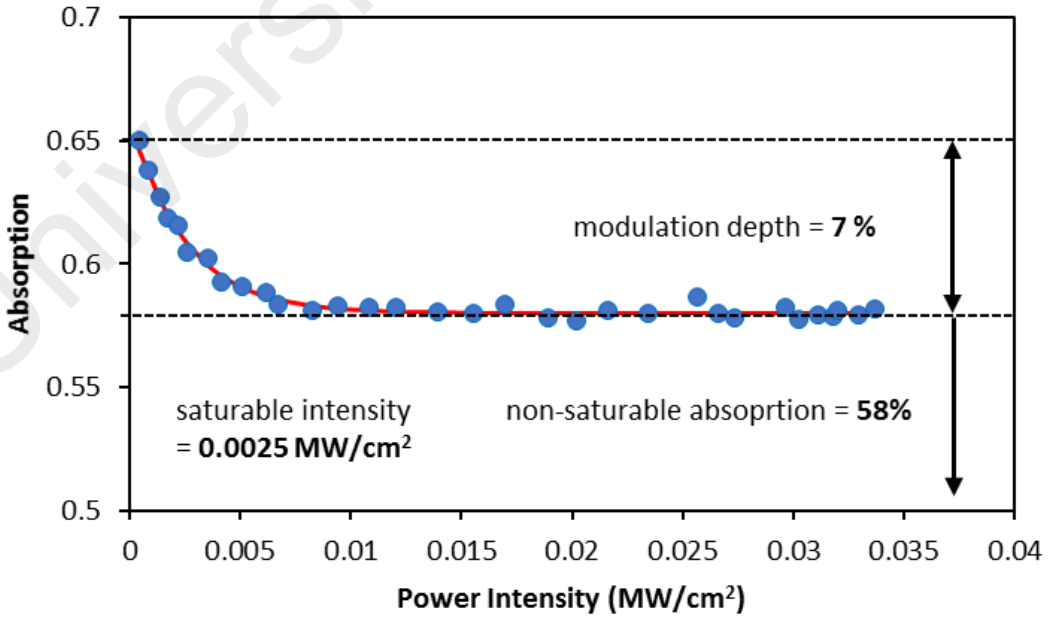

Figure 4.4: Nonlinear saturable absorption profile of the multi-layer BP

4.2.3 Experimental Setup for the Q-switched YDFL

The experimental setup of the proposed Q-switched YDFL is schematically shown in Figure 4.5. The setup is almost similar the proposed MoS_2 based Q-switched YDFL as described in Figure 3.3. The ring cavity consists of a 1.5 m long YDF, a wavelength division multiplexer (WDM), an isolator, a 3dB output coupler and the multi-layer BP nanomaterial based Q-switcher. The total cavity length is about 6 m. The YDF used has a core diameter of 4.0 µm, numerical aperture (NA) of 0.20 and cutoff wavelength of around 980 nm.

The doping level of ytterbium ions in the fiber is 1500 ppm. The YDF is pumped by a 980 nm pump laser diode through a 980/1030 nm WDM. The multilayer BP on the scotch tape is integrated into the cavity as a passive Q-switcher while a polarization insensitive optical isolator is incorporated to ensure unidirectional operation of the laser. The Q-switched pulse train is taken out via a 3dB output coupler which keeps half of the light oscillating in the ring cavity for both spectral and temporal diagnostics.

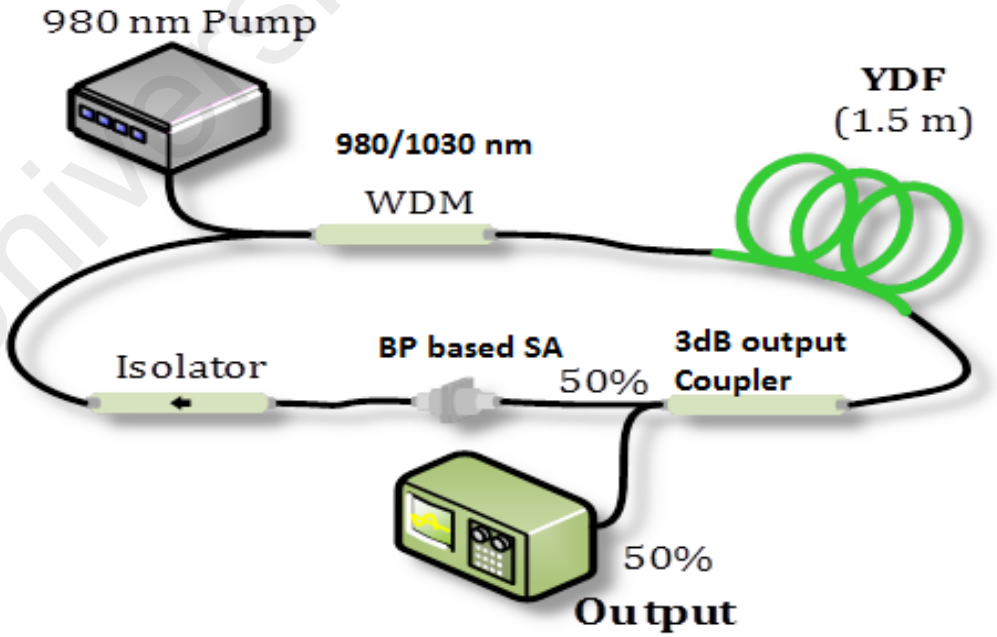

Figure 4.5: Configuration of the proposed BP based Q-switched YDFL

The output is simultaneously monitored using a 350-MHz oscilloscope together with a 2-GHz photodetector, a 7.8 GHz radio-frequency (RF) spectrum analyzer and an optical spectrum analyzer (OSA) with a spectral resolution of 0.02 nm. It is worth noting that the Q-switching performance such as output pulse energy of the laser is observed to be optimum with the use of the 3dB coupler.

4.2.4 Q-switching performance

The YDFL started to operate in the continuous-wave mode at the pump power of 40.5 mW, before transiting to the Q-switching operation at 55.1 mW. When the pump power was gradually increased up to 97.6 mW, a stable pulse train with an increasing repetition rate was observed. This is a typical feature of passive Q-switching. Figure 4.6 shows the spectral and temporal characteristics of the output Q-switching pulse train when the 980 nm pump power was fixed at 76.6 mW. The output spectrum is depicted in Figure 4.6 **(a)**, which indicates that the Q-switched laser operates at 1069.4 nm with 3 dB spectral bandwidth of about 1.0 nm and signal to noise ratio of about 40 dB. Figure 4.6 (b) shows the typical oscilloscope trace of the Q-switched pulse trains. The pulse train has the period of 38.3 μs without noticeable timing jitter.

Figure 4.6 (c) reveals a typical pulse envelope, displaying an almost symmetrical Gaussian-like shape with a pulse duration of 12.2 μs. The RF output spectrum in Figure 4.6 (d) shows that the Q-switched pulses have a repetition rate of 26.1 kHz, which agrees with the pulse period of 38.3 μs measured in Figure 4.6 (b). It is also observed that the rf signal-to-noise ratio is about 23 dB with no spectral modulation, indicating that the passively Q-switching operation was stable.

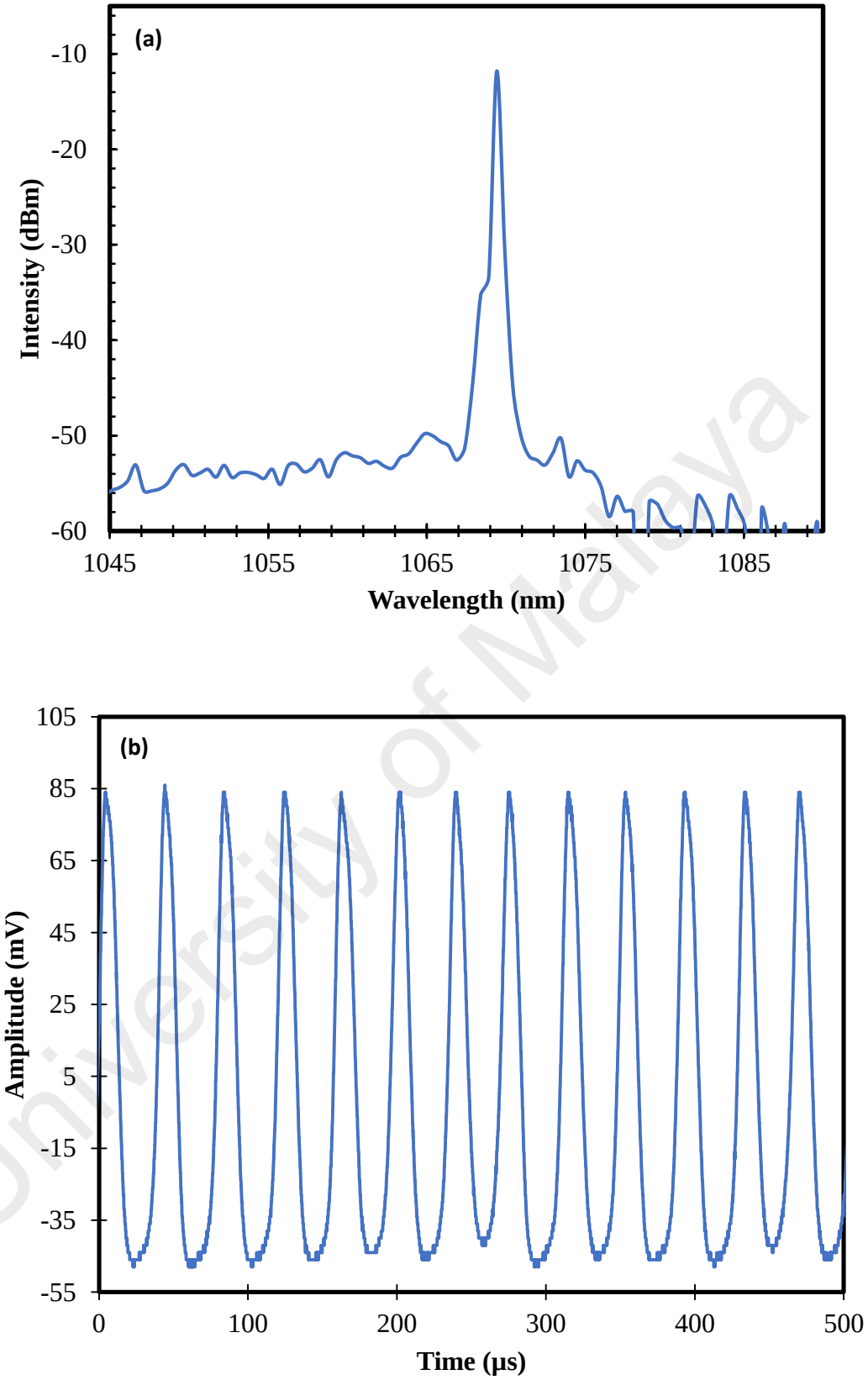

Figure 4.6: Spectral and temporal characteristics of the output Q-switching pulse train at pump power of 76.6 mW (a) output spectrum (b) typical pulse train (c) typical single pulse envelop (d) RF spectrum

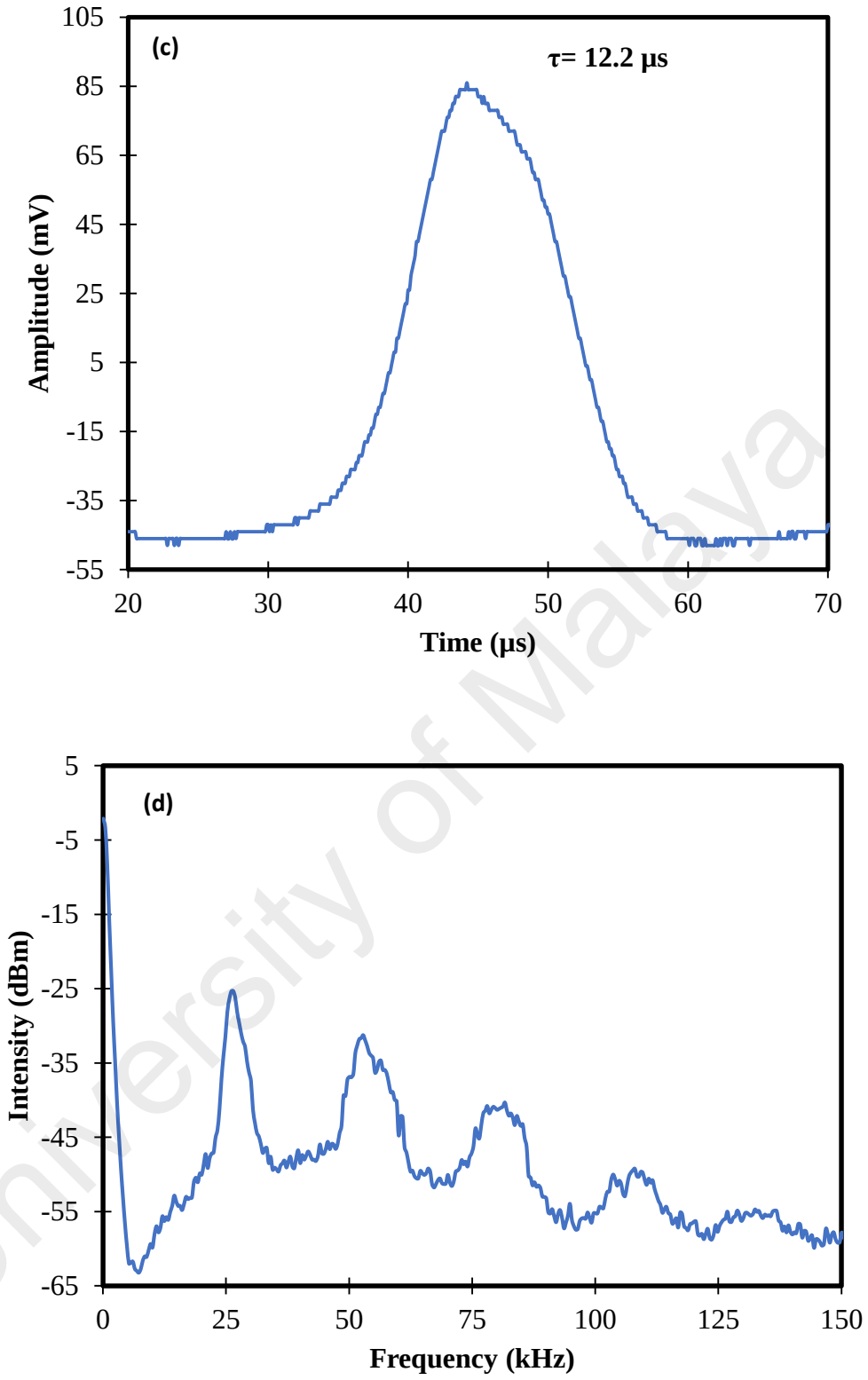

Figure 4.6, continued

Figure 4.7 shows the recorded pulse repetition rate and the pulse duration as a function of the pump power. The repetition rate of the Q-switching pulses linearly increases from

8.1 to 32.9 kHz as the pump power is increased from 55.1 to 82.0 mW. However, the repetition rate reduces as the pump power is further increased before the pulse train becomes unstable and disappears as the pump power is increased above 97.6 mW. This is due to the degradation of BP SA efficiency since the pump power increment increases the heat in the cavity.

Meanwhile the pulse duration significantly decreases from 17.9 to 10.8 μs as the pump power is increased from 55.1 to 97.6 mW. The pulse duration could be further narrowed by optimizing the parameters such as shortening the cavity length and improving the modulation depth of the BP Q-switcher. It is observed in Figure 4.8 that both average output power and pulse energy almost linearly increase with the input pump power up to the pump power of 97.6 mW. At 82 mW pump power, the pulse energy is changed due to the pulse width of the output laser that exhibits the increment trend at this pump power region. The maximum average output power and pulse energy are 10 mW and 328 nJ, respectively.

The experiment is also repeated for different locations of the BP tape sample. It found that a small deviation of tape or BP layer thickness does not change the optical properties of the BP SA and the Q-switched performance. We believe that the pulse energy produced by the laser could be further improved by optimizing the SA parameters of BP tape and the cavity design. The output pulse energy could be further improved if the cavity loss and SA loss can be further improved. The similar performance of Q-switching is also obtained in the erbium-doped fiber laser (EDFL) and the thulium-doped fiber laser (TDFL) setups, which operates at 1550 nm and 1920 nm, respectively. This shows that the proposed BP SA can be used as a wideband SA.

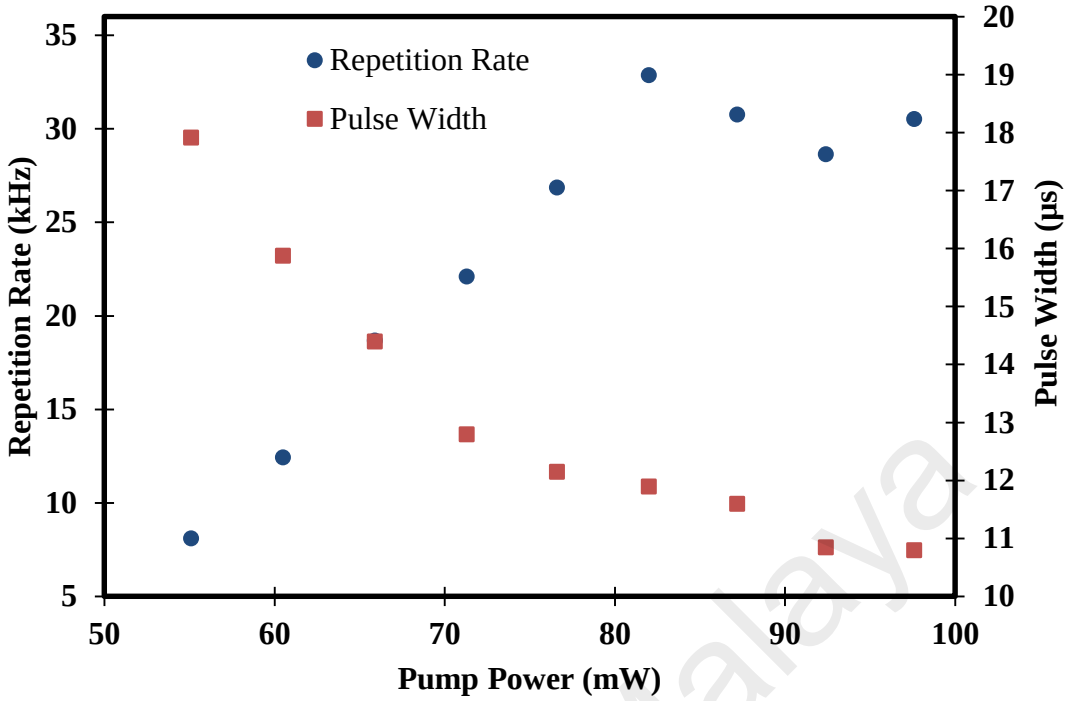

Figure 4.7: Repetition rate and pulse width of the proposed Q-switched YDFL against the pump power

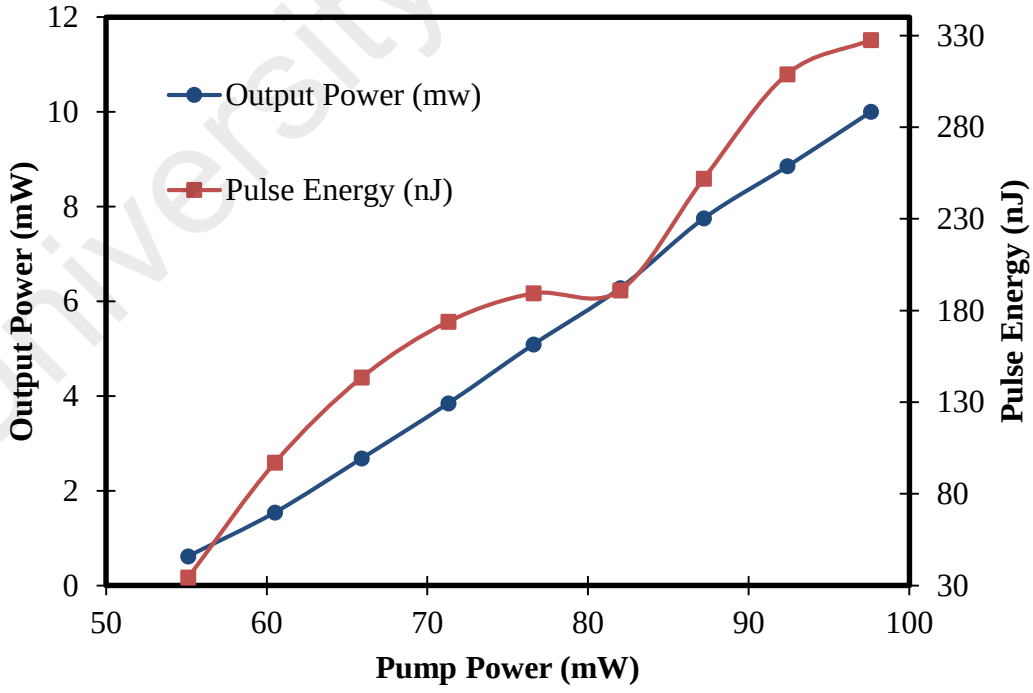

Figure 4.8: Output power and pulse energy of the proposed Q-switched YDFL against the pump power

4.3 Mode-Locked YDFL with BP based SA

As previously discussed, ultra-short optical pulse sources have attracted widespread interests because of their useful applications such as micromachining, communication, and optical systems (Bao et al., 2009; Norihiko Nishizawa, 2014; N Nishizawa et al., 2008). A passive mode-locked method is implemented to generate pulse laser due to their nature being compact, low cost and easy to setup (Grelu et al., 2012; M. Zhang et al., 2009). Furthermore, active mode-locked method requires an additional switching electronics device in the laser cavity such as acousto-optic modulators (Ryu et al., 2007). Passively mode-locked fiber lasers are also widely explored in recent years by utilizing saturable absorption of optical materials. Various SAs have been demonstrated so far such as SESAMs (Gomes et al., 2004; J. Liu et al., 2012), carbon nanotubes (CNTs) (Solodyankin et al., 2008; J Sotor et al., 2015), and 2D materials including graphene (Huang et al., 2014; Z. Sun et al., 2010), TIs and transition metal dichalcogenides (TMDCs) (Dou et al., 2014; Sotor, Sobon, Grodecki, et al., 2014). TMDCs have a large bandgap that is more suitable for visible band (M. Ahmed, A. Latiff, H. Arof, & S. Harun, 2016; Q. H. Wang et al., 2012).

To date, another 2D nanomaterial, BP is also draw more interests as a promising material for ultra-short pulse applications (Park et al., 2015; Song et al., 2017; Jaroslaw Sotor et al., 2015; H. Yu et al., 2015). The reasons for this growing interest is because it has the most thermo-dynamically stable allotrope of phosphorus and a direct energy band structure in any case of its thickness, which can give excellent optical laser properties (Churchill et al., 2014; Lu et al., 2015). Compared to other 2D materials, BP has a direct band gap changing from 0.3 to 2.0 eV in BP layer. The advantage of bandgap is helpful for its optoelectronics applications and that make it more suitable for nonlinear short pulse modulation and can use as a saturable absorber to generate a mode-locking fiber laser (M. Ahmed, A. Latiff, H. Arof, & S. Harun, 2016; Han et al., 2017).

In this section, we have reported a mode-locked YDFL using a fabricated 2D material by the mechanically exfoliated technique of BP incorporate on end surface of a standard FC/PC fiber connector as SA. The mode-locked YDF laser operates at 1033.76 nm wavelength with 10 MHz repetition rate and 2.7 nJ pulse energy.

4.3.1 SA Preparation Process

In our experiment, the multi-layer BP SA was prepared by a mechanical exfoliation method as described in Figure 4.9. Mechanical exfoliation method in 2D materials has been generally employed for generation pulse fiber laser applications, such as graphene and TIs (Martinez et al., 2011; Sotor, Sobon, Macherzynski, et al., 2014), because of its reliability and simple in the fabrication process, which do not have any chemical procedures. First, thin flakes were moderately peeled off from a big block of commercially available BP crystal (purity of 99.995 %) using clear scotch tape. Then, the flakes were repeatedly pressed so that they adhered onto the scotch tape to form a thin layer of BP. Afterward, a fresh standard FC/PC fiber end surface was pushed down on the scotch tape so that the multilayer BP can be transferred onto it. With the aid of index matching gel, the ferrule with BP layers was connected to another fresh FC/PC fiber ferrule with a standard flange adapter. Then, the all-fiber BP based SA was finally ready.

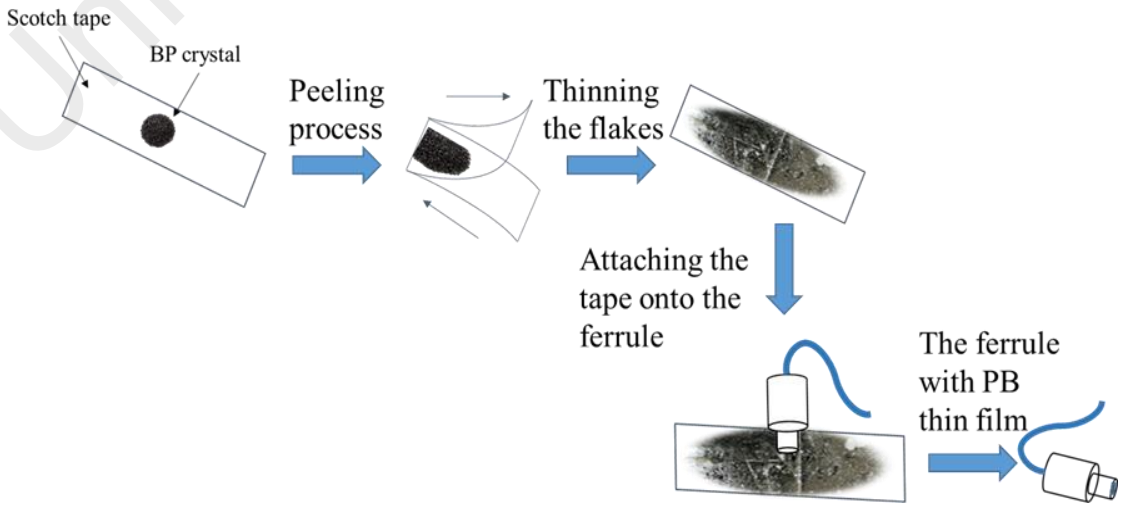

Figure 4.9: The fabrication process of mechanical exfoliation BP based SA

Figure 4.10 shows the Raman spectrum, which is recorded of Argon ion laser is radiated on the tape for 10 ms with an exposure power of 10 mW. As shown in the figure, the sample exhibits three distinct Raman peaks at 360 cm^{-1}, 438 cm^{-1} and 465 cm^{-1}, corresponding to A_g^1, B_{2g} and A_g^2 vibration modes of a layered BP. While B_{2g} and A_g^2 modes correspond to the in-plane oscillation of phosphorus atoms in BP layer, the A_g^1 mode corresponds to the out-of-plane vibration.

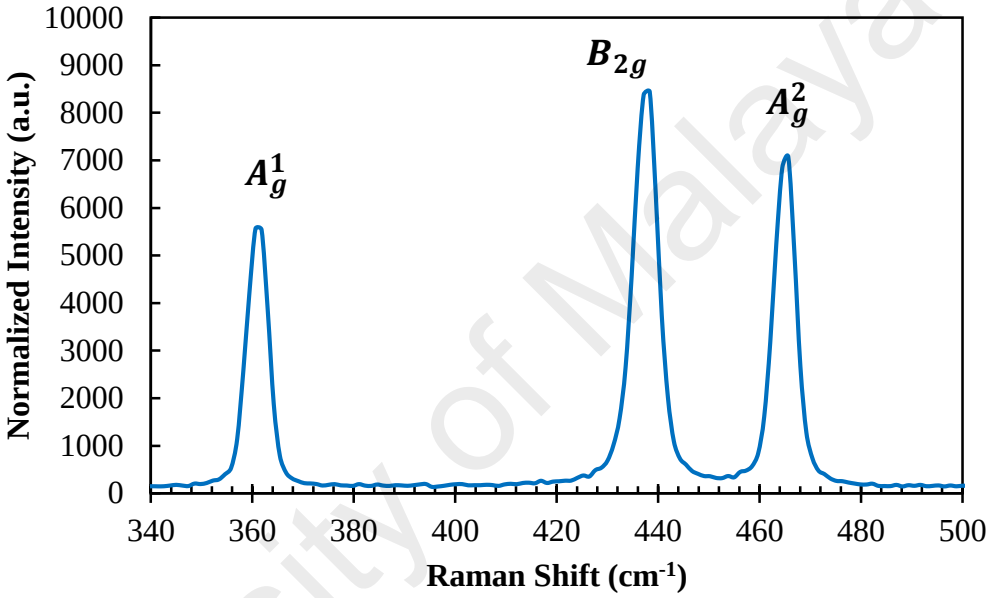

Figure 4.10: Raman spectrum of the BP based SA

The nonlinear optical response property for the BP SA was also experimentally investigated using an absorption technique in order to confirm its saturable absorption level. The nonlinear characterization was carried out using the same setup and approach as described in the previous section. The transmitted power and also a reference power for normalization are recorded as a function of incident intensity on the SA by varying the input laser power. With increasing peak intensity, the material absorption decreases as shown in Figure 4.11, confirming the saturable absorption characteristic of the multi-layer BP. The experimental data for absorption are fitted according to a simple two-level SA model as previously described in Equation (4.1). As shown in Figure 4.11, the

modulation depth, non-saturable intensity, and saturation intensity are 7.5 %, 57.5 % and 0.35 MW/cm^2, respectively. Taking into account its nonlinear optical response leading to absorption saturation at relatively low fluence, the mechanically exfoliated BP meets basic criteria of a passive SA for fiber lasers.

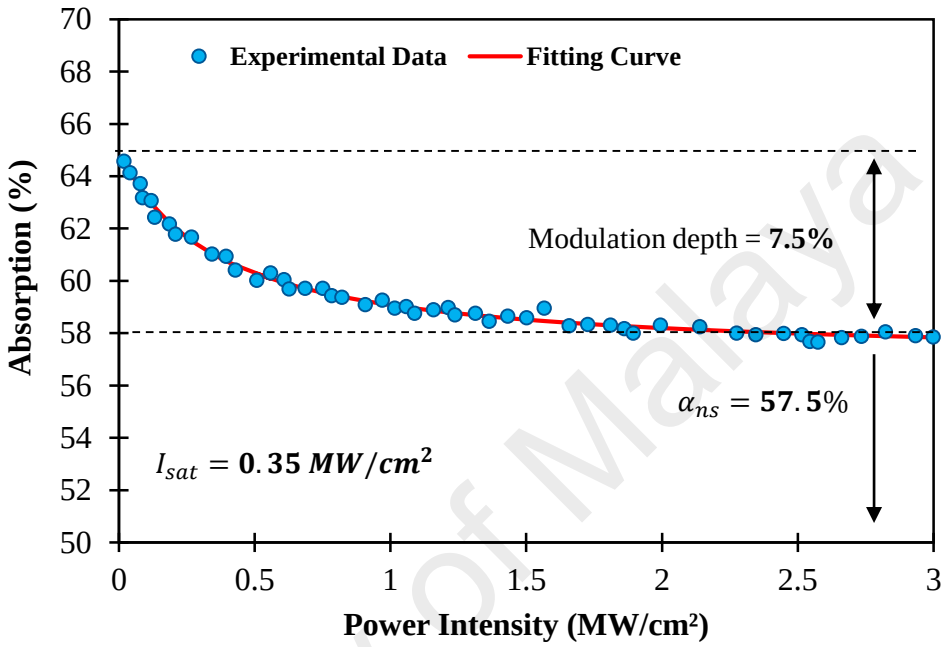

Figure 4.11: Nonlinear absorption profile of BP SA

4.3.2 Experimental Setup for the Mode-locked YDFL

In this work, the performance of the BP SA is investigated for mode-locking application in YDFL cavity. Figure 4.12 shows the experimental setup, which mainly consists of YDF with length of about 1.5 m as a gain medium. The YDF (Yb1200-4/125) has a core and cladding diameters of 4 µm and 125 µm respectively, with a numerical aperture of 0.20, as well as the cut-off wavelength of 1010 nm and ion absorption of 280 dB/m at 920 nm. In order to ensure unidirectional operation, an isolator is spliced into the cavity. The 980 nm laser diode (LD) is coupled into the fiber ring resonator with a 980/1064 nm WDM. A 10 dB output coupler was used in the resonator to extract 10% of the output for analysis while allowing 90% of the light to oscillate in the laser cavity. A

polarization controller (PC) was incorporated inside the laser cavity between the SA device and isolator to adjust the polarization state of the oscillating light and optimizes the laser mode-locking performance. The output laser is analyzed by an OSA with a spectral resolution of 0.02 nm, an optical power meter and a 2 GHz photodetector together with a 350 MHz oscilloscope or 7.8 GHz RF spectrum analyzer. The laser cavity consists of 1.5 m YDF with a group velocity dispersion (GVD) of 24.22 ps^2/km and a single-mode fiber (SMF, HI 1060) with a total length of 19.5 m with GVD of 21.91 ps^2 /km as the other fiber component. The net cavity dispersion was normal with a value estimated to be 0.46 ps^2.

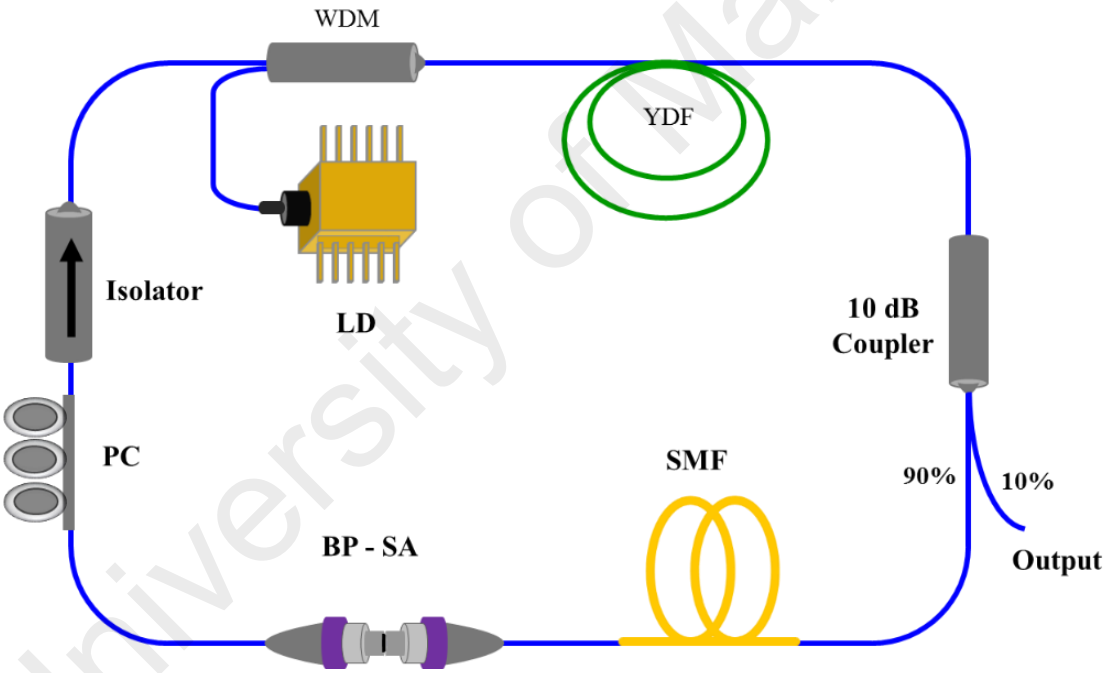

Figure 4.12: Experiment configuration of mode-locked YDFL

4.3.3 Performance of the Mode-locked Laser with BP SA

At first, the laser cavity was tested without incorporation of the SA device to confirm that there is no pulse obtained on the oscilloscope. Then the prepared BP SA is incorporated into the laser cavity as a mode-locker. As the pump power reaches 123.7 mW threshold, a continuous-wave laser was firstly obtained. A stable mode-locking pulse

was obtained as the pump power is further increased to 130.8 mW. The pulses train operating at repetition rate of 10 MHz was easily achieved by carefully controlling the rotation of the PC as the pump power is fixed within 130.8 mW to 200 mW. Figure 4.13 shows output spectrum of the mode-locked pulses at pump power of 200 mW. The spectrum shows a central wavelength of 1033.76 nm and 3dB spectral bandwidth of 0.48 nm with no Kelly sideband, which confirmed the operation of laser in normal dispersion. The narrow spectral bandwidth is due to the minimal nonlinearity and high net cavity dispersion. The Q-switching operation was also realized in the YDFL with the BP SA by increasing the cavity loss. It was achieved by replacing the 90/10 output coupler with a 3dB coupler. The Q-switched laser has a pump threshold of 55 mW, a pulse repetition rate that is tunable from 8 to 33 kHz, and the narrowest pulse width of around 10 μs.

Figure 4.14 shows the typical pulses train trace of the mode-locked YDFL measured by oscilloscope with pulse period of 96 ns at two different pump powers of 151.5 mW and 200 mW. It indicates there is no fluctuations in the pulse train. The achieved repetition rate pulse of 10 MHz is matched with the cavity length of 21 m. As shown in the same figure with the limitation of the oscilloscope resolution, the achieved pulse width of 49 ns is much broader than the actual pulse width. As an alternative, the pulse width can be measured by using calculation based on the time bandwidth product (TBP) formula. A mathematically estimated a minimum possible pulse width of approximately 3.27 ps with TBP of 0.441 for Gaussian pulse profile and 3dB spectral bandwidth of 0.48 nm. The RF spectrum for the proposed YDFL is shown in Figure 4.15, which has confirmed that the mode-locked has a fundamental frequency of 10 MHz with a signal-to-noise ratio (SNR) up to 39 dB. By removing out the BP SA from the ring cavity, the mode-locking operation could not be achieved, no matter how we adjust the PC and pump power. This verified that the mode-locking operation is purely caused by the BP SA. These results show that

black phosphorus and other similar 2D materials may have a good potential for application in ultrafast photonics.

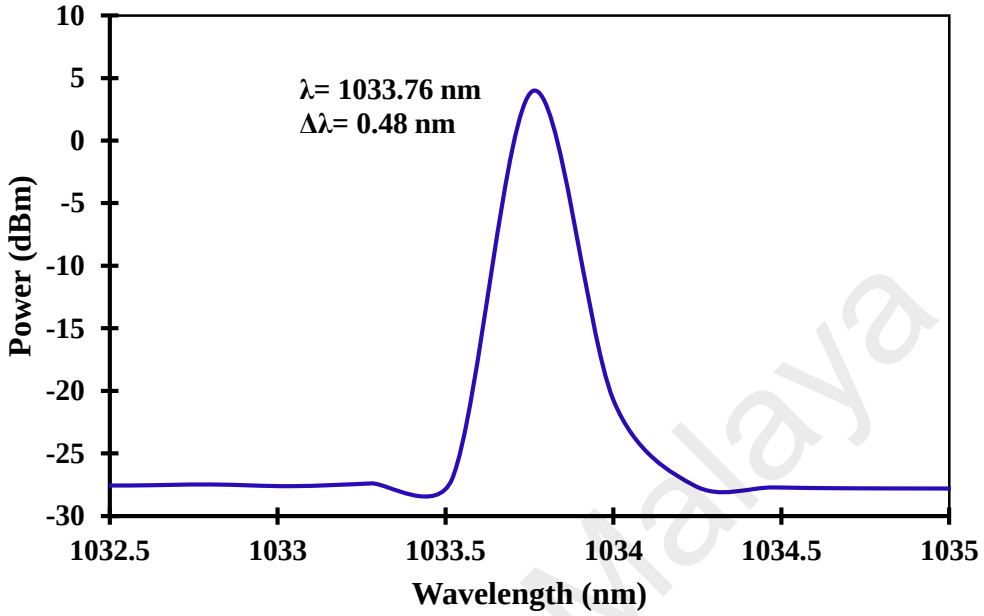

Figure 4.13: Optical spectrum of the proposed mode-locked YDFL at pump power of 200 mW

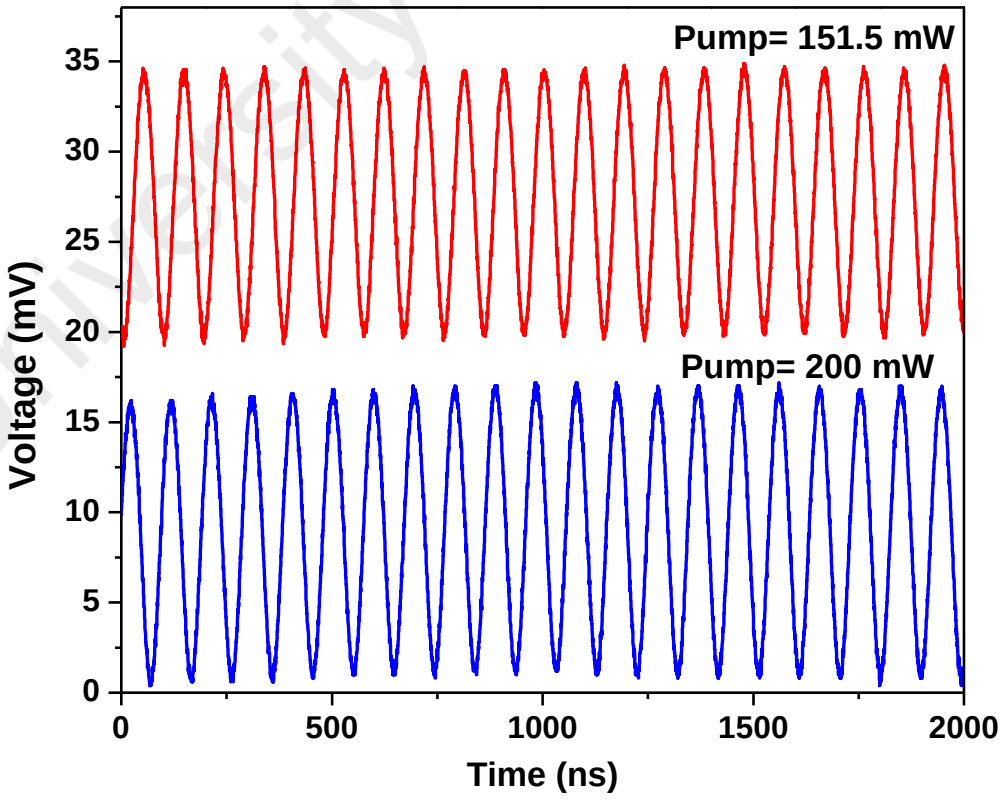

Figure 4.14: Typical pulse train of mode-locking YDFL at two different pump powers

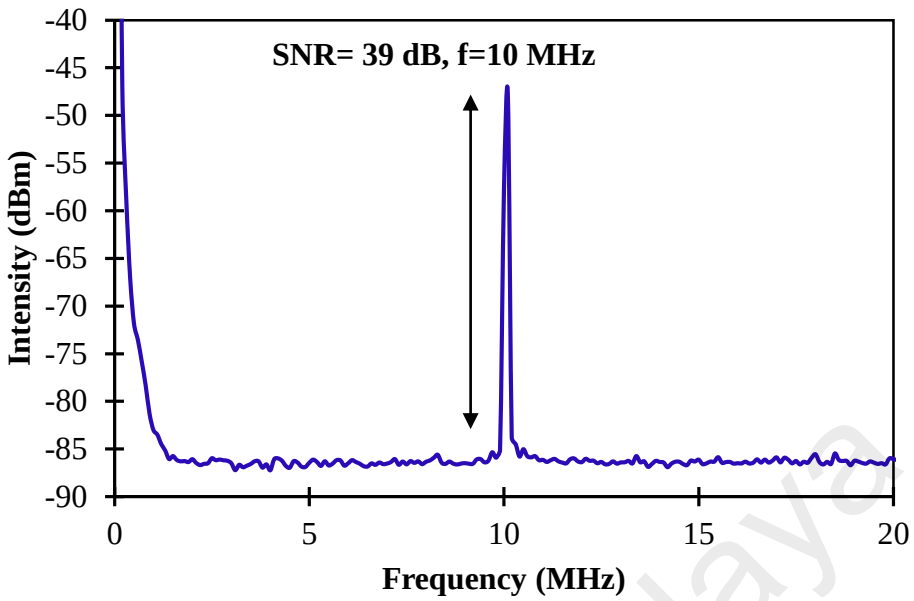

Figure 4.15: RF spectrum of the mode-locked YDFL

Figure 4.16 shows the graphs of an average output, pulse energy and peak power as a function of input pump power for the mode-locked YDFL. As seen, the average output power, pulse energy, peak power rise linearly with the pump power. The average output power is increased from 4.7 to 27 mW as the pump power is increased from 130.8 to 200 mW as shown in Figure 4.16 (a). The pulse energy is measured based on the output power and repetition rate as shown in the Figure 4.16 (b). The maximum pulse energy is 2.7 nJ at the maximum pump power of 200 mW. Figure 4.16 (c) shows the peak power against the pump power, which the maximum peak power is 0.83 kW at 200 mW pump power. In order to examine the long term stability of the mode-locked laser, we continuously monitor the output signal by an optical spectrum analyzer and an oscilloscope for 48 hours. It is observed that central wavelength and 3 dB bandwidth of the spectrum are almost unchanged while the repetition rate stayed constant throughout the experiment. This observation proves the stability of BP as a SA in mode-locked fiber laser.

BP has a direct transition for all thicknesses, which shows a significant benefit for optoelectronic applications, especially at the long-wavelength range. As it can offer a

broad tuning range for a bandgap with number of layers, and can bridge nearly the entire range between the zero bandgap of graphene and the large bandgap of TMDCs. Furthermore, the preparation of the BP is also simple and thus it is preferable compared to TIs, which limit themselves by the complex fabrication processes. However, the BP materials are very hydrophilic and thus the SA is easily damaged with the exposure to oxygen and water molecules.

Nevertheless, the BP SA remain undamaged as we tuned pump power up to 200 mW for more than 2 days. By keeping in an air tight container, less expose to oxygen or water molecules helps to protect BP SA from damage easily. The experimental results verify the mode locking ability of the newly developed BP based SA. This shows that the BP could be used to develop promising optoelectronic devices with high power tolerance, offering inroads for more practical applications, such as large energy laser mode-locking, nonlinear optical modulation and signal processing etc.

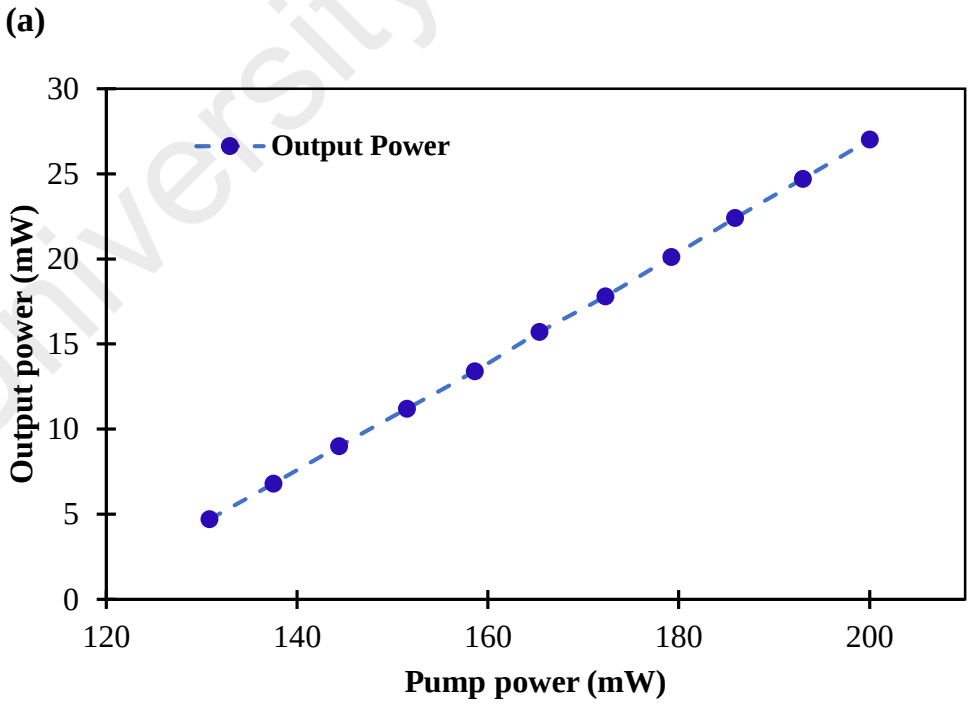

Figure 4.16: Variation in (a) output power, (b) pulse energy, and (c) peak power at different pump power

(b)

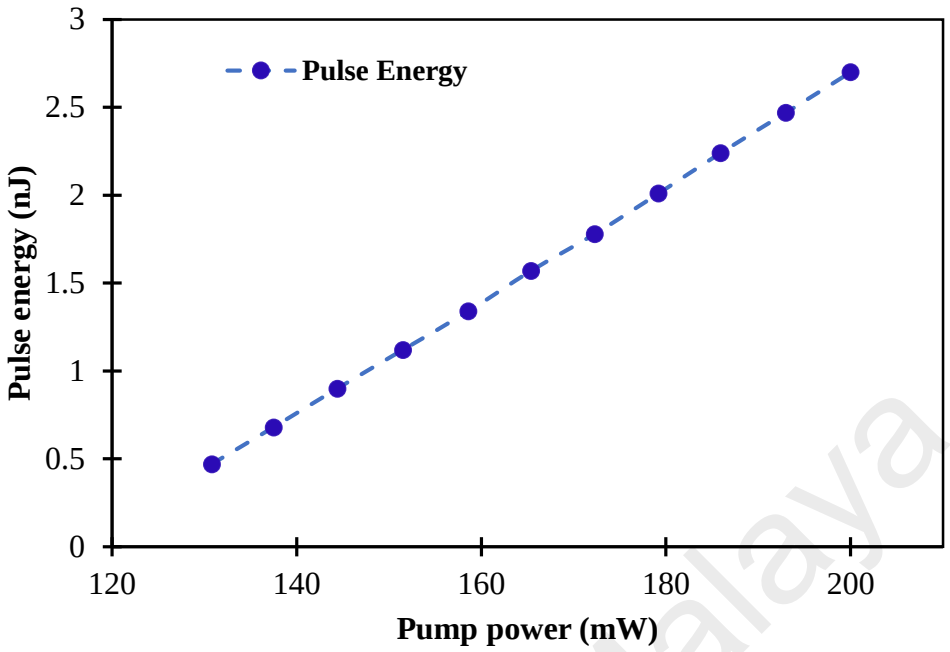

(c)

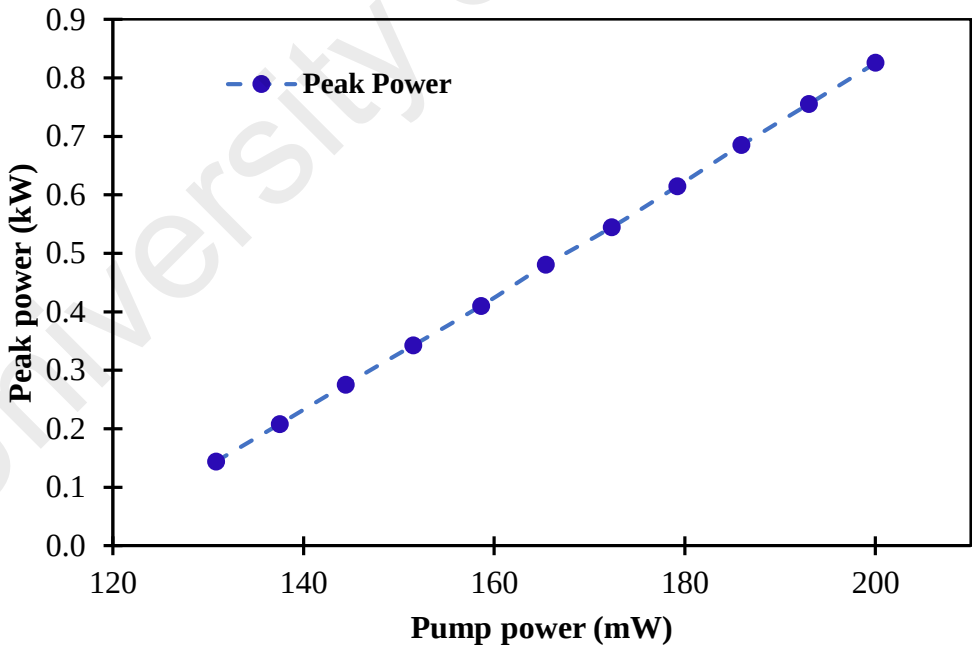

Figure 4.16, continued

4.4 Summary

Multi-layer BP have been successfully demonstrated as an effective SA for both passive Q-switching and mode-locking applications in YDFL cavity. The BP SA was prepared by mechanical exfoliation method and sandwiched between two fiber ferrules via a fiber adapter to form a fiber-compatible SA. Firstly, a stable Q-switched pulses at 1069.4 nm were successfully obtained using the SA tape with BP layers. The laser registered a pump threshold of 55.1 mW and the minimum pulse duration was 10.8 μs. The pulse repetition rate could be varied over a wide range of frequencies, from 8.2 to 32.9 kHz, by adjusting the pump power. The highest pulse energy of 328 nJ was obtained at pump power of 97.6 mW. Secondly, passively mode-locked YDFL was demonstrated using an improved multi-layer BP based SA, which was obtained without the sticky tape. The laser cavity was designed with normal net cavity dispersion of 0.46 ps^2 while inserting additional SMF and PC in the cavity. The proposed mode-locked YDF laser operated at 1033.76 nm wavelength with a repetition rate of 10 MHz. The highest pulse energy and peak power was measured to be around 2.7 nJ and 0.83 kW respectively at pump power of 200 mW. The fabrication of BP SA is easy, cheap and suitable device to generate mode-locked laser in 1 μm wavelength region. These experimental results suggest that a multi-layer BP is a promising material for pulsed laser applications.

CHAPTER 5: TOPOLOGICAL INSULATOR AS SATURABLE ABSORBER

5.1 Introduction

Topological insulators (TIs) have attracted attention of researches due to the high nonlinear susceptibility and large modulation depth with efficient saturable absorption property. They are excellent semiconductors with high surface electron mobility. The mostly used TIs are Bismuth (III) Selenide (Bi_2S_3), Bismuth (III) Telluride (Bi_2Te_3) and Antimony (III) Telluride (Sb_2Te_3), which have a band gap of 0.35, 0.21, and 0.30 eV, respectively and the physical properties of these three TIs are similar because they are composed of two elements (W. Tian et al., 2017). These materials have a thickness of nano-to micro scale (Junsu Lee, Koo, Jhon, et al., 2014) and they show a linear dispersion relation at low pulse energy and nonlinear dispersion relation at the exicitation of high energy pulse and thus suitable for saturable absorber (SA) application. More recently, passive SAs made of topological insulators (TIs) have been shown to be capable of generating Q-switched and mode-locked lasers (Y. Chen et al., 2014; H. Liu, X.-W. Zheng, et al., 2014). Since TIs have a large modulation depth with an efficient saturable absorption property, they are suitable for making SAs. For instance, Bi_2Te_3 has the modulation depth and saturation intensity of about 22% and 57 MW/cm2 respectively (Y. Chen et al., 2014).

In this chapter, passively Q-switched Ytterbium-doped fiber laser (YDFL) are demonstrated using a few-layers Bi_2Se_3, Bi_2Te_3 and antimony telluride (Sb_2Te_3) based SAs while mode-locked YDFL is demonstrated using Sb_2Te_3 material to exploit the wideband saturable-absorption characteristic of the TIs. For this purpose, we prepare free-standing Bi_2Se_3-, Bi_2Te_3- and Sb_2Te_3-polymer composite SA films by implanting the powder of these materials into a polyvinyl alcohol (PVA) host. These films are used in a fully fiber-integrated laser cavity for generating pulses train.

5.2 Q-switching Performance of YDFL with Few-layer Bi_2Se_3 and Bi_2Te_3 based SAs

Recently, passive SAs made of topological insulators (TIs) have been shown to be capable of generating Q-switching pulses train (Y. Chen et al., 2014; H. Liu, X.-W. Zheng, et al., 2014). For instance, Q-switched Erbium-doped fiber lasers (EDFLs) were demonstrated using Bismuth (III) Selenide (Bi_2Se_3) and Bi_2Te_3 SAs (Ahmad et al., 2015; Y. Chen et al., 2014). Chen et al. (2014) demonstrated Bi_2Se_3 based Q-switched EDFL with repetition rates range from 4.5 to 12.9 kHz and the shortest pulse width of 13.4 µs (Y. Chen et al., 2014). Luo et al. used Bi_2Se_3 fabricated by the liquid-phase exfoliation method as SA in YDFL cavity to generate Q-switching pulses with repetition rate ranging from 8.3 to 29.1 kHz, shortest pulse width of 1.95 µs and highest pulse energy of 17.9 nJ (Z. Luo et al., 2013). The SA used has modulation depth of 3.8% and saturable intensity of 53 MW/cm^2.

In this section, two different passively Q-switched YDFLs are demonstrated using Bi_2Se_3 and Bi_2Te_3 nanoparticles based SAs to exploit the wideband saturable-absorption characteristic of the TIs. Compared with the previous YDFL (Z. Luo et al., 2013), higher repetition rate is obtained in both fiber lasers.

5.2.1 Preparation and Characterization of Bi_2Se_3 and Bi_2Te_3 SAs

The commercially available TI powders of Bi_2Se_3 and Bi_2Te_3 with molecular weight of 654.84 g/mol and 800.76 g/mol respectively, are used to prepare the SA in this experiment. The fabrication procedures for both TI films are described in Figure 5.1. To prepare the host polymer, 1 g of polyvinyl Alcohol (PVA) (Sigma Aldrich) is dissolved in 120 ml de-ionized (DI) water with the aid of a magnetic stirrer at room temperature. Next, 14 mg of Bi_2Se_3 powder and 14 mg of Bi_2Te_3 powder are mixed with 3 ml of the PVA solution separately. They are thoroughly mixed using a magnetic stirrer for three

hours. Then the Bi_2Se_3-PVA and Bi_2Te_3-PVA solutions were placed in ultrasonic bath for 10 minutes to make sure the Bi_2Se_3 and Bi_2Te_3 powder fully binds with the PVA. After that, both TI suspensions are carefully poured onto petri dishes to avoid trapping any air bubble and is left to dry at room temperature for 48 hours to form Bi_2Se_3-PVA and Bi_2Te_3-PVA composite films. The thickness of $B_{i2}Se_3$ and Bi_2Te_3 films are about 55 and 68 µm, respectively.

Figure 5.2 (a) and (b) shows the field emission scanning electron microscopy (FESEM) images of Bi_2Se_3 and Bi_2Te_3 film, respectively. As shown in Figure 5.2 (a), the Bi_2Se_3 film has a high dense of micro-rods and micro-grains, which can be clearly viewed on the substrate surface and distributed randomly on the substrate surface. These micro-rods and micro-grains are in irregular shapes with an average size of 0.3 to 1.66 µm. As shown in Figure 5.2 (b), the Bi_2Te_3 film has also a high dense of acicular grains formation like micro-networks, which are in irregular shapes in a size between 0.5 to 1.9 µm.

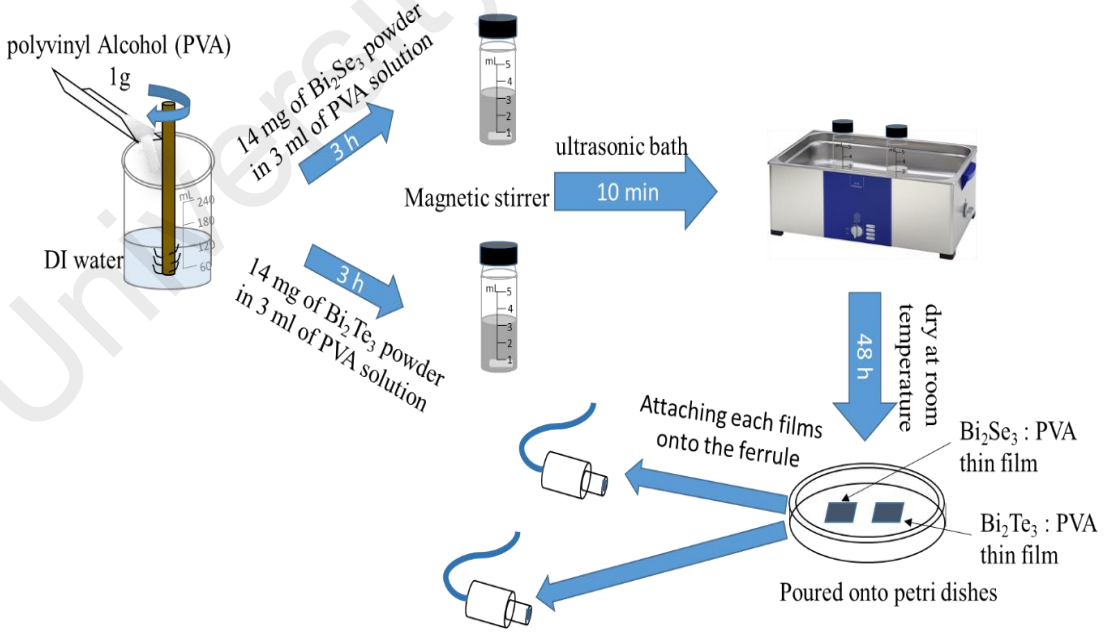

Figure 5.1: The fabrication process of Bi_2Se_3 and Bi_2Te_3 thin film

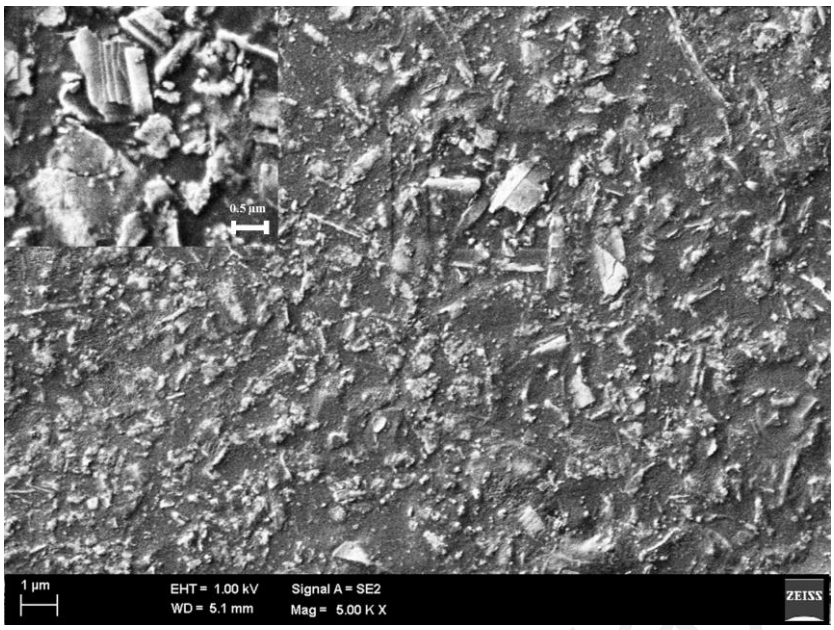

(a)

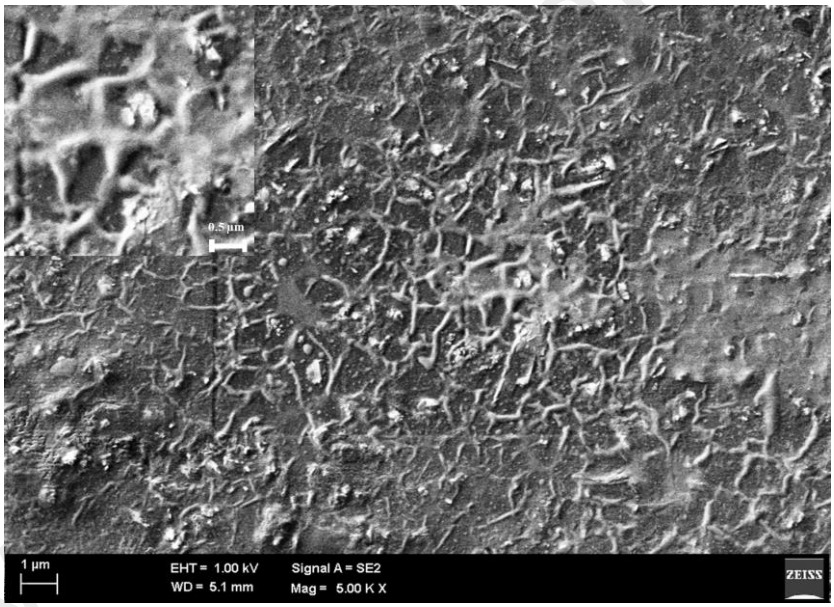

(b)

Figure 5.2: FESEM images of (a) the Bi_2Se_3 and (b) Bi_2Te_3 composite film. Insert of each image represent a high magnification of the respective image

Figure 5.3 illustrates the absorbance spectrum of the prepared PVA only, Bi_2Se_3-PVA and Bi_2Te_3-PVA films in the range of 200 nm to 1100 nm. The figure attests a constant absorbance for both Bi_2Se_3-PVA and Bi_2Te_3-PVA film which indicates that they possess a broadband resonance wavelength like graphene. It is shown that the incorporation of Bi_2Se_3 and Bi_2Te_3 nanoparticles into the PVA increase the loss of the film. The Bi_2Te_3 film is slightly thicker and thus it has a higher loss compared to the Bi_2Se_3 film. However,

at around 1100 nm, both Bi_2Se_3 and Bi_2Te_3 films suffer an almost identical absorption loss. It also shows that PVA polymer is an excellent host material for fabricating high performance TI SA and not affected by this host polymer. Figure 5.4 shows the Raman spectra of the fabricated films. For Bi_2Se_3-PVA film, the three distinct peaks observed at ~67 cm^{-1}, ~126 cm^{-1}, and ~170 cm^{-1} can be assigned to the A^1_{1g}, E^2_g and A^2_{2g} vibrational modes, respectively. It has also shown that the Raman spectrum of the developed Bi_2Te_3-PVA film has three peaks at ~67 cm-1(A^1_{1g}), ~96 (E^2_g) and 118(A^2_{1g}) with a lower power. The lower peak power is most probably due to the lower concentration of the Bismuth (III) Telluride powder in PVA and the effect of the film thickness (Russo et al., 2008). In this experiment, the same ratio of Bi_2Se_3 and Bi_2Te_3 of 14 mg was used in 3 ml PVA, but Bi_2Te_3 powder has a higher molecular weight (800.76 g/mol) compared to Bi_2Se_3 (654.84 g/mol). To improve the Raman resonant in the Bi_2Te_3-PVA film, the weight of Bi_2Te_3 powder could be increased. The simple fabrication method for both Bi_2Se_3 and Bi_2Te_3 PVA films in room temperature is very attractive for scalable production.

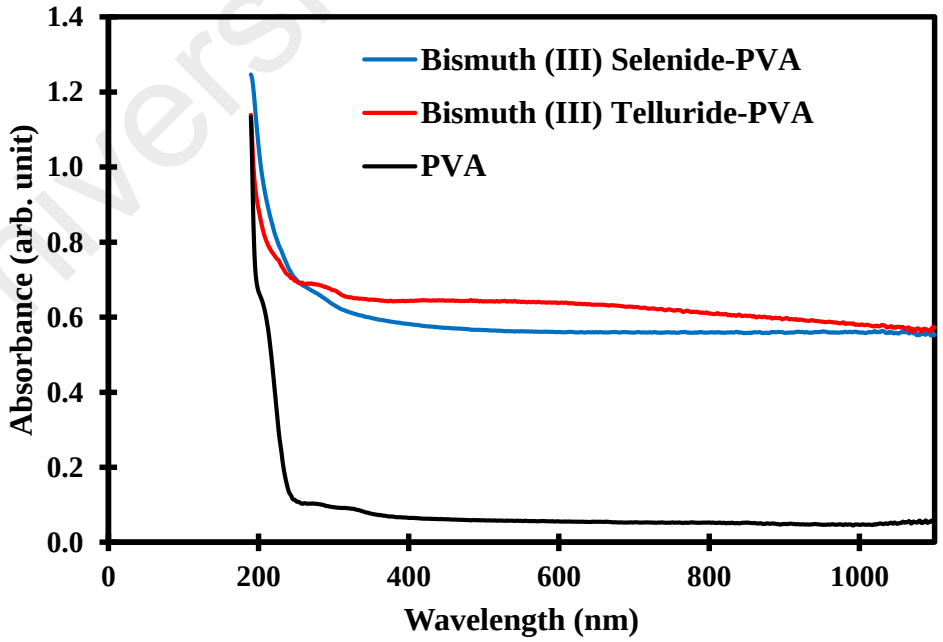

Figure 5.3: Linear transmission of the free standing Bi_2Se_3-PVA and Bi_2Te_3-PVA films

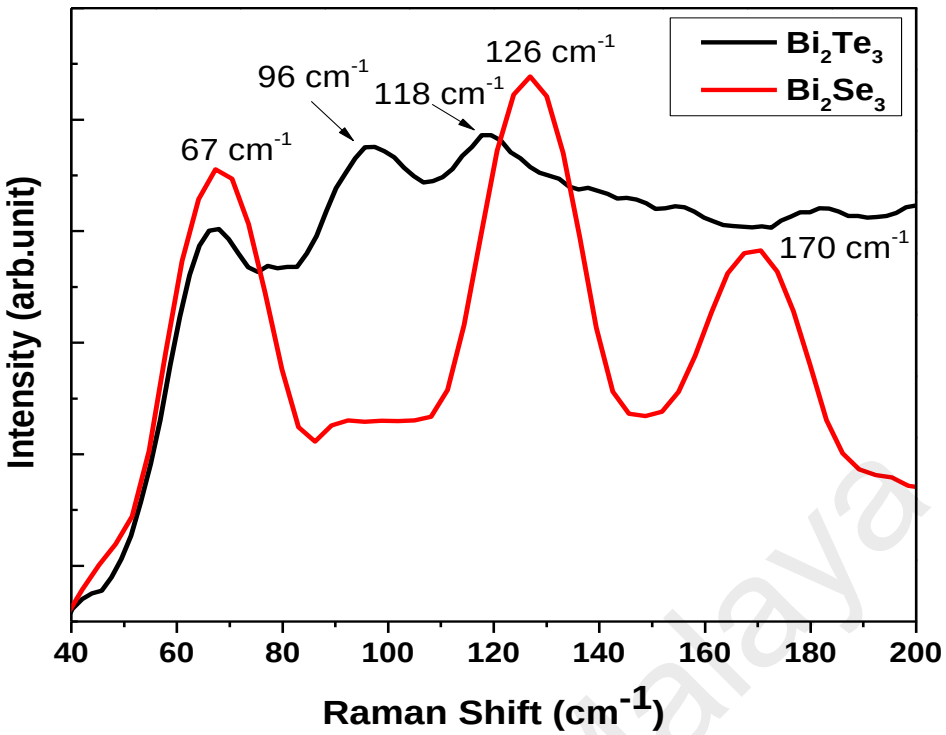

Figure 5.4: Raman spectrum for the free standing Bi_2Se_3-PVA and Bi_2Te_3-PVA films

The nonlinear optical response property for the Bi_2Se_3 and Bi_2Se_3 were also investigated to confirm their saturable absorption by applying the similar technique as described in the previous chapter. The pulse input source used a mode-locked fiber laser, which has femtosecond output pulse with a 17 MHz repetition rate and a 900 fs pulse duration, which the output power is approximately 5 mW. Figure 5.5(a) and (b) show the transmission nonlinear characteristics of the Bi_2Se_3 and Bi_2Te_3 SAs, respectively, which were fitted using the following simple saturable absorption model of

$$T(I) = 1 - \alpha_0 \exp\left(-I/I_{sat}\right) - \alpha_{ns} \tag{5.1}$$

Here, $T(I)$, α_0, I, I_{sat} and α_{ns} stand for the transmission, modulation depth, input intensity, saturation intensity, and non-saturable absorption, respectively (Z. Tian et al., 2015). For Bi_2Se_3 SA, the modulation depth, non-saturable absorption and saturation intensity were measured to be approximately 15.9 %, 77 % and 50 MW/cm^2, respectively as shown in Figure 5.5 (a). As well as in Bi_2Te_3 SA shown in Figure 5.5 (b), the

modulation depth, non-saturable absorption and saturation intensity were obtained to be approximately 30 %, 55 % and 40 MW/cm^2, respectively. In this case, the modulation depth of Bi_2Te_3 sample is higher, however the saturation intensity is smaller than in the Bi_2Se_3 sample.

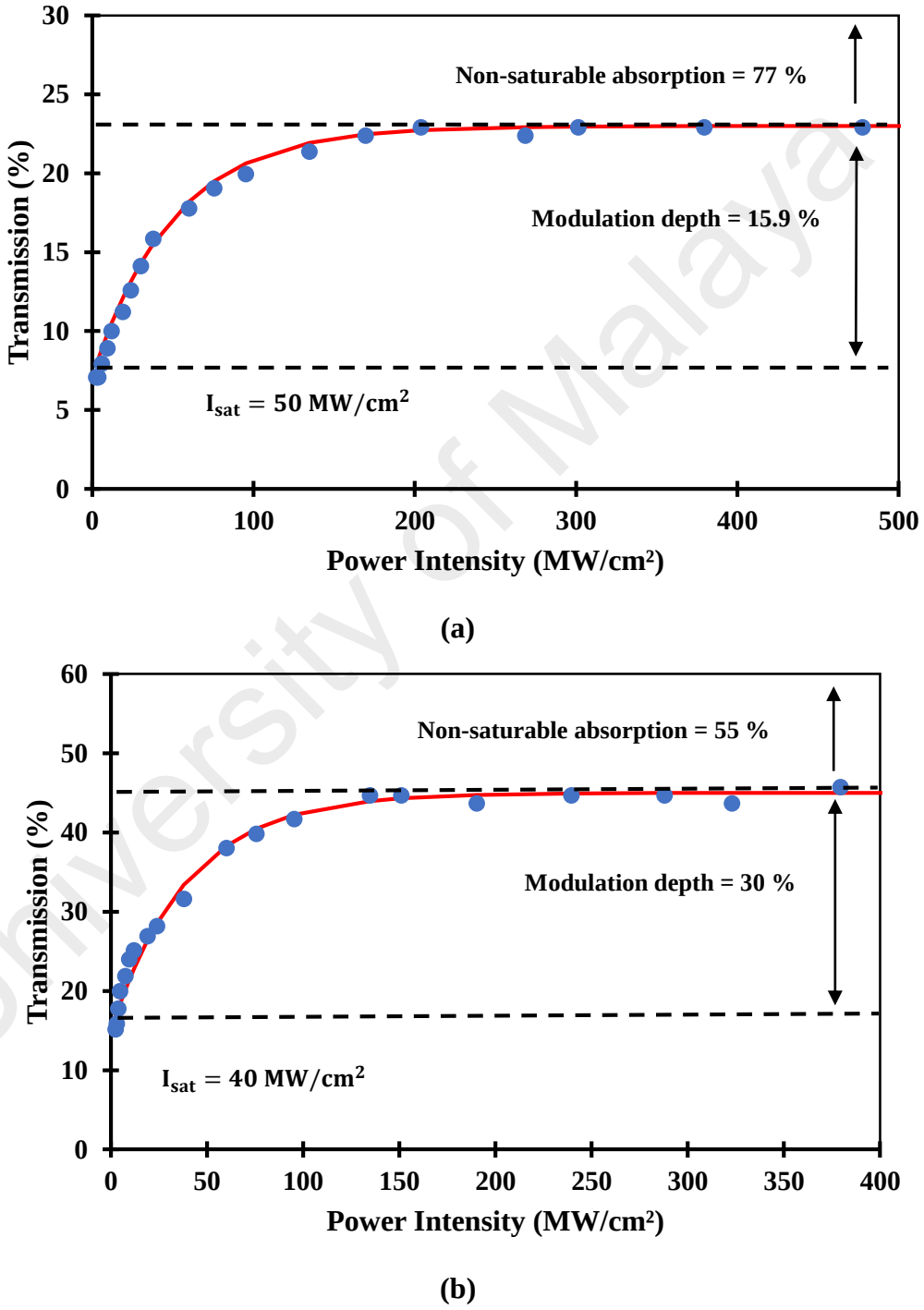

Figure 5.5: Characteristics of nonlinear absorption measurement for (a) Bi_2Se_3-PVA film, and (b) Bi_2Te_3-PVA film

5.2.2 Experimental Arrangement

The schematic experimental setup of the proposed Q-switched YDFL with TI based SA is depicted in Figure 5.6. The ring laser consists of a 1.5 m long YDF as the active medium, a 980/1064 nm wavelength division multiplexer (WDM), an optical isolator, a TI: Bi_2Se_3 or TI: Bi_2Te_3 SA and a 10 dB output coupler. The YDF used has Ytterbium ions concentration of 1500 ppm, a core diameter of 4 µm, numerical aperture of 0.20 and cut-off wavelength of 950 nm. It is pumped by a 980 nm laser diode through the WDM. The other end of the YDF is spliced to the 10 dB output coupler, which allows 10% of the output to be extracted for analysis. The remainder is channeled to the SA device and kept in the cavity to oscillate for laser generation. The SA device is fabricated by sandwiching a ~ 1 mm×1 mm piece of the Bi_2Se_3 or Bi_2Te_3 composite film between two fiber ferrules using a fiber adaptor. Index matching gel is applied at the connection to minimize parasitic reflections. The SA is connected to the isolator, which prevents backward reflection and ensures unidirectional operation. The other port of the isolator is spliced to the 1064 nm port of the WDM to link the ring cavity. The output laser is analysed by an optical spectrum analyzer (OSA) with a spectral resolution of 0.02 nm, an optical power meter and a 2 GHz photodetector together with a 350 MHz oscilloscope or 7.8 GHz radio-frequency (RF) spectrum analyzer. The total cavity length is around 11 m.

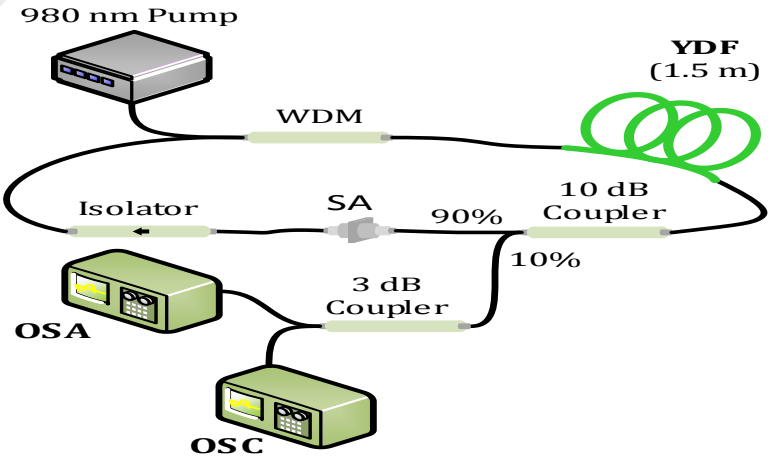

Figure 5.6: Experimental setup for the Q-switched YDFL with TI: Bi_2Se_3 or TI: Bi_2Te_3 based SA

5.2.3 The Performance of the Q-switched Lasers

The performance of the YDFL cavity was investigated by varying the power of the 980 nm pump. The continuous wave (CW) laser started as the power hit the threshold of 43.7 mW. Further, a self-starting and stable Q-switched operation was obtained when the pump power reached the threshold of 67.6 mW and 72.8 mW for Bi_2Se_3 and Bi_2 Te_3, respectively. Figure 5.7 illustrates the output optical spectra of the Q-switched YDFL constructed with Bi_2Se_3 and Bi_2Te_3 based SA at 72.8 mW pump power. As shown, the output optical spectra of Bi_2Se_3 and Bi_2Te_3 based Q-switched YDFLs center at wavelengths of 1057.4, and 1044.5 nm with 3dB bandwidth of 1.32 and 1 nm, and peak output power of -30, and -27.46 dBm, respectively. The CW YDFL output spectrum, which was obtained by removing the SA is also shown for comparison. Without the SA, the YDFL operates at the center wavelength of 1062 nm. The operating wavelength shifts to a shorter wavelength with the employment of SA due to the film insertion loss. The Q-switched lasers operate at a shorter wavelength, which has a higher gain to compensate for the loss.

This result also indicates that the Bi_2Te_3 film has a slightly higher loss than Bi_2Se_3. Spectral broadening is also observed in the Q-switched lasers due to self-phase modulation (SPM) effect in the ring cavity. The same ratio of Bi_2Se_3 and Bi_2Te_3 of 14 mg in 5 ml PVA has used, however Bi_2Te_3 powder is with higher molecular weight (800.76 g/mol) compared to Bi_2Se_3 (654.84 g/mol). The Bi_2Se_3 powder has higher degree of dispersion in PVA compare to Bi_2Te_3 powder and this will affect the performance of the developed film as saturale absorber. Therefore, the bandwidth of output laser of Bi_2Se_3 is much wider than Bi_2Te_3 as shown in Figure 5.7.

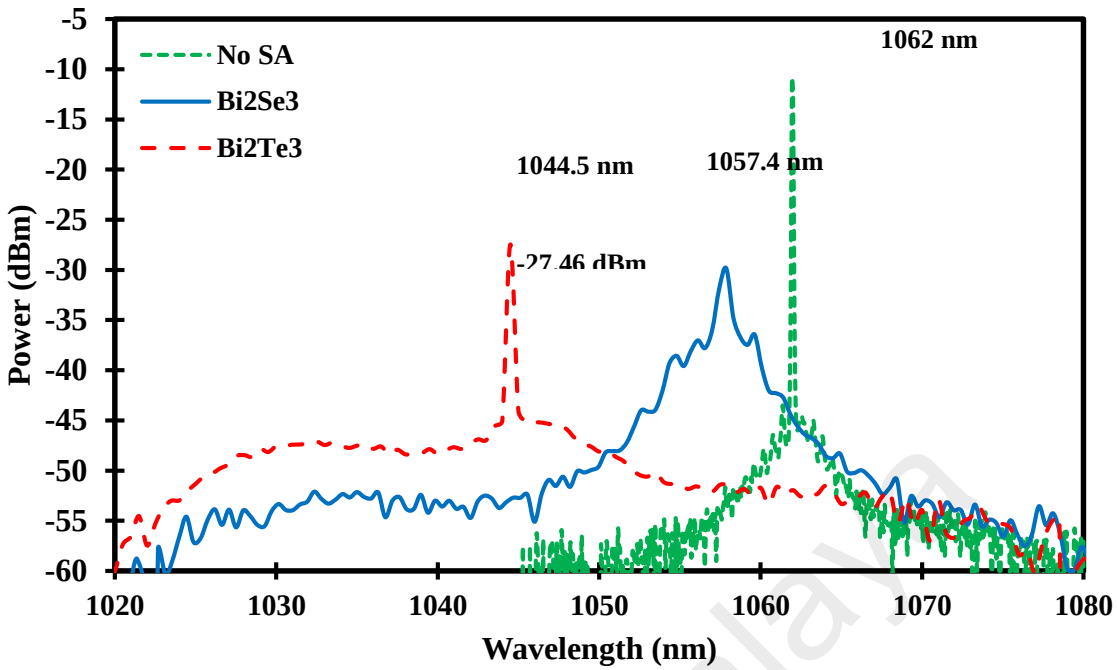

Figure 5.7: Optical spectra of the CW and Q-switched YDFLs at pump power of 72.8 mW

The comparison performance of the Q-switched laser with Bi_2Se_3 and Bi_2Te_3 based SA is summarized in Figure 5.8. A stable Q-switching pulses train is generated by increasing the pump power above 67.6 mW until 88.3 mW for Bi_2Se_3 SA, while from 72.8 mW until 98.4 mW for Bi_2Te_3 SA. Figure 5.8 (a) displays the typical oscilloscope trace at the threshold pump power of both SAs. For Bi_2Se_3 SA, the typical oscilloscope shows at 67.6 mW and threshold pump power, which shows a pulse repetition rate of 48.83 kHz. The pulse train has an average output power of 0.65 mW which matches to the pulse energy of 13.3 nJ. With Bi_2Te_3 SA, the typical oscilloscope trace is shown at the threshold pump power of 72.8 mW, which has a repetition rate of 43.25 kHz and pulse width of 5.65 µs.

Figure 5.8 (b)-(c) compares the pulse train and the envelop of the single pulse at maximum pump power of Q-switching pulses obtained by the Bi_2Se_3 and Bi_2Te_3 SA at pump power of 88.3 mW, and 98.4 mW respectively. The repetition rate between two pulses are measured to be around 102 kHz and 93.63 kHz, whereas the maximum Q-

switching pulse envelope with a period of 3.48 µs and 2.01 µs as measured from the full-width half maximum (FWHM). There is no amplitude fluctuation for the pulse within the tunable range of the repetition rate for both SAs.

Figure 5.8 (d) shows the measured pulse repetition rate and pulse width against the pump power for both Q-switched lasers. It is shown that the pulse repetition rate linearly increases, while the pulse width linearly decreases with the pump power. This matches well with the passive Q-switched theory based on saturable absorber. The pulse repetition rate of Bi_2Se_3 SA based Q-switched YDFL linearly increases from 48.83 to 102 kHz while the pulse width decreases from 8.9 to 3.48 µs as the pump power rises from 67.6 to 88.3 mW. The Q-switching pulse disappears when the pump power is increased above 88.3 mW. Similarly, the pulse width of the Bi_2Te_3 based Q-switched YDFL decreases from 5.65 to 2.01 µs with the increase in pump power from 72.8 to 98.4 mW. The associated repetition rate increases from 43.25 to 93.63 kHz within the same range. This is typical of a Q-switched fiber laser due to the gain compression effect in the laser cavity. Compared to the Bi_2Se_3 laser, the Bi_2Te_3 Q-switched laser shows a narrower tuning range for both repetition rate and pulse width.

The pulse width YDFL of the Bi_2Se_3 is expected to drop further if the pump power can be increased more, as long as the damage threshold of the SA is not exceeded. The Q-switched threshold is also lower for the Bi_2Te_3 laser due to the thicker film layer, which allows more absorption. It is observed that the Q-switching pulse disappears when the pump power is increased above 88.3 mW and 98.4 mW for Bi_2Se_3 and Bi_2Te_3 SA, respectively. We observed pulses in certain range of the pump power, and at high pumping the pulse disappeared, due to the SA is continuously in the saturated state because of the high intensity of light, and there is no time for de-excitation. However, the

two Q-switching lasers are obtained again by reducing the pump power within the range of operation.

Figure 5.8 (e) shows the measured average output power and the calculated pulse energy of both Q-switched YDFLs as a function of pump power. As seen in the figure, the average output power further increases with the pump power, while the pulse energy fluctuates within the pump power for both Q-switching lasers. For Bi_2Se_3 based YDFL, the output power increases from 0.65 to 1.27 mW within the pump power range from 67.6 to 88.3 mW.

The maximum output power of 1.27 mW is obtained at the maximum pump power of 88.3 mW, while the maximum pulse energy of 16.6 nJ is recorded at 72.8 mW. In comparison, the average output power of the Bi_2Te_3 based YDFL linearly increases from 1 to 2.36 mW as the pump power grows from 72.8 to 98.4 mW. As the pump power increases, the non-radiative decay rate of the Yb^{3+} ions also increases. This generates heat in the laser cavity system, which it's absorbed by the SA. This will energize some electrons in the SA's valance band to move up to the conduction band from the strong internal thermal motion. As fewer electrons in the valence band are available for photon absorption, the initial transmittance of the SA becomes greater as the pump power or the levels of absorber heat increases.

Thus, the SA's efficiency as SA is greatly reduced, meaning that the pulse width begins to increase again after the saturation of SA. The maximum pulse energy of 29.95 nJ is obtained at 83.2 mW pump power. After increasing the pump power above 98.4 mW, the SA was working in a good condition, however no indication of mode-locked pulse. Thus, the value of damage threshold cannot be defined due to the limited pump power of 200 mW.

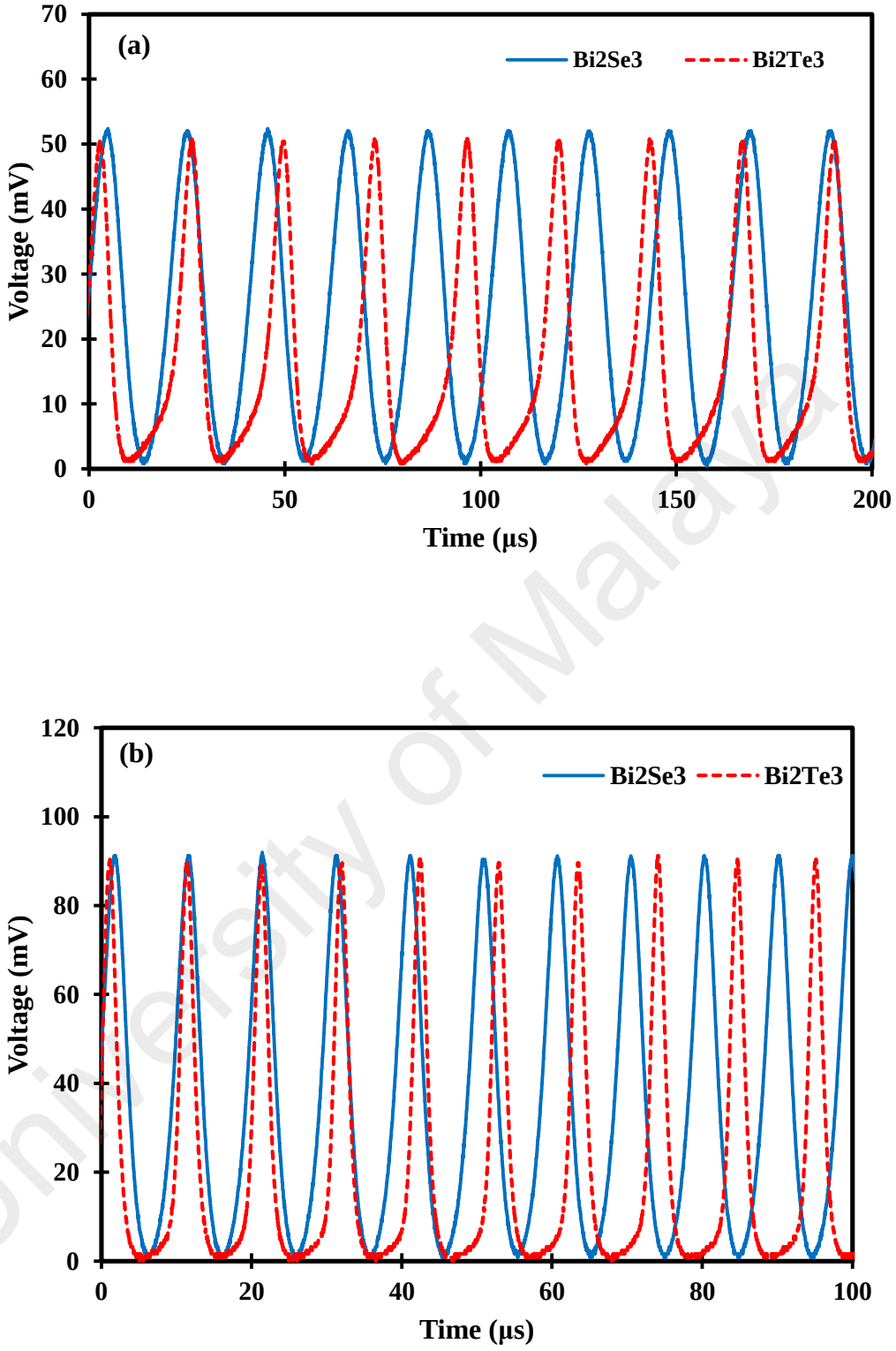

Figure 5.8: The performance of Q-switched YDFL with Bi_2Se_3 and Bi_2Te_3 based SA (a) pulse train at threshold pump power of 67.6 mW and 72.8 mW, respectively (b)-(c) Pulse train and single envelope pulse at maximum pump power of 88.3 mW, and 98.4 mW, respectively (d) Pulse width and repetition rate characteristics at various pump power. (e) The average output power and pulse energy characteristics at various pump power

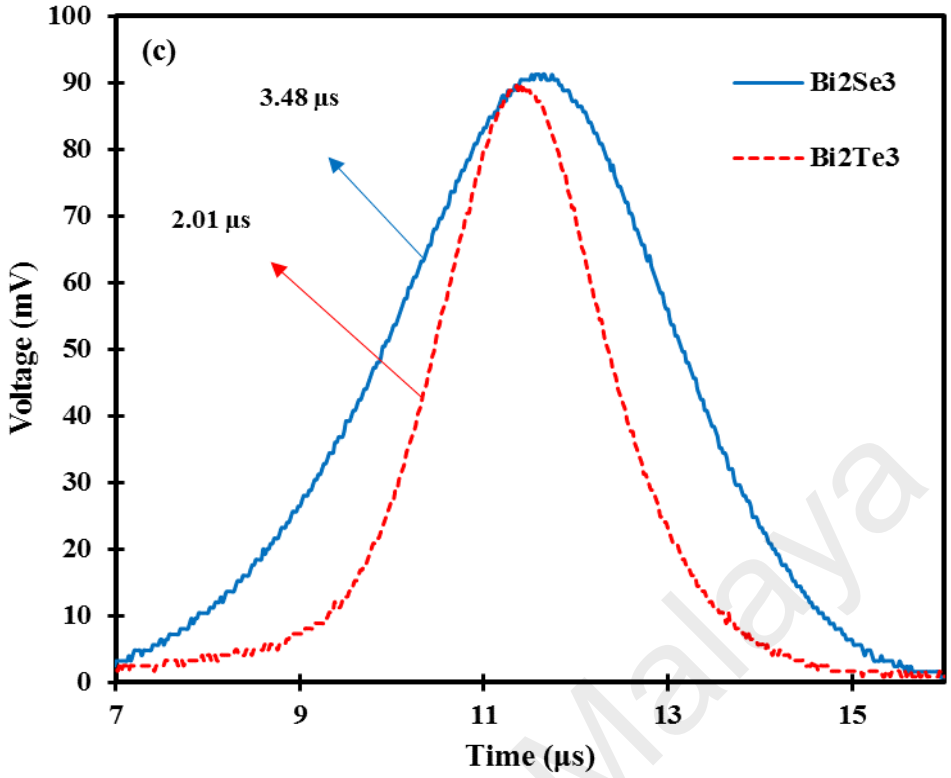

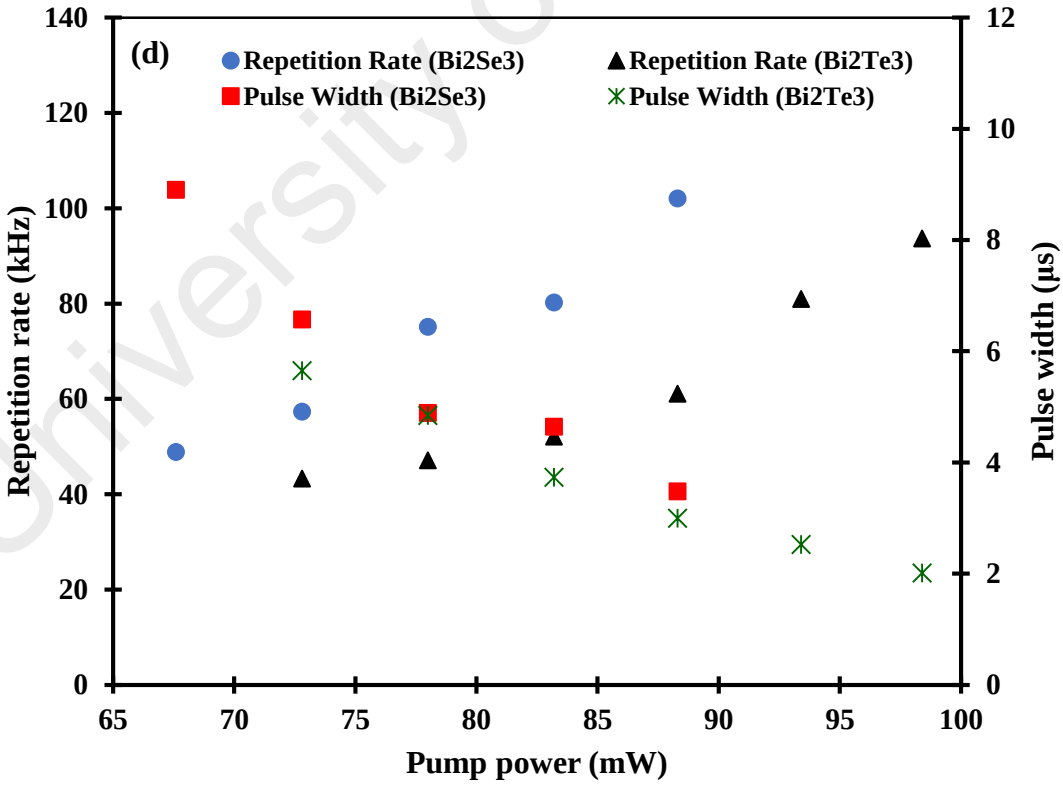

Figure 5.8, continued

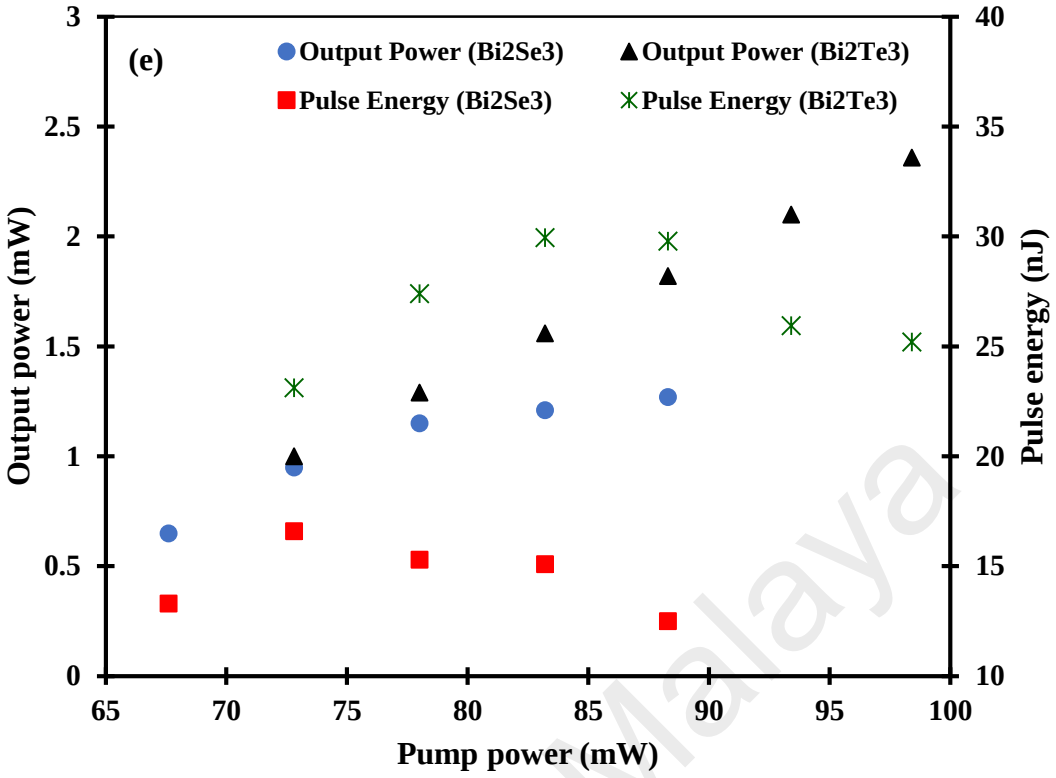

Figure 5.8, continued

Figure 5.9 depicts the radio frequency (RF) spectra of the Q-switched YDFLs configured with Bi_2Se_3 and Bi_2Te_3 SA, which were achieved with resolution bandwidth of 3 kHz at the maximum pump powers of 88.3 and 98.4 mW, respectively. Both spectra were taken using an RF spectrum analyzer via a 1.2 GHz photodetector. The maximum repetition rate of 102 kHz and 93.63 kHz are obtained with the Bi_2Se_3 and Bi_2Te_3 SA, respectively. The corresponding signal to noise ratios (SNR) are 55 and 53 dB respectively. The high SNR values indicate the stability of both Q-switched lasers. The results show that both Bi_2Se_3 and Bi_2Te_3 have a great potential for use in generating Q-switching pulses. The fabrication of both SAs is simple and cheap while the output of both Q-switched lasers is highly stable at room temperature. The pulse width could be further narrowed by employing a shorter laser cavity and improving the modulation depth of the SA. It is found that the Bi_2Te_3 SA produces a smaller minimum pulse width while

the Bi_2Se_3 SA produces a higher maximum repetition rate. In addition, the highest pulse energy of 29.95 nJ is obtained with the Bi_2Te_3 SA.

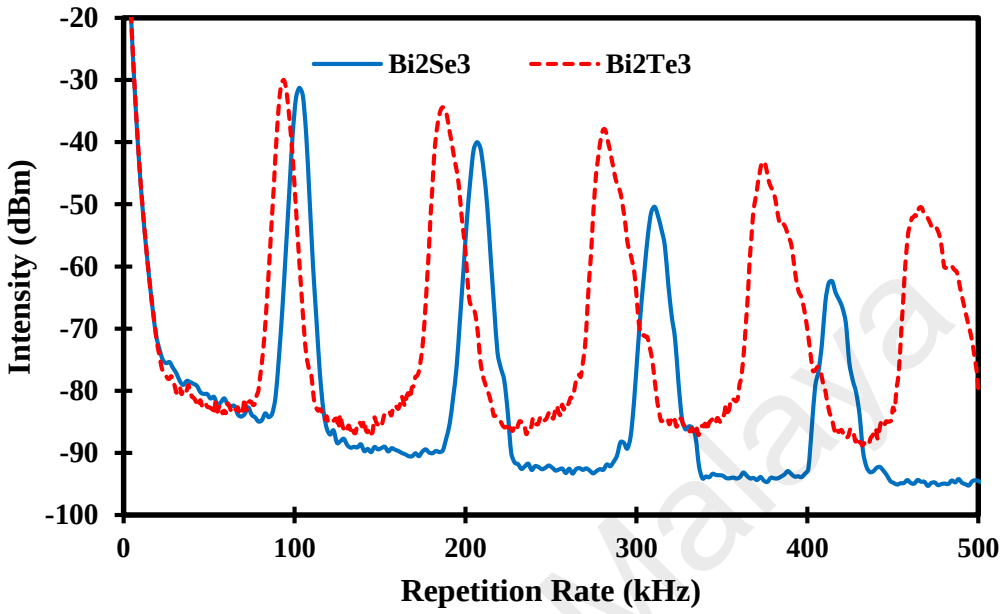

Figure 5.9: RF spectra of the Q-switched YDFLs configured with Bi_2Se_3 and Bi_2Te_3

5.3 Q-Switched and Mode-locked YDFLs with Antimony Telluride TI based SA

In the previous section, both Bi_2Se_3 and Bi_2Te_3 SAs show good Q-switching performance in the 1µm wavelength region . However, the mode-locking operation cannot be achieved by both SAs. This is most probably due to the modulation depth, dispersion and nonlinear properties of the fabricated SAs, which were not suitable for mode-locking operation. However, Sotor et al. demonstrated antimony telluride (Sb_2Te_3) as SA incorporated on a side-polished erbium-doped fiber to generate a passive mode-locking pulse with pulse duration of 128 fs and repetition rate of 22.32 MHz. Its modulation depth and non-saturation loss were 6% and 43%, respectively (Sotor, Sobon, & Abramski, 2014). In another work, Kowalczyk et al. studied the mode-locked YDFL using Sb_2Te_3 SA, which was fabricated by a pulsed magnetron sputtering technique. The YDFL with 2 mm long Sb_2Te_3 SA obtained at pulse width of 5.9 ps (Kowalczyk, Bogusławski, et al., 2016). In this section, the generation of Q-switched and mode-locked

YDFLs are demonstrated using a simpler technique based on the Sb_2Te_3 material deposited on the end-facet of a fiber ferrule as an SA device. By incorporating the Sb_2Te_3 SA into the YDFL cavity, Q-switched and mode-locked operation could be achieved.

5.3.1 Preparation and Characterization of Sb_2Te_3 film SA

In this experiment, the molecular weight of the Sb_3Te_2 is about 626.32 g/mol. In order to prepare the PVA host polymer, 1 g of PVA (Sigma-Aldrich) is dissolved in 120 ml deionized water with the aid of a magnetic stirrer at room temperature as shown in Figure 5.10. The SA was prepared by mixing 5 mg powder [Sigma Aldrich, -325 Mesh, 99.6% trace metal basis] into 5 ml of the PVA solution. Next, the mixture was stirred for 3 hours using magnetic stirrer and followed by ultra-sonication of an hour to prevent any aggregation. Then, the mixture of suspensions is carefully poured onto the petri dish to avoid trapping any air bubbles and then dry in the room temperature for 3 days to form Sb_3Te_2-PVA composite film. The thickness of Sb_3Te_2 is about 34 µm. The advantages of this process are to clean growth environment, low growth temperature, good crystal safety, regular thickness, and easy to dope (W. Tian et al., 2017).

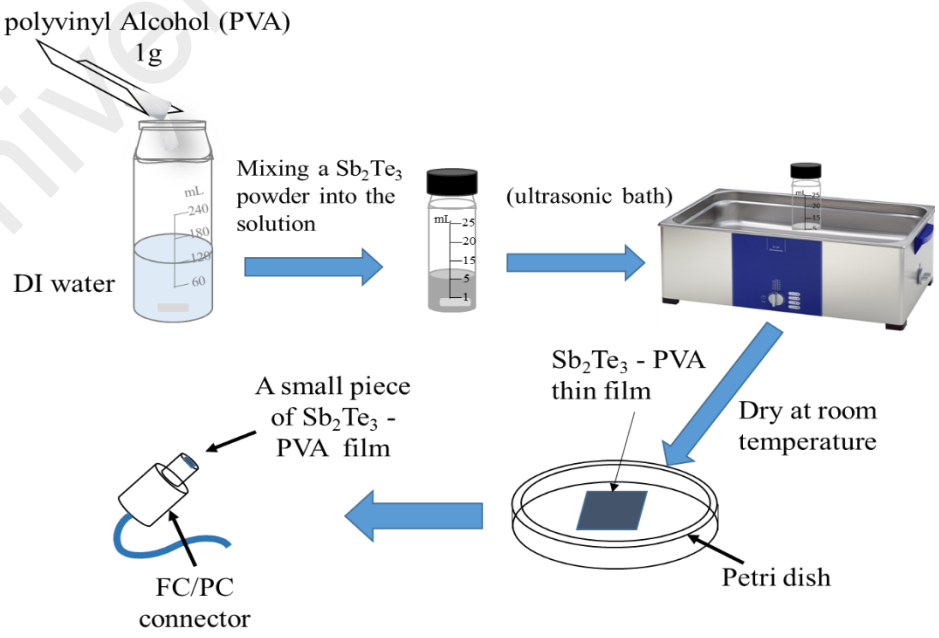

Figure 5.10: The fabrication process of Sb_2Te_3 PVA film

Figure 5.11 (a) shows the FESEM image of a uniform polymeric thin film of Sb_2Te_3. Several bumps is observed on the surface, as seen in an insert figure, in like-spherical shape with a size between 0.2 and 1.33 µm. These formed bumps may have resulted after drying the thin film at room temperature. Figure 5.11 (b) shows the absorbance spectrum of the prepared Sb_2Te_3-PVA and PVA only in range from 200 to 1000 nm. It also shows that PVA polymer is an excellent host material for fabricating high performance Sb_2Te_3 SA and not affected by this host polymer. Figure 5.11 (c) shows the Raman spectrum of Sb_2Te_3-PVA film.

It was obtained using Renishaw InVia Raman microscope with a charge coupled device detector and argon-ion laser with a diffraction grating of 1200 lines/mm. the excitation wavelength and laser power were used at 514 nm and 10 mW, respectively. Two modes were shown at 2947.48 and 1433.18 cm^{-1} which are attributed to valence C-H vibration and shear modes for PVA polymer, respectively (C. Wang et al., 2013). An inset figure shows four modes of Sb_2Te_3 at 49.52, 63.17, 106.72 and 171.68 cm^{-1}, corresponding to E_g^1 (TO), A^1_{1g} (LO), E_g^2 (TO) and A^2_{1g} (LO), respectively (Sotor, Sobon, Grodecki, et al., 2014) and a peak at 133.84 cm^{-1}, which is belong to Te-Te bonds (packet structure) (Bogusławski et al., 2016).

By applying dual-detector measurement technique, the nonlinear optical response property for the Sb_2Te_3 thin film was obtained as depicted in Figure 5.11 (d). It shows the recorded data of transmission at various input intensities for the Sb_2Te_3-PVA SA, which were fitted by using Equation 5.1. As seen in the figure, the modulation depth, non-saturable absorption, and saturation intensity were measured to be 8.5%, 70%, and 36 MW/cm^2, respectively.

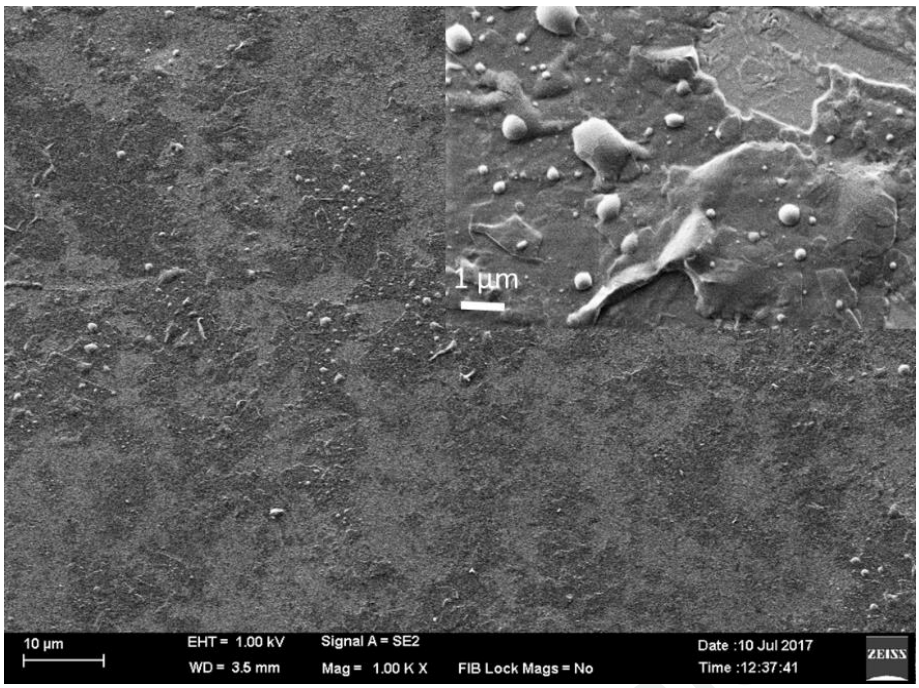

(a)

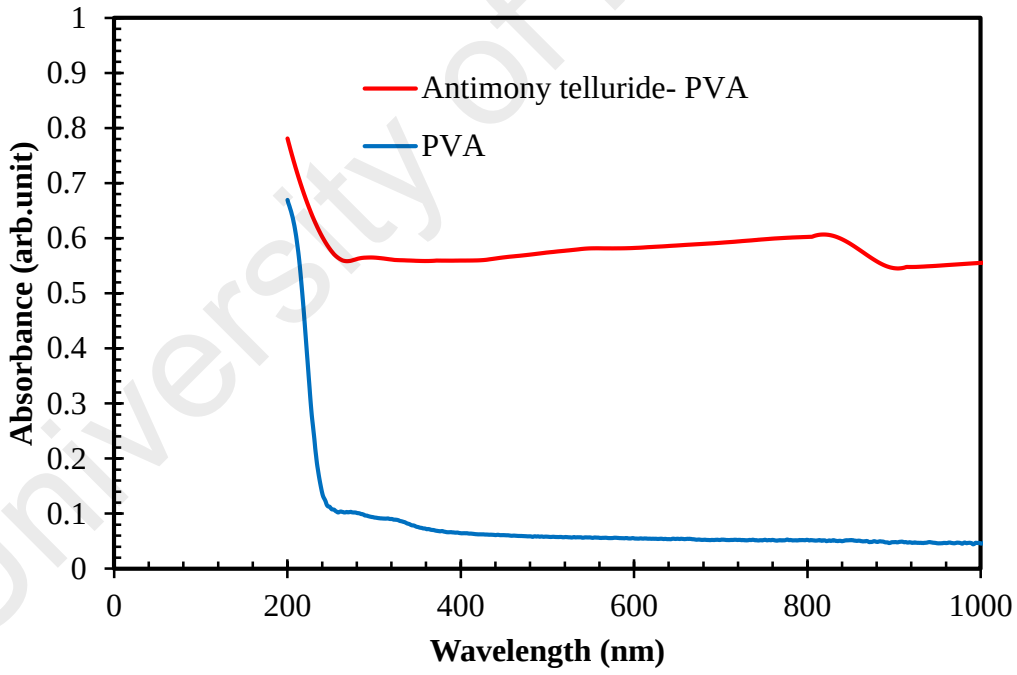

(b)

Figure 5.11: The characteristics of the fabricated Sb_2Te_3 PVA based SA (a) FESEM images of the Sb_2Te_3- PVA composite thin film. Inset shows a high magnification of the image, (b) Linear transmission of the Sb_2Te_3 –PVA as compared with PVA only free standing, (c) Raman spectrum, and (d) Nonlinear transmission measurement

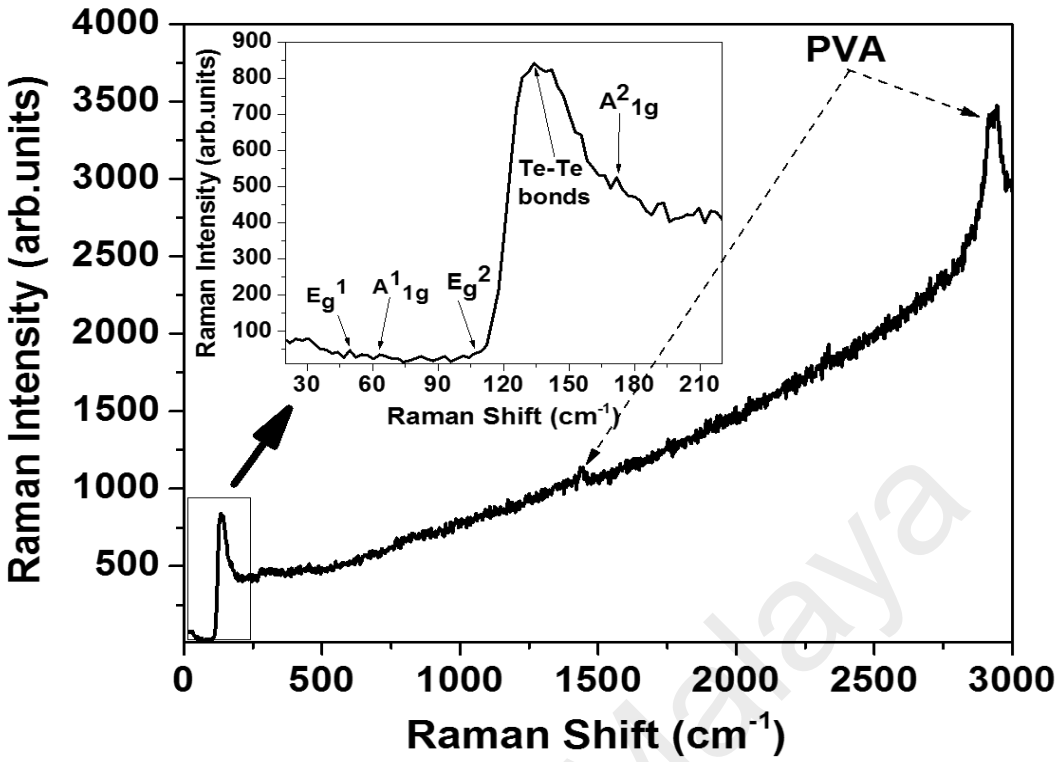

(c)

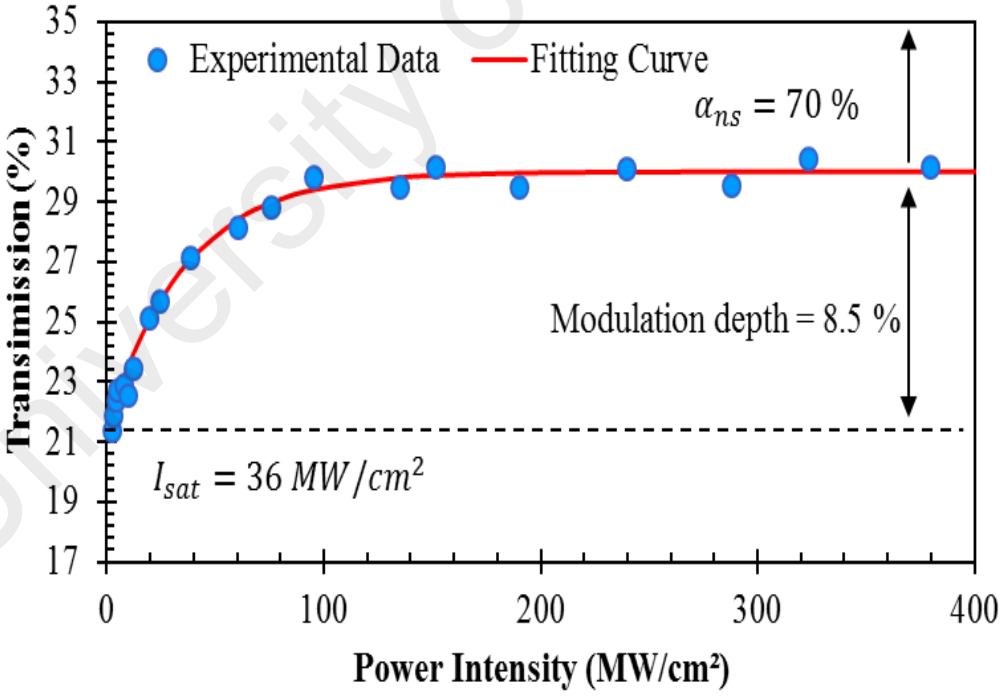

(d)

Figure 5.11, continued

5.3.2 Experimental Setup

The pulses generation in a YDFL ring cavity is investigated by exploiting the absorption property of Sb_2Te_3 SA. Figure 5.12 shows the experimental setup of the proposed Sb_2Te_3 SA based Q-switched YDFL. The laser cavity employs a 1.5 meter-long YDF, which was pumped by a 980 nm pump through a 980/1064 nm WDM as the gain medium. The YDF used is same with the previous work as described in the previous section. An isolator was integrated into the optical ring cavity to ensure unidirectional operation. A 3 dB optical coupler was employed to tap out the laser emission while keeping half of the power inside the cavity to oscillate for laser generation. The Sb_2Te_3 TI SA device was fabricated by sandwiching a ~ 1 mm×1 mm piece between two fiber ferrules using a fiber adaptor and index matching gel was applied at the connection to minimize parasitic reflections.

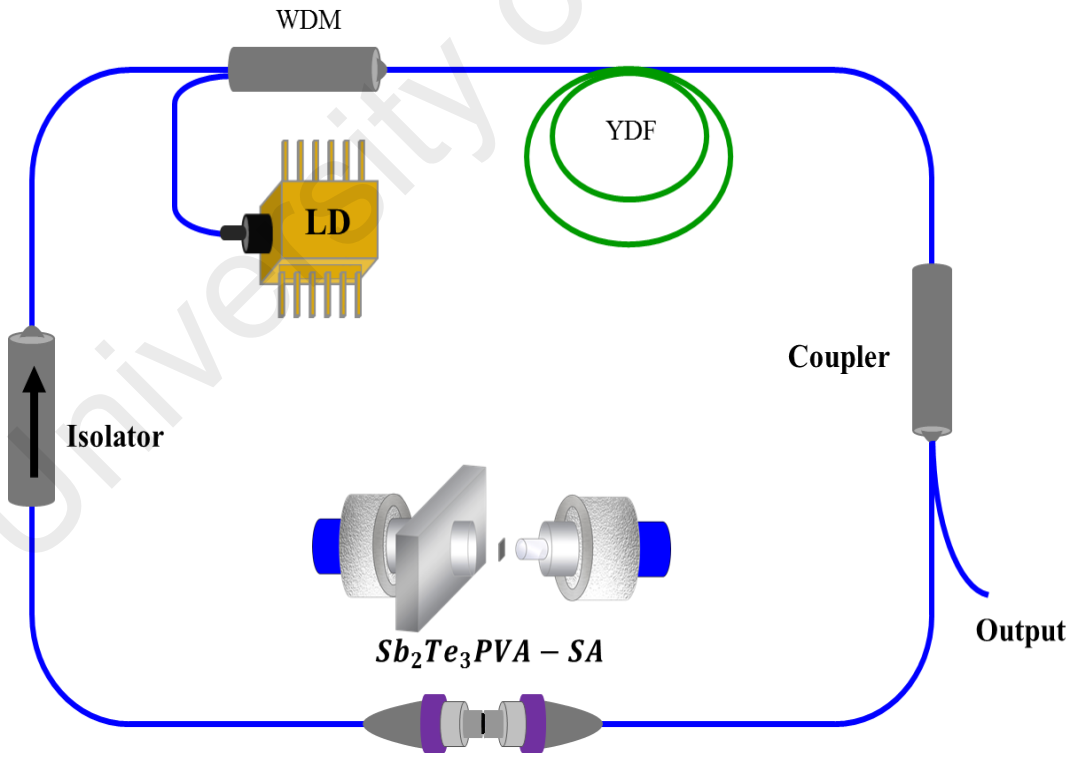

Figure 5.12: The schematic diagram of Sb_2Te_3-PVA SA based Q-switched YDFL. The configuration was converted into a mode-locked laser by employing 90/10 output coupler instead of 50/50 coupler

The output laser was analyzed by an OSA with a spectral resolution of 0.02 nm, an optical power meter and a 2 GHz photodetector together with a 350 MHz oscilloscope or 7.8 GHz RF spectrum analyzer. The laser cavity was then converted into a mode-locked laser by replacing the 3dB coupler with 90/10 coupler. The mode-locking pulses train was tapped out from 10% port while allowing 90% of the light to oscillate in the cavity. The mode-locking operation was achieved since the cavity loss was significantly reduced by the proposed arrangement.

5.3.3 Q-switching Laser Performances

In Q-switched laser cavity, a 3dB coupler was employed and the output pulses were channeled out through one of the output coupler port for analyzing. A continuous wave (CW) operation was observed when the pump power reached to 61.5 mW. A self-started Q-switching operation was achieved at 75.4 mW pump power and the Q-switching operation was maintained up to the pump power of 96.2 mW. Unstable Q-switched state was observed when the pump power was increased higher than 96.2 mW. This is attributed to the Sb_2Te_3 SA, which was over-saturated at high incident intensity. However, there is no damage in SA under high pump power and the Q-switched state is always obtained as the pump power is reduced back within a range between 75.4 and 96.2 mW.

Figure 5.13 shows the evolution of Q-switching pulses train with increasing in pump power. As seen, the pulse repetition rate is 24.4, 28.38, 32.5 and 51.44 kHz at pump power of 75.4, 82.3, 85.8 and 92.7 mW respectively. It indicates the feature of passive Q-switching state where the repetition rate is progressively increased with pump power increment.

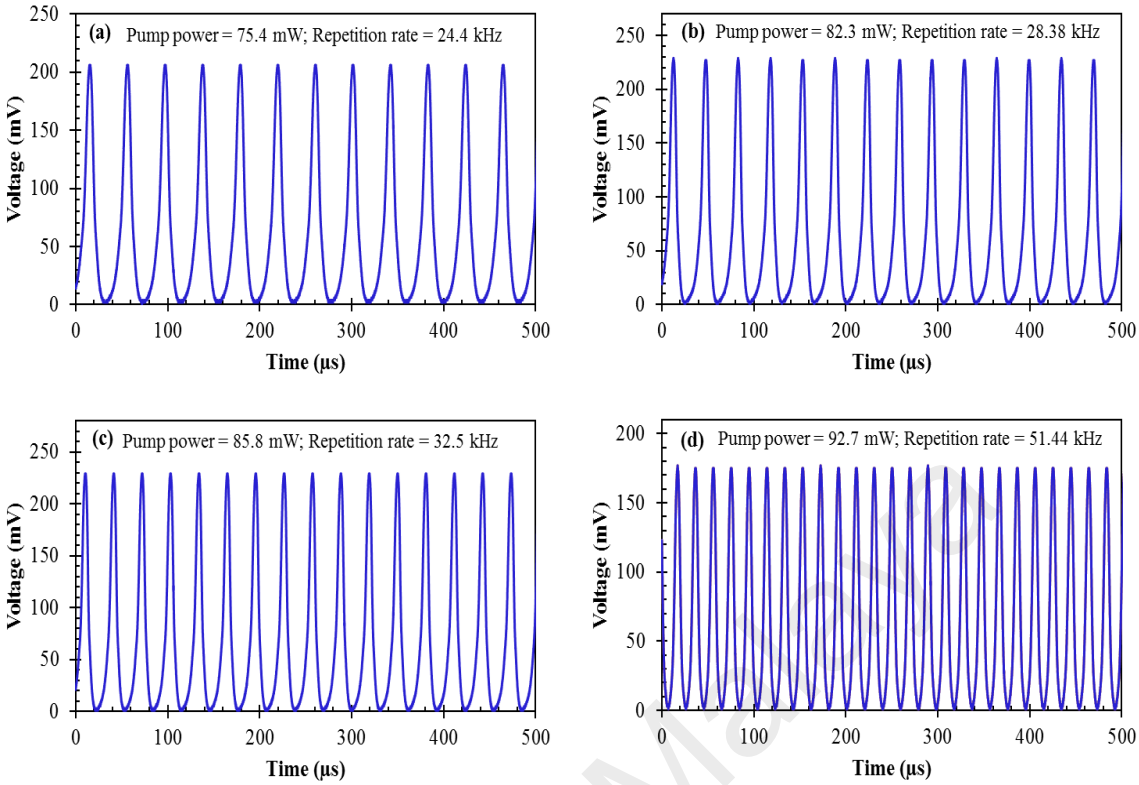

Figure 5.13: Typical pulse train of the Q-switched laser at different pump powers

Figure 5.14 summarizes the typical performance of Q-switching pulse state emitted from YDFL using Sb_2Te_3 SA at maximum pump power of 96.2 mW. Figure 5.14 (a) displays the typical Q-switching oscilloscope trace, which has a repetition rate of 55 kHz and the pulse period (peak to peak spacing) of around 18.2 µs. A single pulse profile has a full-width half maximum (FWHM) of 6.6 µs at the maximum pump power as shown in Figure 5.14 (b). There is no amplitude fluctuation for the pulse within the tunable range of the repetition rate and no peak intensity modulation on pulse train, which indicates the high stability of the Q-switching state. Figure 5.14 (c) shows the optical spectrum of Q-switched YDFL, which operates at wavelength of 1070.2 nm with peak output power of -4.5 dBm. In order to investigate the stability of Q-switching pulses train in the proposed Sb_2Te_3 SA based YDFL, RF spectrum was obtained at this pump power using an RF spectrum analyzer via a 1.2 GHz photodetector as shown in Figure 5.14 (d). The signal to noise ratio (SNR) obtained was about 60 dB, which indicates the excellent stability.

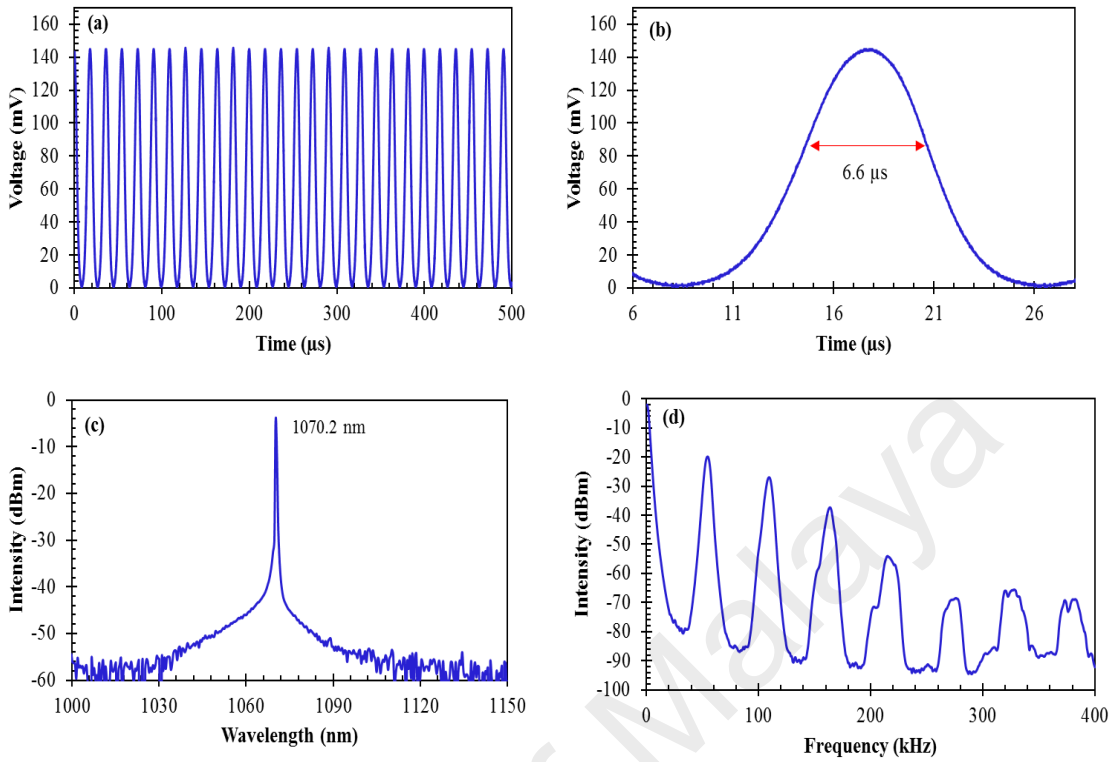

Figure 5.14: Typical performance of Q-switching pulse emitted from our YDF laser using Sb_2Te_3 SA at pump power of 96.2 mW: (a) Oscilloscope pulse train, (b) Single pulse profile, (c) optical spectrum, (d) RF spectrum

Figure 5.15 (a) shows the measurement of repetition rate and pulse width at various pump power for the proposed Q-switched YDFL. It can be seen that the repetition rate linearly increases, while the pulse width is decreased with increasing in pump power. As the pump power increases from 75.4 to 96.2 mW, the pulse repetition rate increases from 24.4 to 55 kHz, while the pulse width decreases rapidly from 9.8 to 6.6 µs. This is most probably due to the fast accumulation of electrons in the upper energy level. Yet, in the high pump power regime, according to the over-saturation, the speed of accumulation slows down, and leading to less significant change of pulse widths. This is a typical characteristic for a Q-switched laser, which mainly due to the gain compression effect in the laser cavity. It is observed that the Q-switching pulse is in range between 75.4 and 96.2 mW and the pulse started to disappear at higher pumping. This is due to the SA, which continuously in the saturated state because of the high intensity of light, and there

is no time for de-excitation. Figure 5.15 (b) shows the measurement of the average output power and pulse energy at various pump power. The average output power increases from 5.3 to 10.9 mW as the pump power is increased from 75.4 to 96.2 mW. On the other hand, the pulse energy fluctuates within the pump power range. The maximum pulse energy of 252.6 nJ is obtained at 82.3 mW pump power.

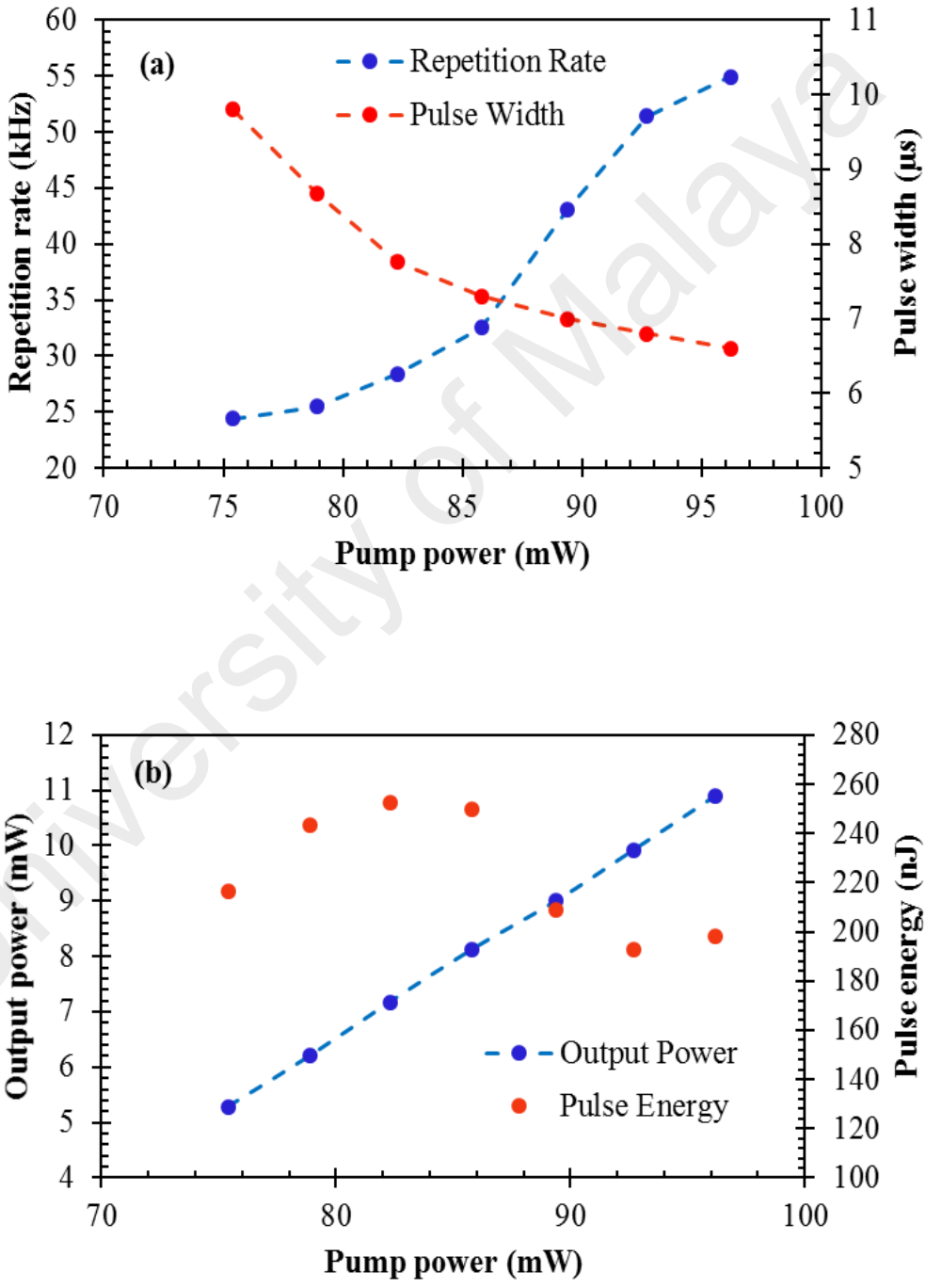

Figure 5.15: The Q-switching performance of the laser (a) Repetition rate and pulse width, and (b) output power and pulse energy at various pump power

5.3.4 Mode-locking Laser Performances

As the output coupler ratio was changed to 90/10 in the YDFL cavity, the laser operation can be converted to mode-locking mode. The change of coupler has significantly reduced the cavity loss and with the help of nonlinear effect and dispersion characteristic inside the cavity, stable mode-locking pulses could be realized. The mode-locked operation also depended on the appropriate cavity length and SA optical properties.

The mode-locked YDFL has a total cavity length of around 9 m with a total net dispersion in normal regime of 0.2 ps^2. The self-started mode-locked operation was achieved at threshold pump power of 47.8 mW. Figure 5.16 summarizes the performance of mode-locking state of the fiber laser at 89.4 mW. The output spectrum is shown in Figure 5.16 (a) where no Kelly spectral sidebands was observed, indicating that the pulses operation of fiber laser is operating in a normal dispersion. It has a peak wavelength of 1072.7 nm and 3 dB bandwidth of 0.09 nm.

Figure 5.16 (b) shows the mode-locked pulse train with pulse repetition rate of 24.2 MHz and the pulses period (peak to peak spacing) of 41 ns which matches with the cavity length. This has confirmed that the operation of laser is in the mode-locking state and the operation was remaining stable until 89.4 mW pump power. As seen in the same figure, the pulse width is about 17.66 ns under the oscilloscope resolution and that is much broader than the real pulse width. As an alternative, the mathematical calculation based on time-bandwidth product (TBP) can be used for estimating the pulse width. As the TBP was assumed to be 0.441 for Gaussian pulse profile (Hisyam et al., 2017), the minimum possible pulse width is estimated to be approximately 18.8 ps.

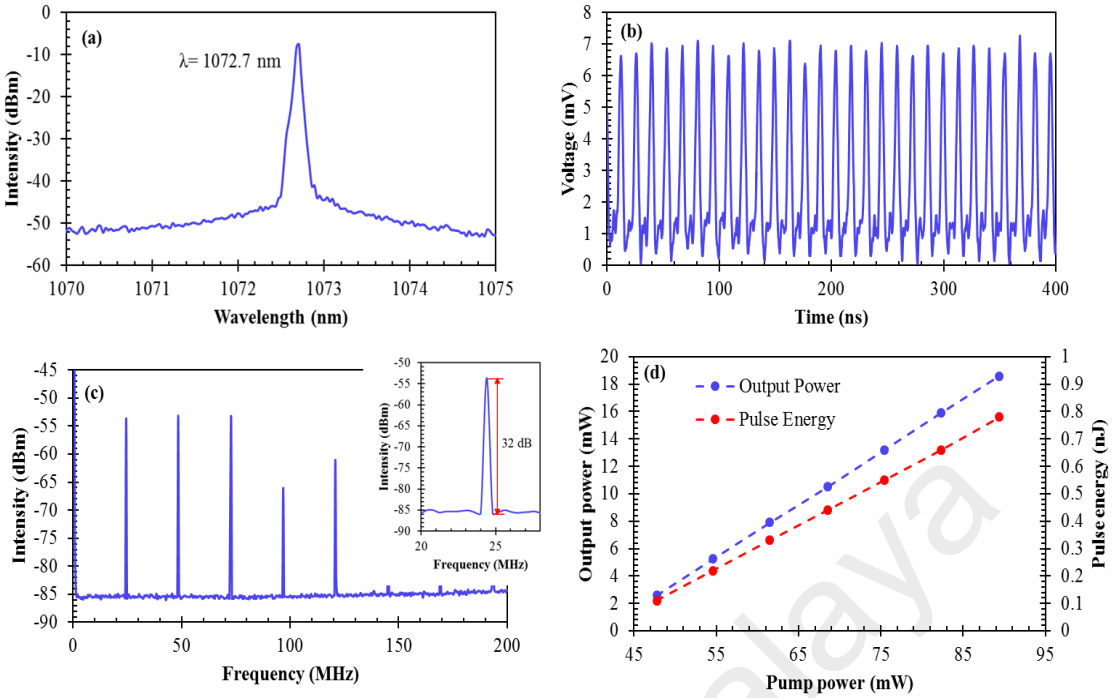

Figure 5.16: The performances of the proposed mode-locked YDFL at pump power of 89.4 mW (a) Optical spectrum, (b) typical pulse train, and (c) The RF spectrum and (d) the output power and pulse energy characteristics against the pump power

Figure 5.16 (c) shows the RF spectrum of the YDFL, which shows a SNR as high as 32 dB. It is worthy to note that no presence of fundamental frequency was observed when the SA is removed. Figure 5.16 (d) shows the output power and pulse energy at various pump powers. Both output power and pulse energy are linearly increased with increasing in pump power. At 89.4 mW pump power, the maximum output power and pulse energy is obtained to be around 18.6 mW and 0.8 nJ, respectively. The mode-locked pulse disappears when the pump power is increased above 89.4 mW.

5.4 Summary

Stable passively Q-switched YDFLs operating at 1057.4, and 1044.5 nm were successfully demonstrated using topological insulators of Bi_2Se_3 and Bi_2Te_3, respectively. Using Bi_2Se_3 saturable absorber, the YDFL obtains a stable train of pulses with a repetition rate frequency that is tunable from 48.83 to 102 kHz. Meanwhile, the corresponding pulse width decreases from 8.9 to 3.48 µs as the pump power increases

from 67.6 to 88.3 mW. For the Bi_2Te_3 based Q-switched YDFL, the repetition rate grows from 43.25 to 93.63 kHz and the pulse width shrinks from 5.65 to 2.01 μs as the 980nm pump power rises from 72.8 to 98.4 mW. Both SAs show good Q-switching performance in the 1 μm wavelength region and the maximum pulse energy of 29.95 nJ was produced with the Bi_2Te_3 SA. A Sb_2Te_3 film was also demonstrated as an effective SA for generation Q-switching and mode-locking pulses in YDFL cavity. The threshold of generation Q-switched was obtained at 75.4 mW pump power and the laser remaining stable until pump power of 96.2 mW. The pulse repetition rate is increased from 24.4 to 55 kHz as the pump power increases from 75.4 to 96.2 mW. The pulse energy was around 252.6 nJ at 82.3 mW pump power, which is significantly higher than the Bi_2Te_3 based Q-switched laser. On the other hand, the mode-locking was also successfully achieved with Sb_2Te_3 SA by significantly reduce the cavity loss. The mode-locked fiber laser was obtained with 24.2 MHz repetition and 18.8 ps pulse width within the pump power between 47.8 to 89.4 mW. The maximum pulse energy was calculated to be around 0.8 nJ at at 89.4 mW pump power. These results verified that the Sb_2Te_3 is a better TI material as SA for Q-switching and mode-locking pulses generating in 1 micron wavelength region.

CHAPTER 6: TRANSITION METAL OXIDE NANOMATERIALS AS SATURABLE ABSORBER

6.1 Introduction

Very recently, a new kind of metal nanoparticles material such as gold, silver nanoparticles and titanium dioxide (TiO_2) were also investigated and demonstrated as a saturable absorber (SA) for Q-switched and mode-locked fiber lasers (Glubokov et al., 2014; T. Jiang et al., 2013). These types of SAs have gained attraction due to their unique properties such as proper modulation depth, low saturation intensity and fast response time. Previously, mode-locked fiber laser was demonstrated using gold nanoparticles based SA for generating 887 fs pulse train (X.-D. Wang et al., 2014). Silver nanoparticles was also proposed as SA for mode-locking and the absorption characteristic of the material was reported as 10 MW cm^{-2} (Glubokov et al., 2014).

In this chapter, two types of metal oxide nanomaterials are explored as SA for Q-switching and mode-locking operations in Ytterbium-doped fiber laser (YDFL) cavity; Nickel Oxide (NiO) and cobalt oxide (Co_3O_4). These materials are embedded into a polymer film and sandwiched between two fiber ferrules, making it an SA device. By incorporating the all-fiber SA device into the YDFL cavity, Q-switching and mode-locking operations operating in 1 μm region could be realized.

6.2 Nickel Oxide Nanoparticles Thin Film based Q-switched and Mode-locked YDFL

Nickel oxide (NiO), a transition metal oxide semiconductor is an electro-chromic, transparent conducting, and antiferromagnetic material that have a wide range of applications in electro-chromic devices, optical fibers, and sensors. Nickel oxide nanoparticle could also be used as an effective SA since it has an appropriate modulation depth and low saturation intensity. The nonlinear refraction properties of NiO film was

also previously investigated using the thermally managed eclipse Z-scan technique (de Melo Jr et al., 2009). Many studies have also reported on NiO absorption properties where its band-gap energy is reported to be within a range from 3.6 to 4.0 eV, which equivalent to wavelength of 309 to 344 nm. However, Duan et. al reported that the nanoparticle absorption can be red-shifted by increasing the nanoparticle size (Duan et al., 2012). Therefore, NiO nanoparticle could be used as an SA in near-infrared region. Most recently, NiO film SA was successfully used to generate Q-switching pulses train in Erbium doped fiber laser (EDFL) cavity (Nady, Ahmed, Latiff, Numan, et al., 2017). However, so far, there are no reports on NiO based pulsed fiber laser operating in 1 μm region. Therefore, in this section, Q-switched and mode-locked fiber laser operating at 1 μm region are demonstrated using a NiO film as SA. The film material was sandwiched among two fiber ferrules, making it an SA device. By incorporating the NiO nanoparticle SA into the YDFL cavity, Q-switched and mode-locked operation could be achieved.

6.2.1 Fabrication and Characterization of Nickel Oxide Nanoparticles Thin Film SA

The fabrication process of the NiO nanoparticles thin film is described in Figure 6.1, which consist of two steps. In the first step, 1 M of $NiCl_2.6H_2O$ was dissolved in 50 ml of deionized (DI) water under constant stirring for 10 min. After that, a freshly prepared solution of NaOH (2 M) was added dropwise to the above solution and consequently, subjected to sonication using a horn sonicator. The whole reaction was carried out using the constant amplitude of 60% for 1 h. The product was collected via centrifugation and washed several times with deionized water. Finally, the obtained sample was calcinated at 350 °C for 3 hours in an electric box furnace. The synthesis of NiO nanoparticles details was reported in (Duraisamy et al., 2016).

In the second step, the NiO nanoparticles was mixed with the polyethylene oxide (PEO) as a host polymer to fabricate the thin film as described in Figure 6.1. The host polymer was prepared by dissolving 1 g of PEO in 120 ml of deionized water. Then, a suitable amount of NiO structure nanoparticles was added to the prepared solution and stirred it for further 2 hours. After that, the uniformly mixed slurry was cast on Teflon petri and dried at 60 ºC in a vacuum oven to fabricate the film. The thickness of the thin film was measured to be around 0.2 mm by using Mitutoyo micrometer screw gauge.

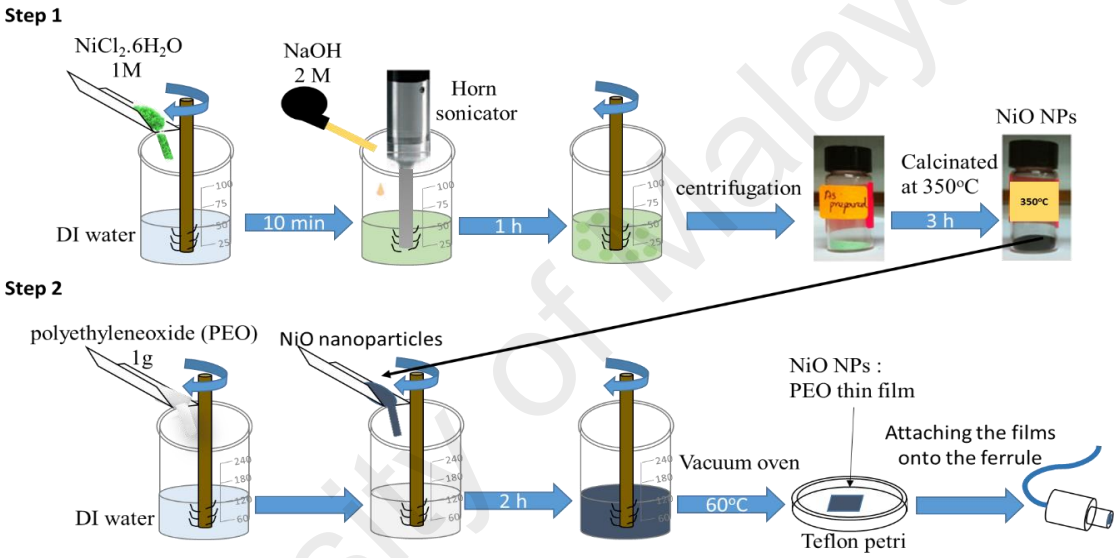

Figure 6.1: The fabrication process of NiO nanoparticles thin film

The X-ray diffraction (XRD) analysis pattern of the NiO nanostructure is shown in Figure 6.2 (a) and obviously indicates three peaks assigned to different vibrational modes. The three peaks are located at 37.28º, 43.28º, and 62.88º corresponding to crystalline NiO planes of (111), (200), and (220), respectively. The observed crystalline planes correspond to the face centered cubic structure of NiO. Compared to a Raman spectrum, the XRD is fit for indicating the phases as well as the crystalline orientation of the NiO. Figure 6.2 (b) shows the field emission scanning electron microscope (FESEM) image of NiO nanoparticles embedded into the PEO thin film. It has a high dense of agglomerated nanoparticles, which are formed as a thin film and randomly distributed on the surface.

These nanoparticles are in like-spherical shape with an average size of 35.78±8.67 nm. The nonlinear optical absorption properties of NiO thin film SA was also investigated using the twin-detector method as shown in Figure 6.3. For the NiO film sample that was used in this work, the modulation depth, non-saturable intensity, and saturation intensity were measured to be approximately 39 %, 49 %, and 0.04 MW/cm^2, respectively.

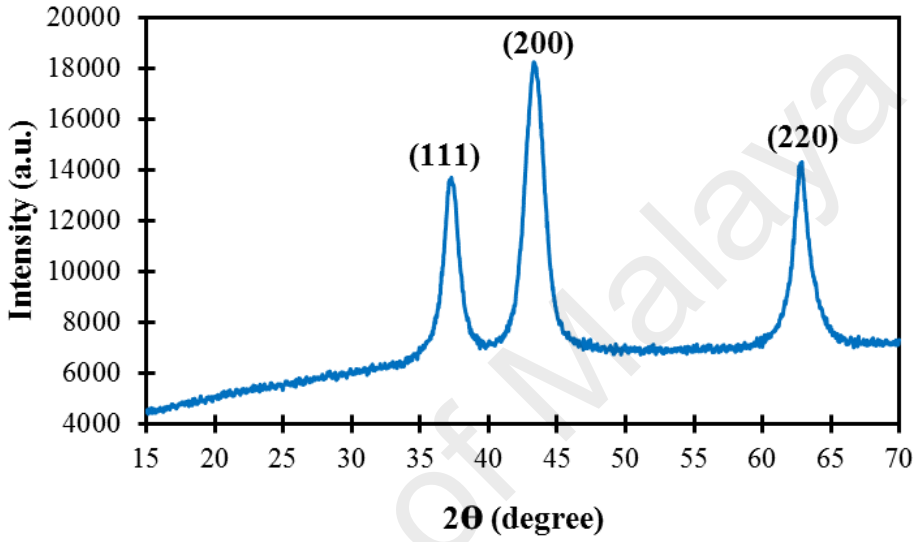

(a)

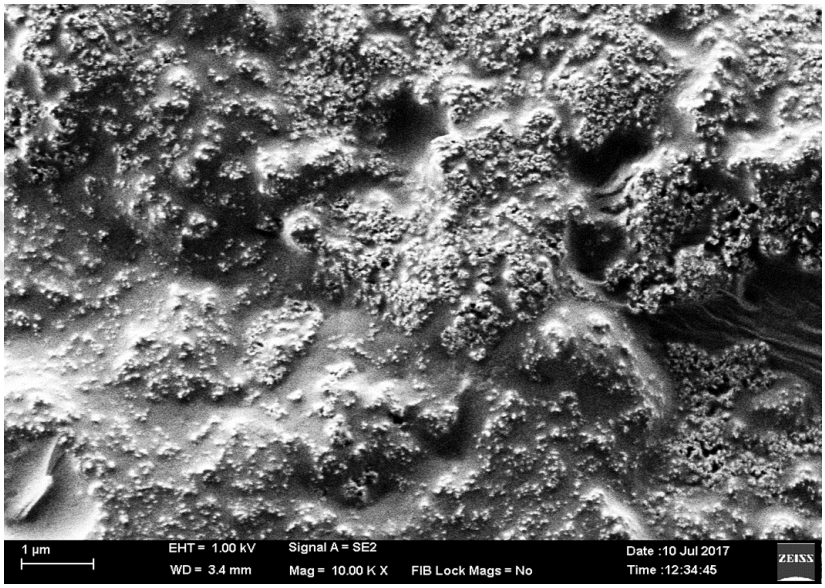

(b)

Figure 6.2: (a) XRD pattern and (b) FESEM images of the NiO nanoparticles embedded on the polymer thin film

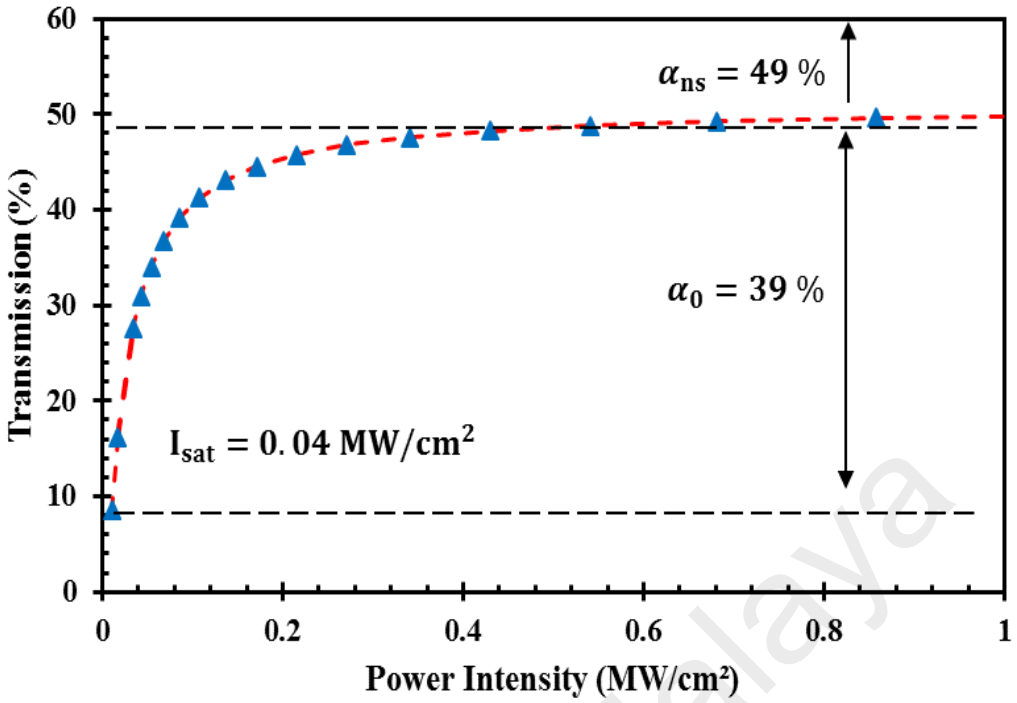

Figure 6.3: Nonlinear absorption measurement of NiO-film SA

6.2.2 The Fiber Laser Ring Configuration

The experimental setup of Q-switched YDFL based on NiO SA is shown in Figure 6.4. The optical ring cavity consists of a 1.5 m long Ytterbium-doped fiber (YDF), was forward pumped by a 980-nm laser diode (LD) through a 980/1064 nm wavelength division multiplexer (WDM). The YDF has a core and cladding diameters of 4 µm and 125 µm respectively, with a numerical aperture of 0.20, as well as the cut-off wavelength of 1010 nm, ion absorption of 280 dB/m at 920 nm and group velocity dispersion (GVD) of 24.22 ps^2/km. An isolator was integrated into the optical ring cavity to ensure unidirectional operation. The NiO nanoparticles SA device was obtained by sandwiching a 1 mm × 1 mm piece of the film between two fiber ferrules using a fiber adaptor. Index matching gel was applied at the connection to minimize parasitic reflections. A 3 dB coupler was used to tap out the laser output. The output laser is analyzed by an optical spectrum analyzer with a spectral resolution of 0.02 nm, an optical power meter, and a 2

GHz photodetector together with a 350 MHz oscilloscope or 7.8 GHz radio-frequency (RF) spectrum analyzer.

The Q-switched laser was then converted into a mode-locked fiber laser by replacing the 50/50 output coupler with 90/10 coupler to reduce the cavity loss and allow the mode-locking pulses generation. The coupler allows 90% of the laser to oscillate in the cavity and only tap out 10 % as an output. The mode-locked YDFL has a total cavity length of 9 m with a total net dispersion in normal regime of 0.2 ps^2, where the rest of the ring cavity is a single-mode fiber (HI 1060) with a GVD of 21.91 ps^2/km.

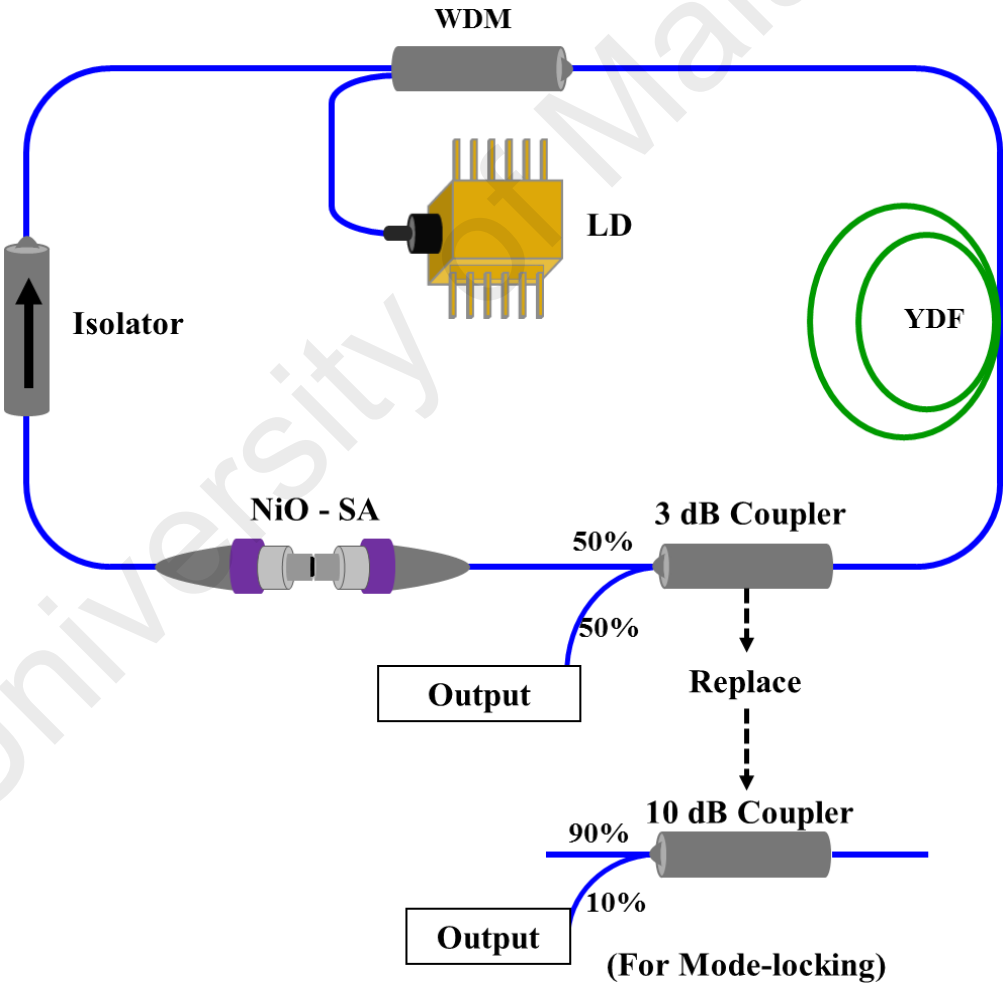

Figure 6.4: The schematic diagram of experimental setup for Q-switched and mode-locked YDFLs with NiO based SA

6.2.3 Result and Discussion for the Q-Switching Operation

The self-starting Q-switched YDFL was obtained at threshold pump power of 117.73 mW and its operation was maintained up to pump power of 133 mW. Figure 6.5 (a) shows the optical spectrum of Q-switched YDFL when the pump power is fixed at 117.73 mW. As seen, the spectrum is centered at 1073.5 nm with a bandwidth of 0.6 nm. Figure 6.5 **(b)** shows the average output power against the pump power. The output power increased from 3.3 to 7.0 mW when the pump power increased from 117.73 to 133 mW.

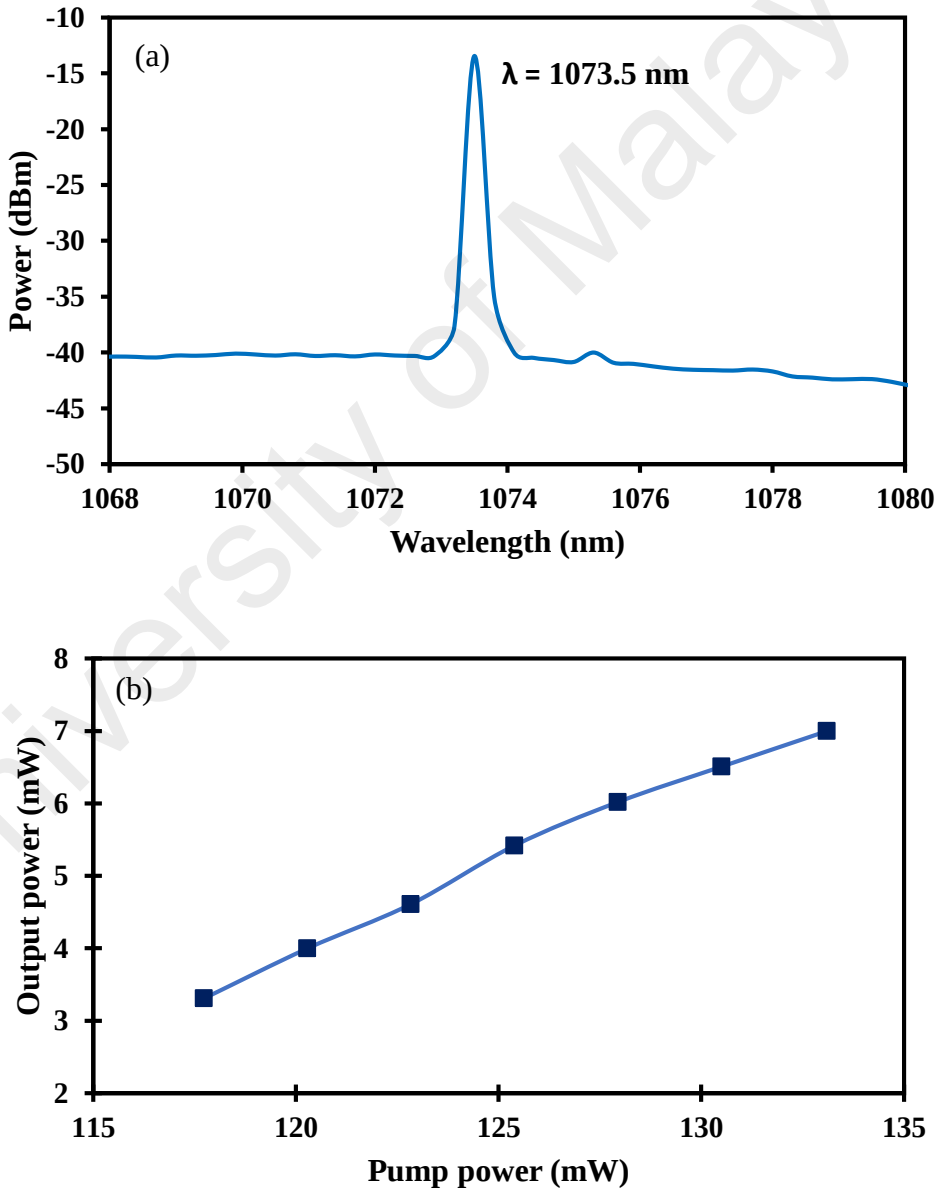

Figure 6.5: (a) Output spectrum at the threshold pump power of 117.73 mW, (b) Output power against pump power

Figure 6.6 (a) shows the Q-switched YDFL pulse trains at three different pump powers of 117.73, 125.4, and 133 mW, respectively. As the pump power increases, more energy can be stored in the laser cavity and this contributes to the rise in the repetition rate accompanied by the reduction in pulse duration. The repetition rates have the period of 9.5, 12, and 15.8 kHz, while the corresponding pulse durations are 14.27, 11.28, and 10.18 μs at pump power of 117.73, 125.4, and 133 mW, respectively. The properties of the Q-switching laser principally rely on upon the gain medium, SA and pump power. Figure 6.6 (b) shows RF spectrum of the Q-switched YDFL at pump power of 133 mW, for which the pulse repetition rate is 15.8 kHz, matching with the oscilloscope data. The RF signal-to-noise ratio (SNR) is about 30 dB with no spectral modulation, indicating that the Q-switching operation is stable.

Figure 6.6 (c) shows the repetition rate and pulse width as a function of 980 nm pump power. At the point when the pump power was expanded from 117.73 to 133 mW, the repetition rate increased in a practically direct manner from 9.5 to 15.8 kHz, while the pulse width gets to be smaller, shortening from 14.27 to 10.18 μs. This is an average normal for Q-switching operation. As pump power increases, more power flows inside the laser cavity, in this manner saturating the SA faster. It can be seen that the SA become almost saturated because of the smaller changes of repetition rate, and pulse width. This appearance can be linked into the modulation depth and the length of the laser cavity. Figure 6.7 shows the variation of peak power and pulse energy against the pump power. As the pump power increased from 117.73 to 133 mW, the peak power was also increased from 22.9 to 40.9 mW. The pulse energy maximum pulse energy is 478 nJ at the same range of pump power, which the measuring based on the repetition rate and output power. The peak power is depended on the pulse energy and pulse duration.

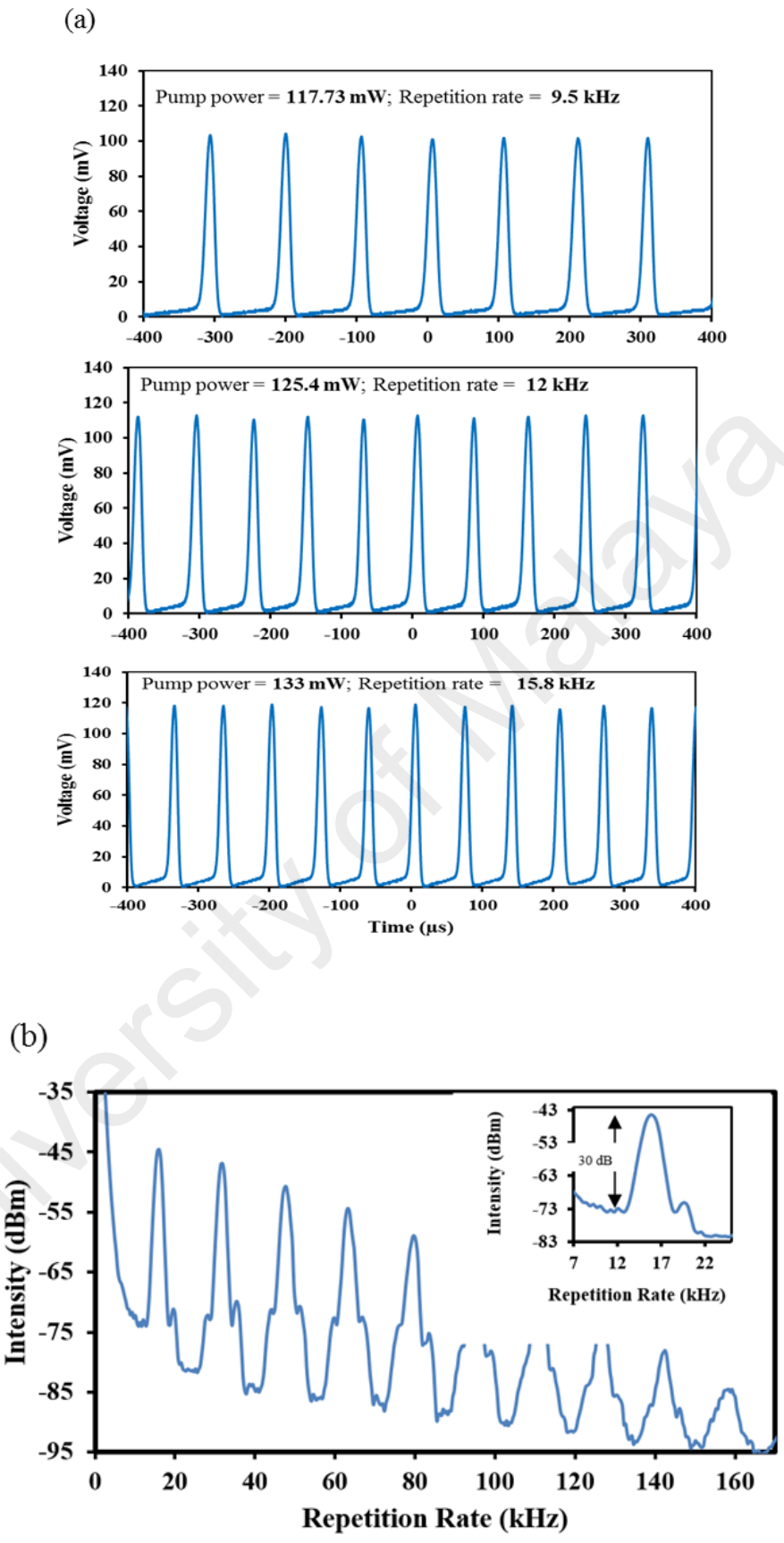

Figure 6.6: Temporal performance of Q-switched YDFL (a) Pulse train at different pump power. (b) RF spectra at pump power of 133 mW with 150 kHz span. Insert is enlarged image of 15.8 kHz repetition rate. (c) Repetition rate and pulse with respect to pump power

(c)

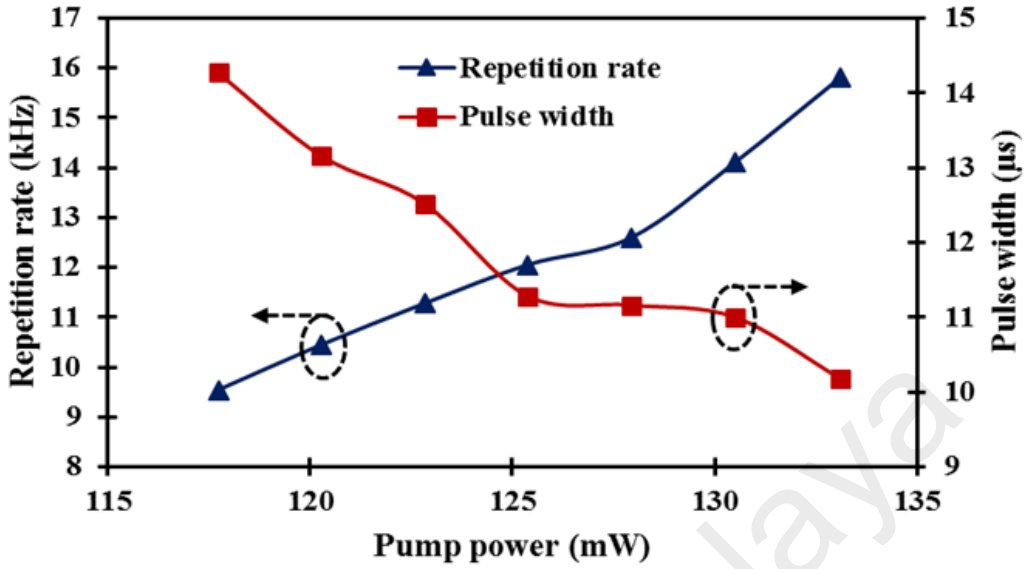

Figure 6.6, continued

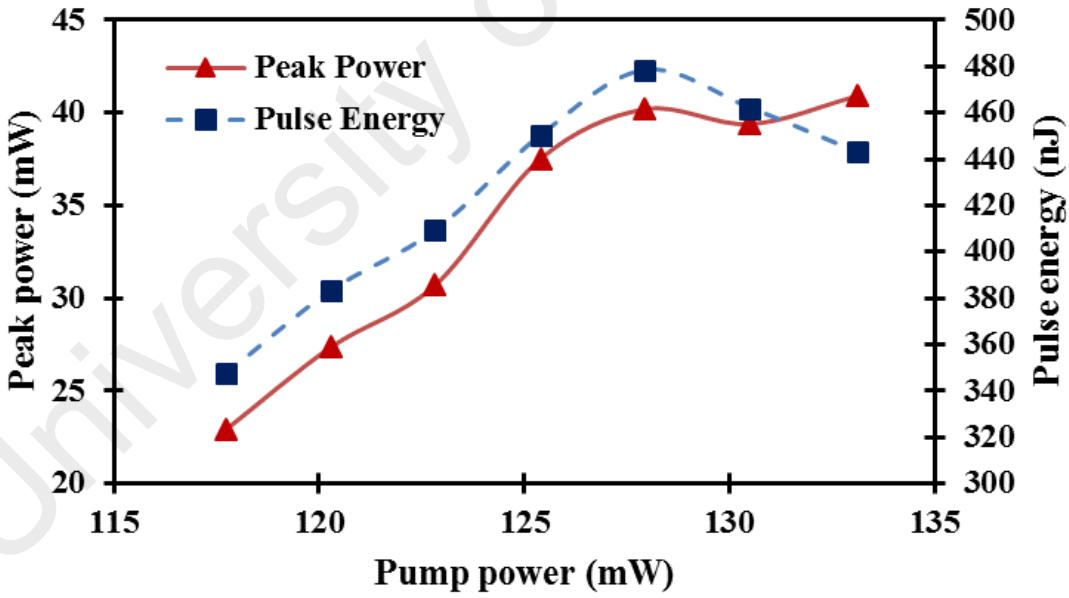

Figure 6.7: Peak power and pulse energy with respect to pump power

6.2.4 Result and Discussion for the Mode-locking Operation

By changing the coupler to 90/10 coupler in the ring cavity, the cavity loss significantly reduces which support the generation of a stable mode-locking pulse. In the

experiment, the continuous-wave laser threshold pump power is approximately 103 mW. A self-started mode-locked was achieved at a pump power of 110 mW until 137.5 mW. The generation of mode-locking operation is completely depended on the SA optical properties and suitable cavity length. Figure 6.8 (a) shows the optical spectrum of the mode-locking pulse at a pump power of 137.5 mW with the peak wavelength of 1037.72 nm and 3 dB spectral bandwidth of 0.08 nm with no Kelly sideband. Thus, it confirmed the pulses operation in the normal dispersion. Figure 6.8 (b) displays the mode-locked YDFL pulse train, which corresponded to 23 MHz repetition rate with the optical cavity length of 9 m and 49 ns pulse period (peak to peak space) while remaining stable until 137.5 mW pump power. As shown in the same figure with the limitation of the oscilloscope resolution, the pulse width is 25 ns, which is much broader than the actual pulse width. As an alternative, the mathematical calculation can be used for measuring the pulse width based on time-bandwidth product (TBP). Assuming the TBP of 0.441 for Gaussian pulse profile (Hisyam et al., 2017), the minimum possible pulse width is mathematically estimated as approximately 19.8 ps. The mode-locking pulse train was observed to run stably at room temperature. Figure 6.8 (c) shows clearly the radio frequency spectrum of the mode-locking operation, which has a SNR up to 29 dB. Once NiO-SA removed from the fiber ferrule, the obtained fundamental frequency will terminate.

The relationship between the output power and input pump power is shown in Figure 6.8 (d), which the maximum output power is about 12.8 mW at 137.5 mW pump power. Overall performance of mode-locked YDFL has a slope efficiency of 38.22%. Figure 6.8 (e) shows the relationship of mode-locked YDFL between pulse energy and peak power against pump powers. Both pulse energy and peak power is linearly increased against pump power. The maximum pulse energy and peak power are 0.56 nJ and 26.4 W,

respectively, at 137.5 mW pump power. The mode-locked pulse disappears when the pump power is increased above 137.5 mW.

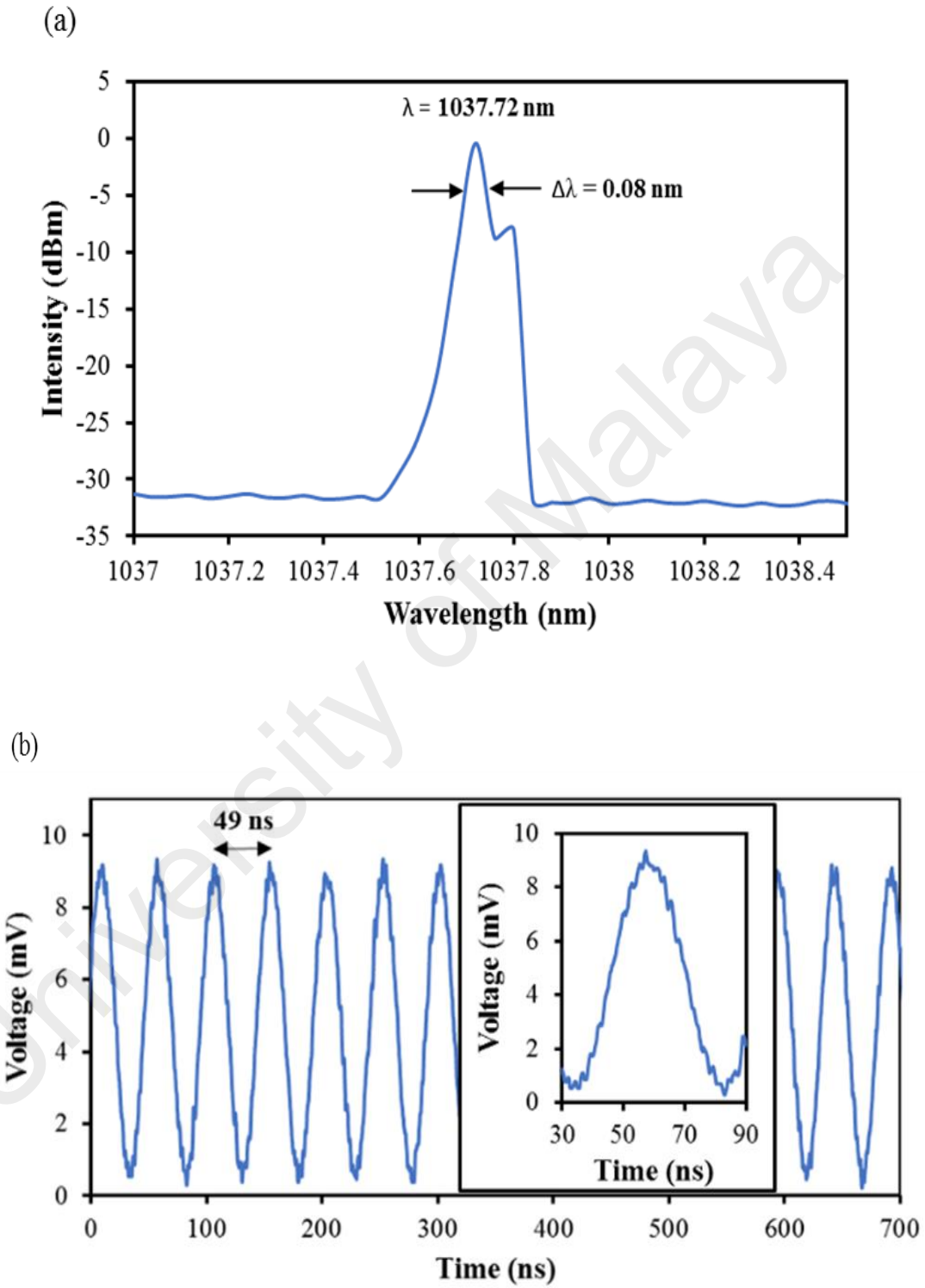

Figure 6.8: Mode-locked performance. (a) The optical spectrum, (b) pulse train (insert the image of single-envelope pulse), (c) the RF spectrum at maximum pump power of 137.5 mW. (d) Output power, and (e) Pulse energy and peak power against the pump power

(c)

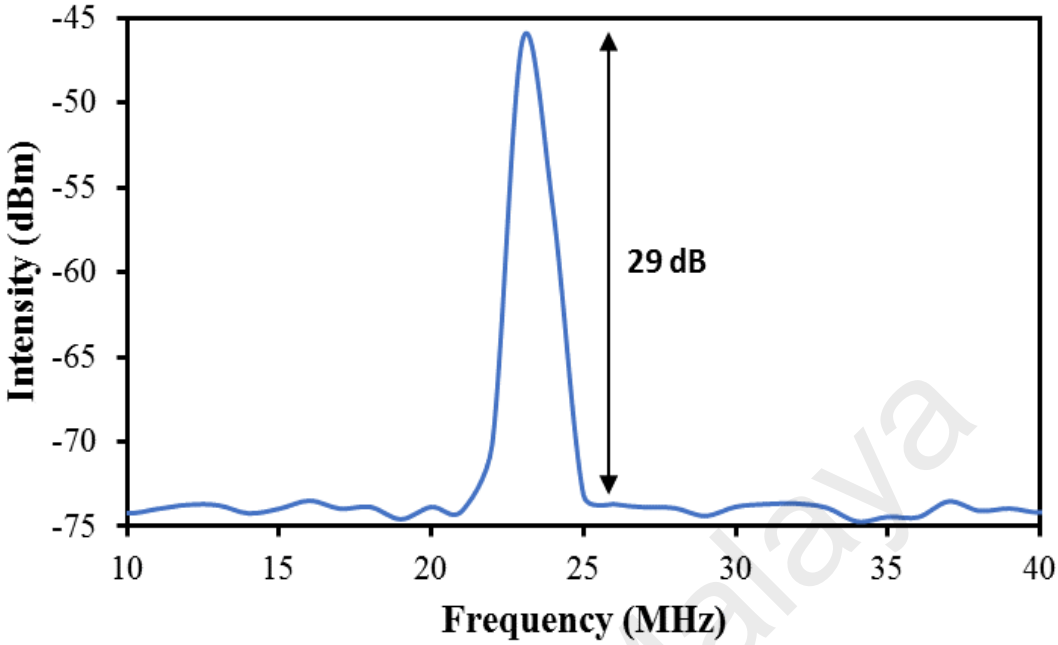

(d)

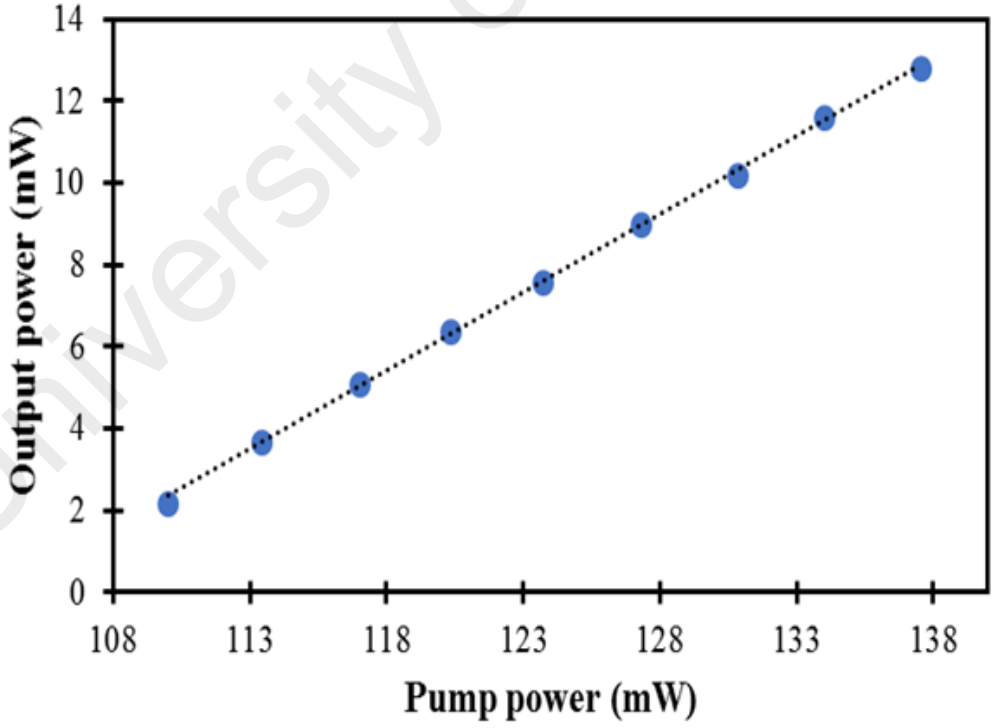

Figure 6.8, continued

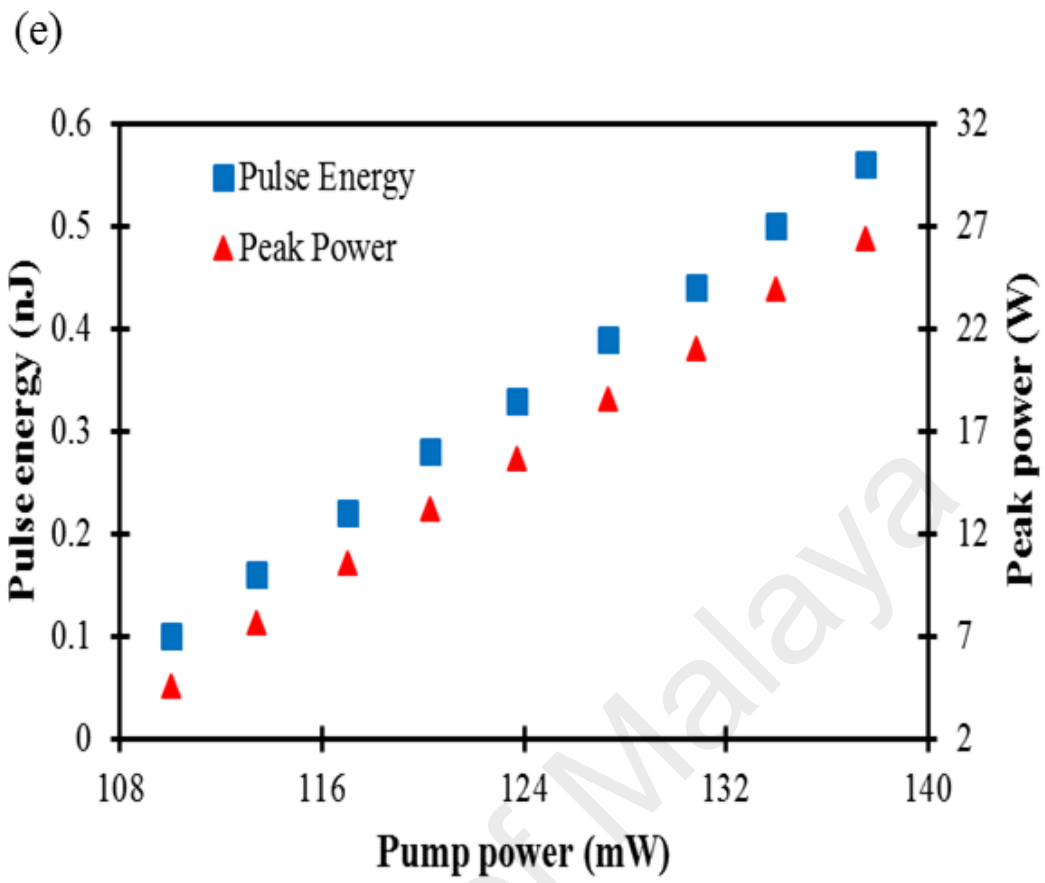

Figure 6.8, continued

6.3 Cobalt Oxide Film SA for Generating Q-Switching and Mode-locking Pulses in YDFL cavity

Very recently, transition metal oxides such as titanium dioxide (TiO_2) and zinc oxide (ZnO) has used as SAs, which have been reported to generate an ultra-short pulse fiber laser (H Ahmad, CSJ Lee, et al., 2016; H Ahmad, Siti Aisyah Reduan, et al., 2016). In the previous section, NiO nanoparticles which were embedded into PEO polymer was demonstrated as SA for operation in YDFL cavity. The transition metal oxides have gained more attentions among many researchers due to their large optical nonlinearity and the advantages of good thermal and the chemical stability as well as the mechanical strength. Among those materials, cobalt (Co_3O_4) has the best ratio performance of the nonlinearity to the linear absorption. It is also a promising material for fabricating highly

nonlinear transmission devices in the visible range. The nonlinear refraction properties of Co_3O_4 film was previously reported (Ando et al., 2004; Yamamoto et al., 2002; X Zhu et al., 2010; Xiushan Zhu et al., 2012). It has a bandgap size at 1.38 eV and 2.0 eV, which corresponds to 898 nm and 620 nm, respectively. This makes the material as promising candidates for fabricating highly nonlinear transmission devices in the visible range. In addition, Barecca et al. (2001) reported that the absorption also presence at 1-micron region, due to internal oxidation-reduction process that caused inter-valence charge transfer from Co(II) to Co(III) (Barreca et al., 2001). The first successful generation of Q-switched fiber laser using Co_3O_4 film SA was demonstrated at 1.55-micron region (Nady, Ahmed, Numan, et al., 2017). It generates stable pulse up to 70.92 kHz with a signal-to-noise ratio (SNR) of 60 dB. However, no scientific report has been found for 1-micron region.

In this section, a Q-switched and mode-locked ytterbium-doped fiber laser (YDFL) is reported based on Co_3O_4 nanocubes thin film as SA. The Co_3O_4 nanocubes were embedded in PEO film, which was then integrated into YDFL cavity. A stable Q-switched laser operating at 1043.64 nm wavelength was obtained and the pulse repetition rates are tunable from 60.3 to 86.66 kHz as the pump power was varied from 144.4 to 165.4 mW. The mode-locked laser operated at 1035.8 nm wavelength with 20 MHz repetition rate. The maximum average output power and pulse energy were 24 mW and 1.2 nJ respectively at pump power of 186 mW. This is the first reporting of Co_3O_4 nanocubes thin film as SA used in a mode-locked laser.

6.3.1 Fabrication and Characterization of Co_3O_4 Film SA

The Co_3O_4 nanocubes used in this study was synthesised via a hydrothermal method as described in Figure 6.9. In the first step, 1 mmole of $Co(CH_3COO)_2$: $4H_2O$ solution was mixed with 45 ml of deionized (DI) water and ethanol (3:1) mixture then sonicated

by ultrasonic bath. Next, the mixture was put together with Carbonyldiamide, as commonly called urea solution, of 15 ml followed by stirring for 30 minutes. After that, the stirring mixture was put in a 100 mL Teflon-lined stainless steel autoclave and subjected to hydrothermal treatment by keeping the temperature of the oven at 150 ^{o}C for 5 hours. Finally, the synthesized Co_3O_4 nanocubes was washed several times by DI water and ethanol under centrifugal force and dried in a hot vacuum oven at 60 ^{o}C for 24 hours.

For practical use of Co_3O_4 nanocubes as SA, the Co_3O_4 nanocubes were embedded into PEO to form thin film via solution casting route as described in the second step of Figure 6.9. Firstly, 1 g of PEO solution was prepared as a diluted solution by dissolving in 120 mL of DI water and then stirring with continuously stirring at 50^{o}C. This diluted solution was kept under continuously stirring for 2 hours. After that, some amount of the synthesized Co_3O_4 nanocubes was mixed to the diluted solution, followed by stirring for 2 hours to form a uniform solution mixture as a mixed slurry. Finally, the mixed slurry was casted to Teflon coated Aluminum foil to form thin film followed by drying in the oven at 60 ^{o}C.

For characterization studies, FESEM image was used to obtain the surface morphology of the synthesized Co_3O_4 nanocubes. For higher magnification, high resolution transmission electron microscopy (HRTEM) was obtained by JEOL JEM-2100F. For analytical structure, micro-Raman scattering spectra was used to investigate the synthesized Co_3O_4 nanocubes structure using an argon-ion laser with excitation wavelength of 514 nm and XRD for structural crystallinity and purity of the Co_3O_4 nanocubes was obtained by Philips X'pert X-ray diffractometer using copper Ka radiation with a wavelength of 1.5406 A° for a scan rate of 0.02 degree per second. Mitutoyo micrometer screw gauge measurement was used to determine the thin film thickness which was about 0.05 mm.

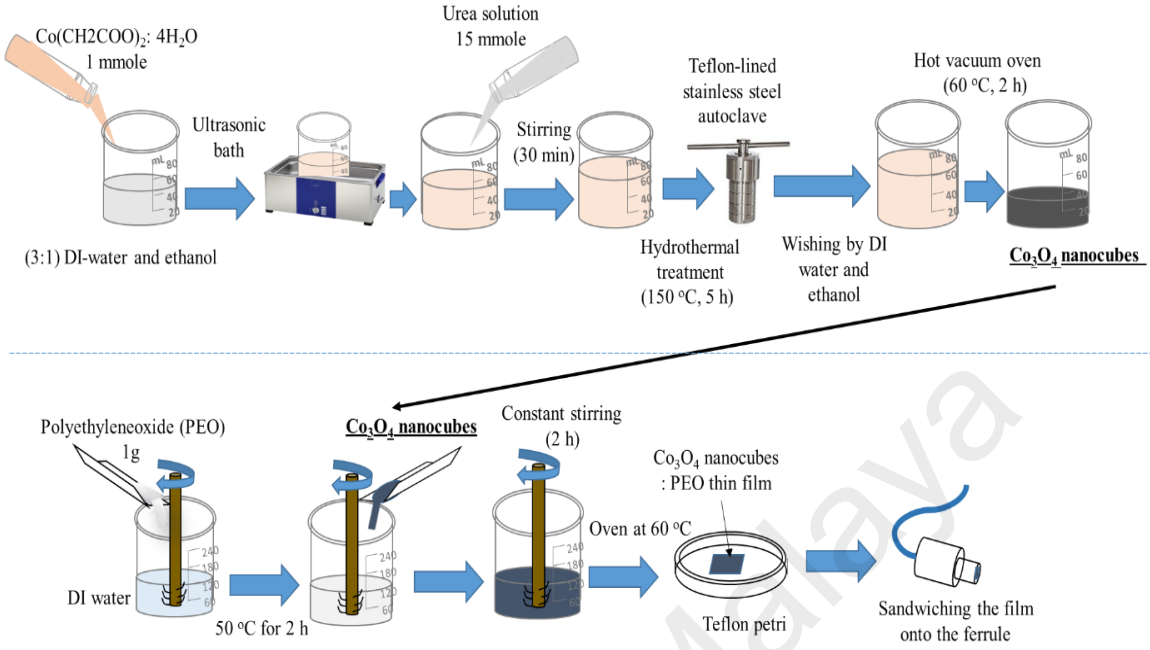

Figure 6.9: The fabrication process of Co_3O_4 nanocubes film

The surface morphology of the synthesized Co_3O_4 nanocubes by hydrothermal method is shown in Figure 6.10 (a). The FESEM image presented nanocubes form with high density that appeared in agglomeration forms. Figure 6.10 (b) shows the synthesized Co_3O_4 nanocubes at higher magnification presented by HRTEM image. Furthermore, the nanocubes approximately appeared in uniformity size with agglomerations which the average size was around 32 nm. Figure 6.11 (a) shows the Raman scattering spectrum of the nanocubes grown by hydrothermal method. This spectra consists of five modes at around 192, 482, 517, 614 and 687 cm^{-1} which can be attributed to the B_{1g}, E_g, F^1_{2g}, F^2_{2g} and A_{1g} modes of Co_3O_4, respectively (Numan et al., 2017) and that confirm the appeared of nanocubes at FESEM image belong to Co_3O_4 nanocubes structure. XRD patterns of the Co_3O_4 nanocubes is shown in Figure 6.11 (b) and mainly presented seven planes of the crystallite of the nanocubes. The crystalline peaks are located at 18.1°, 30.9°, 36.4°, 44.2°, 54.9°, 58.6°, and 64.4° corresponding to crystalline Co_3O_4 planes of (111), (220), (311), (400), (422), (511), and (440), respectively (Numan et al., 2016; Liangmiao Zhang

et al., 2013). The nonlinear optical absorption properties of Co_3O_4 thin film SA was achieved using twin-detector method in order to confirm its saturable absorption as shown in Figure 6.12. For the Co_3O_4 SA sample that was used in this work, the modulation depth and saturation intensity were measured to be approximately 0.35 % and 3 MW/cm^2, respectively, which few materials as SAs have also a small modulation depth (Junsu Lee et al., 2015; Z. Luo et al., 2014).

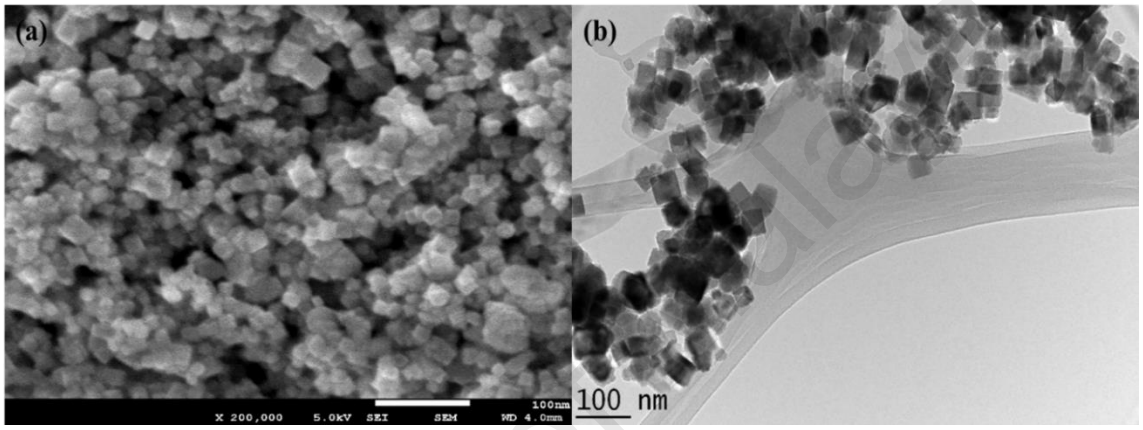

Figure 6.10: The images of Co_3O_4 samples (a) FESEM, and (b) HRTEM

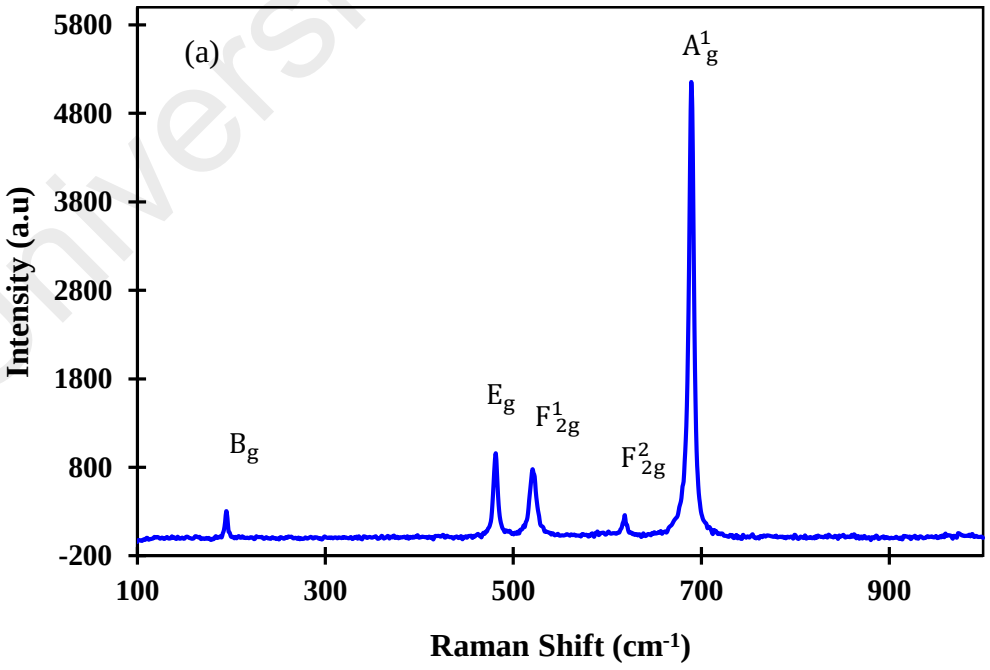

Figure 6.11: (a) Raman spectra and (b) XRD pattern of Raman spectrum of the Co_3O_4 nanocubes

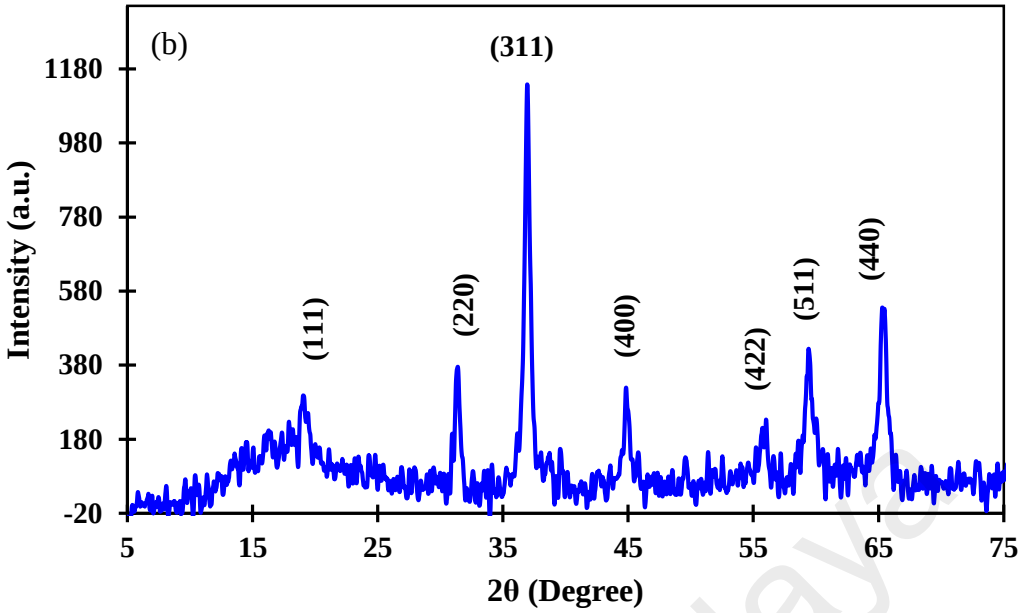

Figure 6.11, continued

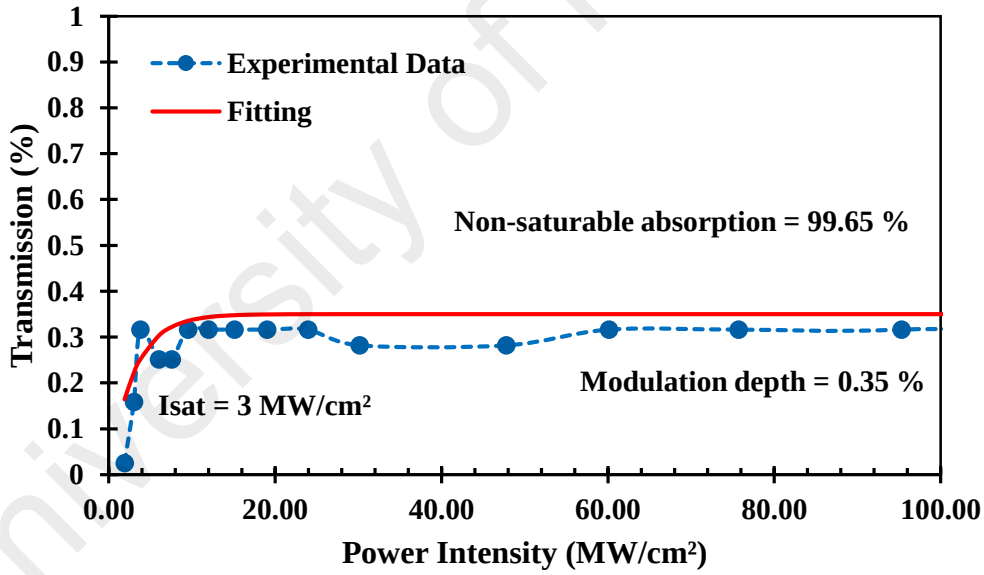

Figure 6.12: Nonlinear optical absorption measurement of Co_3O_4 nanocubes film as SA

6.3.2 Configuration of Co_3O_4 based Q-switched and Mode-locked YDFL

In the experiment, the application of Co_3O_4 nanocubes film as a SA in generating mode-locking pulses train in YDFL was investigated. The experimental setup is shown in Figure 6.13, which mainly consists of 1.5 m long YDF as a gain medium. In order to

prevent the laser reflecting, an isolator is spliced into the cavity. The 980 nm pump is coupled into the fiber ring resonator with a 980/1064 nm wavelength division multiplexer (WDM). The Q-switched laser was obtained by using a 3dB output coupler inside the cavity. A 90/10 output coupler was used in the mode-locked laser cavity to extract 10% of the output for analysis. The remainder of laser power was channeled back to the SA device and kept in the cavity to oscillate for laser generation. The Co_3O_4 nanocubes film SA was constructed by sandwiching a ~ 1 mm×1 mm piece of the film between two fiber ferrules using a fiber adaptor while applying index matching gel at the connection to minimize parasitic reflections. The output laser was routed to an OSA and optical power meter for spectral and output power analysis, respectively. It is also measured by a 2 GHz photodetector, which was connected to a 350 MHz oscilloscope and 7.8 GHz RF spectrum analyzer for temporal and frequency analysis, respectively. The mode-locked YDFL has a total cavity length of 10 m with a total net dispersion in normal regime of 0.22 ps^2.

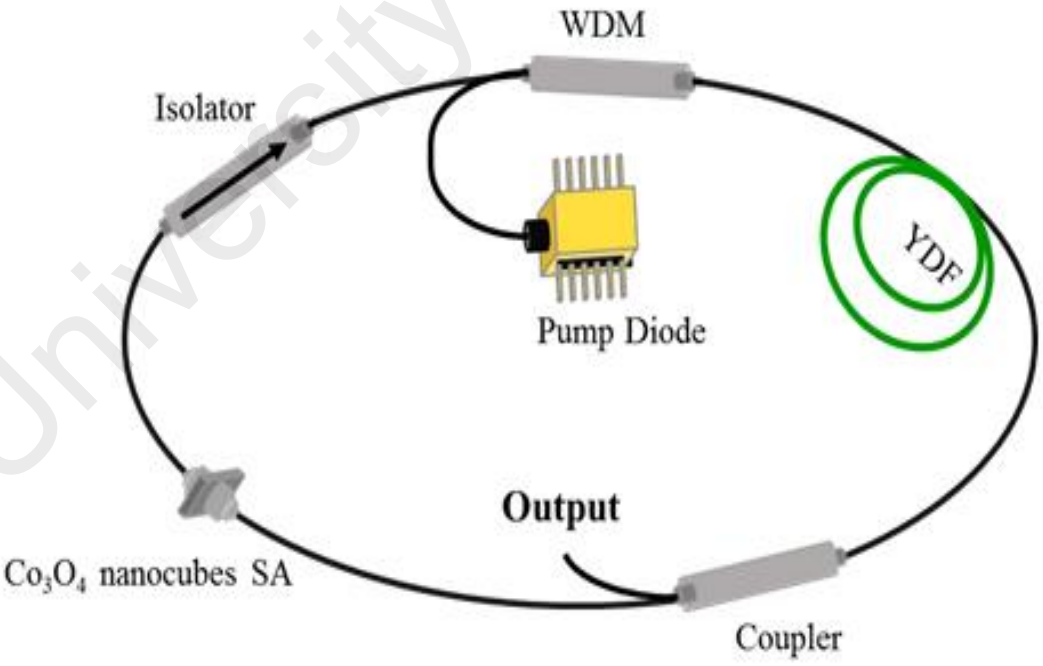

Figure 6.13: The employment of Co_3O_4 nanocubes film based SA for generating Q-switching and mode-locking pulses trains in YDFL cavity. Q-switched and mode-locked lasers employ 50/50 and 90/10 output coupler, respectively

6.3.3 Q-Switching Performance of the Co_3O_4 based YDFL

In this experiment, a self-starting Q-switching pulse was generated in the Co_3O_4 based YDFL cavity at threshold pump power of 144.4 mW. Figure 6.14 shows the optical spectrum of the proposal Q-switched YDFL at the threshold pump power. As shown in the figure, the spectrum centered at wavelength of 1043.64 nm with bandwidth of 0.24 nm. The stable Q-switching pulse trains were maintained up to the pump power of 165.4 mW. The pulses became unstable as the pump power further increased. Figure 6.15 (a)-(c) shows the Q-switching pulse trains with no timing jitter noticeable and its typical pulse envelope at three different pump powers of 144.4, 155, 165.4 mW. The pulse train has the repetition rates of 60.3, 78.13, and 86.66 kHz, which corresponds to the periods of 16.6, 12.8, and 11.5 µs at pump powers of 144.4, 155, 165.4 mW, respectively. The single pulse profile has the symmetrical Gaussian-like shape with full-width half maximum (FWHM) of 4.4, 5, and 4.6 µs at the same three different pump powers, respectively.

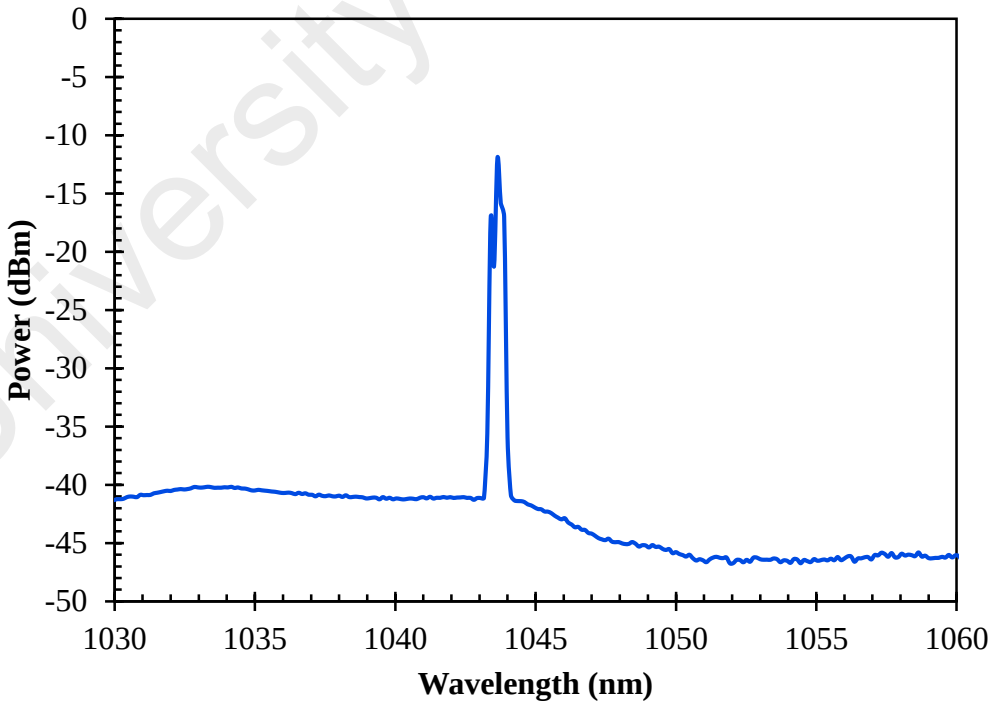

Figure 6.14: Output spectrum of the proposed Q-switched YDFL with Cobalt SA at the threshold pump power of 144.4 mW

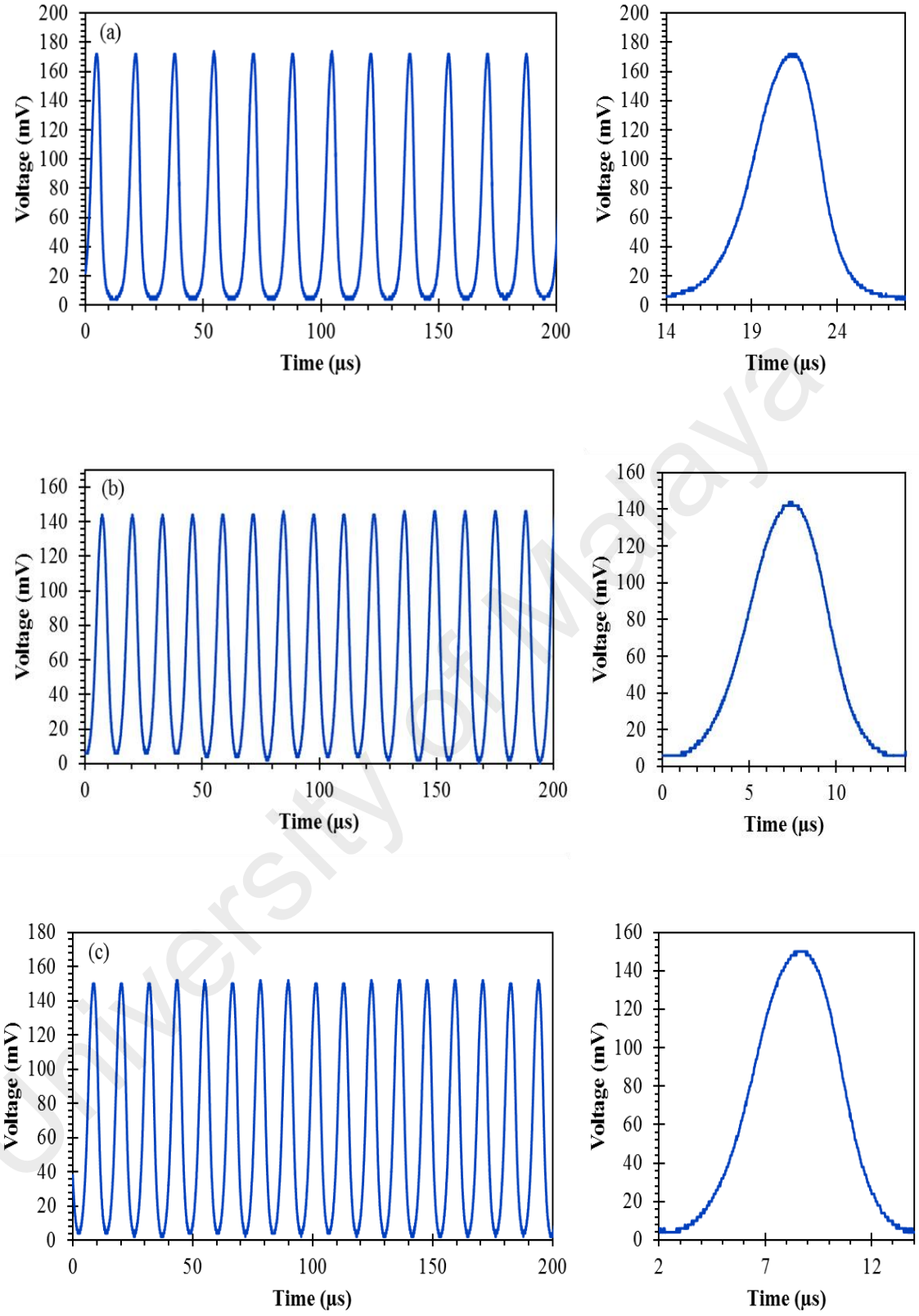

Figure 6.15: Q-switched YDF of pulse train and single-pulse envelope at different pump powers (a) 144.4 mW (repetition rate of 60.3 kHz), (b) 155 mW (repetition rate of 78.13 kHz), and (c) 165.4 mW (repetition rate of 86.66 kHz)

Figure 6.16 shows the characteristics of repetition rate and output power at various 980 nm pump power. Both repetition rate and output power increases with the pump power as shown at the same figure. The pulse repetition rate increases from 60.3 to 86.66 kHz as the pump power is varied from 144.4 to 165.4 mW, which confirm the Q-switching operation of the laser. The repetition rate of Q-switching pulse is able to change due to the lifetime of gain medium and the pump power. On the other hand, the output power linearly increases from 8.9 to 13.2 mW as the pump power is increased from 144.4 to 165.4 mW. This can be related to the ytterbium ion in the gain medium, which excite more electrons to the higher level with more pump power. The Co_3O_4 nanocubes film SA is saturated faster with higher pump power and thus increases the repetition rate.

Figure 6.17 shows the pulse width and pulse energy as function of pump power. It is observed that both pulse width and pulse energy are almost unchanged as the pump power is increased from 144.4 to 165.4 mW. The pulse width fluctuates within 4 to 5.16 μs with the shortest pulse width is obtained at 147.9 mW pump. The maximum pulse energy of 154 nJ is achieved at pump power of 147.9 mW. The pulse energy could be improved by reducing the insertion loss of the SA or by optimizing the laser cavity. As the pump power increases, the non-radiative decay rate of the Yb^{3+} ions also increases. This generates heat in the laser cavity system, which it's absorbed by the SA. This will energize some electrons in the SA's valance band to move up to the conduction band from the strong internal thermal motion. As fewer electrons in the valence band are available for photon absorption, the initial transmittance of the SA becomes greater as the pump power or the levels of absorber heat increases. Thus, the SA's efficiency as SA is greatly reduced, meaning that the pulse width begins to increase again after the saturation of SA. The pulse started to disappear at higher pumping of 165.4 mW due to the SA, which is continuously in the saturated state.

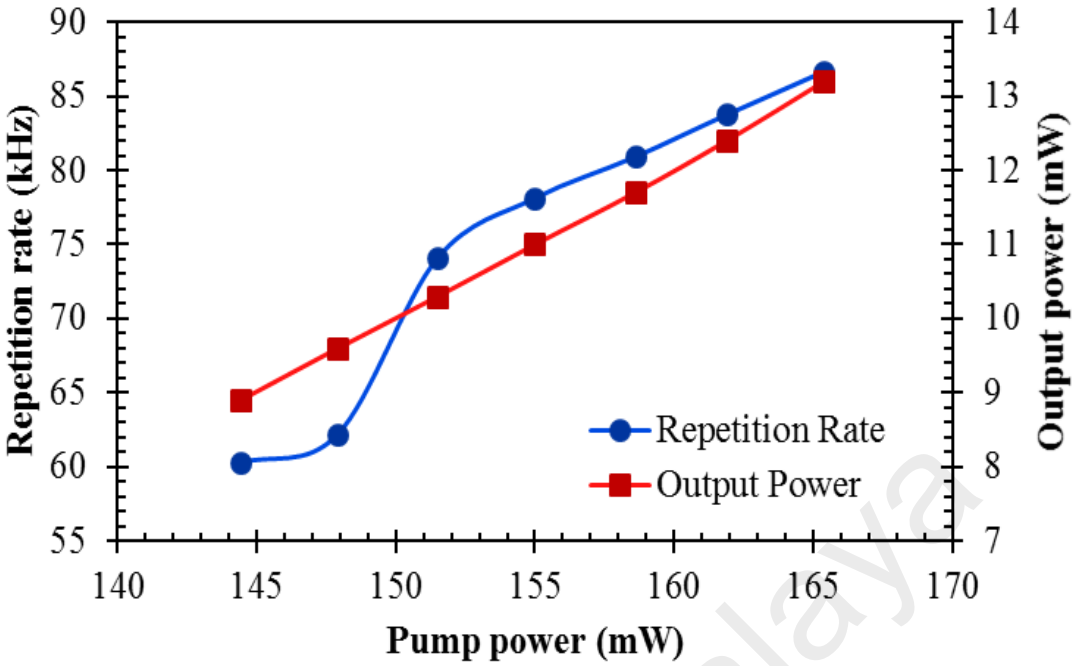

Figure 6.16: The characteristics of repetition rate and output power at various pump power

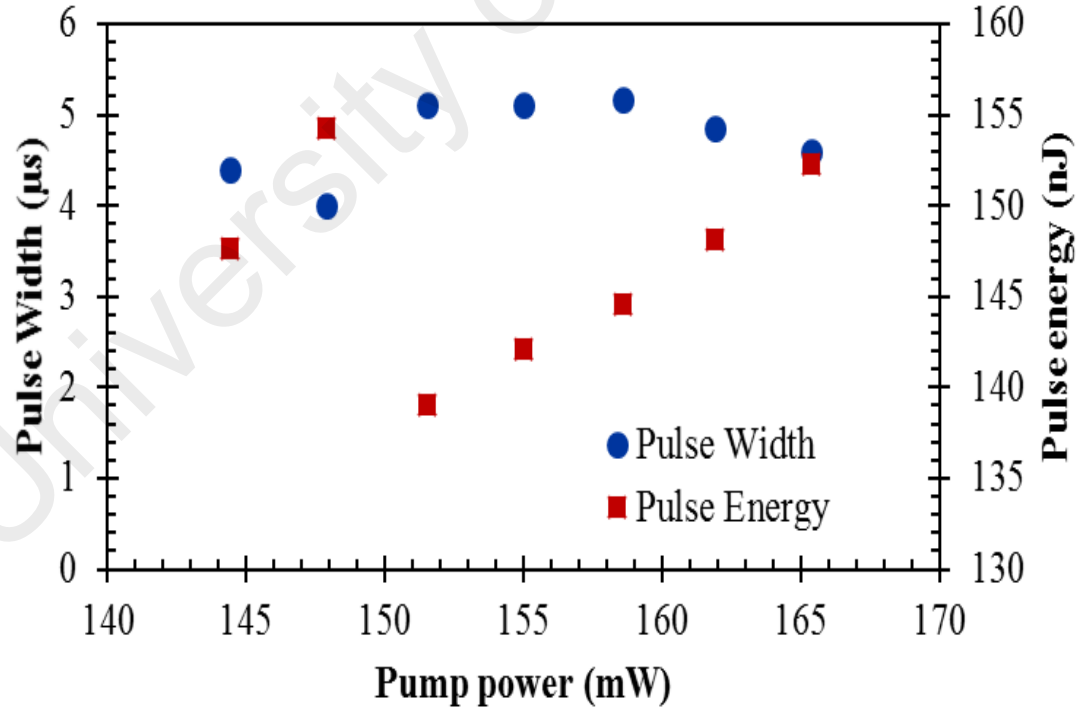

Figure 6.17: The characteristics of pulse width and pulse energy at various pump power

6.3.4 Mode-locking Performance of the Co_3O_4 based YDFL

For the YDFL cavity with 90/10 output coupler, the laser started to laser in CW mode at the threshold pump power of 117 mW. As the pump power was increased gradually to 123.7 mW, the self-starting mode-locking was achieved and its operation was maintained up to 186 mW pump power. The generation of mode-locking pulses was completely depended on the SA optical properties and suitable cavity length. Figure 6.18 (a) shows the output spectrum of the mode-locked YDFL at pump power of 186 mW. It operates at center wavelength of 1035.8 nm with a 3dB spectral bandwidth of 0.32 nm. There was no Kelly sideband observed in the spectrum, which confirmed the normal dispersion operation of the mode-locked laser. The narrow spectral bandwidth was due to the high net cavity dispersion and minimal nonlinearity induced by the high pump power (Sathiyan et al., 2016).

The typical oscilloscope trace of the proposed mode-locked YDFL is shown in Figure 6.18 (b). It is shown that the measured repetition rate of the pulse is approximately 20 MHz, which is matched with the cavity length of 10 m and the pulse period (peak to peak space) of 51 ns. The oscilloscope trace displays a 24 ns pulse width. But, due to the limitation of the oscilloscope resolution, the actual pulse width is much smaller than the value. Since an auto-correlator was not available for 1μm, the actual pulse width was estimated based on mathematical calculation. Assuming the pulse shape follows the Gaussian profile, the TBP should be 0.441 (Hisyam et al., 2017), thus the minimum possible pulse width was estimated to be approximately 4.93 ps. Figure 6.18 (c) shows the RF spectrum for the mode-locked YDFL which showing two modes within 50 MHz frequency range. The SNR of the fundamental frequency was 37 dB, which indicates the stability of the mode-locking pulses.

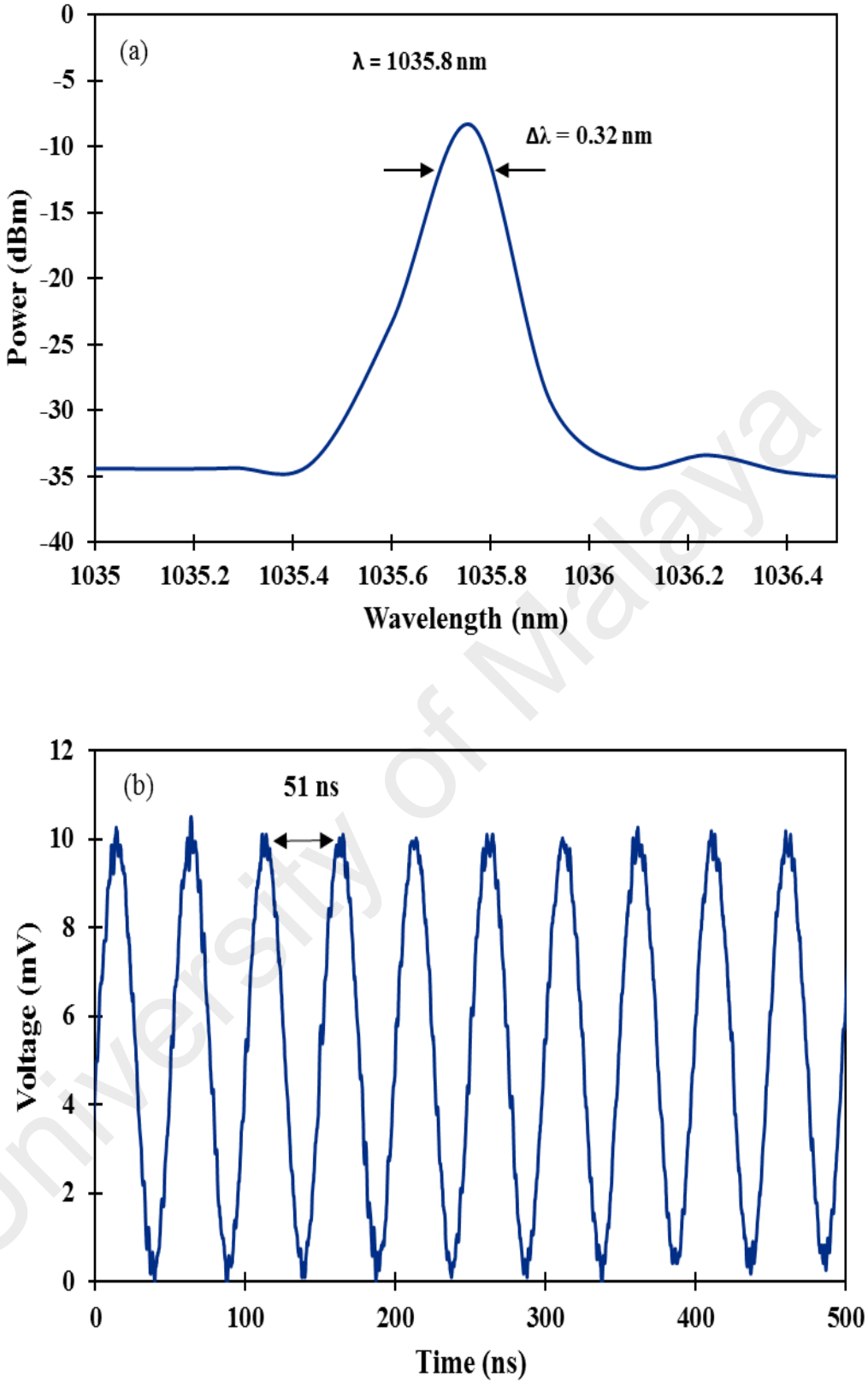

Figure 6.18: Mode-locking performance of the Co_3O_4 based YDFL (a) The optical spectrum, (b) pulse train (insert the image of single-envelope pulse) and (c) the RF spectrum, at the maximum pump power of 186 mW

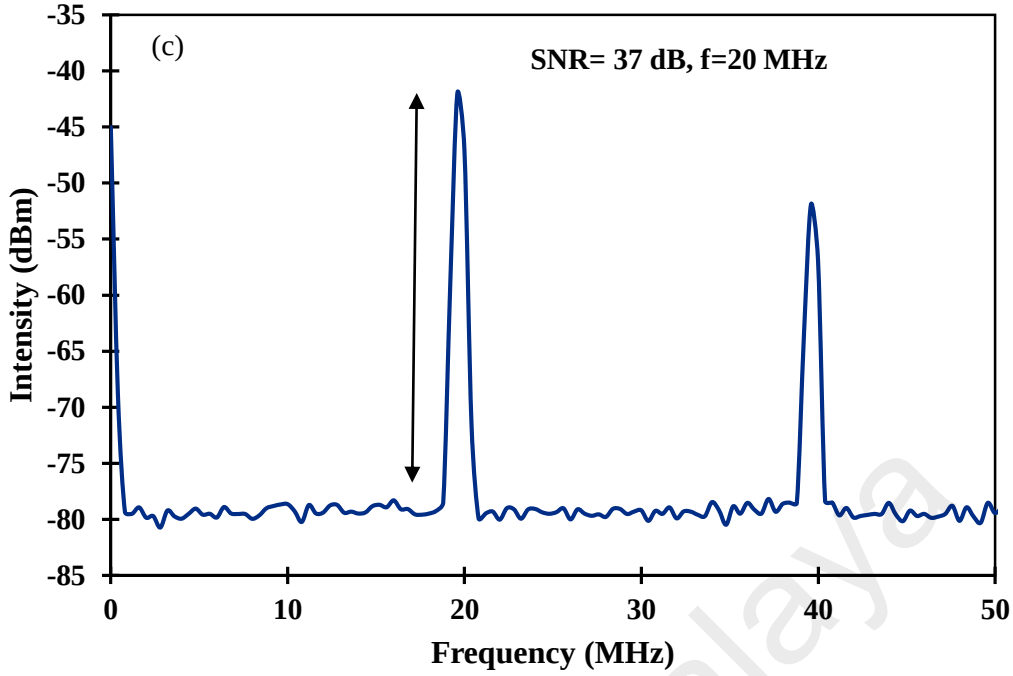

Figure 6.18, continued

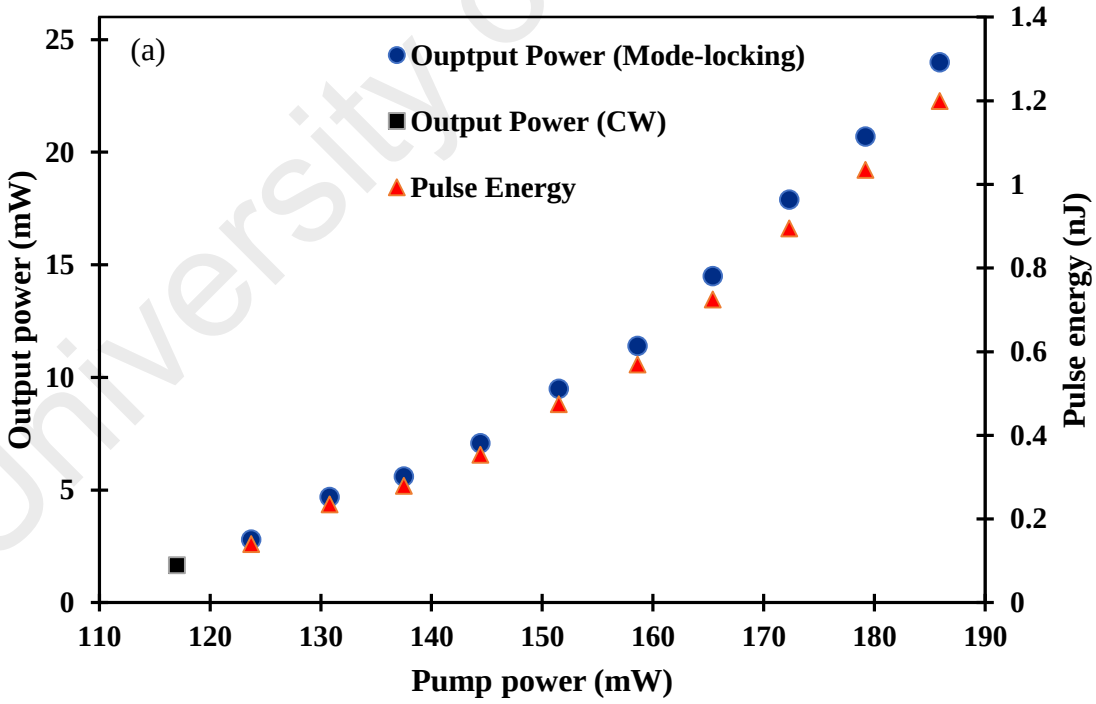

Figure 6.19: (a) Output power and pulse energy, and (b) Peak power against the pump power

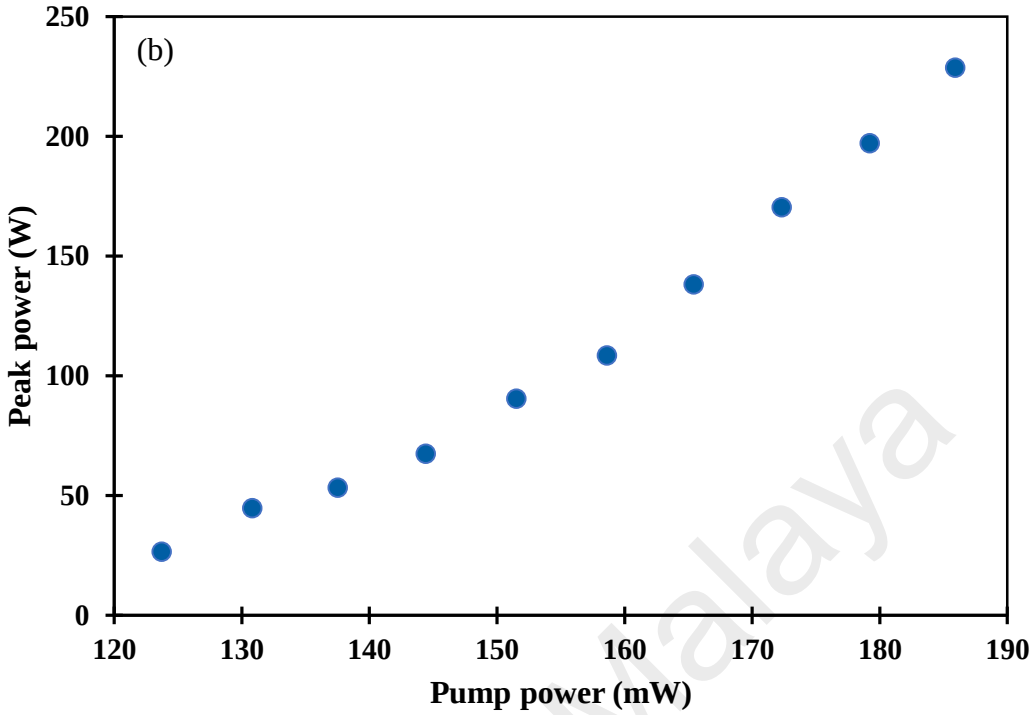

Figure 6.19, continued

Figure 6.19 shows the output power, pulse energy, and the peak power against pump powers. All the output power, pulse energy and peak power show an increasing trend with the pump power. The first lasing was a continuous wave, which its output power was approximately 1.67 mW at pump power of 117 mW. The CW laser was converted into a mode-locked laser at pump power of 123.7 mW. The output power was linearly increased from 2.8 to 24 mW when the pump power increased from 123.7 to 186 mW as shown in Figure 6.19 (a). The maximum pulse energy and peak power are approximated 1.2 nJ and 228.7 W at 186 mW pump power shown in Figures 6.19 (a) and (b), respectively. It is worthy to note that the mode-locking pulses train disappears when the pump power is increased above 186 mW. This is due to the SA, which continuously stay in the saturated state because of the high intensity of light.

6.4 Summary

Passive Q-switched and mode-locked YDFLs were successfully demonstrated based on two types of metal oxide nanomaterials; NiO nanoparticles and Co_3O_4 nanocubes thin film SAs. With NiO nanoparticles film SA, a stable self-starting Q-switched laser was achieved in the YDFL cavity configured with 1.5m long YDF as the pump power is increased above 117.73 mW. The pulses have the maximum pulse energy of 478 nJ, shortest pulse duration of 10.18 μs and repetition rates are tunable from 9.5 to 15.8 kHz. It is also found that the mode-locking pulses can be realized in the cavity by changing the output coupler to 90/10 coupler instead of 3 dB coupler. The mode-locking pulses train was obtained at pump power range from 97.3 mW to 137.5 mW. The mode-locked laser operated at 1037.72 nm wavelength with a fixed repetition rate of 23 MHz and picoseconds pulse width. The maximum pulse energy and peak power were calculated to be around 0.56 nJ and 26.4 W, respectively at 137.5 mW pump power.

Stable Q-switched and mode-locked YDFLs were realized with Co_3O_4 nanocubes SA, which was obtained by embedding the nanocubes into PEO film. The Q-switched laser operated at 1043.64 nm wavelength with the pulse repetition rate obtained varies from 60.3 to 86.66 kHz by increasing the pump power from 144.4 to 165.4 mW. The shortest pulse width and highest pulse energy were 4 μs and 154 nJ, respectively. The mode-locked Co_3O_4 based YDFL was also realized within a pump power range from 123.7 mW to 186 mW by utilizing a 90/10 output coupler inside the cavity. The mode-locked laser operated at 1035.8 nm wavelength with a fixed repetition rate of 20 MHz and picoseconds pulse width. The maximum pulse energy and output power were calculated to be around 1.2 nJ and 24 mW, respectively at 186 mW pump power. These results show that both NiO nanoparticles and Co_3O_4 nanocubes nanomaterials can be engaged for Q-switched and mode-locked fiber laser applications in 1 μm wavelength region.

CHAPTER 7: CONCLUSION AND FUTURE WORKS

7.1 Conclusions

Fiber laser has a broad range of applications ranging from industry to optical communication. Pulsed fiber laser with high peak intensity and high pulse energy is suitable for micromachining and drilling which benefits the medical, electronic and automotive industry because of its simplicity and compactness. Lasers use the quantum impact of excited emission to produce light and they are constructed based on the following elements; an active medium as a gain provider, a pumping source to produce the energy and an optical cavity to reinforce and control the optical field. Ytterbium-doped fiber laser (YDFL) is the most efficient fiber lasers used as a laser active dopant in the form of the trivalent ion Yb^{3+} to generate laser in 1 micron region., which has many applications in various areas. The Ytterbium-doped fiber (YDF) is an attractive gain medium since it has a simple energy level structure, high reliability, compact and the lasing wavelength at 1 μm, within the low-loss of optical laser as well as it is capable for producing high output power.

Q-switched or mode-locked fiber lasers can be generated by either active or passive techniques. The active technique is usually required an additional switching electronics device such as acousto-optic modulators to be incorporated in the laser cavity. Compared with active technique, passive technique is preferable for generation Q-switching and mode-locking pulse in fiber laser due to their advantages such as nature being compact, low cost, flexibility and easy to setup. Passive technique is normally demonstrated by utilizing saturable absorption of optical materials. The main objectives of this research work was to fabricate and demonstrate an efficient and low-cost Q-switched and mode-locked YDFLs operating in 1 μm region by utilizing new nanomaterials as SA.

In the chapter 3, molybdenum disulfide (MoS_2) was proposed as SA for generating Q-switched and mode-locked pulses train in YDFL cavity. MoS_2 is drawing more interest for Q-switching and mode-locked fiber lasers applications. The reason for this growing interest is due to its material's thickness, which gives an excellent optical laser properties as well as the band-gap. The passively Q-switched YDFL was demonstrated by using a few layer MoS_2, which was mechanically exfoliated from a natural MoS_2 crystal. The mechanical exfoliation was done by using a scotch tape and the acquired MoS_2 layers was sandwiched between two fiber ferrules to form a fiber compatible Q-switcher. By introducing the MoS_2 SA into the YDFL cavity, a stable pulse laser is generated at 1070.2 nm wavelength with repetition rate is tunable from 3.817 to 25.25 kHz. A passively mode-locked YDFL was also demonstrated using a MoS_2 polymer film which was prepared using liquid phase exfoliation approach as a SA. The laser was successfully generating a mode-locking pulses with repetition rate of 18.8 MHz and pulse energy of 0.1 nJ. The LPE method was simple, cheap and does not require any complicated procedures.

In chapter 4, another 2D material: Black phosphorus (BP) is proposed as new SA for operation at 1 micron region. Both Q-switching and mode-locking operations were demonstrated using a YDF as a gain medium. BP dubbed as the newly emerging allotrope, has gained much attention for potential applications in the next-generation optoelectronics devices such as sensor, field-effect transistors and solar cells. The BP comprises only the elemental "phosphorus" and thus it could be easily peeled off by mechanical exfoliation. At first, a Q-switched YDFL was obtained by using a multi-layer BP SA, which was prepared by fixing the BP material onto a sticky tape using a mechanical exfoliation technique. The laser has a pump threshold of 55.1 mW, a pulse repetition rate that was tunable from 8.2 to 32.9 kHz, and the narrowest pulse width of 10.8 µs. The highest pulse energy of 328 nJ was achieved at the pump power of 97.6 mW. In mode-locking experiment, the BP SA was prepared using a slightly different method

to reduce the device loss and thus enable the mode-locking operation. The SA was prepared by mechanically exfoliation of the BP crystal and fixed the acquired flakes onto the end surface of a standard FC/PC fiber connector. By incorporating the BP SA into the YDF laser cavity, a stable mode-locked operation was obtained at 1033.76 nm wavelength and the repetition rate was 10 MHz. These experimental results indicate that the BP SA can be used successfully to generate stable Q-switching and mode-locking pulses train at 1 μm region.

In chapter 5, passively Q-switched YDFLs were demonstrated using a few-layers Bi_2Se_3, Bi_2Te_3 and antimony telluride (Sb_2Te_3) based SAs while mode-locked YDFL was demonstrated using Sb_2Te_3 material to exploit the wideband saturable-absorption characteristic of the Topological insulators (TIs). TIs have attracted attention of researchers due to their high nonlinear susceptibility and large modulation depth with efficient saturable absorption property. They are excellent semiconductors with high surface electron mobility. For this purpose, free-standing Bi_2Se_3-, Bi_2Te_3- and Sb_2Te_3-polymer composite SA films were prepared by implanting the powder of these materials into a polyvinyl alcohol (PVA) host. These films are used in a fully fiber-integrated laser cavity for generating pulses train.

Using Bi_2Se_3 saturable absorber, the Q-switched YDFL obtains a stable train of pulses with a repetition rate frequency that is tunable from 48.83 to 102 kH while the corresponding pulse width decreases from 8.9 to 3.48 μs as the pump power increases from 67.6 to 88.3 mW. For the Bi_2Te_3 based Q-switched YDFL, the repetition rate grows from 43.25 to 93.63 kHz and the pulse width shrinks from 5.65 to 2.01 μs as the 980nm pump power rises from 72.8 to 98.4 mW. The Sb_2Te_3 film based Q-switched YDFL produced pulse repetition rate, which is increased from 24.4 to 55 kHz as the pump power increases from 75.4 to 96.2 mW. The pulse energy was around 252.6 nJ at 82.3 mW pump

power, which is significantly higher than both Bi_2Se_3 and Bi_2Te_3 based Q-switched lasers. On the other hand, the mode-locking pulses was also successfully achieved with Bi_2Te_3 SA. It operates at 24.2 MHz repetition and 18.8 ps pulse width within the pump power between 47.8 to 89.4 mW. The maximum pulse energy was calculated to be around 0.8 nJ at at 89.4 mW pump power.

Two types of transition metal oxide nanomaterials were also explored as SA for Q-switching and mode-locking operations in YDFL cavity as described in Chapter 6. These materials were Nickel Oxide (NiO) and cobalt oxide (Co_3O_4), which were embedded into a polymer film to realize Q-switching and mode-locking pulses operating in 1 μm region. With NiO nanoparticles film SA, a stable self-starting Q-switched laser was achieved with the maximum pulse energy of 478 nJ, shortest pulse duration of 10.18 μs and repetition rates were tunable from 9.5 to 15.8 kHz. It is also found that the mode-locking pulses can be realized in the cavity by changing the output coupler to 90/10 coupler instead of 3 dB coupler. The mode-locked laser operated at 1037.72 nm wavelength with a fixed repetition rate of 23 MHz and picoseconds pulse width. Stable Q-switched and mode-locked YDFLs were realized with Co3O4 nanocubes SA. The Q-switched laser operated at 1043.64 nm wavelength with the pulse repetition rate obtained varies from 60.3 to 86.66 kHz by increasing the pump power from 144.4 to 165.4 mW. The mode-locked Co3O4 based YDFL was also realized within a pump power range from 123.7 mW to 186 mW by utilizing a 90/10 output coupler inside the cavity. The mode-locked laser operated at 1035.8 nm wavelength with a fixed repetition rate of 20 MHz and picoseconds pulse width.

Table 7.1: Summary of the SAs performances.

Q-switching					
SA	Repetition rate (kHz)	Min pulse duration (μs)	Max pulse energy (nJ)	Modulation depth (%)	Saturation intensity (MW/cm^2)
MoS_2	3.817-25.25	11.33	295.45	11.3	23.5
BP	8.1-32.9	10.8	328	7	0.0025
Bi_2Se_3	48.83-102	3.48	16.6	15.9	50
Bi_2Te_3	72.8-98.4	2.01	29.95	30	40
Sb_2Te_3	24.4-55	6.6	252.6	8.5	36
NiO NPs	9.5-15.8	10.18	478	39	0.04
Co_3O_4 nanocubes	60.3-86.66	4	154	0.35	3
Mode-locking					
SA	Repetition rate (MHz)	Pulse duration (ps)	Max pulse energy (nJ)	Modulation depth (%)	Saturation intensity (MW/cm^2)
MoS_2-PVA	18.8	28.3	0.1	9.7	40
BP	10	3.27	2.7	7.5	0.35
Sb_2Te_3	24.2	18.8	0.8	8.5	36
NiO NPs	23	19.8	0.56	39	0.04
Co_3O_4 nanocubes	20	4.93	1.2	0.35	3

In conclusion, several types of nanomaterials based SAs such as, Molybdenum disulfide (MoS_2), Black Phosphorus (BP), Topological Insulator (TI), Nickle Oxide (NiO) nanoparticles, and Cobalt oxide (Co_3O_4) nanocubes have been fabricated and characterized. It is obtained that all the fabricated SAs are capable to operate in YDFL cavity for generating Q-switching pulses with high energy. The generation of the mode-locking pulses in YDFL cavity have also been obtained using the fabricated nanomaterials as SA. These nanomaterials based SA could be useful as a simple, low cost, and low-loss

for operation in 1 μm region. Table 7.1 summarizes the performances of those SAs. Each SA has different laser performance and this laser performance can be applied for specific application based on pulse width, pulse energy and peak power. From the summary table we can see that BP produced shorter pulse width, where NiO has higher pulse energy.

7.2 Future Works

This section provides diverse interesting directions for the future work. The future work should focus on exploring the applications of the developed SAs in other wavelength regions such as 1.5, 2 and 3.5 micron using an Erbium-doped fiber (EDF), thulium-doped fiber and ZBLAN EDF as the gain medium, respectively. Further work should also focus on improving the current 1 μm region lasing characteristics and ultra-short pulse generation. The performance of Q-switching and mode-locking pulses state can also be realized and improved by using other types of nanomaterials such as gold, and silver nanoparticles as SAs. The mode-locking pulse generation can also be improved by utilizing more laser configurations with a better controlling of cavity nonlinear effect and dispersion. The main focus of investigation is by replacing the gain medium with higher dopant active fiber that can keep a high gain per length of the lasers. The other key focus for future work is to investigate a dual wavelength or multi-wavelengths pulse fiber laser using a special configuration such as adding PCF or side-polished fiber into the laser cavity. For example, Q-switched multi-wavelength fiber laser maintains good possibility applications such as optoelectronics, sensors, communications and instrumentations.

REFERENCES

Abbas, A. N., Liu, B., Chen, L., Ma, Y., Cong, S., Aroonyadet, N., . . . Zhou, C. (2015). Black Phosphorus Gas Sensors. *ACS nano, 9*(5), 5618-5624. doi:10.1021/acsnano.5b01961

Agrawal, G. P., & Dutta, N. K. (1986). Long wavelength semiconductor lasers.

Ahmad, H., Lee, C., Ismail, M., Ali, Z., Reduan, S., Ruslan, N., . . . Harun, S. (2016). Zinc oxide (ZnO) nanoparticles as saturable absorber in passively Q-switched fiber laser. *Optics Communications, 381*, 72-76.

Ahmad, H., Reduan, S. A., Ali, Z. A., Ismail, M., Ruslan, N., Lee, C., . . . Harun, S. (2016). C-Band Q-Switched Fiber Laser Using Titanium Dioxide (TiO 2) As Saturable Absorber. *IEEE Photonics Journal, 8*(1), 1-7.

Ahmad, H., Salim, M. A. M., Thambiratnam, K., Norizan, S. F., & Harun, S. (2016). A black phosphorus-based tunable Q-switched ytterbium fiber laser. *Laser Physics Letters, 13*(9), 095103.

Ahmad, H., Soltanian, M., Narimani, L., Amiri, I., Khodaei, A., & Harun, S. (2015). Tunable s-band q-switched fiber laser using Bi 2 Se 3 as the saturable absorber. *IEEE Photonics Journal, 7*(3), 1-8.

Ahmed, M., Ali, N., Salleh, Z., Rahman, A., Harun, S., Manaf, M., & Arof, H. (2014). All fiber mode-locked Erbium-doped fiber laser using single-walled carbon nanotubes embedded into polyvinyl alcohol film as saturable absorber. *Optics & Laser Technology, 62*, 40-43.

Ahmed, M., Ali, N., Salleh, Z., Rahman, A., Harun, S., Manaf, M., & Arof, H. (2015). Q-switched erbium doped fiber laser based on single and multiple walled carbon nanotubes embedded in polyethylene oxide film as saturable absorber. *Optics & Laser Technology, 65*, 25-28.

Ahmed, M., Latiff, A., Arof, H., Ahmad, H., & Harun, S. (2016). Femtosecond mode-locked erbium-doped fiber laser based on MoS 2–PVA saturable absorber. *Optics & Laser Technology, 82*, 145-149.

Ahmed, M., Latiff, A., Arof, H., & Harun, S. (2016). Ultrafast erbium-doped fiber laser mode-locked with a black phosphorus saturable absorber. *Laser Physics Letters, 13*(9), 095104.

Ahmed, M. H. M., Latiff, A. A., Arof, H., Ahmad, H., & Harun, S. W. (2016). Soliton mode-locked erbium-doped fibre laser with mechanically exfoliated molybdenum disulphide saturable absorber. *IET Optoelectronics, 10*(5), 169-173.

Akulov, V., Afanasiev, D., Babin, S., Churkin, D., Kablukov, S., Rybakov, M., & Vlasov, A. (2007). Frequency tuning and doubling in Yb-doped fiber lasers. *Laser Physics, 17*(2), 124-129.

Al-Masoodi, A., Ahmad, F., Ahmad, H., & Harun, S. (2015). Q-Switched Yb-doped fiber ring laser with a saturable absorber based on a graphene polyvinyl alcohol film. *Journal of Russian Laser Research, 36*(4), 389-394.

Al-Masoodi, A., Ismail, M., Ahmad, F., Kasim, N., Munajat, Y., Ahmad, H., & Wadi Harun, S. (2014). Q-switched Yb-doped fiber laser operating at 1073 nm using a

carbon nanotubes saturable absorber. *Microwave and Optical Technology Letters, 56*(8), 1770-1773.

Alagiri, M., Ponnusamy, S., & Muthamizhchelvan, C. (2012). Synthesis and characterization of NiO nanoparticles by sol–gel method. *Journal of Materials Science: Materials in Electronics, 23*(3), 728-732.

Ando, M., Kadono, K., Kamada, K., & Ohta, K. (2004). Third-order nonlinear optical responses of nanoparticulate Co 3 O 4 films. *Thin Solid Films, 446*(2), 271-276.

Andres, C.-G., Leonardo, V., Elsa, P., Joshua, O. I., Narasimha-Acharya, K. L., Sofya, I. B., . . . Herre, S. J. v. d. Z. (2014). Isolation and characterization of few-layer black phosphorus. *2D Materials, 1*(2), 025001.

Anwar, S., Anwar, S., & Mishra, B. K. (2014). Synthesis and Characterization of Bismuth Selenide Thin Films by Chemical Bath Deposition Technique. *Advanced Science Letters, 20*(3-4), 854-856.

Aslani, A., Oroojpour, V., & Fallahi, M. (2011). Sonochemical synthesis, size controlling and gas sensing properties of NiO nanoparticles. *Applied Surface Science, 257*(9), 4056-4061.

Bao, Q., Zhang, H., Ni, Z., Wang, Y., Polavarapu, L., Shen, Z., . . . Loh, K. P. (2011). Monolayer graphene as a saturable absorber in a mode-locked laser. *Nano Research, 4*(3), 297-307.

Bao, Q., Zhang, H., Wang, Y., Ni, Z., Yan, Y., Shen, Z. X., . . . Tang, D. Y. (2009). Atomic-layer graphene as a saturable absorber for ultrafast pulsed lasers. *Advanced Functional Materials, 19*(19), 3077-3083.

Barreca, D., Massignan, C., Daolio, S., Fabrizio, M., Piccirillo, C., Armelao, L., & Tondello, E. (2001). Composition and microstructure of cobalt oxide thin films obtained from a novel cobalt (II) precursor by chemical vapor deposition. *Chemistry of Materials, 13*(2), 588-593.

Barua, P., Sekiya, E., Saito, K., & Ikushima, A. (2008). Influences of Yb 3+ ion concentration on the spectroscopic properties of silica glass. *Journal of Non-Crystalline Solids, 354*(42), 4760-4764.

Bello-Jiménez, M., Cuadrado-Laborde, C., Sáez-Rodríguez, D., Diez, A., Cruz, J., & Andrés, M. (2010). Actively mode-locked fiber ring laser by intermodal acousto-optic modulation. *Optics letters, 35*(22), 3781-3783.

Bogusławski, J., Soboń, G., Tarnowski, K., Zybała, R., Mars, K., Mikuła, A., . . . Sotor, J. (2016). All-polarization-maintaining-fiber laser Q-switched by evanescent field interaction with Sb2Te3 saturable absorber. *Optical Engineering, 55*(8), 081316-081316.

Bonaccorso, F., Zerbetto, M., Ferrari, A. C., & Amendola, V. (2013). Sorting nanoparticles by centrifugal fields in clean media. *The Journal of Physical Chemistry C, 117*(25), 13217-13229.

Boyd, R. W. (2003). *Nonlinear optics*: Academic press.

Cao, H., Venkatasubramanian, R., Liu, C., Pierce, J., Yang, H., Zahid Hasan, M., . . . Chen, Y. P. (2012). Topological insulator Bi2Te3 films synthesized by metal organic chemical vapor deposition. *Applied Physics Letters, 101*(16), 162104.

Castellanos-Gomez, A., Vicarelli, L., Prada, E., Island, J. O., Narasimha-Acharya, K., Blanter, S. I., . . . Alvarez, J. (2014). Isolation and characterization of few-layer black phosphorus. *2D Materials, 1*(2), 025001.

Cava, R. J., Ji, H., Fuccillo, M. K., Gibson, Q. D., & Hor, Y. S. (2013). Crystal structure and chemistry of topological insulators. *Journal of Materials Chemistry C, 1*(19), 3176-3189.

Chen, H.-R., Tsai, C.-Y., Cheng, H.-M., Lin, K.-H., & Hsieh, W.-F. (2014). Passive mode locking of ytterbium-and erbium-doped all-fiber lasers using graphene oxide saturable absorbers. *Optics express, 22*(11), 12880-12889.

Chen, L., Zhang, M., Zhou, C., Cai, Y., Ren, L., & Zhang, Z. (2009). *Ultra-low repetition rate SESAM-mode-locked linear-cavity erbium-doped fiber laser.* Paper presented at the Conference on Lasers and Electro-Optics/Pacific Rim.

Chen, X., Wu, Y., Wu, Z., Han, Y., Xu, S., Wang, L., . . . Cai, Y. (2015). High-quality sandwiched black phosphorus heterostructure and its quantum oscillations. *Nature communications, 6*, 7315.

Chen, Y., Zhao, C., Chen, S., Du, J., Tang, P., Jiang, G., . . . Tang, D. (2014). Large energy, wavelength widely tunable, topological insulator Q-switched erbium-doped fiber laser. *IEEE Journal of Selected Topics in Quantum Electronics, 20*(5), 315-322.

Chen, Y., Zhao, C., Huang, H., Chen, S., Tang, P., Wang, Z., . . . Tang, D. (2013). Self-assembled topological insulator: Bi $ _ {2} $ Se $ _ {3} $ membrane as a passive Q-switcher in an Erbium-doped fiber laser. *Journal of Lightwave Technology, 31*(17), 2857-2863.

Cheng, H., Dong, N., Bai, T., Song, Y., Wang, J., Qin, Y., . . . Chen, Y. (2016). Covalent Modification of MoS2 with Poly (N-vinylcarbazole) for Solid-State Broadband Optical Limiters. *Chemistry–A European Journal, 22*(13), 4500-4507.

Cheng, J., Zhao, B., Zhang, W., Shi, F., Zheng, G., Zhang, D., & Yang, J. (2015). High-Performance Supercapacitor Applications of NiO-Nanoparticle-Decorated Millimeter-Long Vertically Aligned Carbon Nanotube Arrays via an Effective Supercritical CO2-Assisted Method. *Advanced Functional Materials, 25*(47), 7381-7391.

Cho, W. B., Schmidt, A., Yim, J. H., Choi, S. Y., Lee, S., Rotermund, F., . . . Mateos, X. (2009). Passive mode-locking of a Tm-doped bulk laser near 2 μm using a carbon nanotube saturable absorber. *Optics express, 17*(13), 11007-11012.

Churchill, H. O., & Jarillo-Herrero, P. (2014). Two-dimensional crystals: Phosphorus joins the family. *Nature nanotechnology, 9*(5), 330-331.

Coleman, J. N., Lotya, M., O'Neill, A., Bergin, S. D., King, P. J., Khan, U., . . . Smith, R. J. (2011). Two-dimensional nanosheets produced by liquid exfoliation of layered materials. *Science, 331*(6017), 568-571.

Conley, H. J., Wang, B., Ziegler, J. I., Haglund Jr, R. F., Pantelides, S. T., & Bolotin, K. I. (2013). Bandgap engineering of strained monolayer and bilayer MoS2. *Nano letters, 13*(8), 3626-3630.

Cui, X., Zhang, C., Hao, R., & Hou, Y. (2011). Liquid-phase exfoliation, functionalization and applications of graphene. *Nanoscale, 3*(5), 2118-2126.

Cunningham, G., Lotya, M., Cucinotta, C. S., Sanvito, S., Bergin, S. D., Menzel, R., . . . Coleman, J. N. (2012). Solvent exfoliation of transition metal dichalcogenides: dispersibility of exfoliated nanosheets varies only weakly between compounds. *ACS nano, 6*(4), 3468-3480.

Dai, J., & Zeng, X. C. (2014). Bilayer Phosphorene: Effect of Stacking Order on Bandgap and Its Potential Applications in Thin-Film Solar Cells. *The Journal of Physical Chemistry Letters, 5*(7), 1289-1293. doi:10.1021/jz500409m

Dai, S., Sugiyama, A., Hu, L., Liu, Z., Huang, G., & Jiang, Z. (2002). The spectrum and laser properties of ytterbium doped phosphate glass at low temperature. *Journal of Non-Crystalline Solids, 311*(2), 138-144.

de Melo Jr, R. P., da Silva, B. J., dos Santos, F. E. P., Azevedo, A., & de Araújo, C. B. (2009). Nonlinear refraction properties of nickel oxide thin films at 800 nm. *Journal of Applied Physics, 106*(9), 093517.

De Tan, W., Tang, D., Xu, X., Zhang, J., Xu, C., Xu, F., . . . Xu, J. (2010). Passive femtosecond mode-locking and cw laser performance of Yb 3+: Sc 2 SiO 5. *Optics express, 18*(16), 16739-16744.

Della Valle, G., Osellame, R., Galzerano, G., Chiodo, N., Cerullo, G., Laporta, P., . . . Scardaci, V. (2006). Passive mode locking by carbon nanotubes in a femtosecond laser written waveguide laser. *Applied Physics Letters, 89*(23), 231115.

Dong, N., Li, Y., Feng, Y., Zhang, S., Zhang, X., Chang, C., . . . Wang, J. (2015). Optical limiting and theoretical modelling of layered transition metal dichalcogenide nanosheets. *Scientific reports, 5*.

Dou, Z., Song, Y., Tian, J., Liu, J., Yu, Z., & Fang, X. (2014). Mode-locked ytterbium-doped fiber laser based on topological insulator: Bi 2 Se 3. *Optics express, 22*(20), 24055-24061.

Du, J., Wang, Q., Jiang, G., Xu, C., Zhao, C., Xiang, Y., . . . Zhang, H. (2014). Ytterbium-doped fiber laser passively mode locked by few-layer Molybdenum Disulfide (MoS2) saturable absorber functioned with evanescent field interaction. *Scientific reports, 4*.

Duan, W., Lu, S., Wu, Z., & Wang, Y. (2012). Size effects on properties of NiO nanoparticles grown in alkalisalts. *The Journal of Physical Chemistry C, 116*(49), 26043-26051.

Duraisamy, N., Numan, A., Fatin, S. O., Ramesh, K., & Ramesh, S. (2016). Facile sonochemical synthesis of nanostructured NiO with different particle sizes and its electrochemical properties for supercapacitor application. *Journal of colloid and interface science, 471*, 136-144.

Eda, G., & Maier, S. A. (2013). Two-dimensional crystals: managing light for optoelectronics. *Acs Nano, 7*(7), 5660-5665.

Fasaki, I., Kandyla, M., & Kompitsas, M. (2012). Properties of pulsed laser deposited nanocomposite NiO: Au thin films for gas sensing applications. *Applied Physics A, 107*(4), 899-904.

Feng, C., Wang, H., Zhang, J., Hu, W., Zou, Z., & Deng, Y. (2014). One-pot facile synthesis of cobalt oxide nanocubes and their magnetic properties. *Journal of Nanoparticle Research, 16*(5), 2413.

Fu, B., Hua, Y., Xiao, X., Zhu, H., Sun, Z., & Yang, C. (2014). Broadband graphene saturable absorber for pulsed fiber lasers at 1, 1.5, and 2 μm. *IEEE Journal of selected topics in quantum electronics, 20*(5), 411-415.

Garmire, E. (2000). Resonant optical nonlinearities in semiconductors. *IEEE Journal of Selected Topics in Quantum Electronics, 6*(6), 1094-1110.

Garnov, S., Solokhin, S., Obraztsova, E., Lobach, A., Obraztsov, P., Chernov, A., . . . Zavartsev, Y. (2007). Passive mode-locking with carbon nanotube saturable absorber in Nd: GdVO4 and Nd: Y0. 9Gd0. 1VO4 lasers operating at 1.34 μm. *Laser Physics Letters, 4*(9), 648-651.

Ge, H., Zhao, S., Li, Y., Li, G., Li, D., Yang, K., . . . Yu, Z. (2009). Diode-pumped passively Q-switched mode-locked Nd: LuVO 4 laser with a semiconductor saturable absorber mirror. *Laser Physics, 19*(6), 1226-1229.

Glubokov, D. A. e., Sychev, V. V. e., Mikhailov, A. S., Korolkov, A. E. e., Chubich, D. A. e., Shapiro, B. I., & Vitukhnovskii, A. G. e. (2014). Saturable absorber based on silver nanoparticles for passively mode-locked lasers. *Quantum Electronics, 44*(4), 314.

Gomes, L. A., Orsila, L., Jouhti, T., & Okhotnikov, O. G. (2004). Picosecond SESAM-based ytterbium mode-locked fiber lasers. *IEEE Journal of Selected Topics in Quantum Electronics, 10*(1), 129-136.

Grelu, P., & Akhmediev, N. (2012). Dissipative solitons for mode-locked lasers. *Nature Photonics, 6*(2), 84-92.

Griffiths, D. J. (2016). *Introduction to quantum mechanics*: Cambridge University Press.

Guerreiro, P., Ten, S., Borrelli, N., Butty, J., Jabbour, G., & Peyghambarian, N. (1997). PbS quantum-dot doped glasses as saturable absorbers for mode locking of a Cr: forsterite laser. *Applied Physics Letters, 71*(12), 1595-1597.

Gupta, A., Arunachalam, V., & Vasudevan, S. (2016). Liquid-Phase Exfoliation of MoS2 Nanosheets: The Critical Role of Trace Water. *The journal of physical chemistry letters, 7*(23), 4884-4890.

Hakulinen, T., & Okhotnikov, O. G. (2007). 8 ns fiber laser Q switched by the resonant saturable absorber mirror. *Optics letters, 32*(18), 2677-2679.

Han, S., Zhang, F., Wang, M., Wang, L., Zhou, Y., Wang, Z., & Xu, X. (2017). Black phosphorus based saturable absorber for Nd-ion doped pulsed solid state laser operation. *Indian Journal of Physics, 91*(4), 439-443.

Haris, H., Harun, S., Muhammad, A., Anyi, C., Tan, S., Ahmad, F., . . . Arof, H. (2017). Passively Q-switched Erbium-doped and Ytterbium-doped fibre lasers with topological insulator bismuth selenide (Bi 2 Se 3) as saturable absorber. *Optics & Laser Technology, 88*, 121-127.

Harun, S., Ismail, M., Ahmad, F., Ismail, M., Nor, R., Zulkepely, N., & Ahmad, H. (2012). A Q-switched erbium-doped fiber laser with a carbon nanotube based saturable absorber. *Chinese Physics Letters, 29*(11), 114202.

Harun, S. W., Ismail, M. A., Ahmad, F., Ismail, M. F., Nor, R. M., Zulkepely, N. R., & Ahmad, H. (2012). A Q-Switched Erbium-Doped Fiber Laser with a Carbon Nanotube Based Saturable Absorber. *Chinese Physics Letters, 29*(11), 114202.

Hasan, T., Torrisi, F., Sun, Z., Popa, D., Nicolosi, V., Privitera, G., . . . Ferrari, A. (2010). Solution-phase exfoliation of graphite for ultrafast photonics. *physica status solidi (b), 247*(11-12), 2953-2957.

He, T., Chen, D., & Jiao, X. (2004). Controlled synthesis of Co3O4 nanoparticles through oriented aggregation. *Chemistry of Materials, 16*(4), 737-743.

Heinz, K., & Hammer, L. (2013). Epitaxial cobalt oxide films on Ir (100)—the importance of crystallographic analyses. *Journal of Physics: Condensed Matter, 25*(17), 173001.

Hisyam, M. B., Rusdi, M. F. M., Latiff, A. A., & Harun, S. W. (2017). Generation of Mode-Locked Ytterbium Doped Fiber Ring Laser Using Few-Layer Black Phosphorus as a Saturable Absorber. *IEEE Journal of Selected Topics in Quantum Electronics, 23*(1), 39-43.

Hong, S. S., Kundhikanjana, W., Cha, J. J., Lai, K., Kong, D., Meister, S., . . . Cui, Y. (2010). Ultrathin topological insulator Bi2Se3 nanoribbons exfoliated by atomic force microscopy. *Nano letters, 10*(8), 3118-3122.

Huang, S., Wang, Y., Yan, P., Zhao, J., Li, H., & Lin, R. (2014). Tunable and switchable multi-wavelength dissipative soliton generation in a graphene oxide mode-locked Yb-doped fiber laser. *Optics express, 22*(10), 11417-11426.

Ippen, E., Shank, C., & Dienes, A. (1972). Passive mode locking of the cw dye laser. *Applied Physics Letters, 21*(8), 348-350.

Ismail, M., Ahmad, F., Harun, S., Arof, H., & Ahmad, H. (2013). A Q-switched erbium-doped fiber laser with a graphene saturable absorber. *Laser Physics Letters, 10*(2), 025102.

Jawaid, A., Nepal, D., Park, K., Jespersen, M., Qualley, A., Mirau, P., . . . Vaia, R. A. (2015). Mechanism for liquid phase exfoliation of MoS2. *Chemistry of Materials, 28*(1), 337-348.

Jiang, C., Jiu, H., Zeng, Q., Wang, Y., Zhang, J., & Gan, F. (2000). Stark Energy Split Characteristics of ytterbium ion in glasses. *Rare-Earth-Doped Materials and Devices IV, 4*.

Jiang, T., Kang, Z., Qin, G., Zhou, J., & Qin, W. (2013). Low mode-locking threshold induced by surface plasmon field enhancement of gold nanoparticles. *Optics express, 21*(23), 27992-28000.

Johal, S. K. (2013). Chemical Exfoliation of graphene and other 2D-materials.

Kambe, T., Sakamoto, R., Kusamoto, T., Pal, T., Fukui, N., Hoshiko, K., . . . Ishizaka, K. (2014). Redox control and high conductivity of nickel bis (dithiolene) complex π-nanosheet: a potential organic two-dimensional topological insulator. *Journal of the American Chemical Society, 136*(41), 14357-14360.

Kang, M., & Zhou, H. (2015). Facile synthesis and structural characterization of Co 3 O 4 nanocubes. *AIMS Mater. Sci, 2*, 16-27.

Kashiwagi, K., & Yamashita, S. (2010). Optical deposition of carbon nanotubes for fiber-based device fabrication *Frontiers in Guided Wave Optics and Optoelectronics*: InTech.

Kasim, N., Al-Masoodi, A., Ahmad, F., Munajat, Y., Ahmad, H., & Harun, S. (2014). Q-switched ytterbium doped fiber laser using multi-walled carbon nanotubes saturable absorber. *Chinese Optics Letters, 12*(3), 031403.

Keller, U., Miller, D., Boyd, G., Chiu, T., Ferguson, J., & Asom, M. (1992). Solid-state low-loss intracavity saturable absorber for Nd: YLF lasers: an antiresonant semiconductor Fabry–Perot saturable absorber. *Optics letters, 17*(7), 505-507.

Keller, U., Weingarten, K. J., Kartner, F. X., Kopf, D., Braun, B., Jung, I. D., . . . Au, J. A. d. (1996). Semiconductor saturable absorber mirrors (SESAM's) for femtosecond to nanosecond pulse generation in solid-state lasers. *IEEE Journal of selected topics in quantum electronics, 2*(3), 435-453. doi:10.1109/2944.571743

Keller, U., Weingarten, K. J., Kartner, F. X., Kopf, D., Braun, B., Jung, I. D., . . . Der Au, J. A. (1996). Semiconductor saturable absorber mirrors (SESAM's) for femtosecond to nanosecond pulse generation in solid-state lasers. *IEEE Journal of selected topics in quantum electronics, 2*(3), 435-453.

Kezirian, G. M., & Stonecipher, K. G. (2004). Comparison of the IntraLase femtosecond laser and mechanical keratomes for laser in situ keratomileusis. *Journal of Cataract & Refractive Surgery, 30*(4), 804-811.

Kis-Csitári, J., Kónya, Z., & Kiricsi, I. (2008). Sonochemical synthesis of inorganic nanoparticles. *Functionalized Nanoscale Materials, Devices and Systems*, 369.

Koester, C. J., & Snitzer, E. (1964). Amplification in a fiber laser. *Applied optics, 3*(10), 1182-1186.

Kong, D., Dang, W., Cha, J. J., Li, H., Meister, S., Peng, H., . . . Cui, Y. (2010). Few-layer nanoplates of Bi2Se3 and Bi2Te3 with highly tunable chemical potential. *Nano letters, 10*(6), 2245-2250.

Kowalczyk, M., Boguslawski, J., Stachowiak, D., Tarka, J., Zybala, R., Mars, K., . . . Abramski, K. M. (2016). *All-normal dispersion Yb-doped fiber laser mode-locked by Sb2Te3 topological insulator.* Paper presented at the SPIE Photonics Europe.

Kowalczyk, M., Bogusławski, J., Zybała, R., Mars, K., Mikuła, A., Soboń, G., & Sotor, J. (2016). Sb 2 Te 3-deposited D-shaped fiber as a saturable absorber for mode-locked Yb-doped fiber lasers. *Optical Materials Express, 6*(7), 2273-2282.

Kumar, R. V., Diamant, Y., & Gedanken, A. (2000). Sonochemical synthesis and characterization of nanometer-size transition metal oxides from metal acetates. *Chemistry of materials, 12*(8), 2301-2305.

Kwon, U., Kim, B.-G., Nguyen, D. C., Park, J.-H., Ha, N. Y., Kim, S.-J., . . . Park, H. J. (2016). Solution-Processible Crystalline NiO Nanoparticles for High-Performance Planar Perovskite Photovoltaic Cells. *Scientific reports, 6*, 30759.

Laroche, M., Chardon, A. M., Nilsson, J., Shepherd, D. P., Clarkson, W. A., Girard, S., & Moncorgé, R. (2002). Compact diode-pumped passively Q-switched tunable Er–Yb double-clad fiber laser. *Optics letters, 27*(22), 1980-1982. doi:10.1364/OL.27.001980

Lecaplain, C., Grelu, P., Soto-Crespo, J., & Akhmediev, N. (2012). Dissipative rogue waves generated by chaotic pulse bunching in a mode-locked laser. *Physical review letters, 108*(23), 233901.

Lee, J., Chi, C., Koo, J., & Lee, J. H. (2015). *Dissipative soliton Yb-doped fiber laser using a bulk-structured Bi 2 Te 3 topological insulator.* Paper presented at the Lasers and Electro-Optics Pacific Rim (CLEO-PR), 2015 11th Conference on.

Lee, J., Koo, J., Chi, C., & Lee, J. H. (2014). All-fiberized, passively Q-switched 1.06 μm laser using a bulk-structured Bi2Te3 topological insulator. *Journal of Optics, 16*(8), 085203.

Lee, J., Koo, J., Debnath, P., Song, Y., & Lee, J. (2013). A Q-switched, mode-locked fiber laser using a graphene oxide-based polarization sensitive saturable absorber. *Laser Physics Letters, 10*(3), 035103.

Lee, J., Koo, J., Jhon, Y. M., & Lee, J. H. (2014). A femtosecond pulse erbium fiber laser incorporating a saturable absorber based on bulk-structured Bi 2 Te 3 topological insulator. *Optics express, 22*(5), 6165-6173.

Lee, Y. H., Zhang, X. Q., Zhang, W., Chang, M. T., Lin, C. T., Chang, K. D., . . . Li, L. J. (2012). Synthesis of large-area MoS2 atomic layers with chemical vapor deposition. *Advanced Materials, 24*(17), 2320-2325.

Leigh, M., Shi, W., Zong, J., Wang, J., Jiang, S., & Peyghambarian, N. (2007). Compact, single-frequency all-fiber Q-switched laser at 1 μm. *Optics letters, 32*(8), 897-899.

Li, H.-P., Xia, H.-D., Wang, Z.-G., Zhang, X.-X., Chen, Y.-F., Zhang, S.-J., . . . Liu, Y. (2014). A compact graphene Q-switched erbium-doped fiber laser using optical circulator and tunable fiber Bragg grating. *Chinese Physics B, 23*(2), 024209.

Li, H., Wu, J., Yin, Z., & Zhang, H. (2014). Preparation and applications of mechanically exfoliated single-layer and multilayer MoS2 and WSe2 nanosheets. *Accounts of chemical research, 47*(4), 1067-1075.

Li, H., Zhang, Q., Yap, C. C. R., Tay, B. K., Edwin, T. H. T., Olivier, A., & Baillargeat, D. (2012). From bulk to monolayer MoS2: evolution of Raman scattering. *Advanced Functional Materials, 22*(7), 1385-1390.

Li, L., Yu, Y., Ye, G. J., Ge, Q., Ou, X., Wu, H., . . . Zhang, Y. (2014). Black phosphorus field-effect transistors. *Nat Nano, 9*(5), 372-377. doi:10.1038/nnano.2014.35

http://www.nature.com/nnano/journal/v9/n5/abs/nnano.2014.35.html#supplementary-information

Li, X.-H., Wang, Y.-G., Wang, Y.-S., Hu, X.-H., Zhao, W., Liu, X.-L., . . . Yang, Z. (2012). Wavelength-switchable and wavelength-tunable all-normal-dispersion mode-locked Yb-doped fiber laser based on single-walled carbon nanotube wall paper absorber. *IEEE Photonics Journal, 4*(1), 234-241.

Li, X., Wang, Y., Wang, Y., Wang, Q., Zhao, W., Zhang, Y., . . . Zhang, Y. (2013). *A single-walled carbon nanotube wall paper as an absorber for simultaneously achieving passively mode-locked and Q-switched Yb-doped fiber lasers.* Paper presented at the Nanoelectronics Conference (INEC), 2013 IEEE 5th International.

Li, X., Wang, Y., Wang, Y., Zhao, W., Yu, X., Sun, Z., . . . Wang, Q. J. (2014). Nonlinear absorption of SWNT film and its effects to the operation state of pulsed fiber laser. *Optics express, 22*(14), 17227-17235.

Li, X., Wu, K., Sun, Z., Meng, B., Wang, Y., Wang, Y., . . . Shum, P. P. (2016). Single-wall carbon nanotubes and graphene oxide-based saturable absorbers for low phase noise mode-locked fiber lasers. *Scientific reports, 6*, 25266.

Lin, S., Chui, Y., Li, Y., & Lau, S. P. (2017). Liquid-phase exfoliation of black phosphorus and its applications. *FlatChem, 2*, 15-37.

Lin, Z., Huang, X., Lan, J., Cui, S., Wang, Y., Xu, B., . . . Xu, X. (2016). Compact diode-pumped continuous-wave and passively Q-switched Nd: GYSO laser at 1.07 μm. *Optics & Laser Technology, 82*, 82-86.

Liu, H., Du, Y., Deng, Y., & Peide, D. Y. (2015). Semiconducting black phosphorus: synthesis, transport properties and electronic applications. *Chemical Society Reviews, 44*(9), 2732-2743.

Liu, H., Du, Y., Deng, Y., & Ye, P. D. (2015). Semiconducting black phosphorus: synthesis, transport properties and electronic applications. *Chemical Society Reviews, 44*(9), 2732-2743. doi:10.1039/C4CS00257A

Liu, H., Luo, A.-P., Wang, F.-Z., Tang, R., Liu, M., Luo, Z.-C., . . . Zhang, H. (2014). Femtosecond pulse erbium-doped fiber laser by a few-layer MoS 2 saturable absorber. *Optics letters, 39*(15), 4591-4594.

Liu, H., Wong, S. L., & Chi, D. (2015). CVD Growth of MoS2-based Two-dimensional Materials. *Chemical Vapor Deposition, 21*(10-11-12), 241-259.

Liu, H., Zheng, X.-W., Liu, M., Zhao, N., Luo, A.-P., Luo, Z.-C., . . . Wen, S.-C. (2014). Femtosecond pulse generation from a topological insulator mode-locked fiber laser. *Optics express, 22*(6), 6868-6873.

Liu, J., Wu, S., Yang, Q.-H., & Wang, P. (2011). Stable nanosecond pulse generation from a graphene-based passively Q-switched Yb-doped fiber laser. *Optics letters, 36*(20), 4008-4010.

Liu, J., Xu, J., & Wang, P. (2012). High repetition-rate narrow bandwidth SESAM mode-locked Yb-doped fiber lasers. *IEEE Photonics technology letters, 24*(5), 539.

Liu, M., Liu, F. Y., Man, B. Y., Bi, D., & Xu, X. Y. (2014). Multi-layered nanostructure Bi 2 Se 3 grown by chemical vapor deposition in selenium-rich atmosphere. *Applied Surface Science, 317*, 257-261.

Liu, X., Qiu, G., & Li, X. (2005). Shape-controlled synthesis and properties of uniform spinel cobalt oxide nanocubes. *Nanotechnology, 16*(12), 3035.

Liu, X., Smith, D., Fan, J., Zhang, Y.-H., Cao, H., Chen, Y., . . . Furdyna, J. (2011). Structural properties of Bi2Te3 and Bi2Se3 topological insulators grown by molecular beam epitaxy on GaAs (001) substrates. *Applied Physics Letters, 99*(17), 171903.

Lu, S., Miao, L., Guo, Z., Qi, X., Zhao, C., Zhang, H., . . . Fan, D. (2015). Broadband nonlinear optical response in multi-layer black phosphorus: an emerging infrared and mid-infrared optical material. *Optics express, 23*(9), 11183-11194.

Luo, A. P., Luo, Z. C., Xu, W. C., Dvoyrin, V., Mashinsky, V., & Dianov, E. (2011). Tunable and switchable dual-wavelength passively mode-locked Bi-doped all-fiber ring laser based on nonlinear polarization rotation. *Laser Physics Letters, 8*(8), 601-605.

Luo, Z.-C., Liu, J.-R., Wang, H.-Y., Luo, A.-P., & Xu, W.-C. (2012). Wide-band tunable passively Q-switched all-fiber ring laser based on nonlinear polarization rotation technique. *Laser physics, 22*(1), 203-206.

Luo, Z., Huang, Y., Weng, J., Cheng, H., Lin, Z., Xu, B., . . . Xu, H. (2013). 1.06 μm Q-switched ytterbium-doped fiber laser using few-layer topological insulator Bi 2 Se 3 as a saturable absorber. *Optics express, 21*(24), 29516-29522.

Luo, Z., Huang, Y., Zhong, M., Li, Y., Wu, J., Xu, B., . . . Weng, J. (2014). 1-, 1.5-, and 2-μm fiber lasers Q-switched by a broadband few-layer MoS 2 saturable absorber. *Journal of Lightwave Technology, 32*(24), 4077-4084.

Luo, Z., Zhou, M., Weng, J., Huang, G., Xu, H., Ye, C., & Cai, Z. (2010). Graphene-based passively Q-switched dual-wavelength erbium-doped fiber laser. *Optics letters, 35*(21), 3709-3711.

Maiman, T. H. (1960). Stimulated optical radiation in ruby. *nature, 187*(4736), 493-494.

Mak, K. F., Lee, C., Hone, J., Shan, J., & Heinz, T. F. (2010). Atomically thin MoS 2: a new direct-gap semiconductor. *Physical review letters, 105*(13), 136805.

Mao, D., Cui, X., Zhang, W., Li, M., Feng, T., Du, B., . . . Zhao, J. (2017). Q-switched fiber laser based on saturable absorption of ferroferric-oxide nanoparticles. *Photonics Research, 5*(1), 52-56.

Martinez, A., Fuse, K., & Yamashita, S. (2011). Mechanical exfoliation of graphene for the passive mode-locking of fiber lasers. *Applied Physics Letters, 99*(12), 121107.

Mou, C., Arif, R., Rozhin, A., & Turitsyn, S. (2012). Passively harmonic mode locked erbium doped fiber soliton laser with carbon nanotubes based saturable absorber. *Optical Materials Express, 2*(6), 884-890.

Mousavi-Kamazani, M., Rahmatolahzadeh, R., Shobeiri, S. A., & Beshkar, F. (2017). Sonochemical synthesis, formation mechanism, and solar cell application of tellurium nanoparticles. *Ultrasonics Sonochemistry, 39*, 233-239.

Mu, H., Lin, S., Wang, Z., Xiao, S., Li, P., Chen, Y., . . . Bao, Q. (2015). Black Phosphorus–Polymer Composites for Pulsed Lasers. *Advanced Optical Materials, 3*(10), 1447-1453. doi:10.1002/adom.201500336

Nady, A., Ahmed, M., Latiff, A., Numan, A., Ooi, C. R., & Harun, S. (2017). Nickel oxide nanoparticles as a saturable absorber for an all-fiber passively Q-switched erbium-doped fiber laser. *Laser Physics, 27*(6), 065105.

Nady, A., Ahmed, M., Latiff, A., Ooi, C. R., & Harun, S. (2017). Femtoseconds soliton mode-locked erbium-doped fiber laser based on nickel oxide nanoparticle saturable absorber. *Chinese Optics Letters, 15*(10), 100602.

Nady, A., Ahmed, M., Numan, A., Ramesh, S., Latiff, A., Ooi, C., . . . Harun, S. (2017). Passively Q-switched erbium-doped fibre laser using cobalt oxide nanocubes as a saturable absorber. *Journal of Modern Optics*, 1-6.

Nikumb, S., Chen, Q., Li, C., Reshef, H., Zheng, H., Qiu, H., & Low, D. (2005). Precision glass machining, drilling and profile cutting by short pulse lasers. *Thin Solid Films, 477*(1), 216-221.

Nishizawa, N. (2014). Ultrashort pulse fiber lasers and their applications. *Japanese Journal of Applied Physics, 53*(9), 090101.

Nishizawa, N., Seno, Y., Sumimura, K., Sakakibara, Y., Itoga, E., Kataura, H., & Itoh, K. (2008). All-polarization-maintaining Er-doped ultrashort-pulse fiber laser using carbon nanotube saturable absorber. *Optics express, 16*(13), 9429-9435.

Noor, Y. M., Tam, S., Lim, L., & Jana, S. (1994). A review of the Nd: YAG laser marking of plastic and ceramic IC packages. *Journal of materials processing technology, 42*(1), 95-133.

Novoselov, K., Jiang, D., Schedin, F., Booth, T., Khotkevich, V., Morozov, S., & Geim, A. (2005). Two-dimensional atomic crystals. *Proceedings of the National Academy of Sciences of the United States of America, 102*(30), 10451-10453.

Numan, A., Duraisamy, N., Omar, F. S., Mahipal, Y., Ramesh, K., & Ramesh, S. (2016). Enhanced electrochemical performance of cobalt oxide nanocube intercalated reduced graphene oxide for supercapacitor application. *RSC Advances, 6*(41), 34894-34902.

Numan, A., Shahid, M. M., Omar, F. S., Ramesh, K., & Ramesh, S. (2017). Facile fabrication of cobalt oxide nanograin-decorated reduced graphene oxide composite as ultrasensitive platform for dopamine detection. *Sensors and Actuators B: Chemical, 238*, 1043-1051.

Park, K., Lee, J., Lee, Y. T., Choi, W. K., Lee, J. H., & Song, Y. W. (2015). Black phosphorus saturable absorber for ultrafast mode-locked pulse laser via evanescent field interaction. *Annalen der Physik, 527*(11-12), 770-776.

Plamann, K., Aptel, F., Arnold, C., Courjaud, A., Crotti, C., Deloison, F., . . . Legeais, J.-M. (2010). Ultrashort pulse laser surgery of the cornea and the sclera. *Journal of Optics, 12*(8), 084002.

Popa, D., Sun, Z., Hasan, T., Torrisi, F., Wang, F., & Ferrari, A. (2011). Graphene Q-switched, tunable fiber laser. *Applied Physics Letters, 98*(7), 073106.

Qiao, J., Kong, X., Hu, Z.-X., Yang, F., & Ji, W. (2014). High-mobility transport anisotropy and linear dichroism in few-layer black phosphorus. *5*, 4475. doi:10.1038/ncomms5475

https://www.nature.com/articles/ncomms5475#supplementary-information

Qiao, Y., Wen, L., Wu, B., Ren, J., Chen, D., & Qiu, J. (2008). Preparation and spectroscopic properties of Yb-doped and Yb–Al-codoped high silica glasses. *Materials Chemistry and Physics, 107*(2), 488-491.

Rahman, M. M., Wang, J.-Z., Deng, X.-L., Li, Y., & Liu, H.-K. (2009). Hydrothermal synthesis of nanostructured Co 3 O 4 materials under pulsed magnetic field and with an aging technique, and their electrochemical performance as anode for lithium-ion battery. *Electrochimica Acta, 55*(2), 504-510.

Rai, A. K., Anh, L. T., Park, C.-J., & Kim, J. (2013). Electrochemical study of NiO nanoparticles electrode for application in rechargeable lithium-ion batteries. *Ceramics International, 39*(6), 6611-6618.

Rashid, F., Azzuhri, S. R., Salim, M., Shaharuddin, R., Ismail, M., Ismail, M., . . . Ahmad, H. (2016). Using a black phosphorus saturable absorber to generate dual wavelengths in a Q-switched ytterbium-doped fiber laser. *Laser Physics Letters, 13*(8), 085102.

Ren, J., Wang, S., Cheng, Z., Yu, H., Zhang, H., Chen, Y., . . . Wang, P. (2015). Passively Q-switched nanosecond erbium-doped fiber laser with MoS 2 saturable absorber. *Optics express*, *23*(5), 5607-5613.

Rusdi, M., Latiff, A., Hanafi, E., Mahyuddin, M., Shamsudin, H., Dimyati, K., & Harun, S. (2016). Molybdenum Disulphide Tape Saturable Absorber for Mode-Locked Double-Clad Ytterbium-Doped All-Fiber Laser Generation. *Chinese Physics Letters*, *33*(11), 114201.

Russo, V., Bailini, A., Zamboni, M., Passoni, M., Conti, C., Casari, C., . . . Bottani, C. (2008). Raman spectroscopy of Bi-Te thin films. *Journal of Raman Spectroscopy, 39*(2), 205-210.

Ryu, H. Y., Moon, H. S., & Suh, H. S. (2007). Optical frequency comb generator based on actively mode-locked fiber ring laser using an acousto-optic modulator with injection-seeding. *Optics express*, *15*(18), 11396-11401.

Santhoshkumar, A., Kavitha, H. P., & Suresh, R. (2016). Hydrothermal Synthesis, Characterization and Antibacterial Activity of NiO Nanoparticles. *Journal of Advanced Chemical Sciences*, 230-232.

Sathiyan, S., Velmurugan, V., Senthilnathan, K., Babu, P. R., & Sivabalan, S. (2016). All-normal dispersion passively mode-locked Yb-doped fiber laser using MoS2–PVA saturable absorber. *Laser physics*, *26*(5), 055103.

Serbin, J., Bauer, T., Fallnich, C., Kasenbacher, A., & Arnold, W. (2002). Femtosecond lasers as novel tool in dental surgery. *applied surface science, 197*, 737-740.

Set, S. Y., Yaguchi, H., Tanaka, Y., & Jablonski, M. (2004). Ultrafast fiber pulsed lasers incorporating carbon nanotubes. *IEEE Journal of Selected Topics in Quantum Electronics*, *10*(1), 137-146.

Sheik-Bahae, M., Said, A. A., Wei, T.-H., Hagan, D. J., & Van Stryland, E. W. (1990). Sensitive measurement of optical nonlinearities using a single beam. *IEEE Journal of quantum electronics*, *26*(4), 760-769.

Siegman, A. E. (1986). Lasers university science books. *Mill Valley, CA*, *37*, 462-466.

Sietsma, J. R., Meeldijk, J. D., den Breejen, J. P., Versluijs-Helder, M., Van Dillen, A. J., de Jongh, P. E., & de Jong, K. P. (2007). The preparation of supported NiO and Co3O4 nanoparticles by the nitric oxide controlled thermal decomposition of nitrates. *Angewandte Chemie*, *119*(24), 4631-4633.

Singh, V., & Major, D. T. (2016). Electronic Structure and Bonding in Co-Based Single and Mixed Valence Oxides: A Quantum Chemical Perspective. *Inorganic chemistry*, *55*(7), 3307-3315.

Snitzer, E. (1961). Proposed fiber cavities for optical masers. *Journal of Applied Physics*, *32*(1), 36-39.

Solodyankin, M. A., Obraztsova, E. D., Lobach, A. S., Chernov, A. I., Tausenev, A. V., Konov, V. I., & Dianov, E. M. (2008). Mode-locked 1.93 μm thulium fiber laser with a carbon nanotube absorber. *Optics letters*, *33*(12), 1336-1338.

Song, H., Wang, Q., Zhang, Y., & Li, L. (2017). Mode-locked ytterbium-doped all-fiber lasers based on few-layer black phosphorus saturable absorbers. *Optics Communications*, *394*, 157-160.

Sotor, J., Sobon, G., & Abramski, K. M. (2014). Sub-130 fs mode-locked Er-doped fiber laser based on topological insulator. *Optics express, 22*(11), 13244-13249.

Sotor, J., Sobon, G., Grodecki, K., & Abramski, K. (2014). Mode-locked erbium-doped fiber laser based on evanescent field interaction with Sb2Te3 topological insulator. *Applied Physics Letters, 104*(25), 251112.

Sotor, J., Sobon, G., Jagiello, J., Lipinska, L., & Abramski, K. (2015). Repetition frequency scaling of an all-polarization maintaining erbium-doped mode-locked fiber laser based on carbon nanotubes saturable absorber. *Journal of Applied Physics, 117*(13), 133103.

Sotor, J., Sobon, G., Kowalczyk, M., Macherzynski, W., Paletko, P., & Abramski, K. M. (2015). Ultrafast thulium-doped fiber laser mode locked with black phosphorus. *Optics letters, 40*(16), 3885-3888.

Sotor, J., Sobon, G., Macherzynski, W., & Abramski, K. (2014). Harmonically mode-locked Er-doped fiber laser based on a Sb2Te3 topological insulator saturable absorber. *Laser Physics Letters, 11*(5), 055102.

Sotor, J., Sobon, G., Macherzynski, W., Paletko, P., Grodecki, K., & Abramski, K. M. (2014). Mode-locking in Er-doped fiber laser based on mechanically exfoliated Sb 2 Te 3 saturable absorber. *Optical Materials Express, 4*(1), 1-6.

Stetser, D., & DeMaria, A. (1966). Optical spectra of ultrashort optical pulses generated by mode-locked glass: Nd lasers. *Applied Physics Letters, 9*(3), 118-120.

Su, X., Wang, Y., Zhang, B., Zhao, R., Yang, K., He, J., . . . Tao, X. (2016). Femtosecond solid-state laser based on a few-layered black phosphorus saturable absorber. *Optics letters, 41*(9), 1945-1948.

Sugai, S., & Shirotani, I. (1985). Raman and infrared reflection spectroscopy in black phosphorus. *Solid state communications, 53*(9), 753-755.

Sun, C., Su, X., Xiao, F., Niu, C., & Wang, J. (2011). Synthesis of nearly monodisperse Co 3 O 4 nanocubes via a microwave-assisted solvothermal process and their gas sensing properties. *Sensors and Actuators B: Chemical, 157*(2), 681-685.

Sun, L., Zhang, L., Yu, H., Guo, L., Ma, J., Zhang, J., . . . Li, J. (2010). 880 nm LD pumped passive mode-locked TEM00 Nd: YVO4 laser based on SESAM. *Laser Physics Letters, 7*(10), 711.

Sun, Z., Hasan, T., & Ferrari, A. (2012). Ultrafast lasers mode-locked by nanotubes and graphene. *Physica E: Low-dimensional Systems and Nanostructures, 44*(6), 1082-1091.

Sun, Z., Hasan, T., Torrisi, F., Popa, D., Privitera, G., Wang, F., . . . Ferrari, A. C. (2010). Graphene mode-locked ultrafast laser. *Acs Nano, 4*(2), 803-810.

Svelto, O., & Hanna, D. C. (1998). *Principles of lasers* (Vol. 4): Springer.

Tang, Y., Li, X., & Wang, Q. J. (2013). High-power passively Q-switched thulium fiber laser with distributed stimulated Brillouin scattering. *Optics letters, 38*(24), 5474-5477.

Tian, W., Yu, W., Shi, J., & Wang, Y. (2017). The Property, Preparation and Application of Topological Insulators: A Review. *Materials, 10*(7), 814.

Tian, Z., Wu, K., Kong, L., Yang, N., Wang, Y., Chen, R., . . . Tang, Y. (2015). Mode-locked thulium fiber laser with MoS2. *Laser Physics Letters, 12*(6), 065104.

Tolstik, N., Pospischil, A., Sorokin, E., & Sorokina, I. T. (2014). Graphene mode-locked Cr: ZnS chirped-pulse oscillator. *Optics express, 22*(6), 7284-7289.

Voiry, D., Salehi, M., Silva, R., Fujita, T., Chen, M., Asefa, T., . . . Chhowalla, M. (2013). Conducting MoS2 nanosheets as catalysts for hydrogen evolution reaction. *Nano Lett, 13*(12), 6222-6227.

Wang, C., Li, Y., Ding, G., Xie, X., & Jiang, M. (2013). Preparation and characterization of graphene oxide/poly (vinyl alcohol) composite nanofibers via electrospinning. *Journal of Applied Polymer Science, 127*(4), 3026-3032.

Wang, F. (2017). Two-dimensional materials for ultrafast lasers. *Chinese Physics B, 26*(3), 034202.

Wang, J., Gu, B., Wang, H.-T., & Ni, X.-W. (2010). Z-scan analytical theory for material with saturable absorption and two-photon absorption. *Optics Communications, 283*(18), 3525-3528.

Wang, K., Feng, Y., Chang, C., Zhan, J., Wang, C., Zhao, Q., . . . Wang, J. (2014). Broadband ultrafast nonlinear absorption and nonlinear refraction of layered molybdenum dichalcogenide semiconductors. *Nanoscale, 6*(18), 10530-10535.

Wang, K., Wang, J., Fan, J., Lotya, M., O'Neill, A., Fox, D., . . . Zhao, Q. (2013). Ultrafast saturable absorption of two-dimensional MoS2 nanosheets. *Acs Nano, 7*(10), 9260-9267.

Wang, Q. H., Kalantar-Zadeh, K., Kis, A., Coleman, J. N., & Strano, M. S. (2012). Electronics and optoelectronics of two-dimensional transition metal dichalcogenides. *Nature nanotechnology, 7*(11), 699-712.

Wang, X.-D., Luo, Z.-C., Liu, H., Liu, M., Luo, A.-P., & Xu, W.-C. (2014). Microfiber-based gold nanorods as saturable absorber for femtosecond pulse generation in a fiber laser. *Applied Physics Letters, 105*(16), 161107.

Wang, X., & Li, M. (2010). Continuous-wave passively mode-locked Nd: YVO 4/KTP green laser with a semiconductor saturable absorber mirror. *Laser Physics, 20*(4), 733-736.

Weber, M., Lynch, J., Blackburn, D., & Cronin, D. (1983). Dependence of the stimulated emission cross section of Yb 3+ on host glass composition. *IEEE Journal of quantum electronics, 19*(10), 1600-1608.

Wen, M., Xu, J., Liu, L., Lai, P.-T., & Tang, W.-M. (2017). Improved Electrical Performance of Multilayer MoS 2 Transistor With NH 3-Annealed ALD HfTiO Gate Dielectric. *IEEE Transactions on Electron Devices, 64*(3), 1020-1025.

Woodward, R., Howe, R., Runcorn, T., Hu, G., Torrisi, F., Kelleher, E., & Hasan, T. (2015). Wideband saturable absorption in few-layer molybdenum diselenide (MoSe 2) for Q-switching Yb-, Er-and Tm-doped fiber lasers. *Optics express, 23*(15), 20051-20061.

Woodward, R., Kelleher, E., Howe, R., Hu, G., Torrisi, F., Hasan, T., . . . Taylor, J. (2014). Tunable Q-switched fiber laser based on saturable edge-state absorption in few-layer molybdenum disulfide (MoS 2). *Optics express, 22*(25), 31113-31122.

Woodward, R. I., Kelleher, E. J., Runcorn, T., Popov, S. V., Torrisi, F., Howe, R. T., & Hasan, T. (2014). *Q-switched fiber laser with MoS2 saturable absorber.* Paper presented at the CLEO: Science and Innovations.

Wu, K., Zhang, X., Wang, J., & Chen, J. (2015). 463-MHz fundamental mode-locked fiber laser based on few-layer MoS2 saturable absorber. *Optics letters, 40*(7), 1374-1377. doi:10.1364/OL.40.001374

Xia, F., Wang, H., & Jia, Y. (2014). Rediscovering black phosphorus as an anisotropic layered material for optoelectronics and electronics. *Nature communications, 5*, 4458.

Xu, J., Wu, S., Liu, J., Wang, Q., Yang, Q.-H., & Wang, P. (2012). Nanosecond-pulsed erbium-doped fiber lasers with graphene saturable absorber. *Optics Communications, 285*(21), 4466-4469.

Yamamoto, H., Tanaka, S., Naito, T., & Hirao, K. (2002). Nonlinear change of refractive index of Co 3 O 4 thin films induced by semiconductor laser (λ= 405 nm) irradiation. *Applied Physics Letters, 81*(6), 999-1001.

Yan, P., Lin, R., Chen, H., Zhang, H., Liu, A., Yang, H., & Ruan, S. (2015). Topological insulator solution filled in photonic crystal fiber for passive mode-locked fiber laser. *IEEE Photonics Technology Letters, 27*(3), 264-267.

Yi, M., & Shen, Z. (2015). A review on mechanical exfoliation for the scalable production of graphene. *Journal of Materials Chemistry A, 3*(22), 11700-11715.

Yu, H., Zheng, X., Yin, K., & Jiang, T. (2015). Thulium/holmium-doped fiber laser passively mode locked by black phosphorus nanoplatelets-based saturable absorber. *Applied optics, 54*(34), 10290-10294.

Yu, Z., Song, Y., Tian, J., Dou, Z., Guoyu, H., Li, K., . . . Zhang, X. (2014). High-repetition-rate Q-switched fiber laser with high quality topological insulator Bi 2 Se 3 film. *Optics express, 22*(10), 11508-11515.

Yuan, L., Ge, J., Peng, X., Zhang, Q., Wu, Z., Jian, Y., . . . Han, J. (2016). A reliable way of mechanical exfoliation of large scale two dimensional materials with high quality. *AIP Advances, 6*(12), 125201.

Zayhowski, J., & Kelley, P. (1991). Optimization of Q-switched lasers. *IEEE journal of quantum electronics, 27*(9), 2220-2225.

Zervas, M. N. (2014). High power ytterbium-doped fiber lasers—fundamentals and applications. *International Journal of Modern Physics B, 28*(12), 1442009.

Zhan, Y., Wang, L., Wang, J. Y., Li, H. W., & Yu, Z. H. (2015). Yb: YAG thin disk laser passively Q-switched by a hydro-thermal grown molybdenum disulfide saturable absorber. *Laser Physics, 25*(2), 025901.

Zhang, H., Bao, Q., Tang, D., Zhao, L., & Loh, K. (2009). Large energy soliton erbium-doped fiber laser with a graphene-polymer composite mode locker. *Applied Physics Letters, 95*(14), 141103.

Zhang, H., Lu, S., Zheng, J., Du, J., Wen, S., Tang, D., & Loh, K. (2014). Molybdenum disulfide (MoS 2) as a broadband saturable absorber for ultra-fast photonics. *Optics express, 22*(6), 7249-7260.

Zhang, H., Tang, D., Zhao, L., Bao, Q., Loh, K. P., Lin, B., & Tjin, S. C. (2010). Compact graphene mode-locked wavelength-tunable erbium-doped fiber lasers: from all anomalous dispersion to all normal dispersion. *Laser Physics Letters, 7*(8), 591.

Zhang, L., Fan, J., Wang, J., Hu, J., Lotya, M., Wang, G., . . . Wang, J. (2012). Graphene incorporated Q-switching of a polarization-maintaining Yb-doped fiber laser. *Laser Physics Letters, 9*(12), 888.

Zhang, L., Guo, L., Xiong, B., Yan, X., Sun, L., Hou, W., . . . Li, J. (2010). LD side-pumped high beam quality passive Q-switched and mode-locked Nd: YAG laser based on SESAM. *Laser physics, 20*(9), 1798-1801.

Zhang, L., Wang, Y., Yu, H., Sun, L., Hou, W., Lin, X., & Li, J. (2011). Passive mode-locked Nd: YVO 4 laser using a multi-walled carbon nanotube saturable absorber. *Laser Physics, 21*(8), 1382-1386.

Zhang, L., Zhao, X., Ma, W., Wu, M., Qian, N., & Lu, W. (2013). Novel three-dimensional Co 3 O 4 dendritic superstructures: hydrothermal synthesis, formation mechanism and magnetic properties. *CrystEngComm, 15*(7), 1389-1396.

Zhang, M., Chen, L., Zhou, C., Cai, Y., Ren, L., & Zhang, Z. (2009). Mode-locked ytterbium-doped linear-cavity fiber laser operated at low repetition rate. *Laser Physics Letters, 6*(9), 657.

Zhang, M., Richard, C., Howe, T., Woodward, R. I., Edmund, J., Kelleher, R., . . . Taylor, J. R. (2015). Solution processed MoS^ sub 2^-PVA composite for sub-bandgap mode-locking of a wideband tunable ultrafast Er: fiber laser. *Nano Research, 8*(5), 1522.

Zhang, S., Dong, N., McEvoy, N., O'Brien, M., Winters, S., Berner, N. C., . . . Chen, Z. (2015). Direct observation of degenerate two-photon absorption and its saturation in WS2 and MoS2 monolayer and few-layer films. *ACS nano, 9*(7), 7142-7150.

Zhao, J., Wang, Y., Yan, P., Ruan, S., Tsang, Y., Zhang, G., & Li, H. (2014). An Ytterbium-doped fiber laser with dark and Q-switched pulse generation using graphene-oxide as saturable absorber. *Optics Communications, 312*, 227-232. doi:http://dx.doi.org/10.1016/j.optcom.2013.09.038

Zhao, L., Tang, D., Zhang, H., Wu, X., Bao, Q., & Loh, K. P. (2010). Dissipative soliton operation of an ytterbium-doped fiber laser mode locked with atomic multilayer graphene. *Optics letters, 35*(21), 3622-3624.

Zhou, D.-P., Wei, L., Dong, B., & Liu, W.-K. (2010). Tunable passively $ Q $-switched erbium-doped fiber laser with carbon nanotubes as a saturable absorber. *IEEE Photonics technology letters, 22*(1), 9-11.

Zhu, X., Wang, J., Lau, P., Nguyen, D., Norwood, R., & Peyghambarian, N. (2010). Nonlinear optical performance of periodic structures made from composites of polymers and Co 3 O 4 nanoparticles. *Applied Physics Letters, 97*(9), 093503.

Zhu, X., Wang, J., Nguyen, D., Thomas, J., Norwood, R. A., & Peyghambarian, N. (2012). Linear and nonlinear optical properties of Co 3 O 4 nanoparticle-doped polyvinyl-alcohol thin films. *Optical Materials Express, 2*(1), 103-110.

Zirngibl, M., Stulz, L., Stone, J., Hugi, J., DiGiovanni, D., & Hansen, P. (1991). 1.2 ps pulses from passively mode-locked laser diode pumped Er-doped fibre ring laser. *Electronics Letters, 27*(19), 1734-1735.

Zorkipli, N. N. M., Kaus, N. H. M., & Mohamad, A. A. (2016). Synthesis of NiO Nanoparticles through Sol-gel Method. *Procedia Chemistry, 19*, 626-631.

Zurhelle, A. F., Deringer, V. L., Stoffel, R. P., & Dronskowski, R. (2016). Ab initio lattice dynamics and thermochemistry of layered bismuth telluride (Bi2Te3). *Journal of Physics: Condensed Matter*, *28*(11), 115401.

LIST OF PUBLICATIONS AND PAPERS PRESENTED

Below is the list of publications and conference during the study;

1) **Al-Masoodi, A. H. H.**, Ahmed, M. H. M., Arof, H., Banabila, A. M., & Harun, S. W. (2015). Q-switched Ytterbium doped fiber laser using a multi-walled carbon nanotubes embedded in polyethylene oxide film. *OPTOELECTRONICS AND ADVANCED MATERIALS-RAPID COMMUNICATIONS*, *9*(9-10), 1104-1109.
2) **Al-Masoodi, A. H. H.**, Ahmad, F., Ahmad, H., & Harun, S. W. (2015). Q-Switched Yb-doped fiber ring laser with a saturable absorber based on a graphene polyvinyl alcohol film. *Journal of Russian Laser Research*, *36*(4), 389-394.
3) **Al-Masoodi, A. H. H.**, Ahmed, M. H. M., Latiff, A. A., Arof, H., & Harun, S. W. (2016). Q-Switched Ytterbium-Doped Fiber Laser Using Black Phosphorus as Saturable Absorber. *Chinese Physics Letters*, *33*(5), 054206.
4) **Al-Masoodi, A. H. H.**, Ahmed, M. H. M., Latiff, A. A., Arof, H., & Harun, S. W. (2017). Passively Q-switched Ytterbium doped fiber laser with mechanically exfoliated MoS2 saturable absorber. *Indian Journal of Physics*, *91*(5), 575-580.
5) **Al-Masoodi, A. H. H**, Ahmad, F., Ahmed, M. H., Arof, H., & Harun, S. W. (2017). Q-switched ytterbium-doped fiber laser with topological insulator-based saturable absorber. *Optical Engineering*, *56*(5), 056103-056103.
6) **Al-Masoodi, A. H. H.**, Ahmed, M. H. M., Latiff, A. A., Azzuhri, S. R., Arof, H., & Harun, S. W. (2017). Passively Mode-locked Ytterbium-doped Fiber Laser Operation with few layer MoS 2 PVA Saturable Absorber. *Optik-International Journal for Light and Electron Optics*, 145, 543-548.
7) **Al-Masoodi, A. H. H.**, Yasin, M., Ahmed, M. H. M., Latiff, A. A., Arof, H., & Harun, S. W. (2017). Mode-locked ytterbium-doped fiber laser using mechanically exfoliated

black phosphorus as saturable absorber. *Optik-International Journal for Light and Electron Optics*.

8) Ahmed, M. H. M., **Al-Masoodi, A. H. H.**, Yasin, M., Arof, H., & Harun, S. W. (2017). Stretched and soliton femtosecond pulse generation with graphene saturable absorber by manipulating cavity dispersion. *Optik-International Journal for Light and Electron Optics*, *138*, 250-255.

9) Ahmed, M. H. M., **Al-Masoodi, A. H. H.**, Latiff, A. A., Arof, H., & Harun, S. W. (2017). Mechanically exfoliated 2D nanomaterials as saturable absorber for Q-switched erbium doped fiber laser. *Indian Journal of Physics*, 1-6.

10) **Al-Masoodi, A. H. H.**, Ahmed, M. H. M., Arof, H., & Harun, S. W. (2016). High energy Q-switched Ytterbium doped fiber laser with topological insulator bismuth selenide (Bi_2Se_3) Saturable Absorber. 1ST INTERNATIONAL RESEARCH CONFERENCE ON ENGINEERING, SCIENCE AND HUMANITIES (IRCESH 2016).